Durability of Cementitious Materials in Arctic Regions: Investigating Freeze-Thaw Damage and Chloride Ingress Diffusion Mechanisms

Md Hasibul Hasan Rahat

Dissertation submitted to the faculty of the Virginia Polytechnic Institute and State University in partial fulfillment of the requirements for the degree of
Doctor of Philosophy
in
Civil Engineering

Alexander S. Brand, Chair
Sherif L. Abdelaziz
Gerardo W. Flintsch
Stefan Jacobsen

June 23, 2025
Blacksburg, Virginia

Keywords: Freeze-Thaw damage; Chloride Ingress; Diffusion Mechanism; Arctic Region; Cellulose nanofiber gel; Repair techniques; Transmission X-ray microscopy; Neutron radiography

Copyright © 2025, Md Hasibul Hasan Rahat
ALL RIGHTS RESERVED

Durability of Cementitious Materials in Arctic Regions: Investigating Freeze-Thaw Damage and Chloride Ingress Diffusion Mechanisms

Md Hasibul Hasan Rahat

Academic Abstract

Concrete infrastructure in the Arctic coastal region faces durability challenges from freeze-thaw (F-T) cycles and chloride ingress due to seawater and deicing salts, resulting in surface scaling, spalling, and cracking. Climate change exacerbates these issues, particularly in high-latitude areas like Alaska, where rising temperatures lead to permafrost thaw and increased infrastructure vulnerability. Projections indicate that climate-related infrastructure costs in Alaska could reach $5.5 billion by 2099, highlighting the need for more resilient infrastructure. This dissertation investigates F-T damage mechanisms, explores strategies to enhance cementitious material durability, optimizes repair techniques for long-term performance, and develops a real-time monitoring technique to track pore water movement within the concrete microstructure and its impact on microstructural cracking.

First, this dissertation investigated the combined effects of F-T cycles and chloride ingress on conventional (Group A) and polyvinyl alcohol (PVA) fiber-reinforced (Group B) concretes cured for 14 days and 70 days in plain water and in simulated seawater conditions. This dissertation also utilized a non-destructive technique, transmission X-ray microscopy (TXM), to quantify the diffusion coefficient (D_c) as a function of F-T cycles for the first time in the literature. The results emphasize the importance of the air void system in reducing F-T damage and chloride ingress, with longer curing durations enhancing concrete's resistance to these issues. Group A showed superior performance due to its improved air void system, which enhanced F-T resistance by accommodating internal pressure changes and reducing crack propagation. In addition, seawater exposure exacerbated F-T damage, accelerating chloride ingress and deterioration compared to F-T cycles in plain water. The findings suggest that while PVA fibers enhance mechanical properties, they may also disrupt the air-void system, reducing its protective capabilities against chloride ingress and F-T damage. These results emphasize optimizing air void characteristics in fiber-reinforced concretes to balance mechanical performance with long-term durability in harsh environmental conditions.

Second, this dissertation explored the role of cellulose nanofiber (CNF) gels in enhancing F-T resistance and reducing chloride ingress in cement paste. CNF suspensions, prepared using a nitro-oxidation process, formed hydrogels in the presence of metal ions (*e.g.*, Na^+, Ca^{2+}) within the pore solution, reducing the freezing point of the pore solution of cement paste. It was found that specimens containing CNF suspensions exhibited improved F-T resistance characteristics when compared to specimens without CNF suspensions. Additionally, TXM analysis showed that specimens containing CNF suspensions exhibited significantly lower diffusion coefficients than conventional cement paste. These findings suggest that CNF gels reduce permeability and enhance durability by modifying the microstructure of the cement paste.

Third, this dissertation investigated the durability of concrete repair-substrate interfaces under F-T cycling, emphasizing the impact of substrate moisture conditions and water-to-cement (w/c) ratios on the overlay transition zone (OTZ), the weakest region of repair-substrate concrete analogous to the interfacial transition zone between aggregates and paste in concrete microstructure. Mechanical properties, fracture characteristics, ion diffusion, water absorption, and F-T resistance were evaluated to assess repair performance under varying conditions. The results demonstrated that repair overlays with lower w/c ratios applied to saturated surface-dry (SSD) substrates exhibited superior durability, reducing water absorption, ion penetration, and F-T damage compared to higher w/c ratio repairs. TXM analyzed the time-dependent diffusion along the OTZ for the first time in the literature, finding that repair-substrate specimens showed a notable increase in diffusion coefficient after F-T cycles compared to the substrate. The findings indicate that in the absence of surface preparation, a lower w/c ratio is recommended to mitigate OTZ deficiencies and enhance the durability of concrete repairs in cold and F-T environments.

Finally, *in situ* neutron radiography was utilized for the first time in the literature to track real-time pore water movement in concrete macropores under subzero conditions. The results demonstrated that unfrozen water moved away from the freezing front, which is suspected to generate hydraulic pressure and contribute to microcracking. These findings underscore the role of moisture redistribution and full saturation in F-T damage, providing insights for creating more durable concrete in cold regions.

In summary, this dissertation integrates advanced experimental techniques to develop a mechanistic understanding of the deterioration of cementitious materials under extreme environmental conditions. By combining TXM, neutron radiography, and comprehensive materials testing, the findings provide new insights into the interplay between F-T damage and chloride ingress. These results inform the design of more resilient cementitious materials, repair strategies, and construction practices for arctic coastal regions, ultimately contributing to infrastructure longevity and sustainability in the face of climate change.

Durability of Cementitious Materials in Arctic Regions: Investigating Freeze-Thaw Damage and Chloride Ingress Diffusion Mechanisms

Md Hasibul Hasan Rahat

General Audience Abstract

Concrete infrastructure in Arctic coastal areas faces severe durability challenges due to extreme weather conditions. One major issue is freeze-thaw (F-T) damage, which causes cracking, spalling, and/or scaling over time. Another challenge is chloride diffusion from seawater and deicing chemicals, which can lead to corrosion of reinforcing steel and further weaken concrete structures. As climate change raises global temperatures, permafrost thawing accelerates, which can exacerbate these problems. This dissertation investigated the combined effects of F-T damage and ion ingress on concrete, explored strategies to enhance durability, evaluated repair techniques, and introduced advanced methods for monitoring real-time pore water movement in concrete microstructure.

First, this dissertation examined how F-T cycles and chloride diffusion affect conventional and fiber-reinforced concrete. Transmission X-ray microscopy (TXM), a non-destructive imaging technique, was used to investigate ion diffusion under F-T conditions. The findings revealed that an optimized air void system improves F-T resistance. However, while fiber reinforcement increases concrete strength, it can disrupt the air void system, potentially reducing F-T resistance and increasing chloride diffusion. Exposure to seawater exacerbates F-T damage, emphasizing the need for cementitious materials suited for coastal environments.

Second, this dissertation explored using cellulose nanofibers (CNF) suspensions produced by biowaste to enhance cement paste resistance to F-T cycles and chloride ingress. These nanofibers can create a hydrogel within the paste microstructure, reducing freezing impact and improving durability. The results showed that CNF-modified cement paste performs significantly better under F-T conditions, presenting a promising approach to extending the lifespan of cementitious materials in cold regions.

Third, this dissertation investigated challenges in concrete repair strategies under F-T cycles. Using TXM, the research demonstrates how deleterious ions diffused through the repair-substrate concrete bond interface. It highlights the importance of the repair mix's water-to-cement ratio and the existing substrate's moisture condition during concrete repairs to improve long-term durability against F-T cycles.

Finally, this dissertation pioneered using *in situ* neutron radiography to track pore water movement within concrete macropores during freezing. This technique reveals that unfrozen water moves away from the freezing front, which can generate internal pressure and contribute to cracking.

This dissertation enhances the understanding of the durability of cementitious materials in Arctic coastal and other cold regions and offers innovative solutions for infrastructure resilience.

Acknowledgements

First and foremost, I extend my deepest gratitude to Allah, whose blessings have guided my academic journey at Virginia Tech.

I am profoundly grateful to my advisor, Prof. Alexander S. Brand, for being an exceptional academic mentor and a guiding force in my professional career. From the beginning, he supported me as I adjusted to a new environment, offering guidance in research, personal matters, and legal concerns without hesitation. Balancing a demanding Ph.D. program with family life would not have been possible without his kindness and encouragement. Dr. Brand granted me complete independence in research, never discouraging any idea and always showing patience during setbacks. His insightful discussions, constructive feedback, and unwavering belief in my potential have shaped my research and career. Working under his mentorship has been my most incredible privilege.

I am sincerely thankful to my committee members, Prof. Sherif L. Abdelaziz, Prof. Gerardo W. Flintsch, and Prof. Stefan Jacobsen, for their invaluable support, thoughtful advice, and careful review of my dissertation. I was fortunate to work on a project led by Prof. Abdelaziz, where his commitment to research excellence and resource support played a pivotal role in enabling this work.

I also extend my gratitude to Dr. David Mokarem, Brett Farmer, Garret Blankenship, Dr. Thomas Staley, Dr. Rituraj Borgohain, and all the personnel at the Civil and Environmental Engineering Department, the Thomas M. Murray Structures and Materials Laboratory, and the Materials Science and Engineering Department for providing the necessary facilities and support throughout this research.

I appreciate the Broad Agency Announcement Program and the Cold Regions Research and Engineering Laboratory (ERDC-CRREL) for funding this research. I am also grateful to my lab colleagues, Dr. Amir Behravan, Dr. Ebenezer Fanijo, Douglas Annand, Dr. Thien Tran, Dr. Rashed Alarrak, Tu-Nam Nguyen, Janelle Davis, Dip Banik, Sung-Won Cho, and Dr. Sung-Eun Cho for their solidarity, support, and collaboration.

Finally, I offer my deepest gratitude to my family. My parents have been my unwavering foundation, instilling the values that carried me through this journey. My beloved wife, Nadia, and our wonderful son, Raiyan, have been my constant companions throughout this Ph.D. Their patience, love, and encouragement made every challenge manageable. I am also thankful to my sister, brother-in-law, and in-laws, whose support and understanding helped sustain me during this demanding period. This achievement belongs to them as much as it does to me.

This material is based upon work supported by the Broad Agency Announcement Program and the Cold Regions Research and Engineering Laboratory (ERDC-CRREL) under Contract No. W913E522C0001.

Annotations

GA	Group A
GB	Group B
PW	Plain Water
SW	Sea Water
UPV	Ultrasonic pulse velocity
SR	Surface Resistivity
F-T	Freeze-Thaw
RDME	Relative Dynamic Modulus of Elasticity
DME	Dynamic Modulus of Elasticity
ML	Mass Loss
PVA	Polyvinyl Alcohol Fiber
AEA	Air Entraining Admixture
RCPT	Rapid chloride penetrability test
CNF	Cellulose Nanofiber
XRD	X-ray diffraction
TGA	Thermogravimetric analysis
LT-DSC	Low Temperature Differential Scanning Calorimetry
FW	Frozen Water
MH	Melting Heat
DOH	Degree of Hydration
BET	Brunauer–Emmett–Teller
BJH	Barrett, Joyner, and Halenda
D_c	Diffusion Coefficient
TXM	Transmission X-ray Microscopy
OTZ	Overlay Transition Zone
RH	Relative Humidity
SSD	Saturated Surface Dry
OD	Oven Dry
w/c	Water-to-cementitious ratio
D_2O	Deuterated Water
NR	Neutron Radiography
HFIR	High Flux Isotope Reactor
ORNL	Oak Ridge National Laboratory
MARS	Multimodal Advanced Radiography Station
TEM	Transmission Electron Microscopy
FTIR	Fourier Transform Infrared Spectroscopy

Table of Contents

List of Figures

List of Tables

Chapter 1. Introduction

Climate change is driving rapid environmental changes in high-latitude regions, where warming rates are approximately twice the global average, especially in the Arctic [1,2]. As shown in Figure 1- 1, the Arctic experienced record-high temperatures in Summer 2023, with a clear upward trend in summer warming from 1940 to 2023 [3]. These changes have significantly reduced sea and land ice [4,5], leading to heightened coastal erosion [6] and accelerated permafrost thaw [7]. This complex interplay between climate systems and environmental stability underscores the need for comprehensive strategies to mitigate further damage. As the only Arctic region in the United States, Alaska is experiencing especially severe impacts, with projected climate-related infrastructure expenses potentially reaching $5.5 billion by 2099; proactive adaptation, however, could reduce these costs to $2.9 billion [8–10].

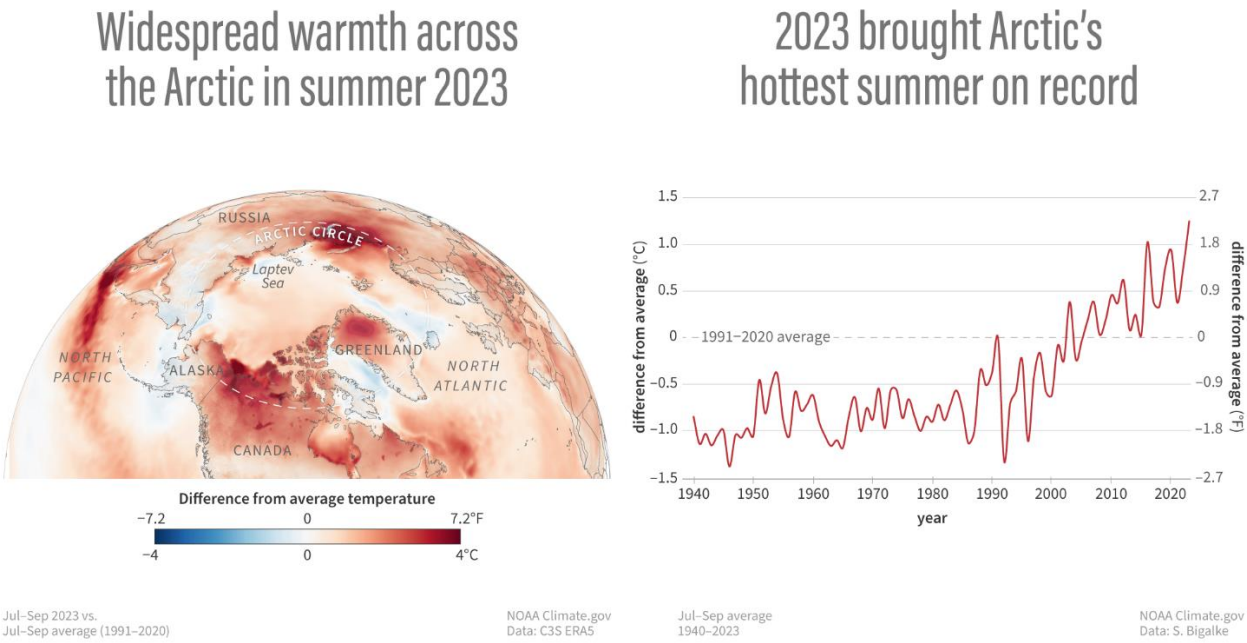

Figure 1- 1. Surface temperatures in Arctic regions during July-September 2023 compared to the 1991-2020 average (map); summer temperatures (July-September) each year from 1940-2023 (graph) [3].

Concrete is widely used in construction materials due to the abundance and affordability of its raw materials [11]. Due to its remarkable strength, concrete is crucial for building infrastructure that can withstand a variety of climates [12,13], including Arctic regions that face harsh environmental conditions [14,15]. However, concrete is prone to deterioration from external factors and the effects of weathering, which can lead to structural damage and cracking, ultimately compromising mechanical strength and durability [12,16]. In particular, concrete structures in Arctic regions are vulnerable to damage from recurrent freeze-thaw (F-T) cycles [17,18]. During F-T cycling,

concrete deterioration arises from multiple mechanisms, including volume expansion of water as it transitions from liquid to ice, hydraulic and osmotic pressures of pore water, pressure from cryosuction and crystallization of ice, and micro-ice lens formation, all of which contribute to internal stresses leading to cracking and degradation, as illustrated in Figure 1- 2 [19–21]. This deterioration reduces structural lifespan and increases maintenance needs. The extent of F-T damage depends on specific geographic and climatic conditions, making it crucial to understand various factors, such as cycle frequency, minimum temperatures, and freezing rates, for effective maintenance planning [22,23].

The effects of climate change, including rising sea levels and thawing permafrost, have heightened the vulnerability of concrete infrastructure in Arctic coastal regions, where chloride ingress from seawater poses a significant threat [24,25]. Concrete structures exposed to seawater face an increased risk of steel rebar corrosion from chloride penetration, a process worsened by F-T cycles that create microcracks and increase penetrability [26,27]. In northern climates, deicing salts pose a similar risk to concrete durability, as chloride-based chemicals used on concrete pavements and bridges further accelerate F-T and corrosion processes [28].

Salt scaling is surface deterioration in concrete due to freezing cycles when saline solutions (i.e., seawater or deicing salts) are present [29]. According to the "glue-spall" model, scaling arises from tensile stresses caused by a mismatch in thermal expansion between the concrete and the ice layer that forms on its surface [30]. Salt scaling occurs when pure ice formation concentrates salts into unfrozen saline pockets that act as stress concentrators. This reduces ice strength and causes cracks that penetrate and detach concrete surface flakes at intermediate salt concentrations [29,30]. High porosity and permeability in concrete amplify these effects, as F-T cycles expand pores and facilitate greater chloride ingress [31,32]. The combined impacts of F-T cycles and chloride ingress not only compromise durability but also alter chloride distribution within the concrete, as freezing can concentrate chloride ions at the ice boundary, leading to more profound penetration during thawing [33,34]. Chlorides from seawater and deicing salts contribute to steel reinforcement corrosion, causing de-passivation, reduced load-bearing capacity, and cracks in the concrete cover [35,36].

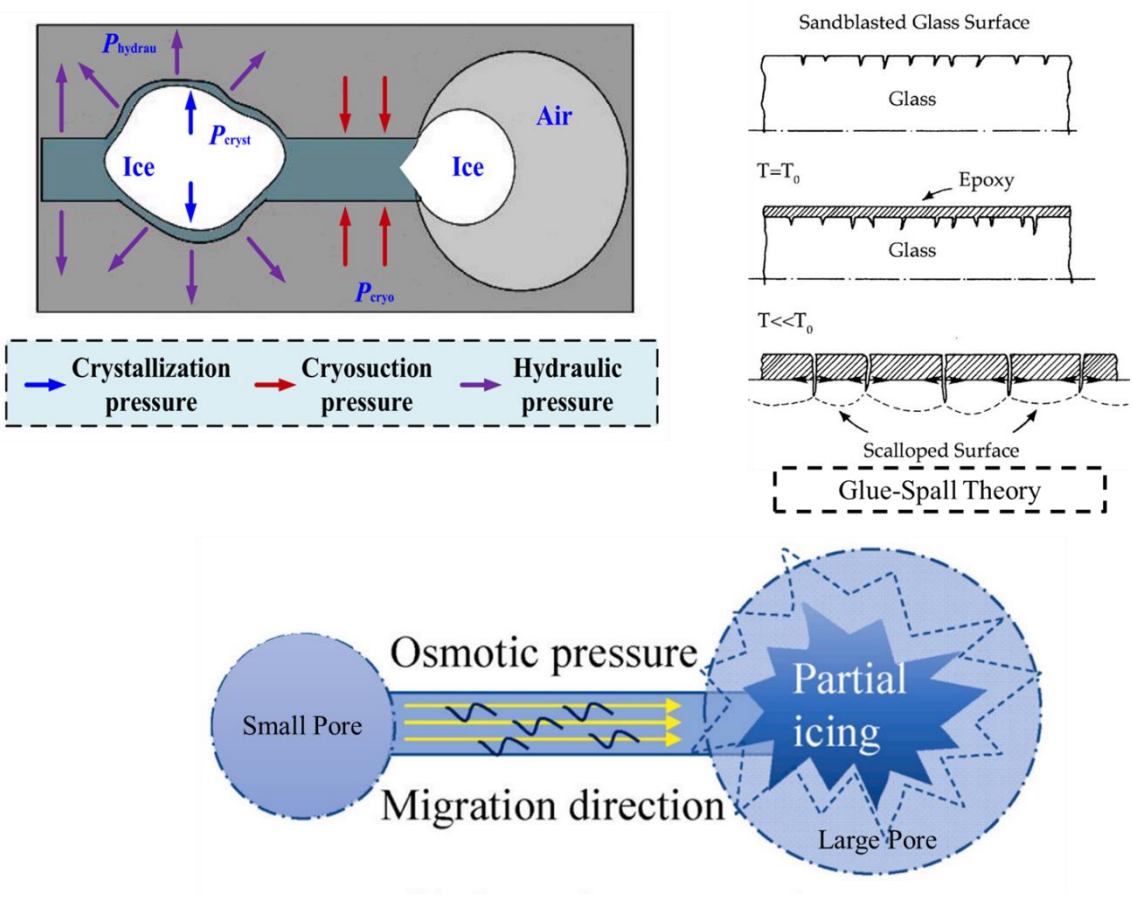

Figure 1- 2 Freeze-thaw-induced pressures in concrete pores, leading to internal stress and potential cracking [21,37,38].

While extensive research has been conducted on F-T and chloride-induced degradation, the synergistic effects of these mechanisms, particularly under continuous submerged seawater conditions and subzero temperatures, remain inadequately studied [35,36,39–41]. Understanding these combined mechanisms is essential to developing strategies that ensure the resilience and durability of concrete structures in arctic, chloride-exposed environments. Existing solutions are limited in fully addressing the intricate mechanisms of F-T cycles and chloride ingress, as they rely primarily on empirical rather than mechanistic approaches. Although it is known that water expansion during freezing contributes to damage, five additional mechanisms have been proposed, and their exact relationships remain unresolved in the literature [19,36–38]. Therefore, to gain a comprehensive understanding of the intricate processes that contribute to F-T damage in concrete, it is essential to monitor the movement of pore water and potentially the crystallization of ice within the concrete during exposure to subzero temperatures, both qualitatively and non-destructively, in real-time. However, there are still significant challenges and gaps in our understanding of the complex interactions between F-T cycles, chloride ingress, pore water movement, and concrete repair strategies.

1.1 Research objectives

The **goal** of this dissertation is to enhance concrete resilience and durability in arctic regions by addressing degradation mechanisms and improving performance strategies. To achieve this, the dissertation pursues three main **objectives**: (1) investigating the damage mechanisms of F-T cycles and chloride ingress in concrete, (2) investigating the role of advanced additives and repair strategies to improve durability, and (3) developing real-time methods for observing pore water movement in concrete macropores under F-T cycles. These objectives will be met by achieving the following research **aims**:

1. *Determining damage mechanisms in arctic regions.* This aim hypothesizes that exposure to F-T cycles in chloride-rich environments, such as seawater, accelerates concrete degradation by inducing microcracks, facilitating chloride ingress, and initiating corrosion. Utilizing PVA fibers and extended curing durations will improve concrete's durability by reinforcing microstructural integrity, minimizing microcrack formation, and reducing chloride diffusion, as verified through transmission X-ray microscopy (TXM) analysis.
2. *Evaluating advanced additives and repair strategies for enhanced concrete durability in Arctic regions.* This aim hypothesizes that incorporating cellulose nanofiber (CNF) suspensions from biowaste sources will significantly enhance F-T resistance and reduce chloride diffusion in cementitious materials by densifying microstructure. Additionally, optimizing moisture conditions and water-to-cement (w/c) ratios in repair materials will improve the durability of the overlay transition zone (OTZ), enhancing bonding and resistance to chloride ingress in cold-region concrete repairs.
3. *Monitoring pore water movement through concrete macropores during F-T cycles.* This aim hypothesizes that real-time monitoring of pore water movement within concrete macropores during F-T cycles using neutron radiography, with its high sensitivity to hydrogen and superior contrast, will reveal critical insights into temporal water redistribution. These observations are expected to identify the specific temperature and timing of water movement that lead to internal stress and damage initiation, providing a mechanistic understanding essential for designing durable concrete infrastructure in arctic regions.

The **intellectual merit** of this dissertation is that it advances the understanding of concrete durability in Arctic regions by addressing fundamental mechanisms of F-T damage and chloride ingress, which are critical for infrastructure resilience. Upon completion, this dissertation will contribute to intellectual merit by (1) conducting the first comprehensive investigation of the combined effects of F-T cycles and seawater on chloride ingress in concrete using TXM, a non-destructive technique capable of tracking chloride ion diffusion; (2) enhancing concrete durability through advanced materials like CNF gel suspensions and optimized repair methods; and (3) providing real-time monitoring for the first time of pore water movement within concrete macropores under F-T cycles using neutron imaging, delivering insights into a primary damage mechanism for F-T degradation.

The **broader impact** of this dissertation lies in its potential to enhance resilient and sustainable concrete infrastructure in Arctic regions. This work is critical for Alaskan coastal communities that face severe risks from accelerated permafrost thaw, rising sea levels, and coastal erosion, which disrupt daily life, force community relocations, and compromise essential infrastructure like roads, airports, and seawalls [42–44]. Upon completion, this dissertation will contribute to broader impacts on climate resilience and public safety by:

1. Informing the design of more durable concrete, utilizing optimized curing durations and PVA reinforcement to withstand F-T cycles and seawater exposure, thus extending the lifespan of Arctic coastal infrastructure.
2. Incorporating CNF suspensions to reduce chloride ingress and improve F-T resistance will support resilient and sustainable infrastructure.
3. Advancing pavement repair practices by optimizing OTZ durability through moisture control and adjusting repair materials w/c ratios, thereby reducing maintenance needs and enhancing the performance of repaired pavements.
4. Providing real-time insights into pore water movement within concrete macropores under F-T cycles, which aids in designing infrastructure better adapted to climate stressors.

1.2 Research tasks

As discussed earlier, this dissertation is comprised of three specific research aims. This dissertation will be comprised of six main tasks that correspond to six manuscripts to meet the three aims:

1) Task 1 (Aim 1) investigates the effects of PVA fibers and curing duration on chloride ingress in concrete during F-T cycles. The study utilizes TXM to quantify the apparent chloride diffusion coefficient (D_c) in conventional and PVA fiber-reinforced concrete with different curing periods. The results provide insights into the role of PVA fibers and curing duration in enhancing concrete durability in arctic regions.
2) Task 2 (Aim 1) focuses on evaluating the combined effects of F-T cycles and seawater exposure on chloride ingress in concrete. This study also uses TXM to quantify the apparent chloride D_c in conventional and PVA fiber-reinforced concrete under varying curing durations. The research explores how seawater exposure accelerates F-T damage and impacts concrete durability, particularly in arctic and coastal environments.
3) Task 3 (Aim 2) investigates the effects of CNF gels on cement paste's F-T durability and chloride ingress. Paste specimens are created by replacing water with nitro-oxidized CNF suspensions, which form hydrogels in the presence of metal ions (*e.g.*, Na^+, Ca^+). CNF suspensions from three biowaste sources (sugarcane bagasse, cabbage, jute) are used in this task, prepared at concentrations of 1% and 2% by mass of water. TXM is used to determine diffusion coefficients and identify the CNF gel characteristics that enhance F-T resistance and reduce chloride diffusion in cement paste.
4) Task 4 (Aim 2) investigates the effects of substrate moisture conditions on the overlay transition zone (OTZ) in concrete pavement repairs under F-T cycles. Mechanical and fracture properties, as well as chloride diffusion kinetics, will be assessed. TXM is used to quantify the apparent chloride D_c before and after F-T cycles. The goal is to understand how different moisture conditions impact OTZ durability and bond performance in concrete repairs in arctic regions.
5) Task 5 (Aim 2) investigates the effects of varying w/c ratios in repair mixtures on the OTZ in concrete pavement repairs. Repair mixtures with w/c ratios of 0.38, 0.40, and 0.45 are batched against a substrate with a fixed moisture condition. The goal is to understand how different w/c ratios influence the bond and durability performance of concrete repairs in Arctic regions. This involves using advanced experimental techniques, including TXM, to investigate the

diffusion mechanism, mechanical properties, chloride ion penetration, water absorption, and freeze-thaw resistance, specifically at the interface between repair materials and concrete substrates.

6) Task 6 (Aim 3) investigates the pore water movement within macropores at subzero temperatures. Neutron radiography is conducted to track pore water movement as concrete samples are cooled from the bottom of the sample to –12.5 ℃. Embedded sensors monitor temperature changes, while 2D radiographic images are captured at 90-second intervals. The study aims to refine experimental methods to understand F-T effects on concrete better, leading to improved infrastructure resilience in arctic regions.

1.3 Dissertation organization

The dissertation comprises six manuscripts within eight chapters covering all the above-mentioned tasks. The arrangement of the dissertation is as follows:

- **Chapter 1:** ***Introduction*****.** This chapter highlights the challenges in maintaining concrete durability in arctic environments, focusing on F-T cycles and chloride ingress. It provides essential background on concrete performance in arctic climates, followed by the problem statement and research objectives. Finally, this chapter outlines the dissertation's organization.
- **Chapter 2:** ***Effects of polyvinyl alcohol fibers and curing duration on chloride ingress in concrete during F-T cycles.*** This chapter covers Task 1 to investigate the influence of PVA fibers and curing duration on chloride penetration in concrete exposed to F-T cycles. Two air-entrained concrete are studied, conventional concrete and PVA fiber-reinforced concrete, with curing durations of 70 and 14 days. Performance metrics such as ultrasonic pulse velocity, surface resistivity, mass loss, relative dynamic modulus of elasticity, and apparent chloride D_c are also evaluated to validate the influence of PVA fibers and curing durations on the F-T resistance of concrete materials. This chapter was published in the *Journal of Building Engineering.*
- **Chapter 3*****: The combined impact of F-T cycles and seawater on chloride ingress in concrete.*** This chapter covers Task 2 to investigate the effects of F-T cycles and seawater exposure on chloride ingress in concrete. Two types of air-entrained concrete are studied: conventional concrete and PVA fiber-reinforced concrete, each with curing durations of 70 and 14 days. Both concrete groups undergoes F-T cycles in simulated seawater. Performance metrics, including ultrasonic pulse velocity, surface resistivity, mass loss, relative dynamic modulus of elasticity, and apparent chloride D_c, are evaluated to assess the synergistic impact of F-T cycles and seawater exposure on the durability of concrete materials. This chapter was published in *Construction and Building Materials.*
- **Chapter 4:** ***Effects of cellulose nanofiber gels on the chloride ingress and freeze/thaw properties of cement paste***. As outlined in Task 3, this study utilizes CNF gels to assess improvements in F-T durability and chloride ingress resistance in cement paste. This chapter explores the impact of CNF gels on F-T resistance and reduction of chloride diffusion in cement paste. Paste specimens are prepared by replacing water with CNF suspensions, which form hydrogels in the presence of metal ions. CNF suspensions from three biowaste sources (sugarcane bagasse, cabbage, and jute) are used in this task, prepared at concentrations of 1% and 2% by mass of water. TXM is employed to determine the apparent chloride D_c, with results

expected to show the durability of CNF-containing specimens compared to controls. This chapter was published in *Construction and Building Materials.*

- **Chapter 5:** ***Effect of freeze/thaw and substrate moisture condition on the concrete repair-substrate interface.*** As outlined in Task 4, this study investigates the impact of substrate moisture conditions on the OTZ in cement-based concrete pavement repairs. This chapter examines how substrate moisture influences bond formation and evaluates its mechanical and fracture properties, along with chloride diffusion under F-T cycling along the OTZ. TXM is used to quantify apparent chloride D_c within the OTZ before and after F-T cycles. Findings provides a deeper understanding of how moisture and F-T cycling influence OTZ durability, contributing to more effective pavement repair strategies. This manuscript was published in the *Proceedings of the 13th International Conference on Concrete Pavements* in 2024.
- **Chapter 6:** ***Impact of water-to-cement ratios of repair mixes on the durability of concrete repair-substrate interfaces during freeze-thaw cycles***. As outlined in Task 5, this study examines the effect of varying w/c ratios of repair mixtures on the OTZ, the critical bonding area in concrete pavement repairs. Repair mixtures with w/c ratios of 0.38, 0.40, and 0.45 are prepared against a substrate at relative humidity (RH) 98%, with mechanical and durability properties (Rapid chloride ion permeability, water absorption, F-T cycle) of the OTZ assessed. TXM is used to quantify apparent chloride D_c in the OTZ. Insights of this chapter provide the influence of w/c ratios in repair materials on OTZ performance, which will inform better pavement repair practices. This chapter is under review in the *Journal of Building Engineering.*
- **Chapter 7:** ***In-situ neutron radiography for real-time monitoring of pore-water movement in portland cement mortar exposed to sub-zero temperature***. As outlined in Task 6, this study aims to improve understanding of F-T damage by monitoring pore water movement within concrete micropores at subzero temperatures, aiding the design of resilient infrastructure for arctic regions. Preliminary work has been completed, including planning at the multimodal advanced radiography station (MARS) in high flux isotope reactor HFIR beamline CG-1D at Oak Ridge National Laboratory and optimizing sample thickness. Samples are prepared using deuterated water (D_2O) and then dried, and vacuum-saturated to fill the micropores with regular water (H_2O) for better contrast in pore water imaging. Neutron radiography is used to track pore water movement as the samples cool from 1D at -12.5°C, with embedded sensors monitoring temperature. The experimental setup involves sealing samples, embedding sensors, temperature control via an external chiller, and capturing 2D images at 90-second intervals. Additional characterizations are conducted to understand hydration kinetics, pore water freezing point, pore structure, and air voids in the hardened concrete using isothermal calorimetry, X-ray diffraction, thermogravimetric analysis, low-temperature differential calorimetry, and Brunauer–Emmett–Teller (BET) surface area analysis. This chapter provides fundamental *in-situ* insights into the timing and movement of water within concrete microstructures under F-T cycles, aiding future research and the design of more resilient concrete structures. This chapter is under review in *CRREL*.
- **Chapter 8:** ***Conclusions and recommendations.*** The purpose of this chapter is to summarize the six manuscripts included in this dissertation, along with recommendations for future research and the practical implications of the findings.

Finally, this dissertation presents a comprehensive practical framework for enhancing the durability of cementitious materials in Arctic environments. Chapters 1 and 2 provide an in-depth

understanding of F-T damage mechanisms under different environmental conditions (plain water and seawater), laying the foundation for targeted interventions. Chapters 3 through 5 introduce and evaluate innovative improvement of cementitious materials and concrete repair techniques to support and enhance the resilience of cold-weather concrete materials. Finally, Chapter 6 employs neutron radiography to monitor pore water movement into concrete macropores in real-time, which can initiate microstructural damage due to the hydraulic pressure, offering critical *in-situ* insights to drive more durable design.

References

[1] R. V Bekryaev, I. V Polyakov, V.A. Alexeev, Role of polar amplification in long-term surface air temperature variations and modern Arctic warming, J Clim 23 (2010) 3888–3906.https://doi.org/10.1175/2010JCLI3297.1

[2] T.F. Stocker, D. Qin, G.-K. Plattner, L. V Alexander, S.K. Allen, N.L. Bindoff, F.-M. Bréon, J.A. Church, U. Cubasch, S. Emori, Technical summary, in: Climate Change 2013: The Physical Science Basis. Contribution of Working Group I to the Fifth Assessment Report of the Intergovernmental Panel on Climate Change, Cambridge University Press, 2013: pp. 33–115.

[3] L.R. Mudryk, A. Elias Chereque, C. Derksen, K. Luojus, B. Decharme, NOAA Arctic Report Card 2023: Terrestrial Snow Cover, (2023).

[4] E. Berthier, E. Schiefer, G.K.C. Clarke, B. Menounos, F. Rémy, Contribution of Alaskan glaciers to sea-level rise derived from satellite imagery, Nat Geosci 3 (2010) 92–95.https://doi.org/10.1038/ngeo737

[5] J.H. Morison, Contributor Type Dynamic Model Type Arctic Extent Antarctic Extent Alaska Extent Hudson Bay Extent Median Range Standard Deviation Estimate Summary Executive Summary Method Summary Sea Ice Concentration Data Sea Ice Thickness Data.

[6] B.M. Jones, C.D. Arp, M.T. Jorgenson, K.M. Hinkel, J.A. Schmutz, P.L. Flint, Increase in the rate and uniformity of coastline erosion in Arctic Alaska, Geophys Res Lett 36 (2009).https://doi.org/10.1029/2008GL036205

[7] V.E. Romanovsky, S.L. Smith, H.H. Christiansen, Permafrost thermal state in the polar Northern Hemisphere during the international polar year 2007–2009: a synthesis, Permafr Periglac Process 21 (2010) 106–116.https://doi.org/10.1002/ppp.689

[8] K.M. Hinkel, F.E. Nelson, W.P.C. Change, Permafrost, and Impacts on Civil Infrastructure In: US Arctic Research Commission, Permafrost Task Force Report (2003).

[9] A.C.I. Assessment, Impacts of a warming Arctic-Arctic climate impact assessment, 2004.

[10] A.M. Melvin, P. Larsen, B. Boehlert, J.E. Neumann, P. Chinowsky, X. Espinet, J. Martinich, M.S. Baumann, L. Rennels, A. Bothner, Climate change damages to Alaska public infrastructure and the economics of proactive adaptation, Proceedings of the National Academy of Sciences 114 (2017) E122–E131.https://doi.org/10.1073/pnas.1611056113

[11] M. Rabi, R. Shamass, K.A. Cashell, Structural performance of stainless steel reinforced concrete members: A review, Constr Build Mater 325 (2022). https://doi.org/10.1016/j.conbuildmat.2022.126673.https://doi.org/10.1016/j.conbuildmat.2022.126673

[12] W.L. Baloch, H. Siad, M. Lachemi, M. Sahmaran, A review on the durability of concrete-to-concrete bond in recent rehabilitated structures, Journal of Building Engineering 44 (2021). https://doi.org/10.1016/j.jobe.2021.103315.

[13] Y. Yi, D. Zhu, S. Guo, Z. Zhang, C. Shi, A review on the deterioration and approaches to enhance the durability of concrete in the marine environment, Cem Concr Compos 113 (2020). https://doi.org/10.1016/j.cemconcomp.2020.103695.

[14] C.J. Korhonen, Antifreeze Admixtures for Cold Regions Concreting A Literature Review, (1990).
[15] J. Khan, G.S. Kumar, Influence of binary antifreeze admixtures on strength performance of concrete under cold weather conditions, Journal of Building Engineering 34 (2021). https://doi.org/10.1016/j.jobe.2020.102055.
[16] M.Z.Y. Ting, K.S. Wong, M.E. Rahman, S.J. Meheron, Deterioration of marine concrete exposed to wetting-drying action, J Clean Prod 278 (2021). https://doi.org/10.1016/j.jclepro.2020.123383.
[17] C. Marketing, K. Nmai, Cold Weather Concreting Admixtures, Cem Concr Compos 20 (1998) 21–128.https://doi.org/10.1016/S0958-9465(97)00063-2
[18] R. Demirboğa, F. Karagöl, Ri. Polat, M.A. Kaygusuz, The effects of urea on strength gaining of fresh concrete under the cold weather conditions, Constr Build Mater 64 (2014) 114–120. https://doi.org/10.1016/j.conbuildmat.2014.04.008.
[19] H. Lin, Y. Han, S. Liang, F. Gong, S. Han, C. Shi, P. Feng, Effects of low temperatures and cryogenic freeze-thaw cycles on concrete mechanical properties: A literature review, Constr Build Mater 345 (2022). https://doi.org/10.1016/j.conbuildmat.2022.128287.
[20] J. Guo, W. Sun, Y. Xu, W. Lin, W. Jing, Damage Mechanism and Modeling of Concrete in Freeze–Thaw Cycles: A Review, Buildings 12 (2022). https://doi.org/10.3390/buildings12091317.
[21] M. Sun, C. Zou, D. Xin, Pore structure evolution mechanism of cement mortar containing diatomite subjected to freeze-thaw cycles by multifractal analysis, Cem Concr Compos 114 (2020) 103731.https://doi.org/10.1016/j.cemconcomp.2020.103731
[22] Y. Şahin, Y. Akkaya, M.A. Taşdemir, Effects of freezing conditions on the frost resistance and microstructure of concrete, Constr Build Mater 270 (2021). https://doi.org/10.1016/j.conbuildmat.2020.121458.
[23] Jacobsen, S., Sœther, D.H. & Sellevold, E.J. Frost testing of high strength concrete: Frost/salt scaling at different cooling rates. Mat. Struct. 30, 33–42 (1997). https://doi.org/10.1007/BF02498738
[24] X.J. Gao, X.Y. Wang, Impacts of globalwarming and sea level rise on service life of chloride-exposed concrete structures, Sustainability (Switzerland) 9 (2017). https://doi.org/10.3390/su9030460.
[25] M. Siegert, R.B. Alley, E. Rignot, J. Englander, R. Corell, Twenty-first century sea-level rise could exceed IPCC projections for strong-warming futures, One Earth 3 (2020) 691–703. https://doi.org/10.1016/j.oneear.2020.11.002.
[26] A. Dousti, M. Moradian, S.R. Taheri, R. Rashetnia, M. Shekarchi, Corrosion Assessment of RC Deck in a Jetty Structure Damaged by Chloride Attack, Journal of Performance of Constructed Facilities 27 (2013) 519–528. https://doi.org/10.1061/(asce)cf.1943-5509.0000348.

[27] Z. Lu, Z. gang Feng, D. Yao, X. Li, H. Ji, Freeze-thaw resistance of Ultra-High performance concrete: Dependence on concrete composition, Constr Build Mater 293 (2021). https://doi.org/10.1016/j.conbuildmat.2021.123523.
[28] C.W. Chung, C.S. Shon, Y.S. Kim, Chloride ion diffusivity of fly ash and silica fume concretes exposed to freeze-thaw cycles, Constr Build Mater 24 (2010) 1739–1745. https://doi.org/10.1016/j.conbuildmat.2010.02.015.
[29] Z. Sun, G.W. Scherer, Effect of air voids on salt scaling and internal freezing, Cem Concr Res 40 (2010) 260–270. https://doi.org/https://doi.org/10.1016/j.cemconres.2009.09.027.
[30] J.J. Valenza, G.W. Scherer, A review of salt scaling: II. Mechanisms, Cem Concr Res 37 (2007) 1022–1034. https://doi.org/https://doi.org/10.1016/j.cemconres.2007.03.003.
[31] C. Tennakoon, A. Shayan, J.G. Sanjayan, A. Xu, Chloride ingress and steel corrosion in geopolymer concrete based on long term tests, Mater Des 116 (2017) 287–299. https://doi.org/10.1016/j.matdes.2016.12.030.
[32] X. Wang, I. Rhee, Y. Wang, Y. Xi, Compressive strength, chloride permeability, and freeze-thaw resistance of mwnt concretes under different chemical treatments, Scientific World Journal 2014 (2014). https://doi.org/10.1155/2014/572102.
[33] L.F. Sun, K. Jiang, X. Zhu, L. Xu, An alternating experimental study on the combined effect of freeze-thaw and chloride penetration in concrete, Constr Build Mater 252 (2020). https://doi.org/10.1016/j.conbuildmat.2020.119025.
[34] M. Dabas, B. Martín-Pérez, H. Almansour, Combined Effects of Freeze-Thaw and Corrosion on Performance of RC Structures: State-of-the-Art Review, Journal of Performance of Constructed Facilities 35 (2021). https://doi.org/10.1061/(asce)cf.1943-5509.0001637.
[35] S. Kessler, C. Thiel, C.U. Grosse, C. Gehlen, Effect of freeze–thaw damage on chloride ingress into concrete, Materials and Structures/Materiaux et Constructions 50 (2017). https://doi.org/10.1617/s11527-016-0984-4.
[36] A. Sarsembayeva, A. Zhussupbekov, Experimental study of deicing chemical redistribution and moisture mass transfer in highway subsoils during the unidirectional freezing, Transportation Geotechnics 26 (2021). https://doi.org/10.1016/j.trgeo.2020.100426.
[37] J.J. Valenza II, G.W. Scherer, Mechanism for Salt Scaling, Journal of the American Ceramic Society 89 (2006) 1161–1179. https://doi.org/https://doi.org/10.1111/j.1551-2916.2006.00913.x.
[38] X. Rong, L. Li, S. Zheng, F. Wang, W. Huang, Y. Zhang, D. Lu, Freeze–thaw damage model for concrete considering a nonuniform temperature field, Journal of Building Engineering 72 (2023) 106747. https://doi.org/https://doi.org/10.1016/j.jobe.2023.106747.
[39] P. Zhang, F.H. Wittmann, M. Vogel, H.S. Müller, T. Zhao, Influence of freeze-thaw cycles on capillary absorption and chloride penetration into concrete, Cem Concr Res 100 (2017) 60–67. https://doi.org/10.1016/j.cemconres.2017.05.018.
[40] H.S. Shang, T.H. Yi, Freeze-thaw durability of air-entrained concrete, The Scientific World Journal 2013 (2013). https://doi.org/10.1155/2013/650791.

[41] A.J.K. Komar, A.J. Boyd, Evaluating Freeze-Thaw Deterioration with Tensile Strength, in: IOP Conf Ser Mater Sci Eng, Institute of Physics Publishing, 2017. https://doi.org/10.1088/1757-899X/216/1/012024.

[42] Schwoerer, T., Berry, K., Rasmus, S.M. et al. Climate policy must account for community-specific socio-economic, health, and biophysical conditions—evidence from coastal Alaska. Reg Environ Change 23, 90 (2023). https://doi.org/10.1007/s10113-023-02080-9

[43] M.J. Brown, P. Passalacqua, K. Faust, Exposure of rural Alaskan infrastructure to coastal erosion and permafrost subsidence, Environmental Research: Infrastructure and Sustainability 4 (2024) 035011.https://doi.org/10.1088/2634-4505/ad6bbe

[44] R.C. Creel, J. Guimond, B. Jones, D.M. Nielsen, E.M. Bristol, C.E. Tweedie, P.P. Overduin, Permafrost thaw subsidence, sea-level rise, and erosion are transforming Alaska's Arctic coastal zone, (2024).https://doi.org/10.1073/pnas.2409411121

Chapter 2. Effects of polyvinyl alcohol fibers and curing duration on chloride ingress in concrete during freeze-thaw cycles[1]

The contributions of the authors to this manuscript are described as follows:

Md Hasibul Hasan Rahat: Conceptualization, Methodology, Formal analysis, Investigation, Writing– review and editing, Writing–original draft.

Thien Q. Tran: Methodology, Formal analysis, Investigation.

Dip Banik: Methodology, Formal analysis, Investigation.

Alexander S. Brand: Conceptualization, Writing – review and editing, Writing – original draft, Supervision, Project administration, Methodology.

[1] **Rahat, M.H.H.,** Tran, T.Q., Banik, D., & Brand, A.S. (2025). Effects of polyvinyl alcohol fibers and curing duration on chloride ingress in concrete during freeze-thaw cycles, *Journal of Building Engineering*, 2025, 112930, ISSN 2352-7102, https://doi.org/10.1016/j.jobe.2025.112930.

Effects of polyvinyl alcohol fibers and curing duration on chloride ingress in concrete during freeze-thaw cycles

Md Hasibul Hasan Rahat[1*], Thien Q. Tran[1], Dip Banik[1] and Alexander S. Brand[1,2,3*]

[1] The Charles E. Via, Jr. Department of Civil and Environmental Engineering, Virginia Polytechnic Institute and State University, Blacksburg, Virginia

[2] Department of Materials Science and Engineering, Virginia Polytechnic Institute and State University, Blacksburg, Virginia

[3] Myers-Lawson School of Construction, Virginia Polytechnic Institute and State University, Blacksburg, Virginia

* Corresponding authors: rahatm21@vt.edu (M.H.H.R.) and asbrand@vt.edu (A.S.B.)

2.1 Abstract

This study investigates the influence of polyvinyl alcohol (PVA) fibers and curing duration on chloride penetration in concrete exposed to freeze-thaw (F-T) cycles. Two air-entrained concretes were studied, conventional concrete (Group A) and PVA fiber-reinforced concrete (Group B), with curing durations of 14 and 70 days. Performance metrics such as ultrasonic pulse velocity, surface resistivity, mass loss, relative dynamic modulus of elasticity, and chloride diffusion coefficient (Dc) were also evaluated. Notably, this study introduces the first application of transmission X-ray microscopy (TXM) to quantify chloride ingress in concrete subjected to F-T cycles using iodide as a tracer, offering a novel non-destructive method for F-T durability assessment. The results revealed that, Group A demonstrated better resistance to F-T cycles than Group B, which was likely due to the fact that Group A had a higher entrained air content. Specifically, after 500 F-T cycles, the Group A samples cured for 70 days exhibited a 62 % increase in diffusion coefficient, while Group B samples showed a 93 % increase. Furthermore, the samples cured for 70 days consistently outperformed those cured for 14 days in all experiments, with the latter showing a higher increase in Dc value of 84 % for Group A and 109 % for Group B after 300 F-T cycles. These findings underscore the significant role of extended curing periods and higher entrained air content in improving concrete durability in cold regions against F-T damage and mitigating chloride ingress in concrete during F-T cycles. This study adds value to the field by offering valuable insights into how curing duration, fiber reinforcement, and F-T cycles are related and how they affect the chloride ingress into concrete. This can guide the development of stronger concrete structures in cold climates.

Keywords: freeze-thaw resistance, transmission X-ray microscopy, polyvinyl alcohol fiber, curing period, chloride ingress, diffusion coefficients

2.2 Introduction

The susceptibility of concrete infrastructure in cold regions to freeze-thaw (F-T) damage is a primary concern for their durability (Lin et al., 2022). Moreover, climate-induced changes, such

as rising sea levels and permafrost thawing, could simultaneously expose concrete structures to F-T damage and chloride ingress. This combined exposure is especially relevant in cold regions where chloride-based deicing agents are applied to concrete surfaces, including bridge decks and pavements. Despite extensive studies on each factor separately, the synergistic degradation effect arising from both F-T cycles and chloride ingress into concrete has not been comprehensively examined in the existing literature (*e.g.*, Sunet al., 2020).

The repetitive nature of F-T cycles poses a significant threat to concrete due to its porous composition. The freezing of the pore solution and the subsequent localized expansion lead to cracking and spalling (Hao et al., 2021; Wang et al., 2022). Cracking and spalling facilitate the ingress of deleterious materials, further exacerbating the damage. Factors such as osmotic pressure, water ejection, and crystallization within the pores also contribute to internal cracking and surface spalling in concrete subjected to F-T cycles (Qin et al., 2019; Sang et al., 2022). An in-depth understanding of the development of concrete damage under F-T cycling is essential to formulate an effective maintenance strategy for infrastructure. Several performance metrics have been identified to evaluate the extent of damage F-T causes in concrete structures, including the relative dynamic modulus of elasticity (RDME), compressive and tensile strengths, mass loss (ML), and ultrasonic pulse velocity (UPV) (Bao et al., 2022; Dabas et al., 2021; Liu et al., 2016a, 2016b). Using these metrics allows engineers to make well-informed decisions about the maintenance and safety of concrete infrastructure, thus helping to assess the severity of F-T damage and preserve structural integrity and safety.

Researchers have underscored the efficacy of fiber integration in augmenting both the microstructural integrity and functional resilience of concrete under low-temperature conditions (Affan and Ali, 2022; Çavdar, 2014; Jang et al., 2014; Şahmaran et al., 2012; Tan et al., 2022). Polyvinyl alcohol (PVA) fibers, an affordable and high-tensile synthetic fiber that bonds strongly with the cement matrix, are widely used in various concrete structures (Felekoğlu et al., 2009; Noushini et al., 2013; Thong et al., 2016; Yew et al., 2015). Previous studies have shown that adding PVA fibers to concrete enhances mechanical performance during repeated freeze-thaw cycles by improving the microstructure, minimizing the decrease in relative dynamic elastic modulus, reducing crack propagation, and slowing the rate of concrete degradation (Liu et al., 2023; Tan et al., 2022; Wang et al., 2021). Therefore, this investigation aims to investigate the effects of PVA fibers on concrete's vulnerability to chloride ingress, particularly under the influence of F-T cycles, thereby offering insights into protective strategies against environmental degradation.

Reinforced concrete infrastructure is notably susceptible to damage induced by F-T cycles, as such deterioration can expose the embedded steel reinforcement to conditions conducive to corrosion (Diao et al., 2012; Rabi et al., 2022; Shi et al., 2012). Moreover, the ingress of chloride ions significantly exacerbates the corrosion rate, posing a heightened risk to structural integrity (Zhang et al., 2017). In cold regions, the application of de-icing salts on roadways and bridges is a prevalent method for preventing ice formation, subsequently leading to the ingress of chloride

ions into concrete structures. These ions ingress through the concrete upon contact due to existing concentration gradients. The mobility of ions within the concrete infrastructure is quantitatively assessed by the diffusion coefficient (D_c), which provides a metric for evaluating the rate of ion movement through the material (Kang et al., 2021; Li et al., 2023; Pilvar et al., 2015). The D_c elucidates the rate and facility of ion diffusion through concrete structures. To evaluate this rate, D_c can be quantified following ASTM C1556. However, owing to the destructive, time-intensive nature of ASTM C1556, there is a marked preference for rapid, economical, and non-destructive methodologies to assess D_c. In this context, transmission X-ray microscopy (TXM) has recently emerged as an innovative imaging technique for cement-based materials, proposed to avoid the limitations inherent in destructive or comparative testing methods (Moradllo and Ley, 2017a, 2017b). This technique affords direct and applicable observations of ion transport within cementitious compositions on a practical scale, offering the advantages of expeditiousness and non-destructiveness. Quantifying D_c in such materials is achievable by analyzing alterations in gray-scale values facilitated by TXM (Behravan et al., 2023, 2021; Darma et al., 2013; Moradllo et al., 2017).

The significance of this study lies in its strategic utilization of a non-destructive approach to examine the effects of PVA fibers and curing periods on the ingress of chloride into concrete during freeze-thaw (F-T) cycles. Two air-entrained concretes were prepared, each subjected to different curing periods: (a) conventional concrete and (b) fiber-reinforced concrete. This research introduces a novel application of TXM to quantify D_c in concrete, a methodology that has not been previously utilized in the context of F-T cycles, thus providing fresh insights into the behavior of both conventional and fiber-reinforced concrete under extreme weather conditions. Additionally, a holistic evaluation incorporating mechanical strengths, UPV, surface resistivity (SR), ML, and RDME was conducted to comprehensively assess the cumulative impact of F-T cycles on the integrity of concrete specimens. By integrating these methods, this study significantly contributes to the body of knowledge on concrete durability and resilience, offering valuable data that can inform future research and practical applications in infrastructure development.

2.3 Materials and methodologies

2.3.1 Materials and mix design

This study evaluated two air-entrained concretes: Group A (conventional) and Group B (fiber-reinforced). The mix design adhered to the ACI 211.11 volumetric procedure for concrete proportioning with a water-to-cement ratio of 0.4. Type I/II portland cement, with a specific gravity of 3.15, was used. A natural sand fine aggregate (FA), with a fineness modulus of 2.6, and crushed limestone coarse aggregate (CA), with a maximum particle size of 19 mm, were used. The absorption capacity of both FA and CA was 1.1%. Before mixing, the aggregates were oven-dried and cooled to room temperature. The mixing water was adjusted to account for their absorption capacity, ensuring the aggregates reached a saturated surface dry (SSD) condition. The chemical composition of the cement used in this study are listed in **Table 2- 1**. An air-entraining admixture

(AEA) was incorporated into both concrete batches at a dosage of 46 mL per 100 kg of cement, in accordance with ACI 211.1 recommendations for air-entrained concrete with 19 mm nominal maximum aggregate, which specify a target air content of 4% to 6% for concrete exposed to mild to severe F-T conditions. The fiber-reinforced batch included PVA fibers, each 12.5 mm long and 100 μm in diameter, at a concentration of 0.4 % by the total mixture volume. This dosage was selected based on prior studies, which recommend PVA fiber contents in the range of 0.1% to 3.0% for concrete applications (M K Yew et al., 2015), with optimum levels for improving mechanical and fracture properties typically reported between 0% and 1.5%(Ling et al., 2019). **Table 2- 2** and **Table 2- 3** list the properties of PVA fibers and mixture proportions for both concrete groups. The air content of fresh concrete was measured using the pressure method in accordance with ASTM C231. The concrete was prepared in two batches for the 14-day and 70-day curing periods. Although the mix design remained consistent, slight variations in measured air content were observed: 5.5% and 5.7% for Group A, and 4.6% and 4.9% for Group B (see Table 3). These differences are likely due to normal variability in mixing conditions, such as ambient temperature and admixture incorporation. A total of 24 Beam prisms (400 mm by 100 mm by 75mm) and 24 cylinders (75 mm diameter by 150 mm height) were prepared for experimental analysis. These specimens were subjected to different curing moist periods (14 and 70 days) and further categorized into subgroups: GA-PW-14d and GA-PW-70d for Group A specimens undergoing 14 and 70 days of curing, respectively, and GB-PW-14d and GB-PW-70d for Group B specimens subjected to the exact curing durations.

Table 2- 1 Chemical composition of cement

Component	CaO	SiO_2	Al_2O_3	Fe_2O_3	SO_3	MgO	Na_2O
Content (%)	62.77	20.80	4.73	3.57	4.08	1.87	0.52

Table 2- 2 PVA fiber properties

Specific Gravity	1.3
Melting Point	200 ^{o}C
Tensile Strength	1235 MPa

Table 2- 3 Mix design of concrete

Groups	Cement (kg/m^3)	FA (kg/m^3)	CA (kg/m^3)	Water (kg/m^3)	w/c	PVA Fibers (kg/m^3)	Fresh Air Content (%)
GA-14d	541.4	628.6	914.2	227.9	0.4	0	5.5
GB-14d	541.4	618.0	914.2	227.9	0.4	5.2	4.6
GA-70d	541.4	628.6	914.2	227.9	0.4	0	5.7
GB-70d	541.4	618.0	914.2	227.9	0.4	5.2	4.9

2.3.2 Characterization of the air-void system in hardened concrete

In this study, the air-void system in hardened concrete was characterized using the point count method following ASTM C457 Procedure B. The samples were polished and then scanned using a digital scanner. The scanned images were processed using ImageJ software, where a grid was applied for manual evaluation. The pixel size was estimated to be 10.6 μm, and the total imaged area was 5.4 cm by 3.6 cm. Based on this analysis, the air content (A), paste-air ratio (p/A), average chord length ($\bar{l}$), void frequency (n), specific surface (α), and spacing factor ($\bar{L}$) of the hardened Group A and Group B concrete specimens were determined. Figure 2- 1 (a) and (b) show representative images of the polished concrete surfaces used for air-void analysis in Group A and Group B, respectively.

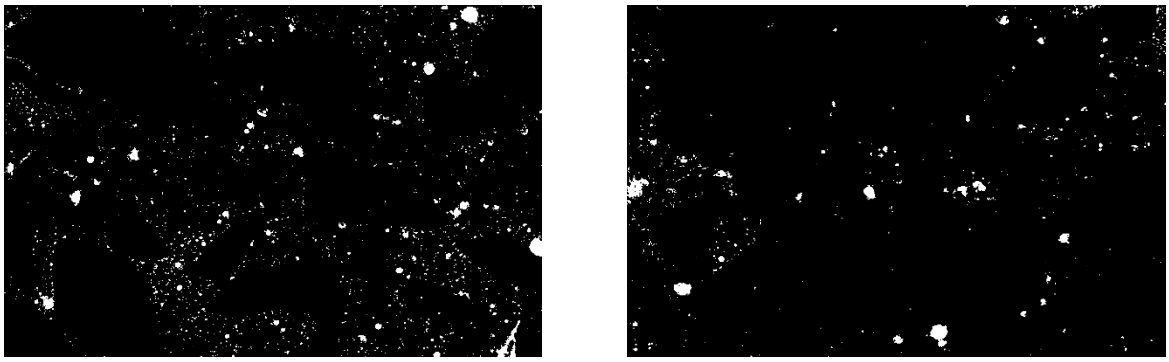

(a) **(b)**

Figure 2- 1 Air-void structure of (a) Group A and (b) Group B concrete showing differences in void distribution; the field of view for each image is approximately 5.4 cm × 3.6 cm.

2.3.3 Replicate testing procedure

Both concrete specimen groups were subjected to a 14-day and 70-day moist curing in a fog room. Subsequently, the specimens were exposed to F-T cycles in plain water, following the guidelines specified in ASTM C666 Procedure A. In this study, the exposure duration of one F-T cycle was 4.5 hours. During a freezing half cycle, the temperature rapidly decreases from 4.4 °C to −18 °C within 1 hour and remains constant at −18 °C for 2 hours. Subsequently, in the thawing half cycle, the temperature rises from −18 °C to 4.4 °C within 0.5 hours and remains stable at 4.4 °C for 1 hour. The combination of these two half cycles constitutes a single F-T cycle. ML and RDME were determined every 28 to 36 F-T cycles following Equations 1 and 2, where m_o is the mass of the specimens at 0 F-T cycles, m_n represents the mass of the specimens after n F-T cycles, Δm is the percentage (%) of the ML of the concrete specimens after n F-T cycles, n_o is the fundamental transverse frequency of the specimens at 0 F-T cycles, n_n represents the fundamental transverse frequency of the specimens after n F-T cycles, and P_n is the RDME of the concrete specimens after n F-T cycles.

$$\Delta m = \frac{m_o - m_n}{m_o} \times 100 \quad (1)$$

$$RDME, P_n = \frac{n_n^2}{n_0^2} \quad (2)$$

In addition, longitudinal UPV (ASTM C597), SR (AASHTO T358) from all four sides of the prisms, and fundamental transverse frequency (ASTM C215) were measured before F-T cycles and at least every 28 to 36 F-T cycles. Furthermore, both the compressive strength (ASTM C39) and flexural strength (ASTM C293) were evaluated before the F-T cycles began and after F-T cycling was ended exposure for all concrete samples.

2.3.4 Testing procedure using TXM

A custom-built TXM was utilized to evaluate the D_c of concrete specimens for pre- and post-F-T cycles. Figure 2- 2 (Rahat et al., 2024) depicts the schematic of the TXM setup, which was designed based on the design by other researchers (Behravan et al., 2021, 2023; Ley et al., 2023; Moradllo and Ley, 2017a, 2017b). This TXM setup offers a non-destructive and swift means of conducting diffusion experiments, with the capability to acquire an X-ray radiograph in roughly 10 seconds. **Table 2- 4** shows the X-ray source and detector details. For the experimental procedure using the TXM, two concrete cores of 19 mm diameter by 25 mm height were cut from all groups of specimens before and after undergoing F-T cycles, specifically from the top and bottom faces of the beam prisms. The samples were then sealed by applying a layer of hydrophobic wax on the sides and bottom surfaces while keeping the top surface uncoated to allow for solution ponding, facilitating 1D diffusion. This study evaluated concrete samples that underwent 70 days of curing for up to 500 F-T cycles. Samples that were cured for 14 days were assessed for up to 375 F-T cycles, as the surface scaling caused by the F-T cycles prevented further analysis for additional F-T cycles.

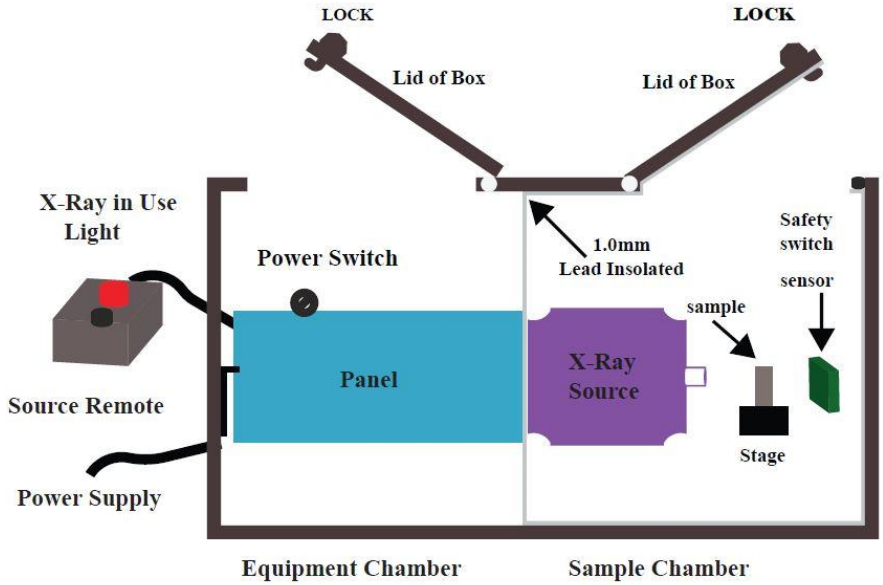

Figure 2- 2 Schematic illustration of the TXM system.

Table 2- 4 Details of the X-ray source

Sensor Resolution (line pairs per mm)	33.78
Pixel Size (μm)	19
Voltage (keV)	65
Current (μA)	7000
Exposure Time (s)	0.25

Previous studies have focused on chloride diffusion in concrete (*e.g.*, Florea and Brouwers, 2012; Jasielec et al., 2020), yet there is limited research on iodide diffusion. In this study, potassium iodide (KI) was utilized as a tracer for NaCl, taking advantage of its chemical stability and diffusion properties that are similar to those of chloride ions (Behravan et al., 2023, 2021; Moradllo and Ley, 2017). Both iodide (I^-) and chloride (Cl^-) are monovalent anions with similar characteristics, which makes iodide an appropriate alternative (Jin et al., 2024). In contrast to chloride, iodide shows very low reactivity within the alkaline conditions of concrete, resulting in only a few minor reaction products, such as $3CaO{\cdot}Al_2O_3{\cdot}CaI_2{\cdot}8H_2O$, with unhydrated C_3A (Jin et al., 2024), which helps to maintain a limited effect on the cement matrix.

A 0.6 M KI solution was used for ponding the cored specimens, selected for its ability to enhance contrast in X-ray imaging, facilitating the observation of iodide ingress into the concrete matrix. Given the comparable ionic radii of iodide and chloride, and the fact that iodide's diffusion coefficient is 24% higher than chloride's, iodide diffusion serves as a more stringent benchmark

for evaluating chloride transport in concrete (Behravan et al., 2023, 2021; Moradllo and Ley, 2017).

In this study, all core samples were initially scanned to serve as reference images. Subsequently, the samples were immersed in the KI solution and rescanned after 3 days, 14 days, and 28 days. This process facilitates a straightforward comparison of these images against a reference image, enabling the evaluation of alterations in gray values by subtracting the reference image. A reference image was captured following F-T cycles for specimens exposed to F-T cycles. Subsequently, these samples were subjected to an identical procedure involving immersion in a KI solution and subsequent X-ray imaging. For the radiographic analysis, a software program matched the radiographic images captured at 3 days, 14 days, and 28 days with their respective reference images for each specimen. This matching process entailed making local adjustments, including shifts and rotations, to ensure that the later radiographs were aligned accurately with the initial reference radiograph. The red box in the subtracted image shown in **Figure 2- 3.** represents the penetrated depth of iodide in the sample after 3 days of ponding in the KI solution. To determine the mean gray values at different depths in each sample, a region was determined approximately 7.37 mm wide (equivalent to approximately 280 pixels in the TXM radiographs), as shown in **Figure 2- 3**. This was performed to minimize the occurrence of cupping artifacts (Behravan et al., 2023, 2021; Khanzadeh Moradllo and Ley, 2017). Each line represents a grayscale value corresponding to a specific depth, and the final gray-value profile was computed by averaging the values from 280 individual lines. Behravan et al. (2023) suggested using radiographs from various angles to estimate D_c for concrete specimens, advocating for presenting these findings as the mean D_c. Given the composite nature of concrete, analysis limited to the central section of radiographs might be influenced by the heterogeneity of the aggregates. Consequently, in this study, radiographs were captured at angles of 0°, 60°, 120°, and 180° for every sample to determine the apparent D_c.

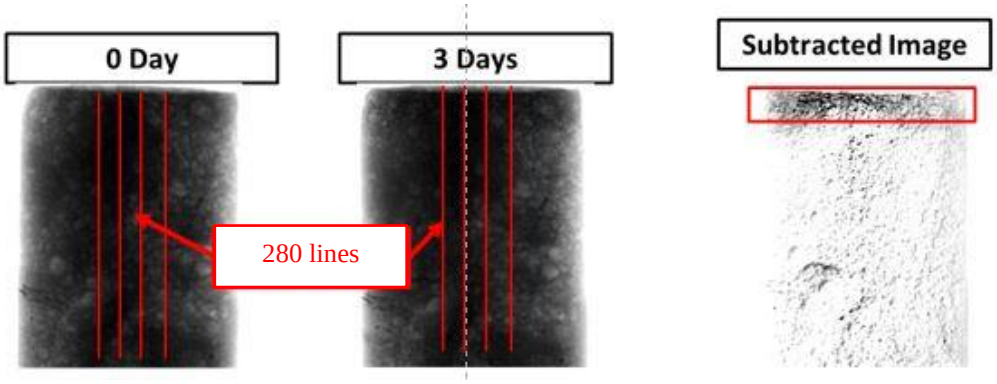

Figure 2- 3 Subtraction of radiographs within a specified area of interest.

Finally, employing nonlinear regression, the apparent D_c is determined based on a solution from Fick's second law of diffusion, as is used in ASTM C1556. Equation 3 defines the solution for the 1D diffusion problem, where x is the distance from the sample surface, C_s is the surface iodide concentration, $C_{(x,t)}$ is the iodide concentration at depth of x from the surface after time t, and erf is the Gaussian error function. The D_c value in this study combines the impact of fluid transport mechanisms such as diffusion, absorption, convection, and chemical binding into one term.

$$C_{(x,t)} = C_s\left(1 - erf\left(\frac{x}{2\sqrt{D_c t}}\right)\right) \quad (3)$$

2.4 Results and discussions

2.4.1 Hardened air-void system characterization results

Table 2- 5 shows the results of the hardened air-void system for Group A and Group B. The air-void system result demonstrates that Group A has an improved air-void system than Group B, as reflected in its lower spacing factor (0.07 mm *vs*. 0.08 mm), higher specific surface (22 mm^{-1} *vs*. 20 mm^{-1}), and greater void frequency (0.239 mm^{-1} *vs*. 0.202 mm^{-1}). Both groups meet the ASTM C457 requirement for moderate F-T exposure (spacing factor < 0.20 mm), but Group A's more refined and evenly distributed void structure suggests superior durability. The fresh air content of Group A (5.7%) and Group B (4.9%) decreased after hardening, with final values of 4.3% and 4.0%, respectively, which agrees with Khayat and Nasser (1991), who suggested that the reduction in air content was due to air loss during consolidation. The inclusion of PVA fibers in Group B may have influenced the formation and stability of air voids. It is hypothesized that reduced workability and potential fiber clustering hindered uniform bubble distribution, resulting in a coarser void structure. Additionally, although no direct studies were found, one plausible hypothesis is that AEA may sorb onto the surfaces of PVA fibers, reducing its effectiveness in stabilizing air bubbles. This interaction may have contributed to the lower air content observed in Group B.

Table 2- 5 Hardened air-void system data for concrete specimens

	A (%)	n (mm^{-1})	p/A	$\bar{l}$ (mm)	α (mm^{-1})	$\bar{L}$ (mm)
Group A	4.3	0.239	7.636	0.182	22	0.07
Group B	4.0	0.202	8.333	0.198	20	0.08

2.4.2 ML and RDME results

Figure 2- 4 (a) and (b) depict the changes in ML and RDME values for concrete samples from Groups A and B, which underwent 14-day and 70-day curing periods over F-T cycles. The degree of deterioration of concrete samples is directly related to the changes in their mass and RDME. In **Figure 2- 4 (a)**, Group A samples experienced a ML of 1.4 %, while Group B samples showed a slightly higher ML of 1.7 % after undergoing 1000 F-T cycles for 70-day cured samples. This

difference in ML aligns with the findings of Al-Kheetan et al., (2020), for concrete with a w/cm ratio of 0.40. Both groups exhibited enhanced resistance to 1000 F-T cycles despite the slightly higher ML in Group B for 70-day cured samples.

However, samples cured for 14 days underwent 300 F-T cycles and exhibited higher ML values than 70 days cured samples. Group A displayed a 1.0 % ML, while Group B showed a slightly higher reduction of 3.2 % after 300 F-T cycles. This result is consistent with the findings of Liu et al. (2021). For the samples cured for 70 days, Group A and Group B experienced an ML of 0.5 % after 300 F-T cycles, highlighting the impact of the curing period on F-T resistance.

As shown in **Figure 2- 4 (b)**, Group A samples exhibited an RDME of 95 %, while Group B samples showed 95 % after completing 1000 F-T cycles for 70-day cured samples. This RDME value for concrete samples with a w/cm ratio of 0.40 aligns with the findings of Shang & Yi, (2013). Concrete with a lower w/cm ratio displays reduced porosity, limiting the exposure of capillary water to frost action, which in turn lowers its susceptibility to frost-related damage.

Nevertheless, samples that were cured for 14 days were subjected to 300 F-T cycles and demonstrated lower RDME values than those that were cured for 70 days. Group A exhibited a 73 % RDME, while Group B showed a lower value of 65 % after 300 F-T cycles. This result is consistent with the findings of Liu et al. (2021). In the case of samples that were cured for 70 days, Group A and Group B experienced RDME of 98 % and 96 % after 300 F-T cycles, respectively, emphasizing the influence of curing duration on F-T resistance. According to ASTM C666 Procedure A, testing should be carried out on each specimen until it has been subjected to 300 cycles or until its relative dynamic modulus of elasticity reaches 60 % of the initial modulus. This study's 14-day cured samples were close to the 60 % threshold value. Compared to Group B, Group A exhibited superior resistance to F-T cycles due to its higher air content. This was evident from the lower ML, and RDME results observed when introducing PVA fibers. The better air-void system, as reported in *Section 2.4.1* in Group A, significantly improved its ability to withstand F-T cycles, highlighting the critical role of air entrainment in preserving concrete durability in challenging conditions. Furthermore, prolonged curing leads to increased resistance to F-T cycles.

Table 2- 6 outlines the mass (kg) measurements of various replicates before and after undergoing F-T cycles for two groups of concrete samples cured for 70 days and 14 days. Similarly, **Table 2-7** presents the fundamental transverse frequency (Hz) values measured prior to and following F-T cycles for both groups, corresponding to the exact curing durations.

After subjecting the samples to 300 F-T cycles, a statistically significant difference was observed in both ML and RDME at a significance level 0.05 when comparing the GA-PW-70d sample with the GA-PW-14d and GB-PW-14d samples. However, there is insufficient evidence to conclude a statistically significant difference between the GA-PW-14d and GB-PW-14d samples after 300 F-T cycles and between the GA-PW-70d and GB-PW-70d samples at 300 and 1000 cycles for both ML and RDME.

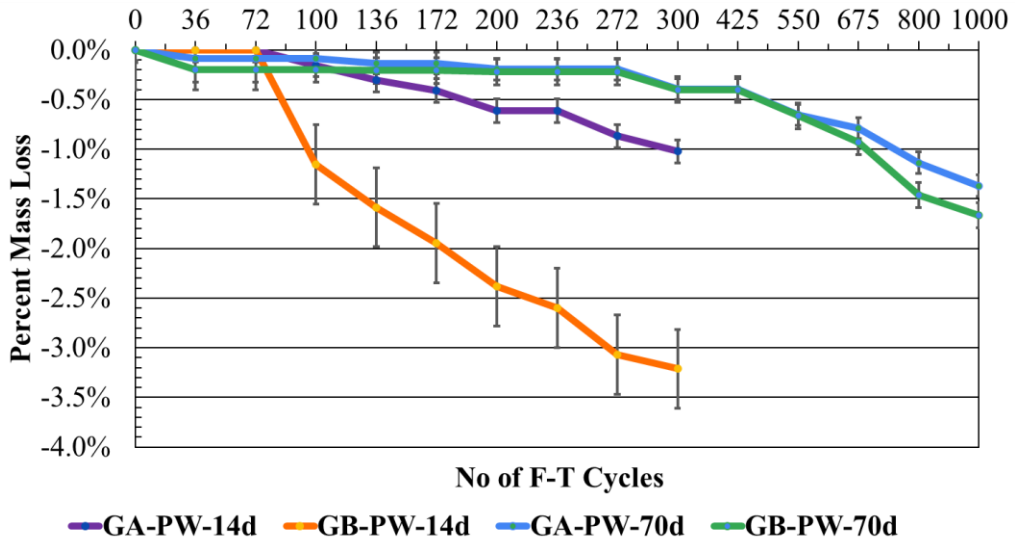

(a)

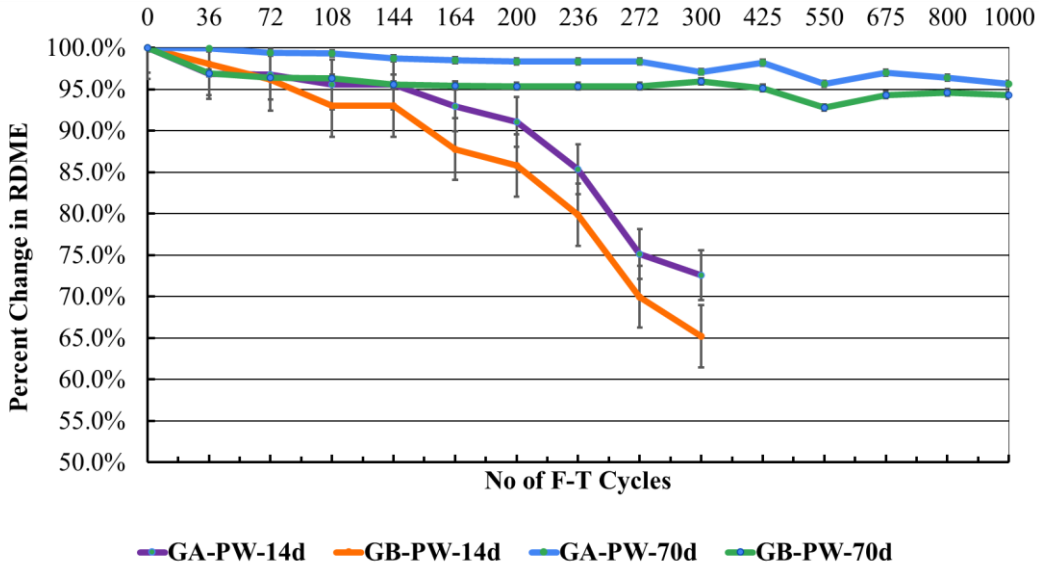

(b)

Figure 2- 4 Change of (a) mass and (b) RDME value over F-T cycles for different curing periods, error bars represent one standard deviation.

Table 2- 6 Mass (kg) measurements for concrete replicates in both concrete groups before and after F-T cycles

70 days curing period										
	Group A					**Group B**				
F-T cycle	R1	R2	R3	**Average**	**STD**	R1	R2	R3	**Average**	**STD**
0	7.652	7.808	7.411	7.624	0.163	7.587	7.543	7.418	7.516	0.072
36	7.651	7.808	7.411	7.623	0.163	7.585	7.543	7.418	7.515	0.071
72	7.651	7.808	7.411	7.623	0.163	7.585	7.543	7.418	7.515	0.071
100	7.651	7.808	7.411	7.623	0.163	7.585	7.543	7.418	7.515	0.071
136	7.650	7.800	7.410	7.620	0.161	7.584	7.542	7.417	7.514	0.071
172	7.650	7.800	7.410	7.620	0.161	7.584	7.542	7.417	7.514	0.071
200	7.648	7.790	7.408	7.615	0.158	7.583	7.541	7.416	7.513	0.071
236	7.648	7.790	7.408	7.615	0.158	7.583	7.541	7.416	7.513	0.071
272	7.648	7.790	7.408	7.615	0.158	7.583	7.541	7.416	7.513	0.071
300	7.648	7.790	7.408	7.615	0.158	7.583	7.541	7.416	7.513	0.071
425	7.640	7.770	7.400	7.603	0.153	7.580	7.530	7.400	7.503	0.076
550	7.620	7.750	7.380	7.583	0.153	7.570	7.510	7.370	7.483	0.084
675	7.600	7.750	7.360	7.570	0.161	7.560	7.490	7.340	7.463	0.092
800	7.570	7.720	7.320	7.537	0.165	7.520	7.460	7.290	7.423	0.097
1000	7.570	7.700	7.320	7.530	0.158	7.510	7.430	7.270	7.403	0.100
14 days curing period										
	Group A					**Group B**				
F-T cycle	R1	R2	R3	**Average**	**STD**	R1	R2	R3	**Average**	**STD**
0	6.501	6.620	6.469	6.530	0.065	6.920	6.940	6.899	6.920	0.017
36	6.501	6.620	6.469	6.530	0.065	6.920	6.940	6.899	6.920	0.017
72	6.501	6.620	6.469	6.530	0.065	6.920	6.940	6.899	6.920	0.017
100	6.490	6.610	6.460	6.520	0.065	6.840	6.860	6.820	6.840	0.016
136	6.480	6.600	6.450	6.510	0.065	6.810	6.820	6.790	6.807	0.012
172	6.470	6.600	6.440	6.503	0.069	6.790	6.800	6.760	6.783	0.017
200	6.450	6.580	6.440	6.490	0.064	6.760	6.790	6.730	6.760	0.024
236	6.450	6.580	6.440	6.490	0.064	6.750	6.760	6.710	6.740	0.022
272	6.440	6.560	6.420	6.473	0.062	6.715	6.720	6.680	6.705	0.018
300	6.430	6.550	6.410	6.463	0.062	6.700	6.713	6.680	6.698	0.014

*Note: R1, R2, and R3 stand for Replicate 1, Replicate 2, and Replicate 3; STD stands for standard deviation

Table 2- 7 Fundamental transverse frequency (Hz) measurements for concrete replicates in both concrete groups before and after F-T cycles

70 days curing period										
	Group A					**Group B**				
F-T cycle	R1	R2	R3	**Average**	**STD**	R1	R2	R3	**Average**	**STD**
0	2350	2360	2260	2320	45	2240	2260	2320	2270	34
36	2340	2350	2250	2310	45	2280	2250	2250	2260	14
72	2340	2350	2250	2310	45	2280	2250	2250	2260	14
100	2340	2350	2250	2310	45	2280	2240	2240	2250	19
136	2340	2350	2250	2310	45	2280	2240	2240	2250	19
172	2340	2340	2250	2310	42	2270	2240	2240	2250	14
200	2340	2340	2250	2310	42	2270	2240	2240	2250	14
236	2330	2340	2250	2310	40	2260	2240	2230	2240	12
272	2330	2340	2250	2310	40	2260	2240	2230	2240	12
300	2320	2320	2240	2290	38	2270	2220	2230	2240	22
425	2320	2320	2230	2290	42	2260	2210	2220	2230	22
550	2320	2320	2230	2290	42	2260	2210	2220	2230	22
675	2300	2320	2240	2290	34	2260	2200	2220	2230	25
800	2330	2340	2250	2310	40	2280	2270	2240	2260	17
1000	2330	2330	2240	2300	42	2280	2260	2240	2260	16
14 days curing period										
	Group A					**Group B**				
F-T cycle	R1	R2	R3	**Average**	**STD**	R1	R2	R3	**Average**	**STD**
0	2220	2200	2240	2220	16	2250	2380	2380	2340	61
36	2200	2180	2140	2170	25	2250	2250	2350	2280	47
72	2220	2180	2130	2180	37	2220	2220	2320	2250	47
100	2220	2160	2130	2150	15	2210	2200	2310	2260	55
136	2220	2160	2130	2150	15	2210	2200	2310	2260	55
172	2170	2160	2110	2140	25	2200	2190	2220	2210	15
200	2160	2120	2100	2110	10	2170	2160	2190	2180	15
236	2090	2060	2030	2050	15	2100	2090	2120	2110	15
272	1960	1930	1900	1920	15	1970	1960	1990	1980	15
300	1910	1890	1860	1880	15	1890	1880	1900	1890	10

*Note: R1, R2, and R3 stand for Replicate 1, Replicate 2, and Replicate 3; STD stands for standard deviation

2.4.3 UPV results

The variations in UPV values during F-T cycles for Groups A and Group B are depicted in **Figure 2- 5**. It is apparent that Group A consistently maintained higher UPV values compared to Group B throughout the cycles. The initial UPV values for the samples cured for 70 days were 4500 m s^{-1} and above, whereas those cured for 14 days exhibited UPV values of 4200 m s^{-1} and above. Group B, reinforced with PVA fibers, experienced a 10 % reduction in UPV after 1000 F-T cycles for the samples cured for 70 days, while Group A experienced a 6 % reduction. Despite the higher decrease in Group B, both groups exhibited enhanced resistance against 1000 F-T cycles.

After 300 F-T cycles, the UPV results showed that samples cured for 14 days degraded more than those cured for 70 days. GA-PW-14d had a 28.7% reduction, while GB-PW-14d showed a 33 % reduction after 300 F-T cycles. In contrast, samples cured for 70 days (Groups A and B) experienced only a 5 % and 5 % decrease after 300 F-T cycles, respectively, highlighting the impact of the curing period on F-T resistance. This result is consistent with a previous study by El-Mir and El-Zahab (2022). The lower air content across all Group B samples, compared to Group A, indicates that the reduced performance under F-T cycles may be more related to the low air content rather than the influence of PVA fibers. The 70-day cured samples demonstrated superior performance, indicating the benefits of a more extended curing period in enhancing F-T resistance. The differing UPV reduction suggests that including PVA fibers in Group B may not effectively combat the effects of F-T cycles on concrete's UPV, with proper curing and a better air-void system likely playing pivotal roles.

The evidence suggests a statistical difference between the GA-PW-70d sample and the GA-PW-14d and GB-PW-14d samples after 300 F-T cycles at a significance level of 0.05. However, when comparing the GA-PW-14d and GB-PW-14d samples after 300 F-T cycles, there is insufficient evidence to conclude that the difference in percent change in UPV is statistically significant at the 0.05 significance level. Similarly, when comparing the GA-PW-70d samples with GB-PW-70d samples at 300 and 1000 cycles of F-T testing, there is insufficient evidence to conclude that the difference in percent change in UPV is statistically significant at the 0.05 significance level.

Table 2- 8 outlines the UPV ($m\ s^{-1}$) measurements of various replicates before and after undergoing F-T cycles for two groups of concrete samples cured for 70 and 14 days.

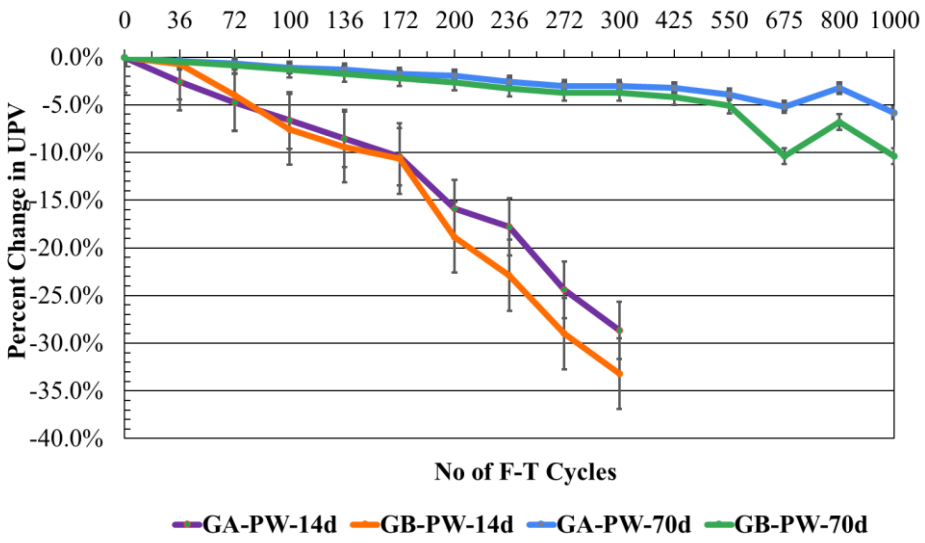

Figure 2- 5 Change of UPV value over F-T cycles for different curing periods, error bars represent one standard deviation.

Table 2- 8 UPV (m s^{-1}) measurements for concrete replicates in both concrete groups before and after F-T cycles

70 days curing period										
	Group A					**Group B**				
F-T cycle	R1	R2	R3	**Average**	**STD**	R1	R2	R3	**Average**	**STD**
0	4590	4690	4570	4620	52	4560	4410	4560	4510	71
36	4580	4670	4550	4600	51	4540	4390	4540	4490	71
72	4570	4650	4540	4590	46	4520	4370	4520	4470	71
100	4550	4640	4510	4570	54	4500	4350	4500	4450	71
136	4540	4630	4500	4560	54	4480	4320	4480	4430	75
172	4530	4600	4480	4540	49	4470	4300	4470	4410	80
200	4520	4590	4470	4530	49	4450	4280	4450	4390	80
236	4500	4570	4420	4500	61	4410	4240	4440	4360	88
272	4490	4530	4410	4480	50	4390	4220	4420	4340	88
300	4490	4530	4410	4480	50	4390	4220	4420	4340	88
425	4490	4520	4390	4470	56	4380	4200	4390	4320	87
550	4470	4500	4350	4440	65	4340	4150	4340	4280	90
675	4360	4480	4300	4380	75	4070	4000	4080	4050	36
800	4440	4580	4390	4470	80	4190	4130	4270	4200	57
1000	4360	4430	4260	4350	70	4050	4000	4080	4040	33
14 days curing period										
	Group A					**Group B**				
F-T cycle	R1	R2	R3	**Average**	**STD**	R1	R2	R3	**Average**	**STD**
0	4190	4290	4170	4220	52	4260	4210	4260	4240	24
36	4110	4180	4030	4110	61	4220	4200	4210	4210	8
72	4000	4100	3960	4020	59	4110	4080	4020	4070	37
100	3880	4070	3880	3940	90	4010	3690	4100	3930	176
136	3850	3920	3820	3860	42	3990	3520	4010	3840	226
172	3720	3840	3770	3780	49	3970	3490	3910	3790	214
200	3400	3510	3730	3550	137	3820	3230	3310	3450	261
236	3230	3530	3650	3470	177	3580	3190	3100	3290	208
272	2970	3240	3350	3190	160	3260	2910	2850	3010	181
300	2810	3010	3220	3010	167	3070	2760	2670	2830	171

*Note: R1, R2, and R3 stand for Replicate 1, Replicate 2, and Replicate 3; STD stands for standard deviation

2.4.4 SR results

The measurement of SR has become the preferred method for assessing concrete susceptibility to chloride ion penetration, replacing the rapid chloride penetration test (Ghosh and Tran, 2015). **Figure 2- 6** shows how the SR values changed during F-T cycles for Groups A and Group B. Group A consistently had higher SR values than Group B. The initial SR values for the samples cured for 70 days were 25 kΩ-cm and above. In contrast, those cured for 14 days were 15 kΩ-cm and above, indicating good-quality concrete samples, lower permeability, and low to moderate risk of corrosion (Lim et. al, 2011).

After 1000 F-T cycles, the samples in Group B, which had PVA fibers, experienced a 53 % decrease in SR after 70 days of curing, while Group A had a slightly lower reduction of 46 %. Both groups showed decreased resistance to 1000 F-T cycles, with Group B showing a more significant decrease. This decrease in SR can be attributed to surface scaling caused by F-T cycles, which disrupts the contact between the electrodes and the concrete, resulting in inconsistent or lower resistivity readings. Scaling can also increase surface permeability, further decreasing the SR values (Sasanipour et al., 2022).

The samples that were cured for 14 days could not withstand more than 300 cycles and showed significant degradation in the SR test results. Specifically, Group A experienced a 51 % reduction, while Group B had a slightly higher reduction of 52 % after 300 F-T cycles. On the other hand, for the samples that were cured for 70 days, Group A and Group B experienced a decrease of 17 % and 27 % after 300 F-T cycles, underscoring the impact of the curing period on F-T resistance. The lower air content across all Group B samples than Group A suggests that PVA fibers may not significantly mitigate the effects of F-T cycles. Furthermore, the samples cured for 70 days demonstrated superior performance, indicating the benefits of a more extended curing period in enhancing F-T resistance. The difference in SR reduction between the groups implies that including PVA fibers in Group B may not effectively counter the effects of F-T cycles on SR, with proper curing and the improved air-void system likely playing pivotal roles.

After 300 F-T cycles, a statistically significant difference in SR values was observed at a significance level of 0.05 when comparing the GA-PW-70d sample with the GA-PW-14d and GB-PW-14d samples. However, there is insufficient evidence to conclude a statistically significant difference in SR values between the GA-PW-14d and GB-PW-14d samples after 300 F-T cycles and between the GA-PW-70d and GB-PW-70d samples at 300 and 1000 cycles.

Table 2- 9 outlines the SR measurements of various replicates before and after undergoing F-T cycles for two groups of concrete samples cured for 70 and 14 days.

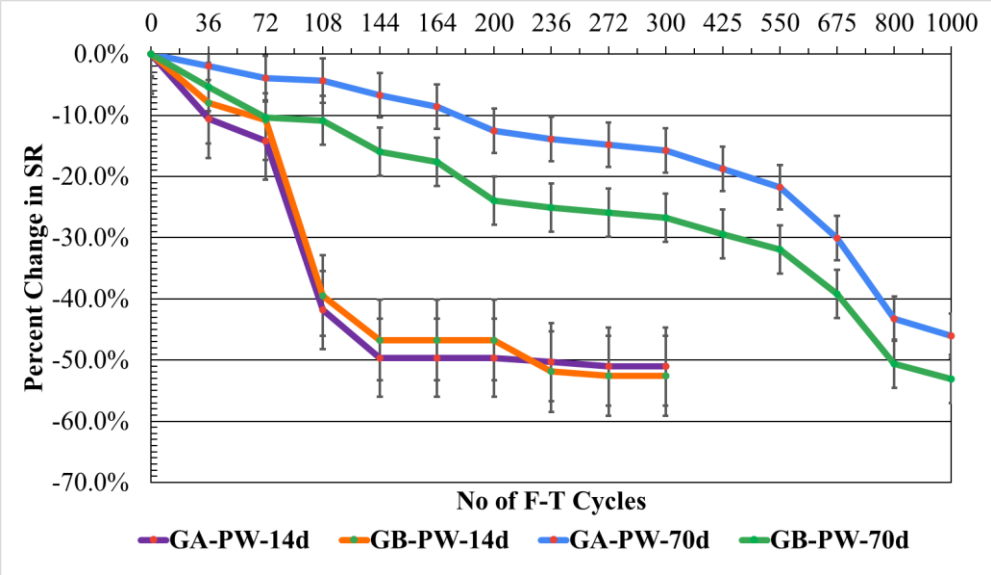

Figure 2- 6 Change of SR value over F-T cycles for different curing periods, error bars represent one standard deviation.

Table 2- 9 SR (kΩ-cm) measurements for concrete replicates in both concrete groups before and after F-T cycles

70 days curing period										
	Group A					Group B				
F-T cycle	R1	R2	R3	**Average**	**STD**	R1	R2	R3	**Average**	**STD**
0	26.0	25.4	25.6	25.7	0.2	23.0	24.0	24.4	23.8	0.6
36	25.5	25.0	25.0	25.2	0.2	22.2	22.6	22.7	22.5	0.2
72	25.0	24.1	25.0	24.7	0.4	21.4	21.3	21.0	21.2	0.2
100	24.9	24.0	24.8	24.6	0.4	21.3	21.2	20.9	21.1	0.2
136	24.0	23.3	24.5	24.0	0.5	20.5	19.8	19.3	19.9	0.5
172	23.3	23.0	24.0	23.5	0.4	20.1	19.4	18.9	19.5	0.5
200	22.0	22.1	23.3	22.5	0.6	18.9	17.9	17.1	17.9	0.7
236	22.1	21.6	22.5	22.1	0.4	18.6	17.6	16.8	17.7	0.7
272	22.0	21.6	22.0	21.9	0.2	18.4	17.4	16.6	17.5	0.7
300	21.9	21.5	21.8	21.7	0.2	18.2	17.2	16.5	17.3	0.7
425	21.1	20.7	21.0	20.9	0.2	17.5	16.6	15.9	16.7	0.7
550	20.4	19.9	20.2	20.1	0.2	16.9	16.0	15.3	16.0	0.7
675	18.2	17.8	17.9	18.0	0.2	15.1	14.3	13.7	14.3	0.6
800	14.8	14.5	14.4	14.5	0.2	12.3	11.6	11.1	11.7	0.5
1000	14.0	13.7	13.6	13.8	0.2	11.7	11.0	10.5	11.1	0.5
14 days curing period										
	Group A					Group B				
F-T cycle	R1	R2	R3	**Average**	**STD**	R1	R2	R3	**Average**	**STD**
0	14.0	14.6	15.0	14.5	0.4	13.9	14.2	14.9	14.3	0.4
36	13.1	12.7	13.2	13.0	0.2	12.4	12.6	12.7	12.6	0.1
72	12.3	13.5	12.5	12.8	0.5	11.8	11.6	13.6	12.3	0.9
100	8.8	8.7	8.2	8.6	0.3	8.6	8.1	8.2	8.3	0.2
136	7.5	7.4	7.2	7.4	0.1	7.6	7.2	7.1	7.3	0.2
172	7.5	7.4	7.2	7.4	0.1	7.6	7.2	7.1	7.3	0.2
200	7.5	7.4	7.2	7.4	0.1	7.6	7.2	7.1	7.3	0.2
236	7.2	7.3	7.2	7.2	0.0	6.9	7.0	7.2	7.0	0.1
272	7.1	7.2	7.1	7.1	0.0	6.8	6.9	7.1	6.9	0.1
300	7.0	7.1	7.0	7.0	0.0	6.7	6.8	7.0	6.8	0.1

*Note: R1, R2, and R3 stand for Replicate 1, Replicate 2, and Replicate 3; STD stands for standard deviation

2.4.4 Strength testing results

Figure 2-7 presents the compressive strength and modulus of rupture results for the different concrete samples before (7 days, 14 days, 28 days, and 70 days) and after 300 F-T (for 14-day cured samples) and 1000 F-T (for 70-day cured samples) cycles.

During the 7-day curing period, the compressive strength values for Group A and Group B were 28.2 MPa and 30.6 Mpa, respectively. Additionally, the modulus of rupture values for Group A and Group B were 8.3 Mpa and 9.4 Mpa, respectively. The samples from Group A exhibited lower

compressive strength and rupture modulus than Group B. This difference in strength is attributed to the reinforcement of Group B with PVA fiber.

Unpaired, two-tailed t-tests for the 7-day results indicated there is insufficient evidence to conclude a statistically significant difference between Group A and Group B compressive strength and modulus of rupture values at a significance level of 0.05.

After 7 days, 14 days, 28 days, and 70 days, the compressive strength and modulus of rupture increased for all samples. Similar to the 7-day results, the Group A samples exhibited lower compressive strength and modulus of rupture compared to Group B, which is attributed to the reinforcement of Group B with PVA fiber.

Unpaired, two-tailed t-tests for the 7-day, 14-day, 28-day, and 70-day results showed insufficient evidence to conclude a statistically significant difference between Group A and Group B compressive strength and modulus of rupture values at a significance level of 0.05.

After enduring 300 F-T cycles, both Group A and Group B samples, which had been cured for 14 days, displayed notable differences. Group B showed the lowest percentage change in compressive strength (10 %) and modulus of rupture (14 %), while Group A exhibited the highest percentage change in both compressive strength (14 %) and modulus of rupture (24 %). It is apparent that although PVA fiber did not significantly improve the durability properties, it did contribute to enhancing the mechanical performance of the concrete samples when subjected to F-T cycles during the 14-day curing process.

In contrast, after subjecting the samples from Group A and Group B, cured for 70 days, to 1000 F-T cycles, both demonstrated significant resistance against F-T cycles for compressive strength and modulus of rupture. Group A experienced a reduction in compressive strength of 4 %, while Group B experienced 2 %. Group A showed a decrease of 7 % for the modulus of rupture, and Group B exhibited an 11 % reduction in values. The results indicate that F-T cycles had a more significant negative impact on concrete's flexural strength than compressive strength. However, PVA fiber enhanced the mechanical performance of all concrete groups. Given that the 70-day cured samples displayed substantial resistance against 1000 F-T cycles, it is clear that the extended curing period plays a crucial role in improving the concrete performance against F-T cycling.

An unpaired, two-tailed t-test was performed on the 14-day cured samples following 300 F-T cycles and the 70-day cured samples following 1000 F-T cycles. The findings suggested insufficient evidence to establish a statistically significant variance in the compressive strength and modulus of rupture values between Group A and Group B at a significance level of 0.05 after 1000 F-T cycles for 70 days of cured samples. For 300 F-T cycles, the findings suggested that there is insufficient evidence to establish a statistically significant variance in the compressive strength values between Group A and Group B at a significance level of 0.05. However, there is a statistically significant difference in modulus of rupture values between Group A and Group B after 300 F-T cycles for 14 days of cured samples.

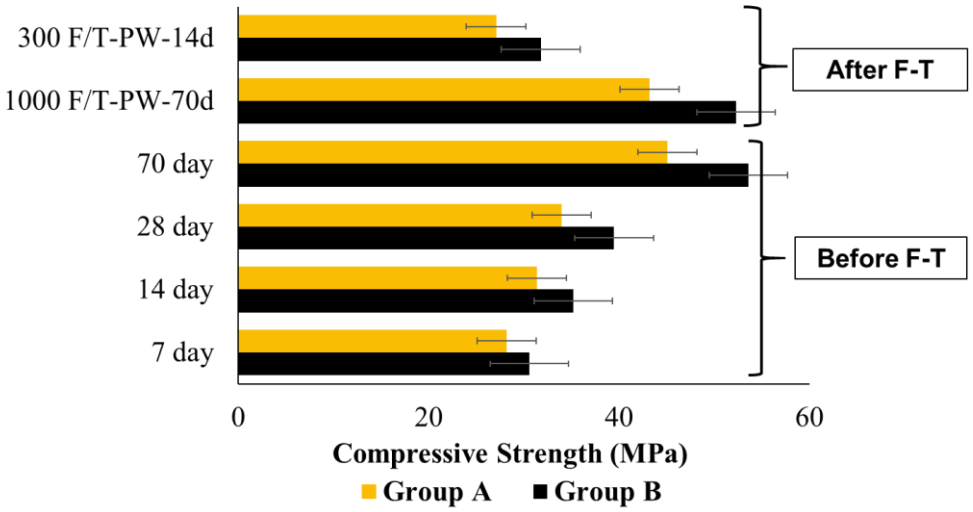

(a)

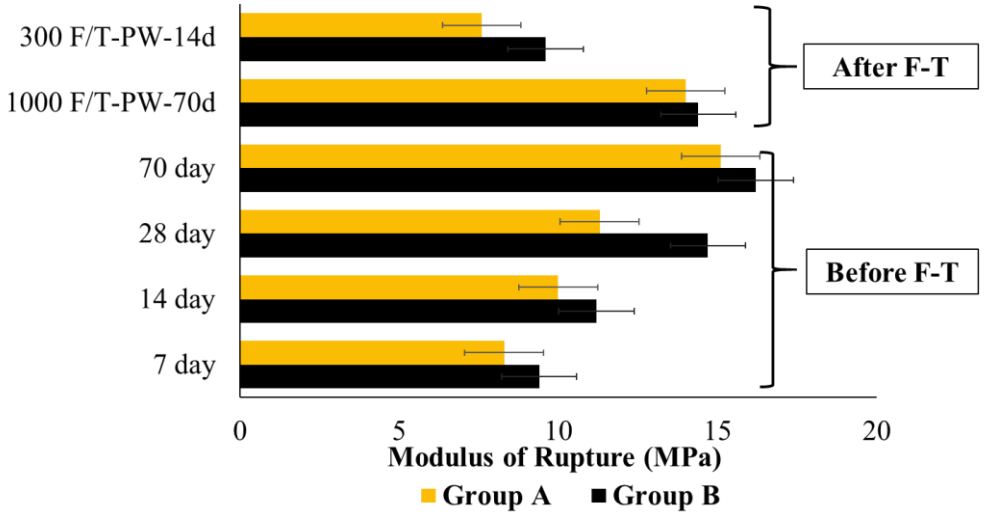

(b)

Figure 2- 7 (a) Compressive strength, and (b) modulus of rupture of different concrete groups for different curing periods before and after F-T cycles.

2.4.5 Time-dependent Dc and concentration profile

Figure 2- 8 depicts the average concentration profiles and D_c for the concrete samples in both Groups A and B after 3 days, 14 days, and 28 days of ponding before the F-T cycles for 70 days and 14 days of curing periods.

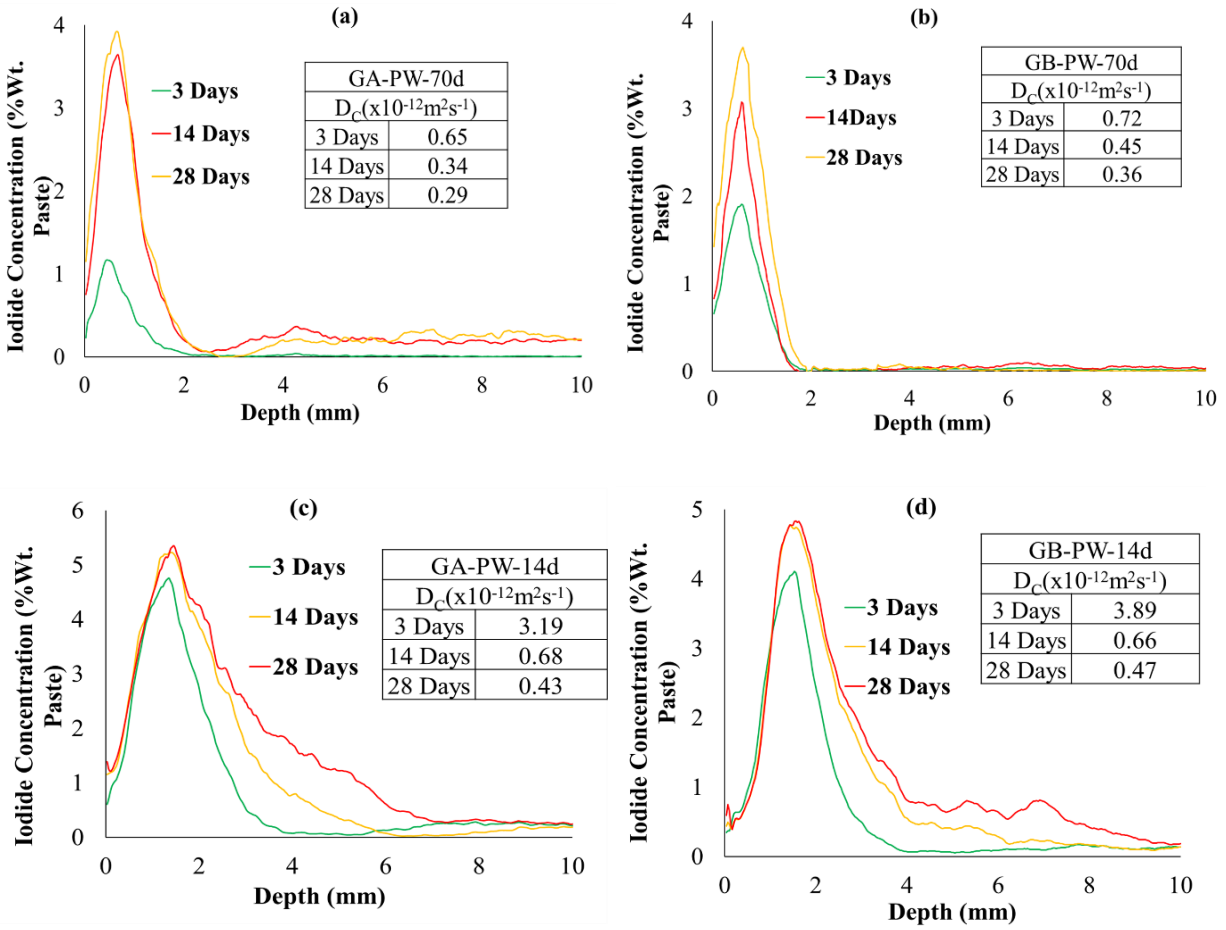

Figure 2- 8 Concentration profiles for the following concrete samples before undergoing F-T cycles : (a) GA-PW-70d, (b) GB-PW-70d, (c) GA-PW-14d, and (d) GB-PW-14d.

Based on the data from **Figure 2- 8 (a), (b), (c), and (d)**, both sets of concrete samples exhibited very low D_c values before undergoing F-T cycles, regardless of whether they were cured for 70 days or 14 days. These findings are consistent with the results of the SR test. **Table 2- 10** shows the average D_c values for GA-PW-70d, GB-PW-70d, GA-PW-14d, and GB-PW-14d samples after 3 days, 14 days, and 28 days of ponding before F-T cycles.

Table 2- 10 Average D_c (x 10^{-12} m^2 s^{-1}) values for concrete samples before F-T cycles

	GA-PW-70d						**GB-PW-70d**					
	3 Days		14 Days		28 Days		3 Days		14 Days		28 Days	
Angle	S-1	S-2	S-1	S-2	S-1	S-2	S-1	S-2	S-1	S-2	S-1	S-2
0	0.70	0.89	0.22	0.28	0.30	0.35	0.28	0.80	0.21	0.19	0.29	0.42
60	0.80	0.80	0.85	0.23	0.31	0.22	0.81	0.97	0.09	0.66	0.35	0.37
120	0.32	0.67	0.30	0.30	0.30	0.40	0.70	0.87	0.99	0.87	0.32	0.56
180	0.53	0.50	0.31	0.20	0.20	0.22	0.50	0.86	0.28	0.28	0.29	0.25
Average	0.65		0.34		0.29		0.72		0.45		0.36	
STD	0.18		0.20		0.07		0.21		0.32		0.09	
	GA-PW-14d						**GB-PW-14d**					
	3 Days		14 Days		28 Days		3 Days		14 Days		28 Days	
Angle	S-1	S-2	S-1	S-2	S-1	S-2	S-1	S-2	S-1	S-2	S-1	S-2
0	2.45	4.76	1.20	0.55	0.35	0.32	2.50	3.97	0.82	0.55	0.54	0.32
60	2.43	2.45	0.60	0.20	0.25	0.32	3.80	3.11	0.25	0.66	0.29	0.25
120	2.54	3.44	0.70	0.80	0.45	0.62	5.55	5.33	0.64	0.86	0.49	0.68
180	2.43	4.98	0.84	0.55	0.60	0.53	4.22	2.61	0.77	0.71	0.70	0.51
Average	3.19		0.68		0.43		3.89		0.66		0.47	
STD	1.02		0.27		0.13		1.07		0.18		0.16	

Note: S-1 and S-2 refer to Sample 1 and Sample 2, respectively; STD stands for standard deviation

These D_c values for concrete with a 0.4 w/cm ratio support the findings of Moradllo et al., (2017). These D_c values confirm that samples cured for 14 days exhibit higher D_c than those cured for 70 days, consistent with other experimental findings. Extended curing periods lead to lower D_c values, indicating enhanced resistance to chloride ingress. This improvement is attributed to the higher degree of hydration in the concrete with extended curing, which results in a denser and more compact matrix, reducing porosity and permeability. However, PVA fiber-reinforced samples demonstrated higher D_c values than conventional concrete for each curing condition, suggesting that including PVA fibers did not significantly improve resistance to chloride ingress. This might be due to potential microstructural changes introduced by the fibers (*e.g.*, Kim et al., 1999; Tran et al., 2022), which could result in increased porosity or microcracking.

It can be seen from the **Figure 2- 8 (a), (b), (c), and (d)**, over the 28-day ponding period, that the iodide concentration reached its peak (C_{max}) of 3.9 % in GA-PW-70d and 3.8 % in GB-PW-70d within the surface layers just below the surface (Δx), followed by a gradual decrease at greater depths. In contrast, the iodide concentration peaked at 5.2 % in GA-PW-14d and 4.7 % in GB-PW-14d within Δx. This rise is likely attributed to capillary absorption and diffusion during the initial solution penetration (Beharavan et al., 2023; Moradllo et al., 2017).

Figure 2- 9. Depicts the average concentration profiles and D_c for the concrete samples in both Groups A and B after 3 days, 14 days, and 28 days of ponding after 125 F-T cycles for 70 days and 14 days of curing periods. **Table 2- 11** shows the average D_c values for GA-PW-70d, GB-

PW-70d, GA-PW-14d, and GB-PW-14d samples after 3 days, 14 days, and 28 days of ponding after 125 F-T cycles.

Table 2- 11 Average D_c (x 10^{-12} m^2 s^{-1}) values for concrete samples after 125 F-T cycles

GA-PW-70d							**GB-PW-70d**					
	3 Days		14 Days		28 Days		3 Days		14 Days		28 Days	
Angle	S-1	S-2	S-1	S-2	S-1	S-2	S-1	S-2	S-1	S-2	S-1	S-2
0	0.16	0.22	0.01	0.49	0.44	0.19	2.00	1.00	0.20	0.42	0.58	0.16
60	0.13	0.42	0.61	0.12	0.51	0.32	3.15	0.60	0.60	0.70	0.94	0.41
120	0.83	1.02	0.46	0.55	0.26	0.35	1.00	1.02	0.48	0.53	0.48	0.11
180	2.21	1.60	0.03	0.71	0.14	0.31	2.94	0.49	0.47	0.70	0.24	0.25
Average	0.82		0.37		0.32		1.53		0.51		0.40	
STD	0.71		0.26		0.11		0.97		0.15		0.25	
GA-PW-14d							**GB-PW-14d**					
	3 Days		14 Days		28 Days		3 Days		14 Days		28 Days	
Angle	S-1	S-2	S-1	S-2	S-1	S-2	S-1	S-2	S-1	S-2	S-1	S-2
0	3.16	2.22	0.87	0.79	0.74	0.59	5.21	2.76	1.20	1.42	0.88	0.76
60	4.13	4.42	1.61	0.92	0.81	0.72	3.15	2.63	1.60	0.81	0.74	0.41
120	3.83	3.02	1.46	0.75	0.66	0.65	3.41	3.77	0.88	0.93	0.98	0.61
180	4.21	2.60	1.03	0.81	0.54	0.61	2.94	4.49	0.77	1.01	1.24	0.25
Average	3.45		1.03		0.67		3.55		1.08		0.73	
STD	0.76		0.30		0.08		0.84		0.28		0.29	

Note: S-1 and S-2 refer to Sample 1 and Sample 2, respectively; STD stands for standard deviation

On the other hand, over the 28-day ponding period after 125 F-T cycles, the iodide concentration reached its peak (C_{max}) of 4.2 % in GA-PW-70d and 4.5 % in GB-PW-70d within the surface layers just below the surface (Δx), followed by a gradual decrease at greater depths. In contrast, the iodide concentration peaked at 5.5 % in GA-PW-14d and 5.2 % in GB-PW-14d within Δx.

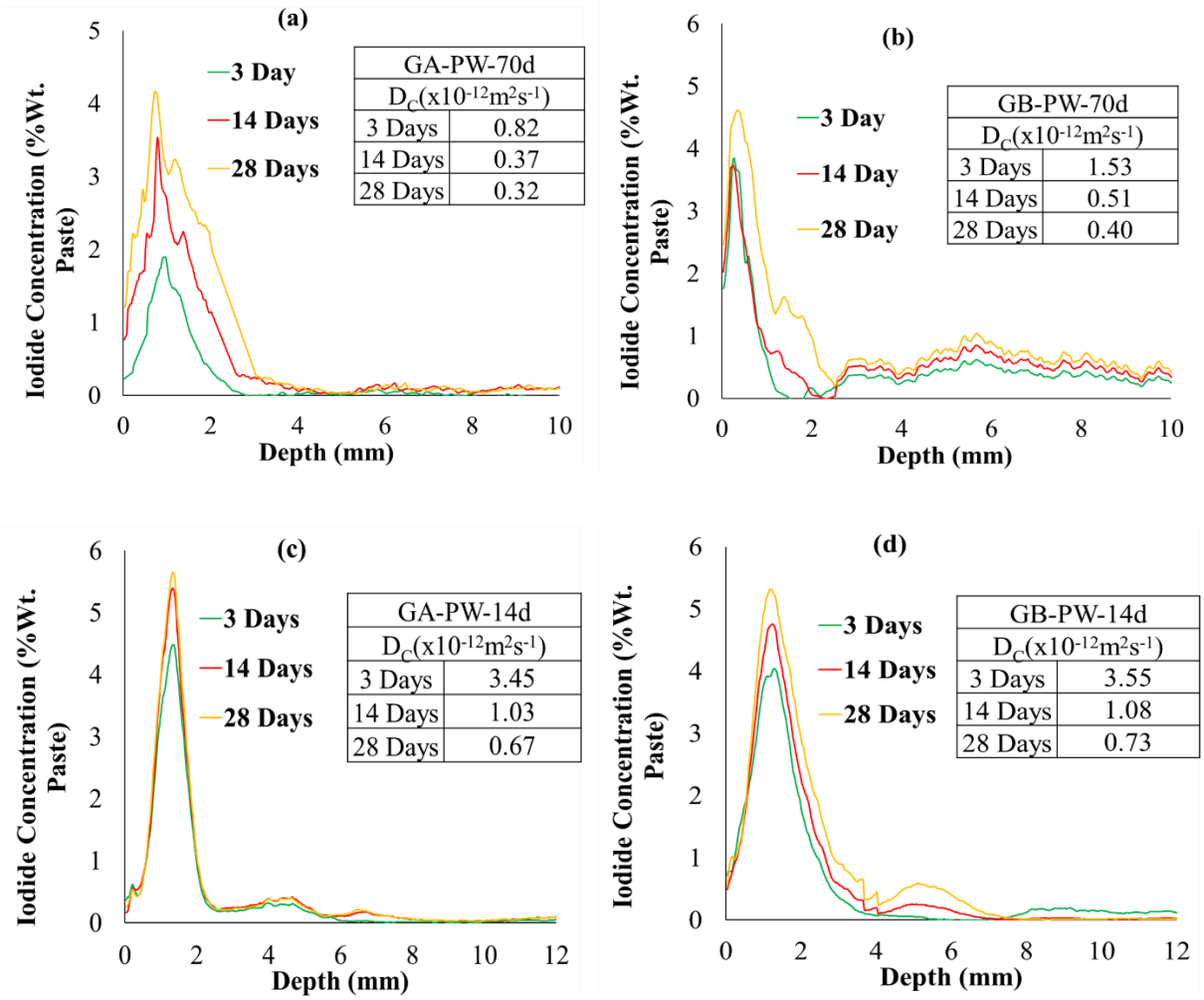

Figure 2- 9 Concentration profiles for the following concrete samples after 125 F-T cycles : (a) GA-PW-70d, (b) GB-PW-70d, (c) GA-PW-14d, and (d) GB-PW-14d.

Figure 2- 10 depicts the average concentration profiles and diffusion coefficients for the concrete samples in both Groups A and B after 3 days, 14 days, and 28 days of ponding after 250 F-T cycles for 70 and 14 days of curing periods. **Table 2- 12** shows the average D_c values for GA-PW-70d, GB-PW-70d, GA-PW-14d, and GB-PW-14d samples after 3 days, 14 days, and 28 days of ponding after 250 F-T cycles.

Table 2- 12 Average D_c (x 10^{-12} m^2 s^{-1}) values for concrete samples after 250 F-T cycles

	GA-PW-70d						**GB-PW-70d**					
	3 Days		14 Days		28 Days		3 Days		14 Days		28 Days	
Angle	S-1	S-2	S-1	S-2	S-1	S-2	S-1	S-2	S-1	S-2	S-1	S-2
0	1.06	0.34	0.94	0.19	0.38	0.19	1.98	1.30	1.98	2.38	0.58	0.81
60	0.62	2.08	0.31	0.29	0.92	0.12	1.11	2.49	0.26	1.00	0.53	0.51
120	0.70	4.55	0.46	0.35	0.40	0.15	1.54	1.02	1.02	1.96	0.64	0.60
180	3.73	7.18	0.34	0.71	0.35	0.41	1.34	1.96	0.12	0.98	0.68	0.45
Average	2.53		0.45		0.37		1.59		1.21		0.60	
STD	2.27		0.24		0.24		0.47		0.77		0.10	
	GA-PW-14d						**GB-PW-14d**					
	3 Days		14 Days		28 Days		3 Days		14 Days		28 Days	
Angle	S-1	S-2	S-1	S-2	S-1	S-2	S-1	S-2	S-1	S-2	S-1	S-2
0	4.06	4.54	1.24	1.19	0.88	0.79	4.68	4.30	1.90	1.55	0.88	0.91
60	4.62	3.58	1.31	0.89	0.59	0.62	4.11	4.69	1.26	1.79	0.93	0.71
120	3.70	4.55	1.16	1.42	0.75	0.95	4.54	4.02	1.70	1.83	1.22	0.67
180	4.73	3.18	0.94	1.71	0.53	0.81	5.84	4.96	1.32	1.39	0.75	0.55
Average	4.12		1.23		0.74		4.64		1.59		0.83	
STD	0.54		0.24		0.14		0.54		0.23		0.19	

Note: S-1 and S-2 refer to Sample 1 and Sample 2, respectively; STD stands for standard deviation

Based on **Figure 2- 10,** it can be found that for the 28-day ponding period after 250 F-T cycles, the iodide concentration reached its peak (C_{max}) of 4.4 % in GA-PW-70d and 5.2 % in GB-PW-70d within the surface layers just below the surface (Δx), followed by a gradual decrease at greater depths. In contrast, the iodide concentration peaked at 6.1 % in GA-PW-14d and 6.5 % in GB-PW-14d within Δx.

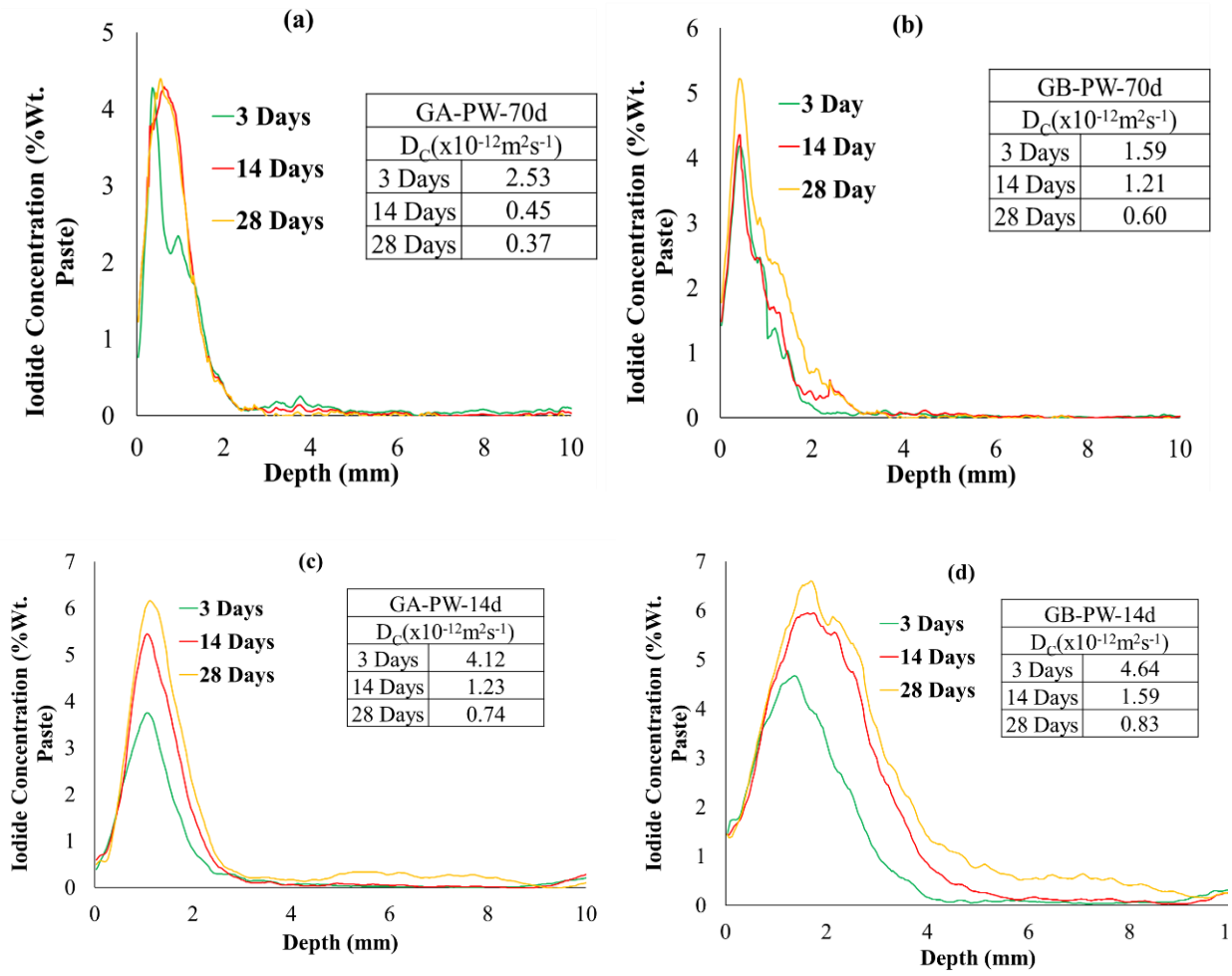

Figure 2- 10 Concentration profiles for the following concrete samples after 250 F-T cycles : (a) GA-PW-70d, (b) GB-PW-70d, (c) GA-PW-14d, and (d) GB-PW-14d.

Figure 2- 11 shows the average concentration profiles and diffusion coefficients for the concrete samples in Groups A and B after 3 days, 14 days, and 28 days of ponding following 375 F-T cycles for curing periods of 70 and 14 days. **Table 2- 13** shows the average D_c values for GA-PW-70d, GB-PW-70d, GA-PW-14d, and GB-PW-14d samples after 3 days, 14 days, and 28 days of ponding after 375 F-T cycles.

Table 2- 13 Average D_c (x 10^{-12} m^2 s^{-1}) values for concrete samples after 375 F-T cycles

	GA-PW-70d						**GB-PW-70d**					
	3 Days		14 Days		28 Days		3 Days		14 Days		28 Days	
Angle	S-1	S-2	S-1	S-2	S-1	S-2	S-1	S-2	S-1	S-2	S-1	S-2
0	2.42	0.10	0.25	0.38	0.74	0.19	0.98	3.95	0.90	0.85	0.58	0.16
60	0.69	0.10	0.34	0.42	0.83	0.15	1.85	0.83	0.26	0.90	0.94	0.69
120	6.90	2.51	0.41	0.55	0.28	0.32	0.98	1.72	0.70	0.83	0.48	0.51
180	6.73	2.87	0.15	0.71	0.35	0.29	2.94	0.45	0.32	0.90	1.42	0.25
Average	2.79		0.40		0.39		1.71		0.71		0.63	
STD	2.54		0.16		0.23		1.12		0.25		0.38	
	GA-PW-14d						**GB-PW-14d**					
	3 Days		14 Days		28 Days		3 Days		14 Days		28 Days	
Angle	S-1	S-2	S-1	S-2	S-1	S-2	S-1	S-2	S-1	S-2	S-1	S-2
0	2.42	2.10	1.55	1.38	0.94	0.59	5.98	3.95	1.18	1.58	1.58	1.16
60	4.69	4.10	1.34	1.42	0.73	0.95	4.85	4.83	1.26	1.39	1.14	0.60
120	6.90	3.51	0.81	0.75	0.68	0.70	4.98	3.72	0.82	2.96	0.48	0.45
180	6.73	3.87	1.15	1.71	0.85	0.89	6.94	4.45	0.92	3.98	1.42	1.05
Average	4.29		1.26		0.79		4.96		1.76		0.99	
STD	1.66		0.32		0.13		0.99		1.04		0.40	

Note: S-1 and S-2 refer to Sample 1 and Sample 2, respectively; STD stands for standard deviation

Figure 2- 11 also shows that for the 28-day ponding period after 375 F-T cycles, the iodide concentration reached its peak (C_{max}) of 5.1 % in GA-PW-70d and 5.4 % in GB-PW-70d within the surface layers just below the surface (Δx), followed by a gradual decrease at greater depths. In contrast, the iodide concentration peaked at 7.0 % in GA-PW-14d and 7.1 % in GB-PW-14d within Δx.

It is worth noting that the samples subjected to 375 F-T cycles experienced severe scaling, preventing further investigation of D_c values in extended F-T cycles. The RDME data from *Section 2.4.3* indicates that the 14-day cured samples were severely damaged after 300 F-T cycles. The D_c values corroborate the results of the F-T experiments, indicating a significant increase in both Group A and Group B samples after 375 cycles. Higher D_c and iodide concentration values indicate faster ingress of ions, which is detrimental to concrete. Further discussion on the changes in D_c and the influencing factors will be presented in greater detail in **Figure 2-13.**

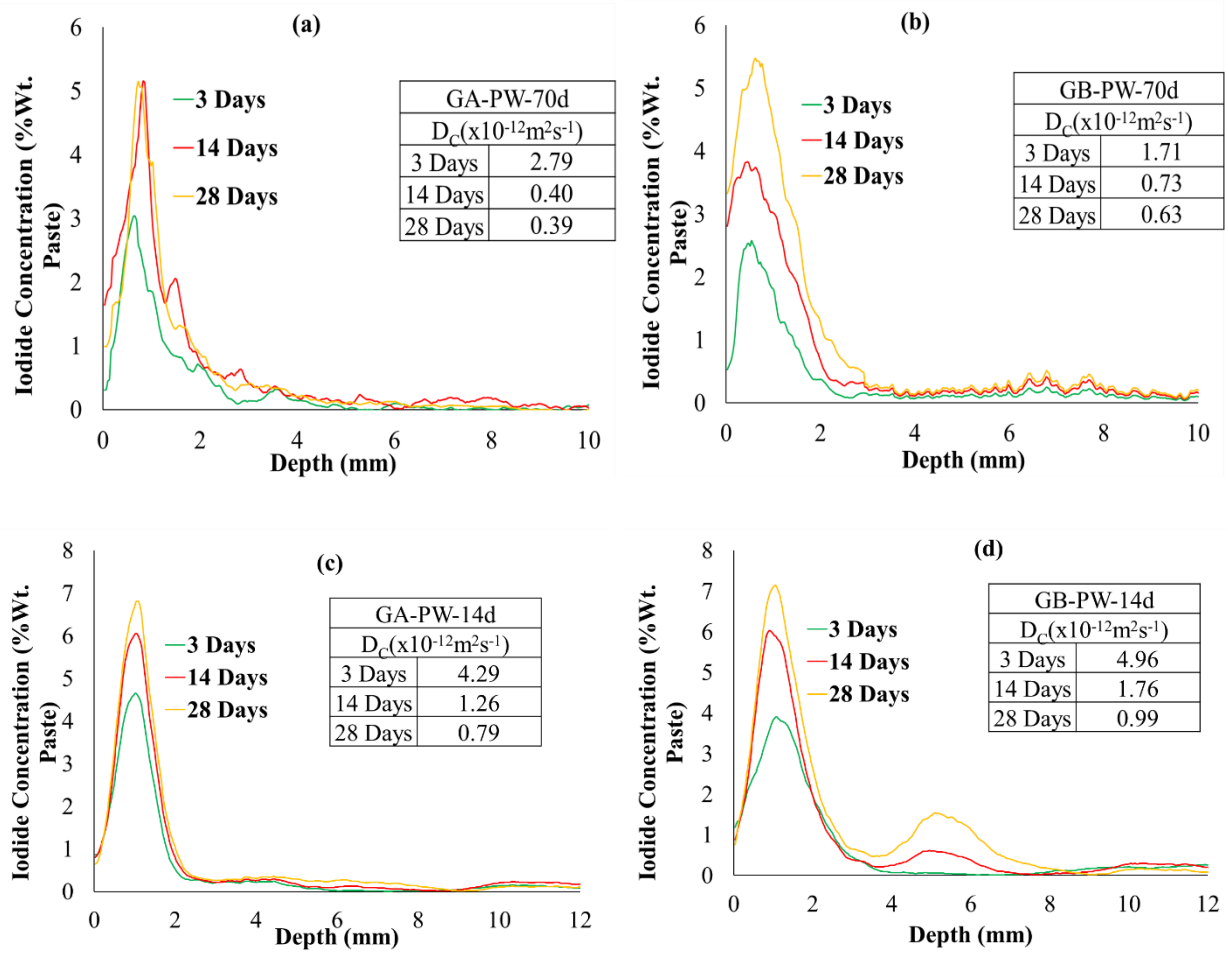

Figure 2- 11 Concentration profiles for the following concrete samples after 375 F-T cycles : (a) GA-PW-70d, (b) GB-PW-70d, (c) GA-PW-14d, and (d) GB-PW-14d.

Figure 2- 12 shows the average concentration profiles and diffusion coefficients for the concrete samples in Groups A and B after 3 days, 14 days, and 28 days of ponding following 500 F-T cycles for 70 days of curing periods. **Table 2- 14** shows the average D_c values for GA-PW-70d, and GB-PW-70d samples after 3 days, 14 days, and 28 days of ponding after 500 F-T cycles.

Table 2- 14 Average D_c (x 10^{-12} m^2 s^{-1}) values for concrete samples after 500 F-T cycles

	GA-PW-70d						GB-PW-70d					
	3 Days		14 Days		28 Days		3 Days		14 Days		28 Days	
Angle	S-1	S-2	S-1	S-2	S-1	S-2	S-1	S-2	S-1	S-2	S-1	S-2
0	0.58	1.59	0.82	0.61	0.89	0.31	2.50	5.85	1.10	0.92	0.58	0.26
60	3.38	3.01	0.83	0.64	0.33	0.38	3.15	4.01	0.96	0.97	0.84	0.31
120	4.48	5.26	0.74	0.75	0.28	0.44	0.60	3.02	0.90	1.03	0.48	0.11
180	2.00	2.10	0.77	0.71	0.48	0.61	2.94	0.95	1.10	0.99	1.42	1.50
Average	2.80		0.73		0.47		2.88		1.00		0.69	
STD	1.45		0.07		0.19		1.55		0.07		0.49	

Note: S-1 and S-2 refer to Sample 1 and Sample 2, respectively; STD stands for standard deviation

In addition, from **Figure 2-12,** it can be observed that for the 28-day ponding period after 500 F-T cycles, the iodide concentration reached its peak (C_{max}) of 5.8 % in GA-PW-70d and 5.9 % in GB-PW-70d within the surface layers just below the surface (Δx), followed by a gradual decrease at greater depths. It can be observed from the TXM results that both sets of concrete exhibited a gradual increase in C_{max} for both curing periods, consistent with the trend of increasing D_c.

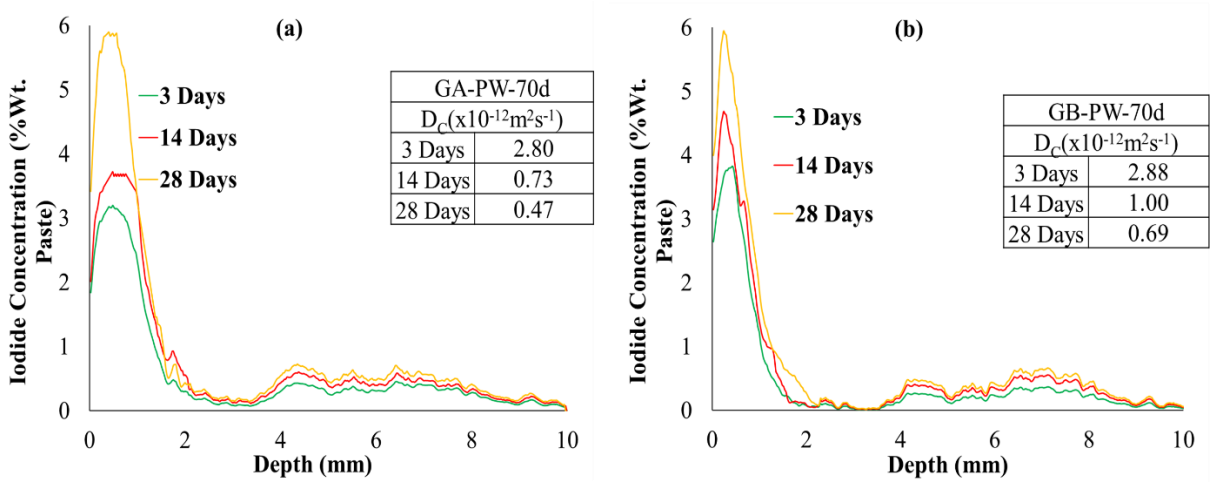

Figure 2- 12 Concentration profiles for the following concrete samples after 500 F-T cycles : (a) GA-PW-70d and (b) GB-PW-70d.

The results from **Figure 2- 8 to Figure 2- 12** demonstrate that the D_c values stabilized when the ponding periods were extended, which is consistent with findings from previous studies (Behravan et al., 2023, 2021; Rahat et al., 2024).**Figure 2- 13** displays the percent change of D_c data for 28 days of ponding periods, the maximum considered in this study. In **Figure 2- 13,** GA-PW-70d samples showed a 62 % increase after 500 F-T cycles, while the GB-PW-70d samples experienced a 93 % increase in D_c value. After 375 F-T cycles, the GA-PW-14d samples demonstrated an 84

% increase, whereas the GB-PW-14d samples experienced an increase of 109 %. GA-PW-70d experienced a 37 % increase, and GB-PW-70d experienced a 77 % increase after 375 F-T cycles.

An analysis of the changes in D_c values before and after F-T cycles reveals that both sets of concrete exhibit significant increases after consecutive F-T cycles, highlighting the influence of F-T cycles on chloride ingress in concrete. For both 14-day and 70-day cured samples, Group A shows better resistance than Group B, suggesting that the PVA fibers did not have the expected impact on improving F-T resistance. Although not directly quantified, the presence of PVA fibers may have influenced the pore structure and interfacial transition zone (ITZ), likely enhancing the connectivity of microstructural pathways. This could contribute to the elevated chloride diffusion coefficient observed in Group B and the reduced air content. Furthermore, the results depicted in **Figure 2- 13** indicate that samples cured for 14 days demonstrate a higher increase compared to the 70-day cured samples in both concrete groups. Notably, even after undergoing 375 F-T cycles, the GB-PW-14d samples exhibit the lowest performance. The superior performance of the 70-day cured samples provides compelling evidence that an extended curing period can enhance the chloride ingress properties of concrete in F-T cycling, surpassing the influence of PVA fibers.

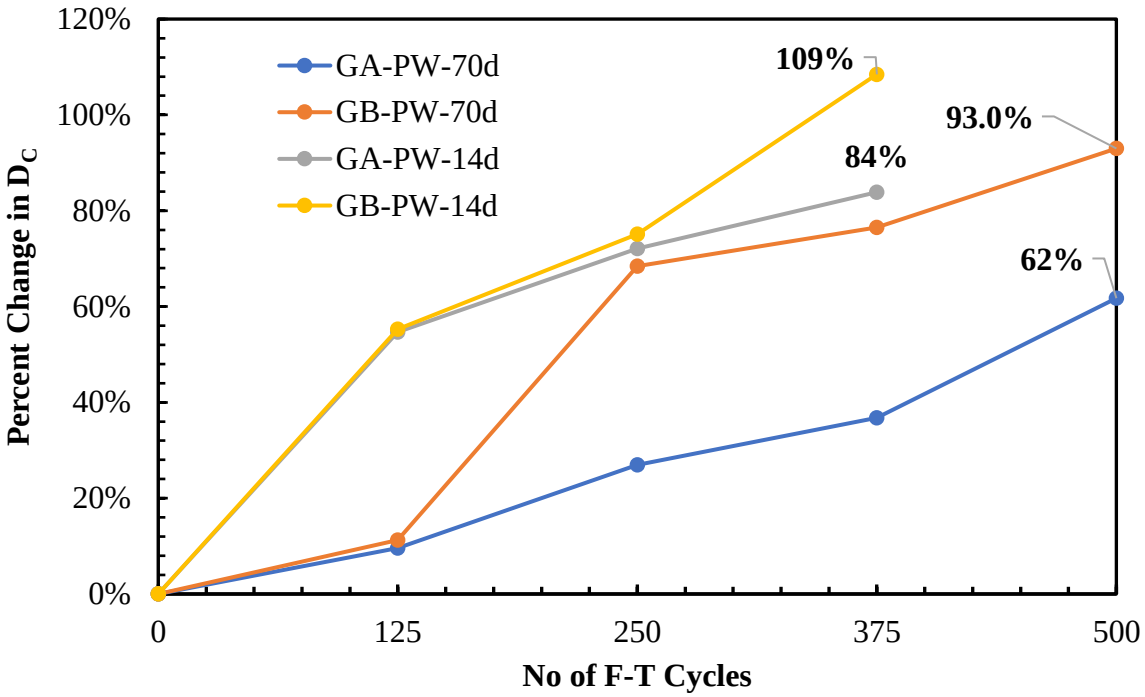

Figure 2- 13 Changes of D_c over F-T cycles for different curing periods.

The results from unpaired, two-tailed t-tests suggest that there is insufficient evidence to support a statistically significant difference in the D_c values between GA-PW-70d and GB-PW-70d at 3 days, 14 days, and 28 days of ponding, both before and after 500 F-T cycles. Similar findings were observed for the D_c values between GA-PW-14d and GB-PW-14d before and after 375 F-T cycles. However, there was a statistically significant difference between the D_c values for the samples that were cured for 70 days and 14 days for both Group A and Group B, both before and after 375 F-T cycles, at a significance level of 0.05.

At a 5 % significance level, there was not enough evidence to conclude that there is a difference between the D_c values of the 3 days, 14 days, and 28 days of ponding specimens of the same mixture before and after 500 F-T cycles (for GA-PW-70d and GB-PW-70d) using unpaired, two-tailed t-tests. However, there is a statistically significant difference between the D_c values of the 3 days, 14 days, and 28 days of ponding specimens of the same mixture before and after 375 F-T cycles (for GA-PW-14d and GB-PW-14d).

2.5 Conclusions and recommendations

This study aimed to evaluate the combined effects of PVA fiber inclusion and curing duration on the F-T durability of air-entrained concrete by analyzing key durability parameters, such as mass loss, RDME, UPV, and SR, and employing TXM to quantify chloride ingress under F-T exposure non-destructively.

- The results showed that the concrete without fibers (Group A), which had a more favorable air-void system (lower spacing factor, higher void frequency), exhibited better overall resistance to F-T cycles compared to the fiber-reinforced concrete (Group B) despite identical mix proportions.
- Longer curing duration (70 days) significantly improved performance across all measured parameters (mass loss, RDME, UPV, SR, and Dc), indicating that extended hydration enhances microstructural integrity and reduces susceptibility to F-T damage and chloride ingress.
- The Dc, quantified using a novel non-destructive TXM method, demonstrated that Dc increased by 62% in Group A and 93% in Group B after 1000 F-T cycles, reinforcing the role of entrained air and microcrack control in mitigating chloride transport.
- While PVA fibers are known to provide crack-bridging benefits in cementitious composites, their presence in this study did not result in significant improvements in F-T durability. This is likely due to the overriding influence of a less favorable air-void system in Group B than in Group A.
- Overall, the findings suggest optimizing the air-void structure and ensuring adequate curing duration are more critical than fiber inclusion for enhancing concrete's F-T and chloride resistance in cold-region applications. The study also establishes TXM as a promising technique for future research on transport phenomena in cementitious materials.

Recommendations. To build upon the findings of this study, the following future research directions are recommended:

- ✓ For future research, an in-depth microstructural analysis of concrete samples is recommended to evaluate the fiber dispersion and the interfacial transition zone to better understand the factors influencing F-T damage or resistance.
- ✓ Future studies should also investigate using lower or optimized PVA fiber dosages to determine whether reduced contents could improve air-void stability while providing mechanical performance benefits in F-T conditions.
- ✓ In addition, conducting controlled experiments in which the air content is equalized between fiber-reinforced and non-fiber-reinforced concretes would help more accurately isolate the specific effects of fiber inclusion on durability performance.
- ✓ Future studies should also investigate using lower or optimized PVA fiber dosages to determine whether reduced contents could improve air-void stability while still providing mechanical performance benefits in F-T conditions.

Future research should also aim to develop mix design strategies that explicitly address the trade-off between fiber reinforcement and air-void system stability to ensure mechanical performance and F-T durability.

CrediT authorship contribution statement

Md Hasibul Hasan Rahat: Conceptualization, Methodology, Formal analysis, Investigation, Writing– review and editing, Writing–original draft. **Thien Q. Tran:** Methodology, Formal analysis, Investigation. **Dip Banik:** Methodology, Formal analysis, Investigation. **Alexander S. Brand:** Conceptualization, Writing – review and editing, Writing – original draft, Supervision, Project administration, Methodology.

Declaration of competing interest

The authors declared that they have no conflicts of interest in this work.

Acknowledgement

This material is based upon work supported by the Broad Agency Announcement Program and the Cold Regions Research and Engineering Laboratory (ERDC-CRREL) under Contract No. W913E522C0001.

Disclaimer

Any opinions, findings and conclusions or recommendations expressed in this material are those of the author(s) and do not necessarily reflect the views of the Broad Agency Announcement Program and ERDC-CRREL.

References

ASTM C192, 2019. Standard practice for making and curing concrete test specimens in the laboratory, ASTM International, West Conshohocken, PA.

ASTM C231-09a. Standard Test Method for Air Content of Freshly Mixed Concrete by the Pressure Method, West Conshohocken, PA.

ASTM C457/C457M-16, 2016. Standard Test Method for Microscopical Determination of Parameters of the Air-Void System in Hardened Concrete, ASTM International, West Conshohocken, PA.

ASTM C39, 2021. Standard test method for compressive strength of cylindrical concrete specimens, ASTM International, West Conshohocken, PA.

ASTM C1202-19. 2019. Standard test method for electrical indication of concrete's ability to resist chloride ion penetration, ASTM International, West Conshohocken, PA.

ASTM C1556, 2016. Standard test method for determining the apparent chloride diffusion coefficient of cementitious mixtures by bulk diffusion, ASTM International, West Conshohocken, PA.

ASTM C293, 2016. Standard test method for flexural strength of concrete (using simple beam with center-point loading), ASTM International, West Conshohocken, PA.

ASTM C597-22, 2022. Standard test method for ultrasonic pulse velocity through concrete, ASTM International, West Conshohocken, PA.

ASTM C666, 2008. Standard test method for resistance of concrete to rapid freezing and thawing, ASTM International, West Conshohocken, PA.

ASTM C215-19, 2019. Standard test method for fundamental transverse, longitudinal, and torsional resonant frequencies of concrete specimens, ASTM International, West Conshohocken, PA.

AASHTO T 358, Standard method of test for surface resistivity indication of concrete's ability to resist chloride ion penetration, American Association of State Highway and Transportation Officials, Washington, DC, 2015.

Affan, M., Ali, M., 2022. Experimental investigation on mechanical properties of jute fiber reinforced concrete under freeze-thaw conditions for pavement applications. *Constr Build Mater* 323. https://doi.org/10.1016/j.conbuildmat.2022.126599

Al-Kheetan, M.J., Rahman, M.M., Ghaffar, S.H., Al-Tarawneh, M., Jweihan, Y.S., 2020. Comprehensive investigation of the long-term performance of internally integrated concrete pavement with sodium acetate. *Results Eng* 6. https://doi.org/10.1016/j.rineng.2020.100110

Bao, J., Zheng, R., Yu, Z., Zhang, P., Song, Q., Xu, J., Gao, S., 2022. Freeze-thaw resistance of recycled aggregate concrete incorporating ferronickel slag as fine aggregate. *Constr Build Mater* 356. https://doi.org/10.1016/j.conbuildmat.2022.129178

Behravan, A., Ley, M.T., Cook, D., Hu, Q., Rywelski, A., Brorsen, R., 2023. Measuring the Diffusion Coefficient of Paste and Concrete by Using Dental X-ray Equipment. *CivilEng* 4, 224–247. https://doi.org/10.3390/civileng4010014

Behravan, A., Ley, M.T., Rywelski, A., Berke, N., 2021. Changes in the rate of ion penetration of alternative cementitious materials with time. *Mater Des* 197. https://doi.org/10.1016/j.matdes.2020.109236

Çavdar, A., 2014. Investigation of freeze-thaw effects on mechanical properties of fiber reinforced cement mortars. *Compos B Eng* 58, 463–472. https://doi.org/10.1016/j.compositesb.2013.11.013

Dabas, M., Martín-Pérez, B., Almansour, H., 2021. Combined Effects of Freeze-Thaw and Corrosion on Performance of RC Structures: State-of-the-Art Review. *J Perform Constr Facil* 35. https://doi.org/10.1061/(asce)cf.1943-5509.0001637

Darma, I.S., Sugiyama, T., Promentilla, M.A.B., 2013. Application of X-ray CT to study diffusivity in cracked concrete through the observation of tracer transport. *J Adv Concr Technol* 11, 266–281. https://doi.org/10.3151/jact.11.266

Diao, B., Sun, Y., Ye, Y. and Cheng, S., 2012. Impact of seawater corrosion and freeze-thaw cycles on the behavior of eccentrically loaded reinforced concrete columns. *Oce Syst Eng*, *2*(2), pp.159-171. https://doi.org/10.12989/ose.2012.2.2.159

Dixon, D.E. et al., 1991. Standard Practice for Selecting Proportions for Normal, Heavyweight, and Mass Concrete (ACI 211.1-91) Chairman, Subcommittee A.

Felekoğlu, B., Tosun, K., Baradan, B., 2009. Effects of fibre type and matrix structure on the mechanical performance of self-compacting micro-concrete composites. *Cem Concr Res* 39, 1023–1032. https://doi.org/10.1016/j.cemconres.2009.07.007

Florea, M.V.A., Brouwers, H.J.H., 2012. Chloride binding related to hydration products: Part I: Ordinary Portland Cement. *Cem Concr Res* 42, 282–290. https://doi.org/10.1016/j.cemconres.2011.09.016

Ghosh, P., Tran, Q., 2015. Correlation Between Bulk and Surface Resistivity of Concrete. *Int J Concr Struct Mater* 9, 119–132. https://doi.org/10.1007/s40069-014-0094-z

Hao, L., Liu, Y., Xiao, J., 2021. Durability of recycled aggregate thermal insulation concrete under combined flexural loading and freeze–thaw cycles. *Constr Build Mater* 272. https://doi.org/10.1016/j.conbuildmat.2020.121652

Jang, J.G., Kim, H.K., Kim, T.S., Min, B.J., Lee, H.K., 2014. Improved flexural fatigue resistance of PVA fiber-reinforced concrete subjected to freezing and thawing cycles. *Constr Build Mater* 59, 129–135. https://doi.org/10.1016/j.conbuildmat.2014.02.040

Jasielec, J.J., Stec, J., Szyszkiewicz-Warzecha, K., Łagosz, A., Deja, J., Lewenstam, A., Filipek, R., 2020. Effective and apparent diffusion coefficients of chloride ions and chloride binding kinetics parameters in mortars: non-stationary diffusion-reaction model and the inverse problem. *Mater* 2020; 13: 5522. https://doi.org/10.3390/ma13235522

Jin, H., Cheng, L., Liu, J., Zhong, S., 2024. Investigation of natural diffusion behavior in concrete using iodide replacing chloride ions: The impact of mineral admixtures types and dosages. *J Mater Res Technol* 29, 1834–1861. https://doi.org/10.1016/j.jmrt.2024.01.206

Kang, S., Lloyd, Z., Behravan, A., Ley, M.T., 2021. The relationship between the apparent diffusion coefficient and surface electrical resistivity of fly ash concrete. *Constr Build Mater* 299. https://doi.org/10.1016/j.conbuildmat.2021.123964

Khanzadeh Moradllo, M., Hu, Q., Ley, M.T., 2017. Using X-ray imaging to investigate in-situ ion diffusion in cementitious materials. *Constr Build Mater* 136, 88–98. https://doi.org/10.1016/j.conbuildmat.2017.01.038

Khanzadeh Moradllo, M., Ley, M.T., 2017. Comparing ion diffusion in alternative cementitious materials in real time by using non-destructive X-ray imaging. *Cem Concr Compos* 82, 67–79. https://doi.org/10.1016/j.cemconcomp.2017.05.014

Khayat, K.H., Nasser, K.W., 1991. Comparison of Air Contents in Fresh and Hardened Concretes Using Different Airmeters. *Cem Concr Aggreg* 13, 18–24. https://doi.org/10.1520/CCA10545J

Ley, M.T., Parestegari, N., Behravan, A., Cook, D. and Hu, Q., 2023. *Measuring concrete permeability with CHIP*. Final report for NCHRP IDEA Project 232. Oklahoma State University, National Cooperative Highway Research Program (NCHRP), Innovations Deserving Exploratory Analysis (IDEA) Programs, Transportation Research Board, National Academies of Sciences, Engineering, and Medicine.

Li, G., Zhou, Q., Wang, W., Lu, Chunhao, Chen, C., Guo, Z., Lu, Caifeng, 2023. Chloride diffusion along the interface between concrete matrix and repair materials under flexural loading. *Constr Build Mater* 372. https://doi.org/10.1016/j.conbuildmat.2023.130829

Lim, D.T., Divsholi, B.S., Xu, D. and Teng, S., 2011. Evaluation of high performance concrete using electrical resistivity technique. *Proceedings of the Our World in Concrete and Structures*.

Lin, H., Han, Y., Liang, S., Gong, F., Han, S., Shi, C., Feng, P., 2022. Effects of low temperatures and cryogenic freeze-thaw cycles on concrete mechanical properties: A literature review. *Constr Build Mater* 345. https://doi.org/10.1016/j.conbuildmat.2022.128287

Ling, Y., Zhang, P., Wang, J., Chen, Y., 2019. Effect of PVA fiber on mechanical properties of cementitious composite with and without nano-SiO2. Constr Build Mater 229, 117068. https://doi.org/https://doi.org/10.1016/j.conbuildmat.2019.117068

Liu, J., Jiang, T., Yang, Y., Zhou, Y., 2023. Effect of PVA Fiber on the Dynamic and Static Mechanical Properties of Concrete under Freeze-thaw Cycles at Extremely Low Temperature (−70 °C). *J Wuhan Univ Technol Mater Sci Ed*. 38, 366–373. https://doi.org/10.1007/s11595-023-2705-5

Liu, K., Yan, J., Hu, Q., Sun, Y., Zou, C., 2016a. Effects of parent concrete and mixing method on the resistance to freezing and thawing of air-entrained recycled aggregate concrete. *Constr Build Mater* 106, 264–273. https://doi.org/10.1016/j.conbuildmat.2015.12.074

Kim, J.H., Robertson, R.E. and Naaman, A.E., 1999. Structure and properties of poly (vinyl alcohol)-modified mortar and concrete. *Cem Con Res*, *29*(3), pp.407-415. https://doi.org/10.1016/S0008-8846(98)00246-4

Moradllo, M.K. and Ley, M.T., 2017a. Quantitative measurement of the influence of degree of saturation on ion penetration in cement paste by using X-ray imaging. *Constr Build Mater*, *141*, pp.113-129. https://doi.org/10.1016/j.conbuildmat.2017.03.007

Moradllo, M.K. and Ley, M.T., 2017b. Comparing ion diffusion in alternative cementitious materials in real time by using non-destructive X-ray imaging. *Cem Concr Compos*, *82*, pp.67-79. https://doi.org/10.1016/j.cemconcomp.2017.05.014

Noushini, A., Samali, B., Vessalas, K., 2013. Effect of polyvinyl alcohol (PVA) fibre on dynamic and material properties of fibre reinforced concrete. *Constr Build Mater* 49, 374–383. https://doi.org/10.1016/j.conbuildmat.2013.08.035

Pilvar, A., Ramezanianpour, A.A., Rajaie, H., 2015. New method development for evaluation concrete chloride ion permeability. *Constr Build Mater* 93, 790–797. https://doi.org/10.1016/j.conbuildmat.2015.05.092

Qin, L., Zhai, C., Xu, J., Liu, S., Zhong, C., Yu, G., 2019. Evolution of the pore structure in coal subjected to freeze−thaw using liquid nitrogen to enhance coalbed methane extraction. *J Pet Sci Eng* 175, 129–139. https://doi.org/10.1016/j.petrol.2018.12.037

Rabi, M., Shamass, R., Cashell, K.A., 2022. Structural performance of stainless steel reinforced concrete members: A review. *Constr Build Mater*. https://doi.org/10.1016/j.conbuildmat.2022.126673

Rahat, Md.H.H., Tran, T.Q., Love, B.D.J.E., Behravan, A., Brand, A.S., 2024. Investigating the Impact of Freeze–Thaw Damage on Chloride Ingress in Concrete, in: Cold Regions Engineering 2024. Pp. 575–585. https://doi.org/10.1061/9780784485460.053

Şahmaran, M., Özbay, E., Yücel, H.E., Lachemi, M., Li, V.C., 2012. Frost resistance and microstructure of Engineered Cementitious Composites: Influence of fly ash and micro poly-vinyl-alcohol fiber. *Cem Concr Compos* 34, 156–165. https://doi.org/10.1016/j.cemconcomp.2011.10.002

Sang, Y., Pan, Y., Ying, W., Yang, Y., 2022. Assessment of mechanical performance and ice content of concrete at low temperature using impact-echo method. *Constr Build Mater* 346. https://doi.org/10.1016/j.conbuildmat.2022.128286

Sasanipour, H., Aslani, F. and Taherinezhad, J., 2022. Deicer Salt-Scaling Resistance of Concrete Using Recycled Concrete Aggregates Pretreated by Silica Fume Slurry. *Mater*, *15*(24), p.8874. https://doi.org/10.3390/ma15248874

Shang, H.S., Yi, T.H., 2013. Freeze-thaw durability of air-entrained concrete. *Sci World J* 2013. https://doi.org/10.1155/2013/650791

Shi, X., Xie, N., Fortune, K., Gong, J., 2012. Durability of steel reinforced concrete in chloride environments: An overview. *Constr Build Mater*. https://doi.org/10.1016/j.conbuildmat.2011.12.038

Sun, L.F., Jiang, K., Zhu, X., Xu, L., 2020. An alternating experimental study on the combined effect of freeze-thaw and chloride penetration in concrete. *Constr Build Mater* 252. https://doi.org/10.1016/j.conbuildmat.2020.119025

Tan, Y., Xu, Z., Liu, Z., Jiang, J., 2022b. Effect of Silica Fume and Polyvinyl Alcohol Fiber on Mechanical Properties and Frost Resistance of Concrete. *Build* 12. https://doi.org/10.3390/buildings12010047

Thong, C.C., Teo, D.C.L., Ng, C.K., 2016. Application of polyvinyl alcohol (PVA) in cement-based composite materials: A review of its engineering properties and microstructure behavior. *Constr Build Mater*. https://doi.org/10.1016/j.conbuildmat.2015.12.188

Tran, N.P., Gunasekara, C., Law, D.W., Houshyar, S., Setunge, S. and Cwirzen, A., 2022. Comprehensive review on sustainable fiber reinforced concrete incorporating recycled textile waste. *J Sustain Cem-Based Mater*, *11*(1), pp.28-42. https://doi.org/10.1080/21650373.2021.1875273

Wang, R., Hu, Z., Li, Y., Wang, K., Zhang, H., 2022. Review on the deterioration and approaches to enhance the durability of concrete in the freeze–thaw environment. *Constr Build Mater*. https://doi.org/10.1016/j.conbuildmat.2022.126371

Yew, M.K., Mahmud, H. Bin, Ang, B.C., Yew, M.C., 2015. Effects of low volume fraction of polyvinyl alcohol fibers on the mechanical properties of oil palm shell lightweight concrete. *Adv Mater Sci Eng* 2015. https://doi.org/10.1155/2015/425236

Zhang, P., Wittmann, F.H., Vogel, M., Müller, H.S., Zhao, T., 2017. Influence of freeze-thaw cycles on capillary absorption and chloride penetration into concrete. *Cem Concr Res* 100, 60–67. https://doi.org/10.1016/j.cemconres.2017.05.018

Chapter 3. The combined effects of freeze-thaw cycles and seawater on chloride ingress in concrete[2]

The contributions of the authors to this manuscript are described as follows:

Md Hasibul Hasan Rahat: Conceptualization; Data curation; Formal analysis; Investigation; Methodology; Visualization; Writing – original draft; Writing – review and editing.

Alexander S. Brand: Conceptualization; Methodology; Project administration; Supervision; Writing – original draft; Writing – review and editing.

[2] **Rahat, M.H.H.** & Brand, A.S. (2025). The combined impact of freeze-thaw cycles and seawater on chloride ingress in concrete. *Construction and Building Materials*. Volume 489, 2025, 142363, ISSN 0950-0618, https://doi.org/10.1016/j.conbuildmat.2025.142363.

The combined effects of freeze-thaw cycles and seawater on chloride ingress in concrete

Md Hasibul Hasan Rahat[1*], and Alexander S. Brand[1,2,3*]

[1] The Charles E. Via, Jr. Department of Civil and Environmental Engineering, Virginia Polytechnic Institute and State University, Blacksburg, Virginia

[2] Department of Materials Science and Engineering, Virginia Polytechnic Institute and State University, Blacksburg, Virginia

[3] Myers-Lawson School of Construction, Virginia Polytechnic Institute and State University, Blacksburg, Virginia

* Corresponding authors: rahatm21@vt.edu (M.H.H.R.) and asbrand@vt.edu (A.S.B.)

3.1 Abstract

This study investigates the effects of freeze-thaw (F-T) cycles and seawater exposure on chloride ingress in concrete. Two concrete groups, conventional (Group A) and polyvinyl alcohol (PVA) fiber-reinforced (Group B), were tested for 14-day and 70-day curing periods. The results showed that longer curing durations significantly enhanced the concrete's resistance to F-T damage and chloride ingress, particularly for Group A. Despite previous studies suggesting that PVA fibers improve durability, Group B exhibited higher chloride penetration and diffusion coefficients (Dc) value than Group A. A transmission X-ray microscope (TXM) was used to quantify Dc, revealing that the Dc value increased significantly after F-T cycles in seawater conditions. Group A consistently outperformed Group B, particularly after 70 days of curing, with lower Dc values and lower change in percent relative dynamic modulus of elasticity (RDME). Seawater exposure worsened the damage caused by F-T cycles, accelerating deterioration compared to F-T cycles in plain water. The findings suggest that salts in seawater amplify internal stresses through crystallization pressure and osmotic effects, accelerating microcracking and material deterioration. These findings highlight the pivotal influence of curing duration and environmental conditions on concrete's resistance to F-T damage, emphasizing the need for tailored strategies to mitigate combined seawater and F-T effects.

Keywords: freeze-thaw resistance, transmission X-ray microscopy, polyvinyl alcohol fiber, curing period, chloride ingress, diffusion coefficients, coastal environment, cold region.

3.2 Introduction

Concrete is a fundamental building material known for its affordability and versatility, making it indispensable in construction projects across diverse environmental conditions (Imbabi et al., 2012; Qaidi et al., 2021; Rabi et al., 2022; Sang et al., 2022a). Moreover, concrete has become the top choice for construction in harsh environments. However, concrete is susceptible to damage and deterioration caused by external durability factors. The adverse effects of structural damage and cracks in concrete can significantly compromise its mechanical strength and longevity (Baloch et al., 2021; Brandt, 2008; Ting et al., 2021). Specifically, concrete structures in low-temperature

areas are prone to damage from freeze-thaw (F-T) cycles, leading to reduced lifespan and degradation (Lin et al., 2022a; Skripkiunas et al., 2013) . In addition, global warming and climate change contribute to the rise of sea levels (Gao and Wang, 2017; Siegert et al., 2020), which increases the risk of submerging concrete structures in coastal areas of cold regions. As a result, seawater intrusion into concrete structures can cause significant damage through chloride ingress. In cold regions, this damage can be further compounded due to the combined effect of F-T cycles and seawater intrusion (Dousti et al., 2013; Lu et al., 2021; Moradi-Marani et al., 2010; Costa and Appleton, 2002; Sun et al., 2020; Wang et al., 2022; Yi et al., 2020). However, the effect of F-T cycles on concrete in seawater has not been extensively explored in literature, despite significant research on each mechanism individually.

The extent of damage caused by F-T cycles is influenced by the specific geographic and atmospheric conditions of the structure's location (Şahin et al., 2021). Due to F-T cycles, concrete experiences both internal and surface damage (Gao et al., 2023). Previous studies have shown that F-T cycles cause three main internal damage pressures in cement mortar: hydraulic pressure from water expansion during freezing, cryosuction pressure from water movement into freezing zones, and crystallization pressure from salt or ice crystal growth (Coussy and Monteiro, 2008; Gong and Jacobsen, 2019; Liu et al., 2014, 2011). These pressures significantly degrade mechanical properties. On the other hand, deicing salts, widely used to melt snow on concrete pavements and bridges in cold regions (Valenza and Scherer, 2007), cause significant surface scaling. Unlike F-T cycles with plain water, which primarily induce internal damage through microcracking and reduced stiffness (Scherer, 1993; Sun et al., 2019), F-T cycles combined with deicing salts exacerbate surface scaling by removing surface layers and exposing coarse aggregates (Nili and Zaheri, 2011). While scaling can occur without deicing salts under extreme conditions, such as excessive F-T cycles or mechanical loading (Mu et al., 2002), deicing salts can cause severe scaling within a few F-T cycles (Nili and Zaheri, 2011). This damage facilitates the ingress of aggressive species like chlorides and carbon dioxide, promoting reinforcing steel corrosion and further compromising durability (Valenza and Scherer, 2007).

Therefore, it is imperative to gain a thorough understanding of the various damage mechanisms, including the number of cycles, minimum temperature, and freezing rate, to develop an effective maintenance plan for the structure (Jacobsen et al., 1997; Şahin et al., 2021). Several indicators have been identified in the literature as effective means for assessing the degree of F-T damage in concrete structures (Wang et al., 2022; Xiao et al., 2013). These indicators include, but are not limited to, the relative dynamic modulus of elasticity (RDME), decreases in compressive and splitting tensile strength, mass loss (ML), durability factor, length change in percent, and ultrasonic pulse velocity (UPV) (Bao et al., 2022b; Dabas et al., 2021; Liu et al., 2016). By utilizing these parameters to evaluate the extent of F-T damage, engineers and maintenance personnel can make informed decisions regarding the necessary remedial actions to ensure the longevity and safety of concrete structures. One of the most used methods for designing concrete resistant to F-T damage is the addition of an air-entrained admixture (AEA). These admixtures reduce surface tension and stabilize air bubbles through surfactant adsorption and electrostatic repulsion (Du and Folliard,

2005; Li and Sun, 2024; Shah et al., 2021a). These mechanisms create a stable air-void system that accommodates (Chu et al., 2022; Qin et al., 2019; Sang et al., 2022b; Zhang et al., 2019). Dosage and timing of the AEA are critical to maintaining the optimal air content and stability of the air bubbles within the concrete (Şahin et al., 2023; Shah et al., 2021b). Additionally, it is crucial to consider the fatigue characteristics of concrete under freezing and thawing conditions in the design and maintenance of concrete structures. The available experimental data on this topic remains insufficient. According to existing research (Yan et al., 2000), the inclusion of fibers in concrete is known to have a positive impact on its dynamic properties, particularly by increasing the damping ratio of plain concrete. Moreover, fiber reinforcement is widely acknowledged as an effective strategy for improving brittle materials' strength, ductility, and toughness (Noushini et al., 2013a; Noushini et al., 2013b). Furthermore, there is limited research examining the impact of synthetic fibers on the flexural fatigue durability of concrete subjected to freezing and thawing cycles. Jang et al., (2014) investigated that incorporating PVA fiber-reinforcement into concrete subjected to freezing and thawing cycles enhances resistance against these actions and improves flexural fatigue strength, thereby mitigating the risk of failure. Other strategies, such as optimizing cementitious material content, use of supplementary cementitious materials, mix water content, carbon nanocellulose fiber gel, etc., can also enhance the durability of concrete structures against F-T cycles (Chung et al., 2010; Tennakoon et al., 2017; Tikalsky et al., 2004; Wang et al., 2022, 2019; Zhang et al., 2018).

With climate change, sea level rise and thawing permafrost can introduce combined freeze/thaw with chloride ingress to concrete infrastructure that had previously not experienced either deterioration mechanism. These two mechanisms can also be experienced in northern climates that use chloride-based deicing chemicals on concrete bridge decks and pavements. Various factors, such as the concrete's porosity, permeability, moisture availability, and the duration and severity of F-T conditions, affect its vulnerability to chloride ingress (Chung et al., 2010; Tikalsky et al., 2004). Concrete with higher porosity and permeability tends to be more vulnerable to chloride ingress during F-T cycles (Tennakoon et al., 2017; Wang et al., 2019; Zhang et al., 2018, 2017a, 2017b). The process of chloride ingress in concrete during F-T cycles is a complex phenomenon influenced by multiple factors. Freezing of water within concrete pores leads to expansion and generates internal pressure, inducing microcracks or widening existing cracks, which act as pathways for chloride ions to penetrate in the concrete (Hao et al., 2021; Wang et al., 2022). Furthermore, the combined effect of chloride ingress and F-T cycles can result in changes in the concentration of pore solution (Farnam et al., 2014). During ice formation, chloride ions are pushed toward the remaining liquid phase, leading to an elevated chloride concentration near the freezing front. Subsequently, during the thawing phase, the concentrated chloride ions are transported more profoundly into the concrete by the thawed water (Sarsembayeva and Zhussupbekov, 2021). Chloride ions present in seawater or deicing salt have the potential to infiltrate concrete, leading to the de-passivation of steel reinforcement and subsequent corrosion (Kessler et al., 2017). Chloride-ingress corrosion has a detrimental impact on concrete structures, leading to reductions in the cross-sectional area of steel reinforcement, decreased loading

resistance, and cracking of the concrete cover (Gao and Wang, 2017; Tian et al., 2023). Numerous investigations have explored the corrosion resulting from chloride ingress in seawater concrete (Bai et al., 2003; Bao et al., 2022a; Andrade, 2009; De Weerdt et al., 2019; Lindvall, 2007), as well as the detrimental effects of F-T cycles on concrete (Kim et al., 2022; Lin et al., 2022b; Luo et al., 2022; Shang and Song, 2006). While several studies have explored the combined effect of seawater and F-T damage, it is important to acknowledge a specific limitation in the experimental methodology employed by Peng et al., (2022) and Diao et al., (2012): in their studies, the researchers aimed to characterize the behavior of offshore reinforced concrete (RC) bridges, eccentrically loaded RC columns, and air-entrained RC beams during F-T cycles. However, their approach involved placing the samples in an F-T chamber and submerging them in a salt solution. It is worth noting that this procedure, although enabling the assessment of seawater's impact during F-T conditions, does not fully replicate the continuous submersion of seawater throughout the entirety of the F-T cycle. Consequently, this approach may introduce some disparity between the experimental conditions and real-world scenarios. Nonetheless, understanding the impact of F-T cycles on concrete submerged in seawater is paramount for ensuring the durability and longevity of coastal concrete structures.

The diffusion coefficient (Dc) measures ion mobility within a material (Pilvar et al., 2015). The expected ion transport rate in concrete mixtures can be assessed using ASTM C1202, ASTM C1556, and AASHTO T358 test methods. However, ASTM C1556 is the only ASTM standard that quantifies Dc. Since ASTM C1556 is destructive and time-consuming, a rapid, cost-effective, and non-invasive method is preferred to quantify Dc. Transmission X-ray microscopy (TXM) is a recent and novel method for imaging cementitious materials owing to the limitations of destructive or correlative test procedures (Moradllo & Ley, 2017a;2017b). This technique provides direct, practical insights into ion transport in cement-based materials on a realistic scale and is quick and nondestructive. The diffusion coefficient of cementitious materials can be determined by measuring the changes in the gray value using TXM (Behravan et al., 2021, 2023; Darma et al., 2013). However, this technique, based on Fick's second law, does not consider the binding of chlorides when determining the Dc. The chemical binding of chlorides in concrete is influenced by factors such as binder composition, water-to-binder ratio, cement hydration, supplementary cementitious material reactions, temperature, and pore solution alkalinity (Florea and Brouwers, 2012; Jasielec et al., 2020).The type of salt significantly impacts concrete deterioration (Pruckner and Gjørv, 2004). For instance, calcium chloride (CaCl2) reacts with portlandite to form calcium oxychloride, causing leaching of portlandite, pH reduction, and steel corrosion (Pruckner and Gjørv, 2004; Reiterman and Keppert, 2020; Xu et al., 2011). Magnesium chloride (MgCl2) exposure produces secondary phases, such as brucite, magnesium-silicate-hydrate, and Friedel's salt, leading to cracking and mechanical degradation. Unlike CaCl2, which lowers pore solution pH and destabilizes concrete, NaCl maintains high alkalinity and forms Friedel's salt, binding chloride ions and reducing their free concentration (Jasielec et al., 2020), and this delays steel de-passivation and corrosion, making NaCl less harmful to concrete durability. Although extensive research has been conducted on chloride transport within concrete (*e.g.*, Florea and Brouwers,

2012; Jasielec et al., 2020), comparatively little attention has been given to the diffusion of iodide. In this study, potassium iodide (KI) was utilized as a representative tracer for NaCl, as the TXM method relies on Fick's second law and primarily addresses the diffusion of free ions, without accounting for the effects of chloride binding or the chemical interactions occurring within the cement matrix (Jasielec et al., 2020). KI was used as a tracer for NaCl in this study due to its chemical stability and comparable diffusion behavior to chloride ions (Moradllo and Ley, 2017a, 2017b). Since both iodide (I^-) and chloride (Cl^-) are monovalent anions with analogous physicochemical properties, iodide serves as a reliable proxy for studying chloride movement in concrete (Jin et al., 2024). Unlike chloride, iodide exhibits limited chemical interaction in the alkaline environment of concrete, producing only a small amount of secondary compounds, such as 3CaO·Al2O3·CaI2·8H2O, when exposed to unhydrated cement phases like C3A (Jin et al., 2024). Due to its lower reactivity, iodide has minimal impact on the cement microstructure during testing, making it a suitable alternative to chloride for evaluating diffusion kinetics in cement-based materials, as suggested by previous studies (Jin et al., 2024, 2022a, 2022b; Liu et al., 2022).

The novelty of this study lies in its systematic investigation of the effects of F-T cycles on chloride ingress in concrete while submerged in seawater using TXM, which has not previously reported in the literature. The primary objective of this study is to comprehend the mechanisms of concrete damage caused by the combined effects of the F-T cycle and seawater, and their impact on chloride ingress in concrete. Two types of air-entrained concrete were cast for the study: conventional concrete and fiber-reinforced concrete. Various mechanical, performance metrics, and durability parameter assessments, including compressive strength, flexural strength, UPV, SR, ML, and RDME, were carried out to assess the damage in both types of concrete for different curing duration due to F-T exposure in seawater. Additionally, TXM was used to examine the change in the Dc value for both groups of concrete resulting from the combined effects of F-T cycles and seawater.

3.3 Experimental design

3.3.1 Materials and mix design

Two groups of air-entrained concrete were created in this study: Group A is a conventional concrete and Group B is a fiber-reinforced concrete. The mix design followed the volumetric standard outlined in the American Concrete Institute (ACI) 211.1-91, with a water-to-cementitious materials (w/cm) ratio of 0.4 which is similar to Rahat et al., (2025). The cementitious materials used were Type I/II ordinary Portland cement, possessing a specific gravity of 3.15. Table 3- 1 provides the chemical compositions of the cement used.

Table 3- 1 Chemical compositions of cement

Component	CaO	SiO_2	Al_2O_3	Fe_2O_3	SO_3	MgO	Na_2O
Content (%)	62.8	20.8	4.7	3.6	4.1	1.9	0.5

For the aggregates, natural silica sand with a fineness modulus of 2.6 was utilized as the fine aggregate (FA), and crushed limestone with a maximum size of 19 mm served as the coarse aggregate (CA). Before mixing, the aggregates were oven-dried and allowed to cool to room temperature. The required amount of water was added to the mix to adjust the moisture content to account for their absorption capacity, ensuring the aggregates reached a saturated surface dry (SSD) condition. During the mixing process, a commercially available AEA was added to both concrete groups at a dosage of 46 mL per 100 kg of cement. PVA fibers, measuring 12.5 mm in length and 100 microns in diameter, were incorporated into the fiber-reinforced concrete at a content of 0.4 % of the total volume. To achieve a uniform mixture of PVA fiber-reinforced concrete, the FA was first blended thoroughly with the fibers prior to its addition into the concrete mixer. The air content of the freshly mixed concrete was determined using the volumetric method outlined in ASTM C173 for both concrete groups. The hardened air-void system was further evaluated following ASTM C457, as reported by Rahat et al. (2025), which confirmed Group A's more refined air-void distribution and enhanced freeze-thaw resistance. The results in Table 3- 4 indicate that Group A exhibited a lower spacing factor, higher specific surface, and greater void frequency than Group B, reinforcing its superior durability. Table 3- 2 and Table 3- 3 provide the physical properties of aggregates, and mixture proportions for both groups of concrete correspondingly.

Table 3- 2 Physical properties of coarse aggregate and fine aggregate

Physical property	**Fine aggregate**	**Coarse aggregate**
Specific gravity	2.61	2.72
Moisture content (%)	0	0
Absorption (%)	1.1	1.1

Table 3- 3 Concrete mix design

Groups	**Cement (kg/m^3)**	**FA (kg/m^3)**	**CA (kg/m^3)**	**Water (kg/m^3)**	**w/c**	**PVA Fibers (kg/m^3)**	**Fresh Air Content (%)**
GA-14d	541.4	628.6	914.2	227.9	0.4	0	5.5
GB-14d	541.4	618.0	914.2	227.9	0.4	5.2	4.6
GA-70d	541.4	628.6	914.2	227.9	0.4	0	5.7
GB-70d	541.4	618.0	914.2	227.9	0.4	5.2	4.9

Table 3- 4 Hardened air-void system data for concrete specimens

	A (%)	n (mm^{-1})	p/A	$\bar{l}$ (mm)	α (mm^{-1})	$\bar{L}$ (mm)
Group A	4.3	0.239	7.636	0.182	22	0.07
Group B	4.0	0.202	8.333	0.198	20	0.08

*Note: here, A = air content, p/A = paste-air ratio, $\bar{l}$ = average chord length, n = void frequency, α = specific surface, and $\bar{L}$ = spacing factor

Samples were created for experimental evaluation, consisting of 24 beam prisms with dimensions of 400 mm by 100 mm by 75 mm and 24 cylinders with a diameter of 75 mm and a height of 150 mm. These samples were moist-cured for different periods (14 days and 70 days) in a fog room. Samples are divided into subgroups: GA-SW-14d and GA-SW-70d for Group A specimens cured for 14 and 70 days, respectively, and GB-SW-14d and GB-SW-70d for Group B specimens cured for 14 and 70 days, respectively.

3.3.2 Preparation of seawater

This study utilized simulated seawater prepared according to ASTM D1141 for the F-T cycle exposure. The seawater was created using two stock solutions: Stock No. 1 and Stock No. 2. The chemical composition for preparing the stock solutions is provided in Table 3- 5. Deionized water was used to prepare the stock solutions. To create a 10 L substitute seawater solution, 245.34 g of sodium chloride and 40.94 g of anhydrous sodium sulfate were dissolved in 9.5 L deionized water. Then, 200 mL of Stock Solution No. 1 was added with vigorous stirring, followed by 100 mL of Stock Solution No. 2 to prepare the solution. The final volume was adjusted to 10 L by dilution. A pH of 8.2 was achieved using a pH meter (APERA PH400S), with a few milliliters of 0.1 N sodium hydroxide solution.

Table 3- 5. Chemical composition of seawater and stock solutions

Stock no. 1	
Component	**g L^{-1}**
$MgCl_2.6H_2O$	556.6
$CaCl_2$	57.9
$SrCl_2.6H_2O$	2.1
Stock no. 2	
Component	**g L^{-1}**
KCl	69.5
$NaHCO_3$	20.1
KBr	10
H_3BO_3	2.7
NaF	0.3
Seawater solution	
Component	**g L^{-1}**
NaCl	24.5
$NaSO_4$	4.1

3.3.3 Testing procedures

In this study, both groups of concrete specimens were subjected to 70-day and 14-day curing in a moisture curing room. After the curing period, the samples underwent F-T cycles in seawater environments, following the specifications outlined in ASTM C666 Procedure A. Before initiating the F-T cycles, a comprehensive assessment of both sets of concrete specimens was conducted to determine their compressive strength, flexural strength, UPV, RDME, ML, and SR following ASTM and AASHTO standards. Following this, the specimens were placed in water tanks

containing seawater inside an environmental chamber and subjected to the F-T cycles. During this study, the duration of one F-T cycle was 4.5 hours. In a freezing half cycle, the temperature dropped rapidly from 4.4°C to –18°C within one hour and remained constant at -18°C for two hours. Subsequently, in the thawing half cycle, the temperature increased from -18°C to 4.4°C in thirty minutes and remained stable at 4.4°C for one hour. The combination of these two half cycles constituted a single F-T cycle.

After every 28 to 36 F-T cycles, all the specimens from both groups were removed from the environmental chamber. The surface water was wiped off, and then the mass, resonant frequency, UPV, and SR were measured in that order. Equations (1) and (2) were subsequently employed to calculate the ML and RDME, respectively. It is important to highlight that the RDME value represents the specimens' durability factor (DF). The ML percentage is:

$$\Delta m = \frac{m_o - m_n}{m_o} \times 100 \quad (1)$$

where m_0 refers to the mass of the specimens at 0 F-T cycles, m_n represents the mass of the specimens after n F-T cycles, and $\Delta \boldsymbol{m}$ is the percentage of the ML of the concrete specimens after N F-T cycles. The RDME is:

$$P_c = \frac{n_c^2}{n_0^2} \quad (2)$$

where n_o is the fundamental transverse frequency of the specimens at 0 F-T cycles, n_c represents the fundamental transverse frequency of the specimens after c F-T cycles, and P_c is the RDME of the concrete specimens after c F-T cycles.

Following numerous F-T cycles that led to the failure of specific specimens, the specimens were removed from the environmental chamber. Following ASTM and AASHTO standards, the specimens were comprehensively evaluated to determine their compressive strength (ASTM C39), flexural strength (ASTM C293), longitudinal UPV (ASTM C597), SR (AASHTO T358) from all four sides of beam prisms, and fundamental transverse frequency (ASTM C215).

3.3.4 TXM procedure

A custom-developed TXM system quantified Dc in concrete samples from both groups across all curing durations before and after F-T cycles. This system was constructed following the design from other researchers (Behravan et al., 2021, 2023; Ley et al., 2023; Moradllo and Ley, 2017a, 2017b; Moradllo et al., 2017). Figure 3- 1 shows the schematic of the system (Rahat et al., 2024b). Images were taken in a consistent orientation to track the gray value changes over time. The X-ray exposure time was 0.25 s.

Table 3- 6 shows the details of the X-ray source.

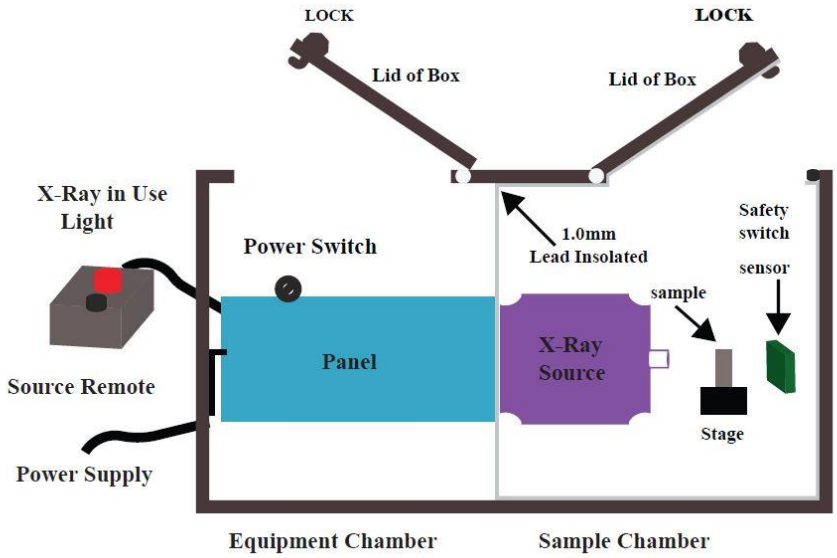

Figure 3- 1 Schematic illustration of the TXM system.

Table 3- 6 X-ray source details

Sensor resolution (line pairs per mm)	33.78
Pixel size (μm)	19
Voltage (keV)	65
Current (μA)	7000
Exposure time (s)	0.25

In the TXM experimental procedure, 19 mm diameter concrete cores were extracted from all specimen groups before and after being subjected to F-T cycles. The two cores were obtained from the top and bottom surfaces of the beam prisms from each group of concrete samples, sealed with hydrophobic wax on the sides and bottoms, and left uncoated on the top surface to facilitate 1D diffusion. The study assessed concrete samples that had been cured for 70 days and exposed to up to 500 F-T cycles, as well as those cured for 14 days and subjected to a maximum of 375 F-T cycles due to surface scaling resulting from the cycles. A 0.6 M potassium iodide (KI) solution was utilized to improve the differentiation between the tracer and the specimens under examination in concrete. X-ray imaging was employed to record the penetration of iodide ions into the concrete structure. The diffusion coefficient of iodide surpasses chloride by 24 %, serving as a robust standard for evaluating the diffusion properties of chloride ions in concrete (Behravan et al., 2023, 2021 ; Moradllo and Ley, 2017a).

In this study, all core samples underwent an initial scanning to create reference images. The samples were then ponded in the KI solution and re-scanned after 3 days, 14 days, and 28 days,

allowing for a direct comparison with the reference image. By subtracting the reference image, changes in gray values were evaluated. Additionally, a reference image was captured after the cycles for specimens exposed to F-T cycles, mirroring the other samples' subsequent process. Using a software program, the X-ray images obtained at 3 days, 14 days, and 28 days for each specimen were aligned with their respective reference images through local adjustments, such as shifts and rotations. The subtracted image in Fig. 2 indicates the depth of iodide penetration in the sample after 3 days in the KI solution. To determine the average gray values at different depths in each sample, a region approximately 7.4 mm wide was identified, as shown in Figure 3- 1, to minimize cupping artifacts. Each line in the grayscale value corresponds to a specific depth, and the final gray-value profile was derived by averaging the values from 280 individual lines. Behravan et al., (2023) recommended using X-rays from various angles to estimate the Dc for concrete specimens and suggested presenting the findings as the mean Dc. The irregularities of the aggregates may affect the X-ray analysis of concrete due to their uneven nature. Therefore, X-rays were captured at angles of 0°, 60°, 120°, and 180° for each sample to determine the apparent Dc.

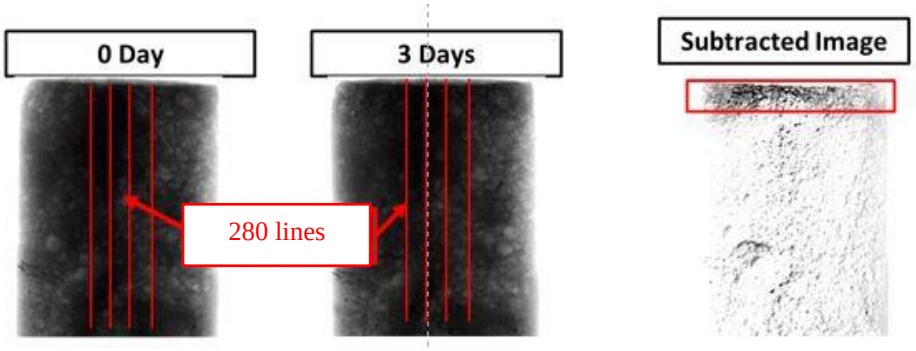

Figure 3- 2 Subtraction of radiographs within a specified area of interest

The apparent D_c is determined using regression and is based on a solution obtained from Fick's second law of diffusion, which is employed in ASTM C1556. The solution for the 1D diffusion problem is defined in Equation 3, where *x* represents the distance from the sample surface, C_s is the surface iodide concentration, $C_{(x,t)}$ is the iodide concentration at a depth *x* from the surface after time *t*, and *erf* denotes the Gaussian error function.

$$C_{(x,t)} = C_s\left(1 - erf\left(\frac{x}{2\sqrt{D_c t}}\right)\right) \quad (3)$$

3.4 Results and discussion

3.4.1 UPV results

UPV tests were conducted in this study to assess the uniformity and relative quality of concrete due to F-T cycles in seawater. Group A consistently exhibited higher UPV values throughout the

F-T cycles than Group B, as shown in Figure 3- 3 After 70 days of curing, both groups demonstrated better resistance to 1000 F-T cycles, with GA-SW-70d showing a 13 % reduction and GB-SW-70d a 19 % reduction in UPV results. In contrast, samples cured for 14 days showed a significant reduction in UPV, with GA-SW-14d experiencing a 30 % decrease and GB-SW-14d a 44 % decrease after 300 F-T cycles. However, samples cured for 70 days (GA-SW-70d and GB-SW-70d) only experienced a 6 % and 10 % reduction, respectively, after the same number of F-T cycles. The lower air content across all Group B samples than Group A suggests that PVA fibers may not have significantly mitigated the effects of F-T cycles. Furthermore, this indicates that a more extended curing period enhances resistance to F-T cycles.

However, it was found by Rahat et al., (2025) that when subjected to 1000 F-T cycles in plain water under the same mix design and 70-day curing period, Group A samples exhibited a 6 % reduction and Group B showed a 10 % reduction. In contrast, after 300 F-T cycles, 14-day cured samples from Group A showed a 29 % reduction, and Group B showed a 33 % reduction, while 70-day cured samples experienced only a 5 % and 5 % reduction, respectively. These results emphasize the greater impact of seawater compared to plain water during F-T cycles.

The data indicates a statistical difference between the GA-SW-70d sample and the GA-SW-14d and GB-SW-14d samples after 300 F-T cycles at a significance level of 0.05. However, there is not enough evidence to conclude that the difference in percent change in UPV is statistically significant at the 0.05 significance level when comparing the GA-SW-14d and GB-SW-14d samples after 300 F-T cycles. Similarly, when comparing the GA-SW-70d samples with GB-SW-70d samples at 300 and 1000 cycles of F-T testing, there is insufficient evidence to support the conclusion that the difference in percent change in UPV is statistically significant at the 0.05 significance level. Table 3- 7 presents UPV (m s^{-1}) data for different replicates before and after F-T cycles for both groups of concrete samples cured for 70 days and 14 days.

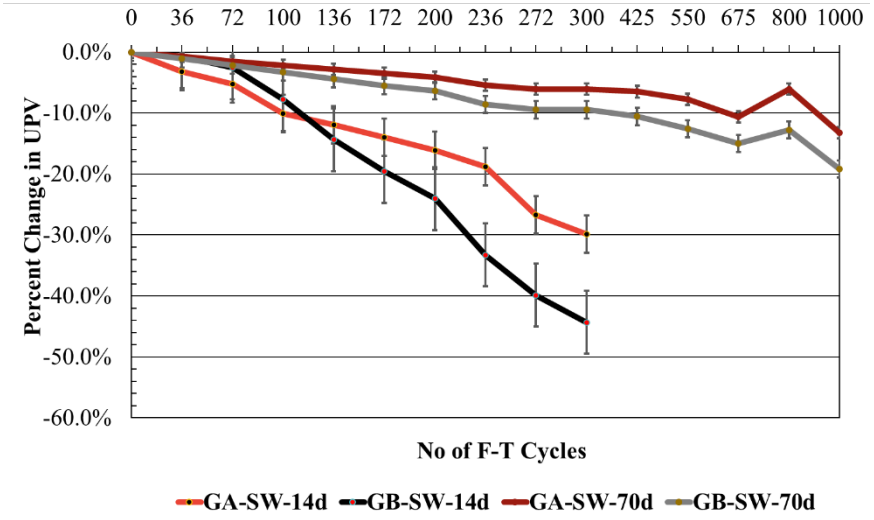

Figure 3- 3 Change of UPV value over F-T cycles in seawater for different curing periods, error bars represent one standard deviation

Table 3- 7 UPV (m s^{-1}) data of concrete replicates for both groups of concrete

70 days curing period										
	Group A					Group B				
F-T cycle	R1	R2	R3	**Average**	**STD**	R1	R2	R3	**Average**	**STD**
0	4590	4690	4570	4620	52	4560	4410	4560	4510	71
36	4560	4660	4520	4580	59	4500	4380	4500	4460	57
72	4530	4640	4480	4550	67	4450	4340	4450	4410	52
100	4510	4610	4430	4520	74	4390	4310	4390	4360	38
136	4480	4580	4390	4480	78	4340	4270	4340	4310	33
172	4450	4550	4340	4450	86	4290	4240	4290	4270	24
200	4430	4530	4300	4420	94	4240	4200	4240	4220	19
236	4370	4470	4220	4350	103	4090	4180	4100	4140	40
272	4350	4440	4170	4320	112	4090	4100	4090	4100	5
300	4350	4440	4170	4320	112	4090	4100	4090	4100	5
425	4320	4420	4130	4290	120	4040	4070	4040	4060	14
550	4270	4370	4050	4230	134	3940	4010	3940	3980	33
675	4100	4200	4090	4130	50	3880	3760	3880	3820	57
800	4320	4410	4300	4340	48	3970	3850	3970	3910	57
1000	3980	4070	3960	4000	48	3690	3570	3690	3630	57
14 days curing period										
	Group A					Group B				
F-T cycle	R1	R2	R3	**Average**	**STD**	R1	R2	R3	**Average**	**STD**
0	4370	4400	4330	4370	29	4290	4250	4190	4240	41
36	4280	4200	4220	4230	34	4260	4240	4140	4210	52
72	4090	4140	4200	4140	45	4200	4180	4020	4130	81
100	3940	3970	3820	3910	65	3920	4000	3810	3910	78
136	3900	3820	3840	3850	34	3820	3490	3560	3620	142
172	3740	3580	3940	3750	147	3470	3320	3420	3400	62
200	3730	3450	3830	3670	161	3190	3200	3270	3220	36
236	3530	3380	3800	3570	174	2860	2730	2890	2830	69
272	3020	3270	3350	3210	141	2580	2460	2610	2550	65
300	2950	3090	3130	3060	77	2370	2260	2410	2350	63

*Note: R1, R2, and R3 stand for Replicate 1, Replicate 2, and Replicate 3; STD stands for standard deviation

3.4.2 SR results

SR tests were conducted in this study to assess concrete resistance against chloride ingress and the probability of corrosion due to F-T cycles in seawater. In Figure 3- 4, the SR values for all the concrete sample groups drastically change over F-T cycles. After being subjected to 1000 F-T cycles, GA-SW-70d displayed a 57 % reduction, and GB-SW-70d showed a 62 % reduction in SR results. For samples subjected to a 14-day curing period, there was a significant reduction in SR results, with GA-SW-14d experiencing a 52 % decrease and GB-SW-14d showing a 62 % decrease after 300 F-T cycles. In contrast, samples cured for 70 days (GA-SW-70d and GB-SW-70d) only

experienced a 33 % and 29 % decrease after the same number of F-T cycles, implying that a more extended curing period improves resistance to F-T cycles.

Rahat et al. (2025) found that, with the same mix design and curing period, 14-day-cured samples immersed in plain water showed reductions of 51 % in Group A and 52 % in Group B after 300 F-T cycles, while 70-day-cured samples showed significantly lower reductions of 17 % and 27 %, respectively. For 1000 F-T cycles, Groups A and B experienced 46 % and 53 % reductions, respectively.

The reduction in SR is primarily attributed to the combined effects of seawater exposure and F-T cycles. Chloride ions from seawater infiltrate the concrete and intensify microcracking (Ma et al., 2023), scaling, and corrosion. It is likely true that these effects increase permeability and potentially reduce resistivity. The more significant SR decline in seawater-exposed samples highlights the amplified damage caused by chloride ingress during F-T cycles, emphasizing the need for enhanced durability strategies in coastal structures. The results suggest that PVA fibers may not significantly mitigate F-T cycle effects.

The data indicate a statistical difference when comparing the GA-SW-70d sample with GA-SW-14d and GB-SW-14d samples after 300 F-T cycles at a significance level of 0.05. However, there is insufficient evidence to conclude that the difference in percent change in SR is statistically significant at the 0.05 significance level when comparing the GA-SW-14d and GB-SW-14d samples after 300 F-T cycles. Similarly, when comparing the GA-SW-70d samples with GB-SW-70d samples at 300 and 1000 cycles of F-T testing, there is insufficient evidence to support the conclusion that the difference in percent change in SR is statistically significant at the 0.05 significance level. Table 3- 8 presents SR (kΩ-cm) data for different replicates before and after F-T cycles for both groups of concrete samples cured for 70 days and 14 days.

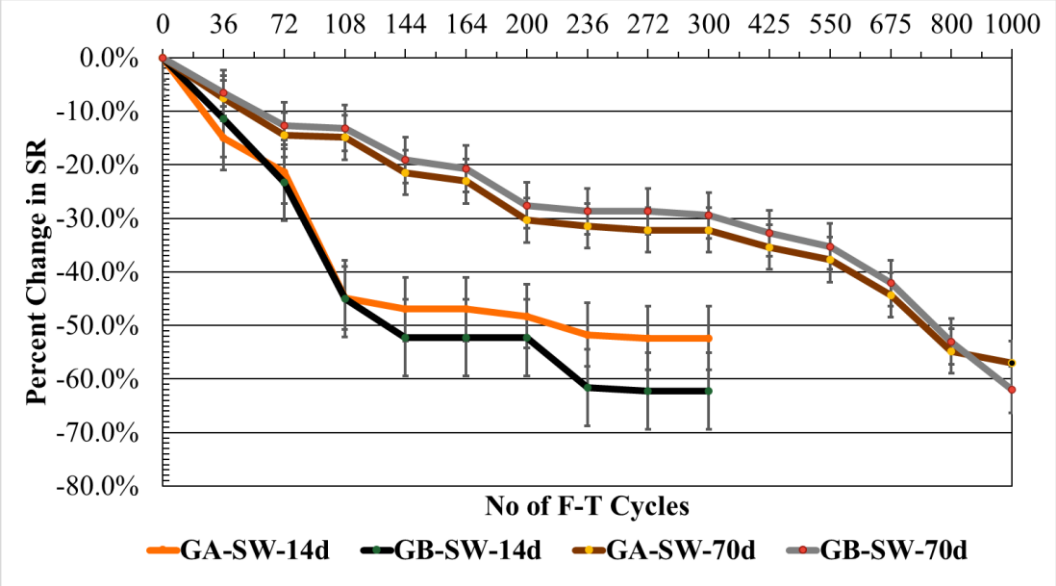

Figure 3- 4 Change of SR value over F-T cycles in seawater for different curing periods, error bars represent one standard deviation

Table 3- 8 Average SR (kΩ-cm) from four-side measurements of concrete replicates for both groups

70 days curing period										
	Group A					Group B				
F-T cycle	R1	R2	R3	**Average**	**STD**	R1	R2	R3	**Average**	**STD**
0	24.0	25.5	25.8	25.1	0.8	24.2	23.9	23.5	23.9	0.3
36	22.9	23.6	23.2	23.2	0.3	22.7	22.0	22.1	22.3	0.3
72	21.9	21.8	22.1	21.9	0.1	22.0	20.1	20.8	20.9	0.8
100	20.5	21.1	21.5	21.0	0.4	21.9	20.0	20.7	20.9	0.8
136	20.9	20.0	21.4	20.8	0.6	20.0	19.0	19.2	19.4	0.1
172	21.0	20.0	20.9	20.6	0.5	19.9	18.3	18.8	19.0	0.3
200	19.8	18.7	19.4	19.3	0.5	17.9	17.0	17.1	17.4	0.1
236	18.5	18.4	19.1	18.7	0.3	16.9	17.0	17.1	17.0	0.1
272	17.3	17.0	17.7	17.4	0.3	17.0	17.0	17.0	17.0	0.0
300	17.1	17.1	16.7	17.0	0.2	16.8	16.5	17.0	16.8	0.3
425	17.5	16.2	15.0	16.2	1.0	16.5	15.7	16.1	16.1	0.2
550	15.8	15.5	15.4	15.6	0.2	16.3	14.5	15.6	15.4	0.5
675	14.6	14.2	13.5	14.1	0.4	15.1	13.0	13.6	13.9	0.3
800	10.9	11.2	12.1	11.4	0.5	11.9	10.5	11.3	11.3	0.4
1000	11.6	10.9	10.0	10.8	0.7	9.5	9.2	8.5	9.1	0.4
14 days curing period										
	Group A					Group B				
F-T cycle	R1	R2	R3	**Average**	**STD**	R1	R2	R3	**Average**	**STD**
0	15.0	14.2	14.9	14.7	0.4	13.8	13.5	15.0	14.1	0.6
36	12.0	12.9	12.7	12.5	0.4	12.7	12.3	11.9	12.3	0.3
72	12.4	10.2	11.9	11.5	0.9	9.6	10.9	10.7	10.4	0.6
100	7.9	8.2	8.2	8.1	0.1	7.8	7.7	7.4	7.6	0.2
136	7.8	7.7	8.0	7.8	0.1	6.8	6.7	6.4	6.6	0.2
172	7.8	7.7	8.0	7.8	0.1	6.8	6.7	6.4	6.6	0.2
200	7.8	7.3	7.7	7.6	0.2	6.8	6.7	6.4	6.6	0.2
236	7.0	7.4	7.0	7.1	0.2	6.3	5.4	5.3	5.7	0.4
272	6.9	7.1	7.1	7.0	0.1	6.2	5.3	5.2	5.6	0.4
300	6.9	7.2	6.7	6.9	0.2	6.1	5.2	5.1	5.5	0.4

*Note: R1, R2, and R3 stand for Replicate 1, Replicate 2, and Replicate 3; STD stands for standard deviation

3.4.3 ML and RDME results

Figure 3- 5(a) and (b) illustrate the changes in ML and RDME for concrete samples from Groups A and B, subjected to F-T cycles in seawater after 14 and 70 days of curing. The deterioration level of the concrete is related to change in both ML and RDME, specifically RDME can give us the idea of severity of internal damage. In Fig. 5(a), after 1000 F-T cycles, 70-day cured samples from Group A showed an ML of 2.5 %, while Group B had a slightly higher ML of 3.5 %.

On the other hand, 14-day cured samples subjected to 300 F-T cycles exhibited higher ML values, with Group A losing 3.0 % of its mass and Group B losing 5.5 %. After 300 F-T cycles, the 70-day cured samples from Group A had an ML of 0.5 %, and Group B had an ML of 0.5 %, underscoring the impact of curing duration on F-T resistance.

However, Rahat et al. (2025) found that F-T cycles in plain water led to better performance than seawater, with Group A and Group B showing ML values of 1.4 % and 1.7 % after 1000 F-T cycles for 70-day cured samples. The 14-day cured samples had higher ML values, with Group A at 1.0 % and Group B at 3.2 %, compared to 0.5 % for both groups after 70-day curing.

Fig 5(b) shows that after 1000 F-T cycles, 70-day cured samples from Group A had an RDME of 95 %, while Group B had 91 %. The 14-day cured samples subjected to 300 F-T cycles showed lower RDME values, with Group A at 69 % and Group B at 55 %. In contrast, after 300 F-T cycles, the 70-day cured samples had RDME values of 96 % and 95 % for Groups A and B, respectively, emphasizing the importance of extended curing for enhanced F-T resistance.

However, Rahat et al. (2025) found that F-T cycles in plain water resulted in higher RDME values compared to seawater, with Group A and Group B showing RDME values of 95 % and 95 %, respectively, after 1000 F-T cycles. For 14-day cured samples, RDME values were 73 % for Group A and 65 % for Group B, while 70-day cured samples showed improved values of 98 % for Group A and 96 % for Group B.

According to ASTM C666 Procedure A, testing continues until each specimen undergoes 300 cycles or its RDME falls to 60 % of the initial modulus. In this study, 14-day cured samples were close to the threshold value; Group B samples exceeded the 60 % threshold. Group A showed better resistance to F-T cycles than Group B. The prolonged curing improves F-T resistance. The lower RDME values observed in this study demonstrate that seawater exacerbates concrete degradation during F-T cycles more than plain water. This heightened impact is attributed to the salts in seawater, which amplify internal stresses through crystallization pressure and osmotic effects, accelerating microcracking and material deterioration (Guo et al., 2024). These findings highlight the pivotal influence of curing duration and environmental conditions on concrete's resistance to F-T damage, emphasizing the need for tailored strategies to mitigate combined seawater and F-T effects.

After 300 F-T cycles, a statistically significant difference in ML and RDME was observed at a significance level of 0.05 when comparing the GA-SW-70d sample with the GA-SW-14d and GB-SW-14d samples. However, there was no statistically significant difference between the GA-SW-14d and GB-SW-14d samples after 300 F-T cycles or between the GA-SW-70d and GB-SW-70d samples after 300 and 1000 cycles for both ML and RDME.

Table 3- 9 presents mass (kg) values for different replicates before and after F-T cycles for both groups of concrete samples cured for 70 days and 14 days. Similarly, Table 3- 10 displays the fundamental transverse frequency (Hz) values before and after F-T cycles for both groups of concrete samples following 70 days and 14 days curing periods.

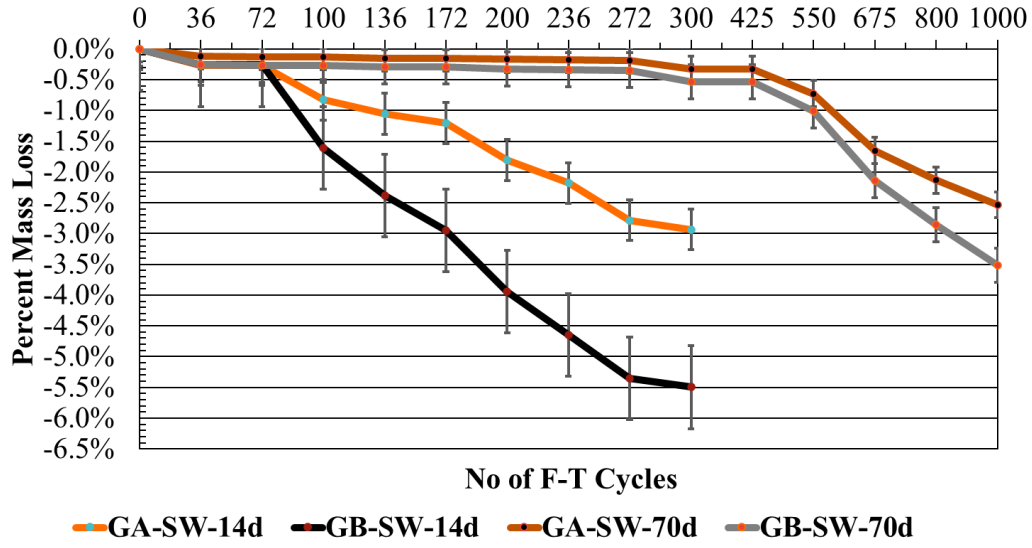

(a)

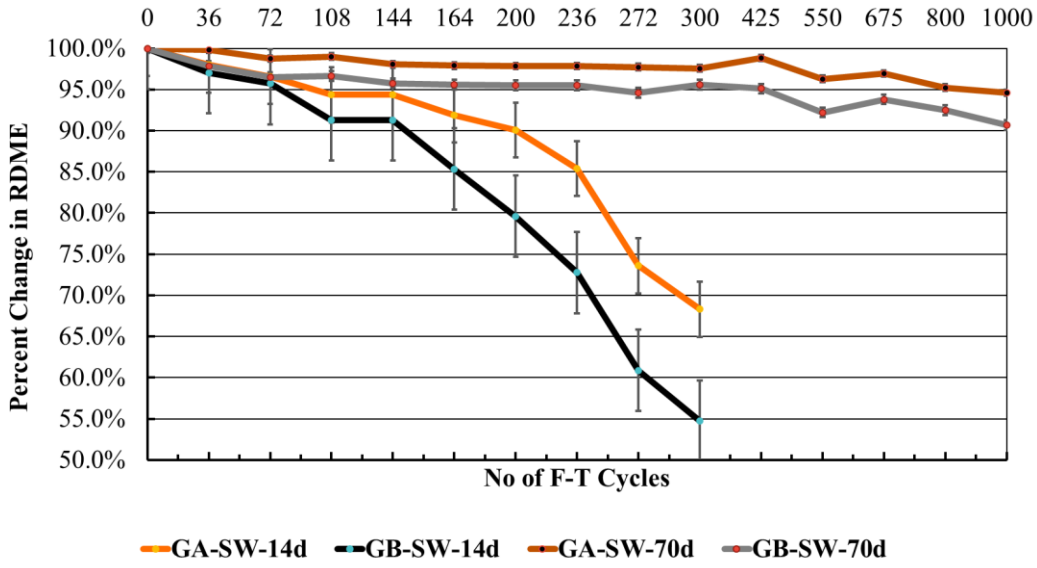

(b)

Figure 3- 5 Change of (a) mass and (b) RDME value over F-T cycles in seawater for different curing periods, error bars represent one standard deviation

Table 3- 9 Mass (kg) data of concrete replicates for both groups of concrete

70 days curing period										
	Group A					**Group B**				
F-T cycle	R1	R2	R3	**Average**	**STD**	R1	R2	R3	**Average**	**STD**
0	7.712	7.613	7.410	7.578	0.126	7.557	7.421	7.463	7.480	0.057
36	7.696	7.605	7.398	7.566	0.125	7.539	7.406	7.438	7.461	0.057
72	7.695	7.604	7.397	7.565	0.125	7.538	7.405	7.437	7.460	0.057
100	7.695	7.604	7.397	7.565	0.125	7.538	7.405	7.437	7.460	0.057
136	7.693	7.602	7.396	7.564	0.124	7.535	7.403	7.436	7.458	0.056
172	7.693	7.602	7.396	7.564	0.124	7.535	7.403	7.436	7.458	0.056
200	7.691	7.601	7.395	7.562	0.124	7.533	7.402	7.433	7.456	0.056
236	7.690	7.601	7.394	7.562	0.124	7.532	7.400	7.433	7.455	0.056
272	7.690	7.600	7.393	7.561	0.124	7.531	7.400	7.432	7.454	0.056
300	7.690	7.600	7.393	7.561	0.124	7.531	7.400	7.432	7.454	0.056
425	7.680	7.590	7.393	7.554	0.120	7.527	7.380	7.425	7.444	0.061
550	7.660	7.550	7.360	7.523	0.124	7.500	7.340	7.400	7.413	0.066
675	7.580	7.480	7.300	7.453	0.116	7.410	7.250	7.300	7.320	0.067
800	7.520	7.450	7.270	7.413	0.105	7.350	7.200	7.270	7.273	0.061
1000	7.490	7.420	7.240	7.383	0.105	7.290	7.170	7.210	7.223	0.050
14 days curing period										
	Group A					**Group B**				
F-T cycle	R1	R2	R3	**Average**	**STD**	R1	R2	R3	**Average**	**STD**
0	6.568	6.670	6.732	6.657	0.068	7.045	6.950	7.092	7.029	0.059
36	6.565	6.640	6.714	6.640	0.061	7.028	6.930	7.072	7.010	0.059
72	6.565	6.640	6.714	6.640	0.061	7.028	6.935	7.070	7.011	0.056
100	6.515	6.610	6.680	6.602	0.068	6.960	6.882	6.905	6.916	0.033
136	6.510	6.591	6.659	6.587	0.061	6.899	6.821	6.871	6.864	0.032
172	6.489	6.591	6.648	6.576	0.066	6.861	6.789	6.810	6.820	0.030
200	6.452	6.548	6.611	6.537	0.065	6.810	6.719	6.735	6.755	0.040
236	6.405	6.541	6.591	6.512	0.079	6.752	6.649	6.711	6.704	0.042
272	6.355	6.510	6.549	6.471	0.084	6.682	6.611	6.668	6.654	0.031
300	6.349	6.492	6.545	6.462	0.083	6.678	6.585	6.662	6.642	0.041

*Note: R1, R2, and R3 stand for Replicate 1, Replicate 2, and Replicate 3; STD stands for standard deviation

Table 3- 10 Fundamental transverse frequency (Hz) data of concrete replicates for both groups of concrete

70 days curing period										
	Group A					Group B				
F-T cycle	R1	R2	R3	**Average**	**STD**	R1	R2	R3	**Average**	**STD**
0	2340	2380	2230	2320	63	2290	2260	2280	2280	12
36	2320	2390	2220	2310	70	2280	2240	2270	2260	17
72	2320	2380	2220	2310	66	2280	2240	2260	2260	16
100	2320	2380	2220	2310	66	2280	2240	2260	2260	16
136	2320	2380	2210	2300	70	2280	2240	2260	2260	16
172	2310	2370	2210	2300	66	2280	2230	2260	2260	21
200	2300	2360	2210	2290	62	2270	2220	2250	2250	21
236	2300	2360	2200	2290	66	2260	2220	2250	2240	17
272	2300	2360	2200	2290	66	2260	2220	2250	2240	17
300	2290	2330	2190	2270	59	2260	2220	2230	2240	17
425	2290	2320	2190	2270	56	2250	2210	2230	2230	16
550	2290	2320	2190	2270	56	2250	2210	2230	2230	16
675	2280	2320	2180	2260	59	2240	2200	2210	2220	17
800	2310	2350	2200	2290	63	2220	2210	2200	2210	8
1000	2230	2320	2200	2250	51	2200	2190	2200	2200	5
14 days curing period										
	Group A					Group B				
F-T cycle	R1	R2	R3	**Average**	**STD**	R1	R2	R3	**Average**	**STD**
0	2330	2340	2310	2330	12	2400	2400	2420	2410	9
36	2200	2200	2240	2210	19	2320	2320	2340	2330	9
72	2200	2180	2200	2190	9	2300	2320	2320	2310	9
100	2180	2170	2170	2170	5	2280	2290	2300	2290	8
136	2180	2170	2170	2170	5	2280	2290	2300	2290	8
172	2130	2140	2180	2150	22	2260	2230	2230	2240	14
200	2110	2120	2140	2120	12	2120	2220	2130	2180	45
236	2070	2080	2150	2100	36	2080	2170	2020	2100	75
272	1920	1930	1990	1950	31	1900	1990	1840	1920	75
300	1830	1850	1910	1860	34	1780	1860	1720	1790	70

*Note: R1, R2, and R3 stand for Replicate 1, Replicate 2, and Replicate 3; STD stands for standard deviation

3.4.4 Strength testing results

Figure 3- 6(a) and (b) depict the results for the compressive strength and modulus of rupture of various concrete samples at different stages: before F-T, after 300 F-T cycles (for 14-day cured samples), and after 1000 F-T cycles (for 70-day cured samples) in seawater.

After 7 days of curing, Group A exhibited a compressive strength of 28.2 Mpa, while Group B had a compressive strength of 30.6 Mpa. Additionally, the modulus of rupture values for Group A and Group B were 8.35 Mpa and 9.45 Mpa, respectively. Group A's samples showed lower

compressive strength and rupture modulus than Group B's. The difference in strength is attributed to Group B's reinforcement with PVA fiber.

Over the 7 days, 14 days, 28 days, and 70 days of curing, the compressive strength and modulus of rupture for all samples consistently increased. Group A samples continued to show lower strength and modulus of rupture compared to Group B, a trend attributed to the reinforcement of Group B with PVA fiber.

Following 300 F-T cycles in seawater, both Group A and Group B samples, cured for 14 days, displayed noticeable differences. Group B showed the lowest percentage change in compressive strength (14 %) and modulus of rupture (21 %), while Group A exhibited the highest percentage change in both compressive strength (18 %) and modulus of rupture (25 %). Conversely, after being cured for 70 days, the samples were subjected to 1000 F-T cycles in seawater; Group B showed the lowest percentage change in compressive strength (5 %) and modulus of rupture (8 %), while Group A exhibited the highest percentage change in both compressive strength (5 %) and modulus of rupture (10 %). These data clearly show that extending the curing period significantly enhances seawater's resistance to F-T cycles. However, the mechanical properties do not substantially improve when PVA fibers are included against F-T cycles in seawater. It should be noted that an improved air-void system in Group A helps to enhance resistance against F-T cycles in seawater. When comparing these results with a previous study by Rahat et al. (2025) on F-T cycles in plain water for the same concrete groups, it is apparent that F-T cycles in seawater exert a more severe impact on concrete's mechanical strength than plain water conditions.

An unpaired, two-tailed t-test was conducted on the 14-day cured samples following 300 F-T cycles and the 70-day cured samples following 1000 F-T cycles, and the findings suggested insufficient evidence to establish a statistically significant variance in the compressive strength and modulus of rupture values between Group A and Group B at a significance level of 0.05 after 1000 F-T cycles for 70 days of cured samples. For 300 F-T cycles, the findings suggested insufficient evidence to establish a statistically significant variance in the compressive strength values between Group A and Group B at a significance level of 0.05. However, there is a statistically significant difference in modulus of rupture values between Group A and Group B after 300 F-T cycles for 14 days of cured samples.

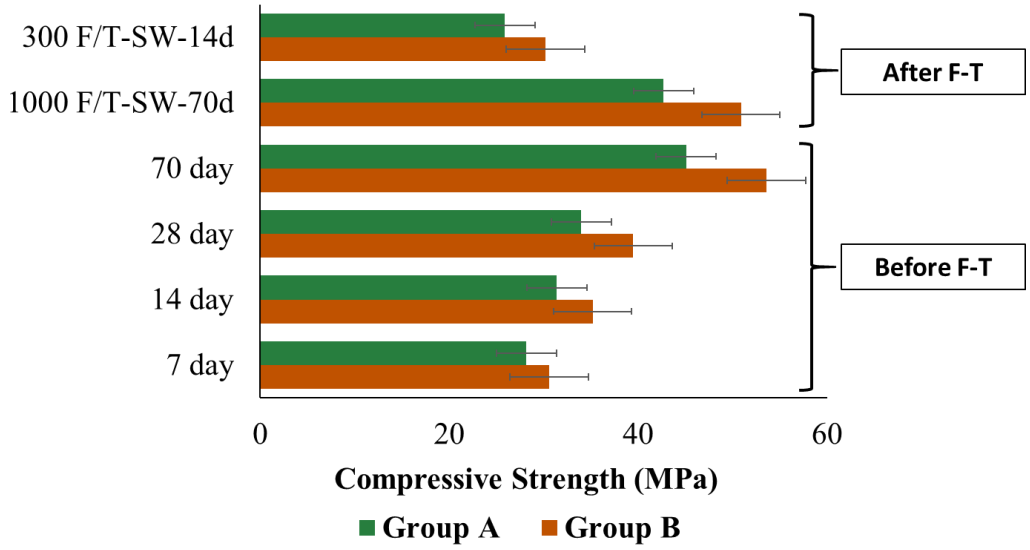

(a)

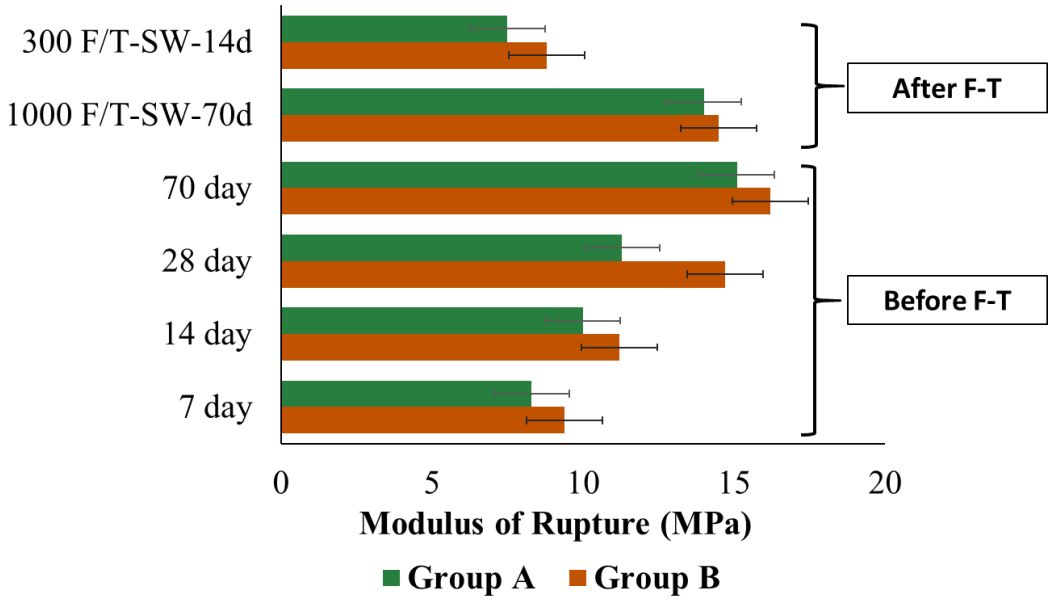

(b)

Figure 3- 6 (a) Compressive strength, and (b) modulus of rupture of different concrete groups for different curing periods before and after F-T cycles in seawater.

3.4.5 Time-dependent D_c and concentration profile

Figure 3- 7 shows the concentration profiles and D_c values for the concrete samples in Groups A and B after 3, 14, and 28 days of ponding, prior to exposure to F-T cycles in seawater.

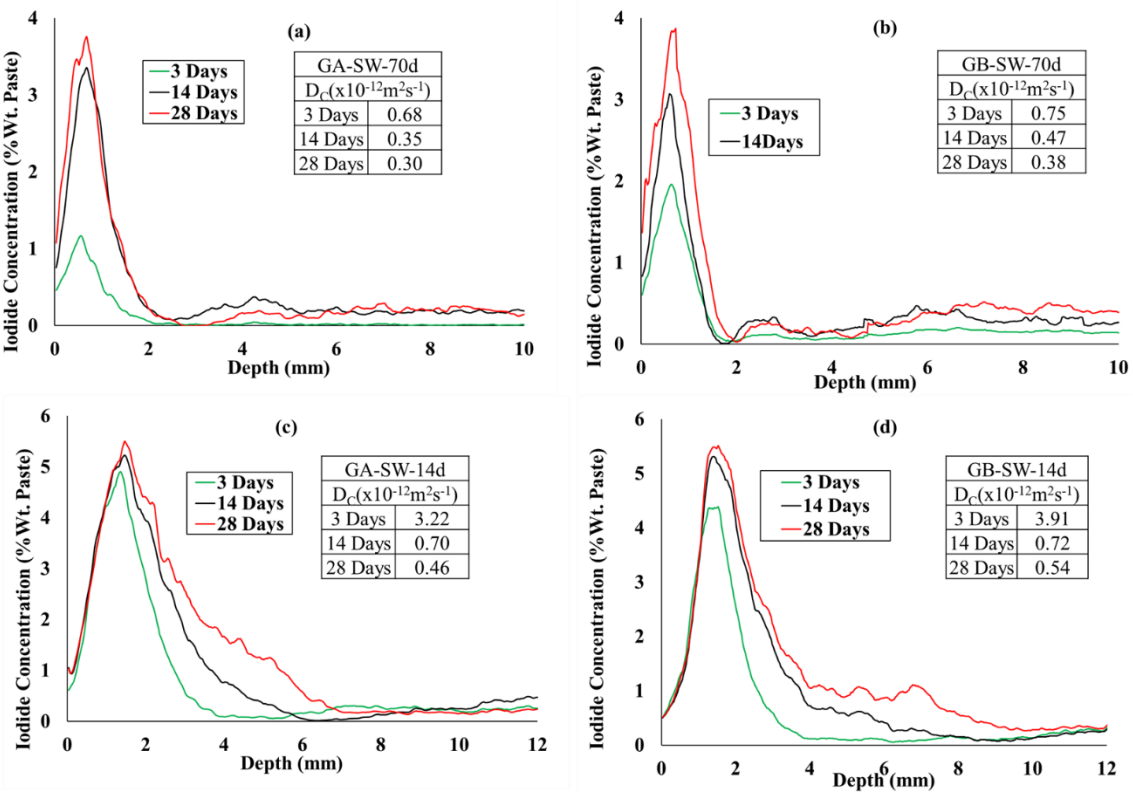

Figure 3- 7 Concentration profiles for the following concrete samples before undergoing F-T cycles : (a) GA-SW-70d, (b) GB-SW-70d, (c) GA-SW-14d, and (d) GB-SW-14d.

As depicted in Figure 3- 7, the Group A concrete samples consistently exhibited lower D_c values than Group B before experiencing F-T cycles in seawater, regardless of the 70-day or 14-day curing period. Table 11 shows the average D_c values for GA-SW-70d, GB-SW-70d, GA-SW-14d, and GB-SW-14d samples after 3 days, 14 days, and 28 days of ponding before F-T cycles.

Table 3- 11 Average D_c (x 10^{-12} m^2 s^{-1}) values for concrete samples before F-T cycles

GA-SW-70d							**GB-SW-70d**					
	3 Days		14 Days		28 Days		3 Days		14 Days		28 Days	
Angle	S-1	S-2	S-1	S-2	S-1	S-2	S-1	S-2	S-1	S-2	S-1	S-2
0	0.93	0.89	0.22	0.38	0.30	0.45	0.28	0.98	0.41	0.19	0.29	0.42
60	0.80	0.80	0.85	0.23	0.31	0.22	0.81	0.97	0.09	0.66	0.35	0.37
120	0.32	0.67	0.30	0.30	0.30	0.40	0.70	0.87	0.99	0.87	0.32	0.56
180	0.53	0.50	0.31	0.20	0.20	0.22	0.50	0.86	0.28	0.28	0.29	0.45
Average	0.68		0.35		0.30		0.75		0.47		0.38	
STD	0.20		0.20		0.08		0.23		0.31		0.09	
GA-SW-14d							**GB-SW-14d**					
	3 Days		14 Days		28 Days		3 Days		14 Days		28 Days	
Angle	S-1	S-2	S-1	S-2	S-1	S-2	S-1	S-2	S-1	S-2	S-1	S-2
0	2.76	4.76	1.29	0.55	0.35	0.52	2.70	3.97	0.82	0.85	0.54	0.82
60	2.43	2.45	0.68	0.20	0.25	0.32	3.80	3.11	0.25	0.86	0.29	0.25
120	2.54	3.44	0.70	0.80	0.45	0.62	5.55	5.33	0.64	0.86	0.49	0.68
180	2.43	4.98	0.84	0.55	0.60	0.53	4.22	2.61	0.77	0.71	0.70	0.51
Average	3.22		0.70		0.46		3.91		0.72		0.54	
STD	1.00		0.29		0.13		1.04		0.19		0.18	

*Note: S-1 and S-2 refer to Sample 1 and Sample 2, respectively; STD stands for standard deviation

Extended curing periods result in lower D_c values, reflecting enhanced resistance to chloride ingress due to a denser and more compact matrix, reduced porosity, and permeability from a higher degree of hydration. However, including PVA fibers did not significantly improve resistance to chloride ingress, as PVA fiber-reinforced samples demonstrated higher D_c values than conventional concrete for each curing condition. For the 28-day ponding period, the iodide concentration reached its peak (C_{max}) of 3.9 % in GA-SW-70d and 4.0 % in GB-SW-70d within the surface layers just below the surface (Δx), followed by a gradual decrease at greater depths. In contrast, the iodide concentration peaked at 5.2 % in GA-SW-14d and 5.7 % in GB-SW-14d within Δx.

Figure 3- 8 displays the average concentration profiles and D_c values for the concrete samples in Groups A and B following 3 days, 14 days, and 28 days of ponding after 125 F-T cycles in seawater. Table 3- 12 shows the average D_c values for GA-SW-70d, GB-SW-70d, GA-SW-14d, and GB-SW-14d samples after 3 days, 14 days, and 28 days of ponding after 125 F-T cycles.

Table 3- 12 Average Dc (x 10^{-12} m^2 s^{-1}) values for concrete samples after 125 F-T cycles

GA-SW-70d							**GB-SW-70d**					
	3 Days		14 Days		28 Days		3 Days		14 Days		28 Days	
Angle	S-1	S-2	S-1	S-2	S-1	S-2	S-1	S-2	S-1	S-2	S-1	S-2
0	1.16	1.98	0.72	0.29	0.32	0.30	1.21	1.63	0.46	0.20	0.28	0.83
60	0.13	0.82	0.39	0.22	0.37	0.25	2.41	1.80	0.65	0.70	0.44	0.41
120	0.76	1.02	0.36	0.25	0.20	0.53	0.90	1.59	0.43	0.83	0.27	0.56
180	2.21	0.53	0.23	0.41	0.44	0.21	1.35	1.79	0.37	0.35	0.24	0.25
Average	1.08		0.36		0.33		1.59		0.50		0.41	
STD	0.66		0.15		0.11		0.42		0.20		0.19	
GA-SW-14d							**GB-SW-14d**					
	3 Days		14 Days		28 Days		3 Days		14 Days		28 Days	
Angle	S-1	S-2	S-1	S-2	S-1	S-2	S-1	S-2	S-1	S-2	S-1	S-2
0	4.11	4.13	0.69	1.02	0.45	0.33	3.96	2.12	0.74	0.92	0.67	0.78
60	4.76	2.52	0.76	1.34	0.75	0.56	4.43	4.98	1.81	1.20	0.92	0.94
120	2.11	3.61	1.25	0.82	0.98	0.65	5.23	3.32	1.88	0.94	0.87	0.44
180	4.58	3.31	1.83	1.30	0.79	1.12	4.88	2.88	0.83	0.93	0.79	0.97
Average	3.64		1.13		0.70		3.98		1.16		0.80	
STD	0.89		0.36		0.25		1.04		0.42		0.16	

*Note: S-1 and S-2 refer to Sample 1 and Sample 2, respectively; STD stands for standard deviation

During the 28-day ponding period after 125 F-T cycles in seawater, C_{max} is 4.0 % in GA-SW-70d and 4.53% in GB-SW-70d within Δx, followed by a gradual decrease at greater depths. In contrast, C_{max} is 5.9 % in GA-SW-14d and 6.0 % in GB-SW-14d within Δx.

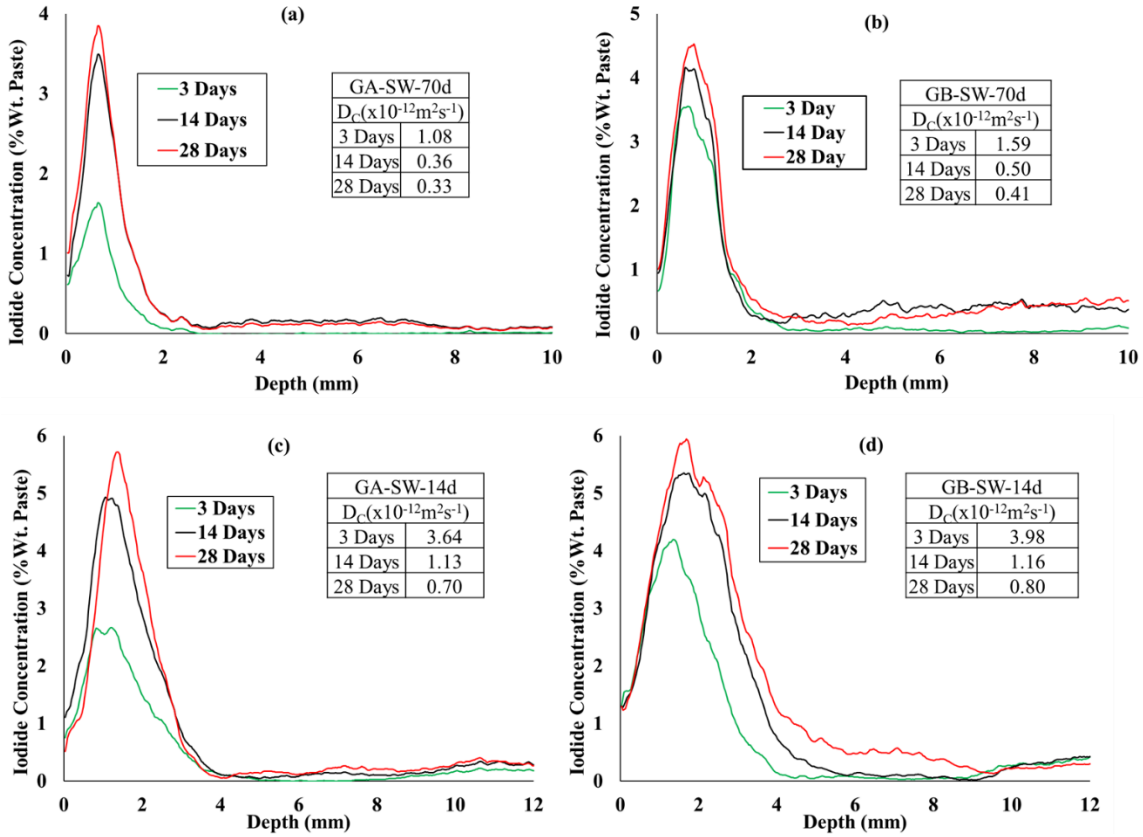

Figure 3- 8 Concentration profiles for the following concrete samples after 125 F-T cycles : (a) GA-SW-70d, (b) GB-SW-70d, (c) GA-SW-14d, and (d) GB-SW-14d.

Figure 3- 9 depicts the average concentration profiles and D_c values for the concrete samples in Groups A and B after 250 F-T cycles in seawater. Table 3- 13 shows the average D_c values for GA-SW-70d, GB-SW-70d, GA-SW-14d, and GB-SW-14d samples after 3 days, 14 days, and 28 days of ponding after 250 F-T cycles.

Table 3- 13 Average D_c (x 10^{-12} m2 s^{-1}) values for concrete samples after 250 F-T cycles

GA-SW-70d							**GB-SW-70d**					
	3 Days		14 Days		28 Days		3 Days		14 Days		28 Days	
Angle	S-1	S-2	S-1	S-2	S-1	S-2	S-1	S-2	S-1	S-2	S-1	S-2
0	2.90	1.73	0.58	0.29	0.30	0.49	1.11	3.43	0.98	0.42	0.42	0.25
60	2.10	2.65	0.31	0.87	0.22	0.12	3.10	1.90	0.60	0.73	0.71	0.42
120	1.70	1.12	0.26	0.35	0.33	0.75	1.00	1.99	0.48	0.53	0.88	0.39
180	1.22	1.38	0.34	0.51	0.65	0.19	0.90	1.49	0.47	0.30	0.54	0.35
Average	1.85		0.44		0.38		1.87		0.56		0.50	
STD	0.61		0.19		0.21		0.89		0.20		0.19	
GA-SW-14d							**GB-SW-14d**					
	3 Days		14 Days		28 Days		3 Days		14 Days		28 Days	
Angle	S-1	S-2	S-1	S-2	S-1	S-2	S-1	S-2	S-1	S-2	S-1	S-2
0	3.11	4.33	1.09	1.19	0.76	0.85	4.92	4.99	1.49	1.19	0.97	0.90
60	4.06	4.02	1.08	1.89	0.67	0.96	5.52	3.98	2.78	1.89	0.78	0.86
120	5.01	5.87	1.62	1.42	0.66	0.83	4.86	4.81	1.62	1.42	0.96	0.93
180	4.58	3.16	0.89	1.98	0.70	1.00	4.88	5.85	0.79	1.98	0.69	1.19
Average	4.27		1.40		0.80		4.98		1.65		0.91	
STD	0.86		0.38		0.12		0.51		0.56		0.14	

*Note: S-1 and S-2 refer to Sample 1 and Sample 2, respectively; STD stands for standard deviation

After undergoing 250 F-T cycles in seawater, C_{max} is 4.0 % in GA-SW-70d and 4.6 % in GB-SW-70d within Δx, with a gradual decrease observed at greater depths. In contrast, the Cmax is 6.0 % in GA-SW-14d and 6.2 % in GB-SW-14d within Δx during the 28-day ponding period. It is important to note that a small concentration peak is observed at a depth of 5.75 mm after the gradual decrease from C_{max} in GB-SW-70d, and at a depth of 5.17 mm in GB-SW-14d. This suggests that Group B experienced more damage after 250 F-T cycles in seawater, likely resulting to the creation of microcracks at greater depths compared to Group A, which allows for the ingress of iodide ions at greater depths.

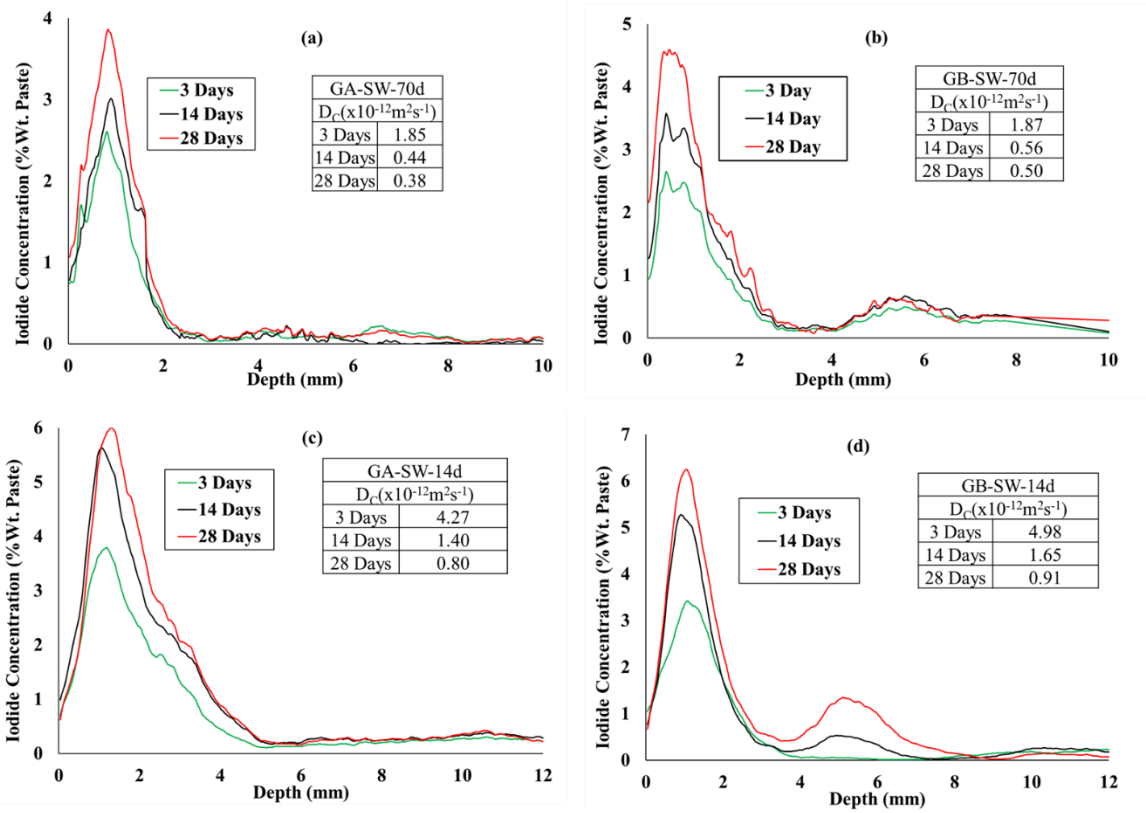

Figure 3- 9 Concentration profiles for the following concrete samples after 250 F-T cycles : (a) GA-SW-70d, (b) GB-SW-70d, (c) GA-SW-14d, and (d) GB-SW-14d.

Figure 3- 10 depicts the average concentration profiles and D_c values for the concrete samples in Groups A and B after 3 days, 14 days, and 28 days of ponding following 375 F-T cycles in seawater. Table 3- 14 shows the average D_c values for GA-SW-70d, GB-SW-70d, GA-SW-14d, and GB-SW-14d samples after 3 days, 14 days, and 28 days of ponding after 375 F-T cycles.

Table 3- 14 Average D_c (x 10^{-12} m2 s^{-1}) values for concrete samples after 375 F-T cycles

GA-SW-70d							**GB-SW-70d**					
	3 Days		14 Days		28 Days		3 Days		14 Days		28 Days	
Angle	S-1	S-2	S-1	S-2	S-1	S-2	S-1	S-2	S-1	S-2	S-1	S-2
0	3.21	2.17	0.51	0.42	0.38	0.39	1.76	0.87	0.70	0.91	0.58	0.88
60	2.34	1.87	0.61	0.66	0.32	0.50	3.23	2.90	0.96	0.56	0.83	0.51
120	2.19	3.10	0.59	0.55	0.40	0.62	1.10	3.10	0.63	0.39	0.34	0.60
180	1.25	1.02	0.71	0.72	0.35	0.54	3.10	2.50	0.30	0.71	0.68	0.45
Average	2.14		0.60		0.44		2.32		0.64		0.61	
STD	0.73		0.10		0.10		0.89		0.21		0.17	
GA-SW-14d							**GB-SW-14d**					
	3 Days		14 Days		28 Days		3 Days		14 Days		28 Days	
Angle	S-1	S-2	S-1	S-2	S-1	S-2	S-1	S-2	S-1	S-2	S-1	S-2
0	4.98	4.98	1.37	1.43	0.70	1.88	4.65	6.62	1.87	1.96	0.99	1.78
60	5.23	5.12	1.81	1.97	0.90	0.71	5.91	5.75	1.98	1.88	1.87	0.95
120	5.23	6.88	1.90	1.45	0.81	0.87	4.93	6.55	1.97	2.37	1.98	1.20
180	5.65	5.92	0.98	1.70	0.87	0.87	5.98	5.76	1.55	1.79	1.25	1.65
Average	5.50		1.58		0.95		5.77		1.92		1.46	
STD	0.61		0.31		0.36		0.65		0.21		0.38	

*Note: S-1 and S-2 refer to Sample 1 and Sample 2, respectively; STD stands for standard deviation

During the 28-day ponding period after 375 F-T cycles, C_{max} is 4.0 % in GA-SW-70d and 5.0 % in GB-SW-70d within Δx, followed by a gradual decrease at greater depths. In contrast, C_{max} is 6.7 % in GA-SW-14d and 8.2 % in GB-SW-14d within Δx. After 350 F-T cycles, higher concentrations of iodide can be observed at greater depths in all concrete samples, similar to the observations after 250 cycles. This suggests that microcracks are likely gradually increasing due to F-T damage with extended cycles across all concrete samples.

It is important to note that the samples subjected to 375 F-T cycles experienced severe scaling, which hindered further investigation of D_c values in extended F-T cycles. The RDME data from Section 3.3 indicates that the samples cured for 14 days were severely damaged after 300 F-T cycles. The D_c values align with the results of the F-T experiments, marking a significant increase in both Group A and Group B samples after 375 cycles. Higher D_c values indicate faster ingress of ions, which is detrimental to concrete. Further discussion on the changes in D_c and the influencing factors will be presented in greater detail in Figure 3- 12.

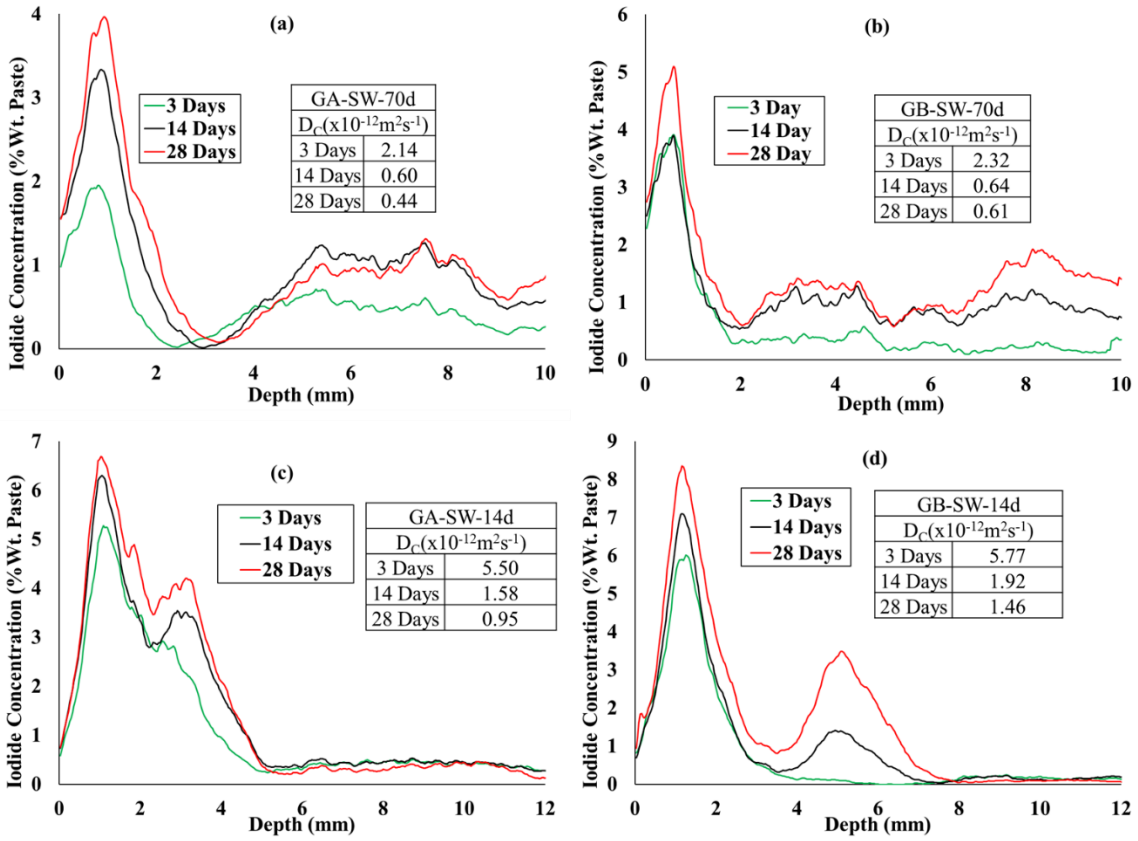

Figure 3- 10 Concentration profiles for the following concrete samples after 375 F-T cycles : (a) GA-SW-70d, (b) GB-SW-70d, (c) GA-SW-14d, and (d) GB-SW-14d.

Figure 3- 11 displays the average concentration profiles and D_c values for the concrete samples in Groups A and B after 3 days, 14 days, and 28 days of ponding following 500 F-T cycles for 70 days of curing periods. Table 3- 15 shows the average D_c values for GA-SW-70d, and GB-SW-70d samples after 3 days, 14 days, and 28 days of ponding after 500 F-T cycles.

Table 3- 15 Average D_c (x 10^{-12} m2 s^{-1}) values for concrete samples after 500 F-T cycles

	GA-SW-70d						**GB-SW-70d**					
	3 Days		14 Days		28 Days		3 Days		14 Days		28 Days	
Angle	S-1	S-2	S-1	S-2	S-1	S-2	S-1	S-2	S-1	S-2	S-1	S-2
0	2.20	3.10	0.82	0.65	0.72	0.29	2.40	2.04	1.22	1.54	0.75	1.02
60	2.90	2.40	0.77	0.87	0.65	0.35	3.67	3.20	2.67	2.11	1.07	1.10
120	1.23	1.98	0.93	0.85	0.55	0.92	2.74	1.20	1.54	1.12	0.98	1.12
180	0.97	2.90	0.71	0.88	0.43	0.44	1.97	2.44	0.97	2.53	1.01	0.87
Average	2.21		0.81		0.54		2.46		1.71		0.99	
STD	0.74		0.09		0.20		0.72		0.61		0.12	

*Note: S-1 and S-2 refer to Sample 1 and Sample 2, respectively; STD stands for standard deviation

Over the 28-day ponding period after 500 F-T cycles, the C_{max} is 5.4 % in GA-SW-70d and 6.3 % in GB-SW-70d within the Δx, followed by a gradual decrease at greater depths. The results from TXM indicate a gradual increase in C_{max} for both sets of concrete during the curing periods, aligning with the trend of increasing D_c. It's evident that C_{max} increased after 500 F-T cycles for all concrete groups, indicating damage caused by the combined effect of F-T cycles and seawater. Group B showed higher C_{max} values for both curing periods, with the 14-day cured samples displaying higher C_{max} than the 70-day cured samples after 375 F-T cycles. This suggests that a higher AEA content in Group A may have outweighed the effect of PVA fibers in Group B. Moreover, the extended curing period seems to improve the concrete's resistance to the combined impact of F-T and seawater.

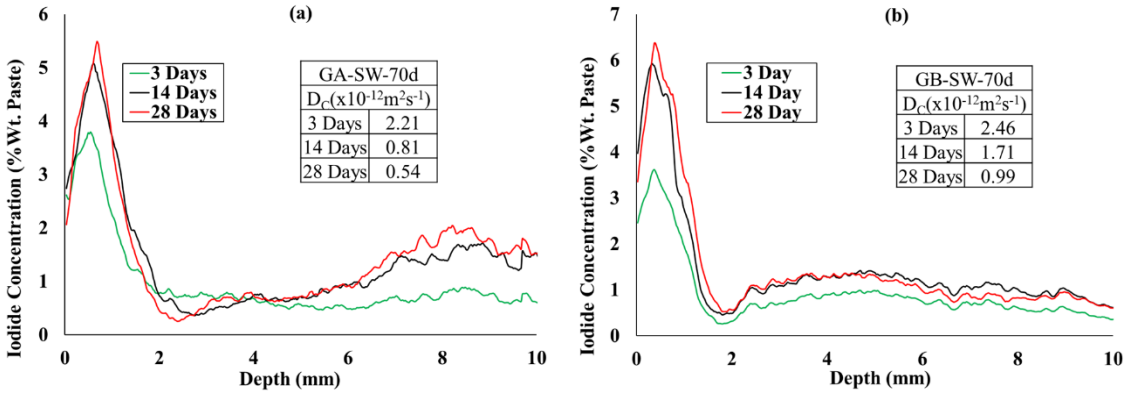

Figure 3- 11 Concentration profiles for the following concrete samples after 500 F-T cycles : (a) GA-SW-70d and (b) GB-SW-70d.

The findings presented in Figure 3- 7 to Figure 3- 11 indicate that the D_c values reached a stable state as the ponding periods were prolonged, which aligns with conclusions from previous research (Behravan et al., 2023, 2021; Rahat et al., 2024). Figure 3- 12 illustrates the percentage change of D_c data for ponding periods lasting 28 days, the maximum duration considered in this study. In Figure 3- 12**,** it is observed that the GA-SW-70d samples showed an 81 % increase after 500 F-T cycles, while the GB-SW-70d samples experienced a 160 % rise in the D_c value. Following 375 F-T cycles, the GA-SW-14d samples displayed a 109 % increase, whereas the GB-SW-14d samples experienced an increase of 173 %. Whereas, GA-SW-70d and GB-SW-70d saw a 46 % and 60 % increase, respectively, after 375 F-T cycles. Examining the changes in D_c values pre and post-F-T cycles reveals significant increases for both concrete sets after consecutive F-T cycles, underscoring the combined impact of F-T cycles and seawater on chloride ingress in concrete. For both the 14-day and 70-day cured samples, Group A demonstrates superior resistance compared to Group B, suggesting that the anticipated impact of PVA fibers on enhancing F-T resistance did not appear as expected. However, this could also be attributed to Group A having an improved air-void system compared to Group B, which may have affected its resistance to F-T cycles. Furthermore, the findings depicted in Figure 3- 12 highlight that samples cured for 14 days exhibit

a greater increase compared to the 70-day cured samples in both concrete groups. Notably, even after undergoing 375 F-T cycles, the GB-SW-14d samples showcase the poorest performance. The superior performance of the 70-day cured samples presents compelling evidence that an extended curing period can improve the chloride ingress properties of concrete in F-T cycling, surpassing the influence of PVA fibers.

In contrast to the F-T cycles in plain water conducted by Rahat et al. (2025), the D_c increased by 32 % for GA-SW-70d and 72 % for GB-SW-70d after 500 F-T cycles compared to the samples subjected to F-T cycles in plain water. After 375 F-T cycles, the D_c increased by 32 % for GA-SW-14d and 60 % for GB-SW-14d compared to the plain water F-T cycles. These results clearly demonstrate that the combined effect of F-T cycles and seawater has a significantly more negative impact on chloride ingress in concrete.

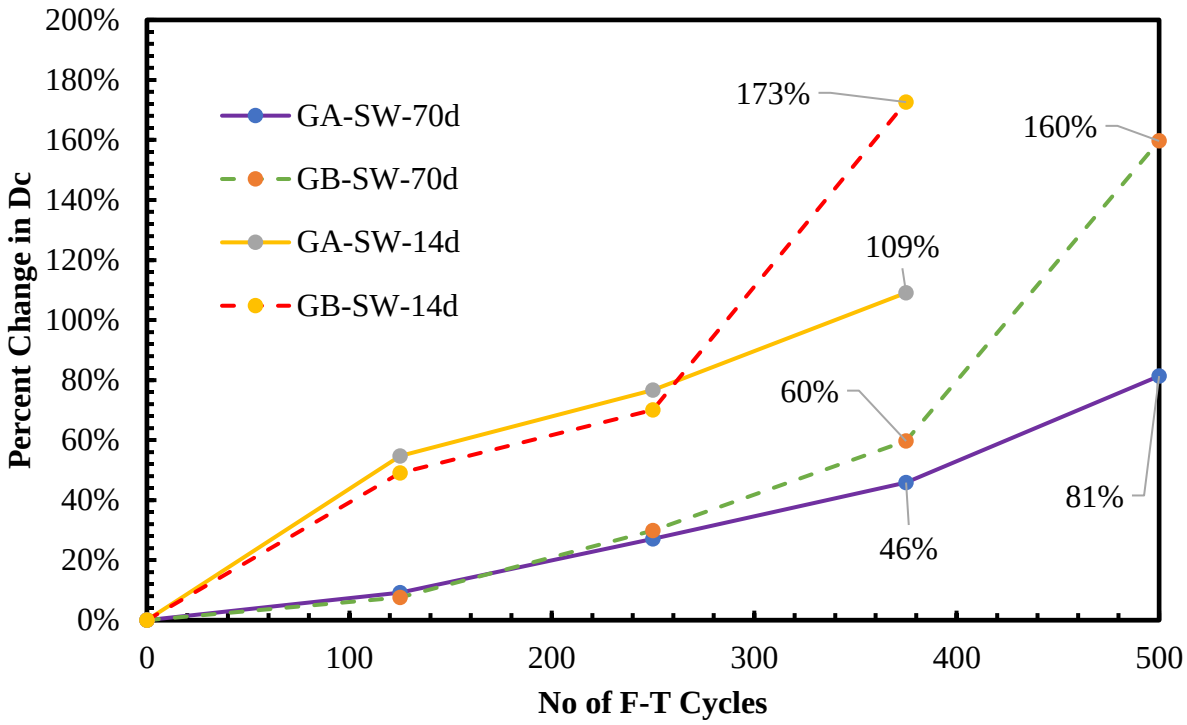

Figure 3- 12 Changes of Dc over F-T cycles for different curing periods.

Analysis from unpaired, two-tailed t-tests indicates there is insufficient evidence to support a statistically significant difference in the D_c values between GA-SW-70d and GB-SW-70d at 3 days, 14 days, and 28 days of ponding, both before and after 500 F-T cycles. Similar findings were noted for the D_c values between GA-SW-14d and GB-SW-14d before and after 375 F-T cycles. However, there was a statistically significant difference between the D_c values for the samples that

were cured for 70 days and 14 days for both Group A and Group B, both before and after 375 F-T cycles, at a significance level of 0.05.

At a 5 % confidence level, there is a statistically significant difference between the D_c values of the 3 days, 14 days, and 28 days of ponding specimens of the same mixture before and after 500 F-T cycles (for GA-SW-70d and GB-SW-70d) using unpaired, two-tailed t-tests. However, there is a statistically significant difference between the D_c values of the 3 days, 14 days, and 28 days of ponding specimens of the same mixture before and after 375 F-T cycles (for GA-SW-14d and GB-SW-14d).

3.5 Conclusions

This study investigated the combined effects of F-T cycles and seawater on chloride ingress in concrete. Two groups of concrete, regular purpose concrete and PVA fiber reinforced concrete, were investigated for two different curing periods (70 days and 14 days). TXM analysis was employed to examine the combined effects of F-T cycles and seawater on the D_c of different concrete samples. Additionally, the study also evaluated UPV, SR, ML, and RDME, leading to the following conclusions:

The addition of PVA fibers did not improve F-T resistance or decrease chloride ingress in concrete as anticipated. Interestingly, Group B displayed higher diffusion rates than Group A, which contradicts earlier studies indicating that fibers enhance durability under F-T conditions. However, the improved air-void system in Group A could be a reason behind Group A's superior performance.

Longer curing periods (70 days) significantly improved resistance to F-T cycles and diffusion mechanisms compared to 14-day cured samples. With an improved air-void system, Group A consistently outperformed Group B in performance indicators such as UPV, SR, and mechanical strengths.

Group A, particularly with extended curing, exhibited lower D_c values, reduced ML, and higher RDME after 300 and 1000 F-T cycles. In addition, TXM revealed that Group A had significantly lower D_c values after exposure to F-T cycles in seawater, confirming its superior resistance to chloride ingress compared to Group B.

The study showed that concrete exposed to F-T cycles in seawater experiences accelerated deterioration compared to plain water, supporting earlier findings while offering new insights into the chloride diffusion coefficient. Seawater exposure notably intensified the damaging effects of F-T cycles, as seen in the marked increase in the D_c values, aligning with other experimental results.

Finally, extended curing durations are recommended to enhance the durability of concrete structures subjected to F-T cycles in coastal environments. Air entrainment remains crucial for improving resistance to chloride ingress and F-T damage, while the anticipated benefits of PVA fibers were not observed under these conditions.

Acknowledgement
This material is based upon work supported by the Broad Agency Announcement Program and the Cold Regions Research and Engineering Laboratory (ERDC-CRREL) under Contract No. W913E522C0001.
The authors express their gratitude to Thien Q. Tran and Dip Banik from Brand's research group in the Department of Civil Engineering at Virginia Tech for their assistance with experimental procedures.

Disclaimer
Any opinions, findings and conclusions or recommendations expressed in this material are those of the author(s) and do not necessarily reflect the views of the Broad Agency Announcement Program and ERDC-CRREL.

References
ASTM C192, 2019. Standard practice for making and curing concrete test specimens in the laboratory, ASTM International, West Conshohocken, PA.

ASTM C173/C173M-16, 2016. Standard test method for air content of freshly mixed concrete by the volumetric method, ASTM International, West Conshohocken, PA.

ASTM C457/C457M-16, 2016. Standard Test Method for Microscopical Determination of Parameters of the Air-Void System in Hardened Concrete, ASTM International, West Conshohocken, PA.

ASTM C39, 2021. Standard test method for compressive strength of cylindrical concrete specimens, ASTM International, West Conshohocken, PA.

ASTM C1202-19. 2019. Standard test method for electrical indication of concrete's ability to resist chloride ion penetration, ASTM International, West Conshohocken, PA.

ASTM C1556, 2016. Standard test method for determining the apparent chloride diffusion coefficient of cementitious mixtures by bulk diffusion, ASTM International, West Conshohocken, PA.

ASTM C293, 2016. Standard test method for flexural strength of concrete (using simple beam with center-point loading), ASTM International, West Conshohocken, PA.

ASTM C597-22, 2022. Standard test method for ultrasonic pulse velocity through concrete, ASTM International, West Conshohocken, PA.

ASTM C666, 2008. Standard test method for resistance of concrete to rapid freezing and thawing, ASTM International, West Conshohocken, PA.

ASTM C215-19, 2019. Standard test method for fundamental transverse, longitudinal, and torsional resonant frequencies of concrete specimens, ASTM International, West Conshohocken, PA.

AASHTO T 358, Standard method of test for surface resistivity indication of concrete's ability to resist chloride ion penetration, American Association of State Highway and Transportation Officials, Washington, DC, 2015.

Andrade, C., Sagrera, J.L. and Sanjuán, M.A., 2001. Several years study on chloride ion penetration into concrete exposed to Atlantic Ocean water. In Proceedings of the RILEM Proc. 19: 2nd International Rilem Workshop on Testing and Modeling the Chloride Ingress into Concrete, C. Andrade and J. Kropp, Eds (Vol. 19, pp. 121-134).

Bai, J., Wild, S., Sabir, B.B., 2003. Chloride ingress and strength loss in concrete with different PC-PFA-MK binder compositions exposed to synthetic seawater. Cem. Concr. Res. 33, 353–362. https://doi.org/10.1016/S0008-8846(02)00961-4

Baloch, W.L., Siad, H., Lachemi, M., Sahmaran, M., 2021. A review on the durability of concrete-to-concrete bond in recent rehabilitated structures. J. Build. Eng. https://doi.org/10.1016/j.jobe.2021.103315

Bao, J., Wei, J., Zhang, P., Zhuang, Z., Zhao, T., 2022a. Experimental and theoretical investigation of chloride ingress into concrete exposed to real marine environment. Cem. Concr. Compos. 130, 104511. https://doi.org/10.1016/j.cemconcomp.2022.104511

Bao, J., Zheng, R., Yu, Z., Zhang, P., Song, Q., Xu, J., Gao, S., 2022b. Freeze-thaw resistance of recycled aggregate concrete incorporating ferronickel slag as fine aggregate. Constr. Build. Mater. 356. https://doi.org/10.1016/j.conbuildmat.2022.129178

Behravan, A., Ley, M.T., Cook, D., Hu, Q., Rywelski, A. and Brorsen, R., 2023. Measuring the Diffusion Coefficient of Paste and Concrete by Using Dental X-ray Equipment. CivilEng., 4(1), pp.224-247. https://doi.org/10.3390/civileng4010014

Behravan, A., Ley, M.T., Rywelski, A. and Berke, N., 2021. Changes in the rate of ion penetration of alternative cementitious materials with time. Mater.& Des., 197, p.109236. https://doi.org/10.1016/j.matdes.2020.109236

Brandt, A.M., 2008. Fibre reinforced cement-based (FRC) composites after over 40 years of development in building and civil engineering. Compos. Struct .86, 3–9. https://doi.org/10.1016/j.compstruct.2008.03.006

Chu, Y., Zhang, D., Liu, H., Wu, X., Zhai, P., Sheng, T., 2022. Experimental study on mechanical properties, acoustic emission characteristics and energy evolution of coal samples after freezing with liquid nitrogen. Fuel 321. https://doi.org/10.1016/j.fuel.2022.123955

Chung, C.W., Shon, C.S., Kim, Y.S., 2010. Chloride ion diffusivity of fly ash and silica fume concretes exposed to freeze-thaw cycles. Constr. Build. Mater. 24, 1739–1745. https://doi.org/10.1016/j.conbuildmat.2010.02.015

Coussy, O., Monteiro, P.J.M., 2008. Poroelastic model for concrete exposed to freezing temperatures. Cem. Concr. Res. 38, 40–48. https://doi.org/https://doi.org/10.1016/j.cemconres.2007.06.006

Costa, A. and Appleton, J., 2002. Case studies of concrete deterioration in a marine environment in Portugal. Cem. Conc. Comp., 24(1), pp.169-179. https://doi.org/10.1016/S0958-9465(01)00037-3

Dabas, M., Martín-Pérez, B., Almansour, H., 2021. Combined Effects of Freeze-Thaw and Corrosion on Performance of RC Structures: State-of-the-Art Review. J. Perform. Constr. Facil. 35. https://doi.org/10.1061/(asce)cf.1943-5509.0001637

De Weerdt, K., Lothenbach, B., Geiker, M.R., 2019. Comparing chloride ingress from seawater and NaCl solution in Portland cement mortar. Cem. Concr. Res. 115, 80–89. https://doi.org/10.1016/j.cemconres.2018.09.014

Diao, B., Sun, Y., Ye, Y. and Cheng, S., 2012. Impact of seawater corrosion and freeze-thaw cycles on the behavior of eccentrically loaded reinforced concrete columns. Oce. Syst. Eng., 2(2), pp.159-171. https://doi.org/10.12989/ose.2012.2.2.159

Diao, B., Zhang, J., Ye, Y., Cheng, S., Eng, P., 2012. Effects of Freeze-Thaw Cycles and Seawater Corrosion on the Behavior of Reinforced Air-Entrained Concrete Beams with Persistent Loads. J. Cold Reg. Eng. 27. https://doi.org/10.1061/(ASCE)CR.1943-5495

Dixon, D.E. et al., 1991. Standard Practice for Selecting Proportions for Normal, Heavyweight, and Mass Concrete (ACI 211.1-91) Chairman, Subcommittee A.

Dousti, A., Moradian, M., Taheri, S.R., Rashetnia, R., Shekarchi, M., 2013. Corrosion Assessment of RC Deck in a Jetty Structure Damaged by Chloride Attack. J. Perform. Construct. Facil. 27, 519–528. https://doi.org/10.1061/(asce)cf.1943-5509.0000348

Du, L., Folliard, K.J., 2005. Mechanisms of air entrainment in concrete. Cem. Concr. Res. 35, 1463–1471. https://doi.org/https://doi.org/10.1016/j.cemconres.2004.07.026

Farnam, Y., Bentz, D., Hampton, A., Weiss, W.J., 2014. Acoustic emission and low-temperature calorimetry study of freeze and thaw behavior in cementitious materials exposed to sodium chloride salt. Transp. Res. Rec. https://doi.org/10.3141/2441-11

Florea, M.V.A., Brouwers, H.J.H., 2012. Chloride binding related to hydration products: Part I: Ordinary Portland Cement. Cem. Concr. Res. 42, 282–290. https://doi.org/10.1016/j.cemconres.2011.09.016

Gao, X.J., Wang, X.Y., 2017. Impacts of globalwarming and sea level rise on service life of chloride-exposed concrete structures. Sustain 9. https://doi.org/10.3390/su9030460

Gao, Z., Wang, L., Wang, Z., Fang, J., 2023. Surface features of frost damaged concrete: A study using multi-point micro displacement laser ranging method. J. Build. Eng. 76, 107051. https://doi.org/10.1016/j.jobe.2023.107051

Gong, F., Jacobsen, S., 2019. Modeling of water transport in highly saturated concrete with wet surface during freeze/thaw. Cem. Concr. Res. 115, 294–307. https://doi.org/https://doi.org/10.1016/j.cemconres.2018.08.013

Gao, X.J., Wang, X.Y., 2017. Impacts of globalwarming and sea level rise on service life of chloride-exposed concrete structures. Sustain 9. https://doi.org/10.3390/su9030460

Hao, L., Liu, Y., Xiao, J., 2021. Durability of recycled aggregate thermal insulation concrete under combined flexural loading and freeze–thaw cycles. Constr. Build. Mater. 272. https://doi.org/10.1016/j.conbuildmat.2020.121652

Imbabi, M.S., Carrigan, C., McKenna, S., 2012. Trends and developments in green cement and concrete technology. Int. J. Sustain. Built Environ. https://doi.org/10.1016/j.ijsbe.2013.05.001

Jacobsen, S., Sœther, D.H., Sellevold, E.J., 1997. Frost testing of high strength concrete: Frost/salt scaling at different cooling rates. Mater. Struct. 30, 33–42. https://doi.org/10.1007/BF02498738

Jang, J.G., Kim, H.K., Kim, T.S., Min, B.J., Lee, H.K., 2014. Improved flexural fatigue resistance of PVA fiber-reinforced concrete subjected to freezing and thawing cycles. Constr. Build. Mater. 59, 129–135. https://doi.org/10.1016/j.conbuildmat.2014.02.040

Jasielec, J.J., Stec, J., Szyszkiewicz-Warzecha, K., Łagosz, A., Deja, J., Lewenstam, A., Filipek, R., 2020. Effective and apparent diffusion coefficients of chloride ions and chloride binding kinetics parameters in mortars: non-stationary diffusion-reaction model and the inverse problem. Mater. 2020; 13: 5522. https://doi.org/10.3390/ma13235522

Jin, H., Cheng, L., Liu, J., Zhong, S., 2024. Investigation of natural diffusion behavior in concrete using iodide replacing chloride ions: The impact of mineral admixtures types and dosages. J. Mater. Res. Technol. 29, 1834–1861. https://doi.org/10.1016/j.jmrt.2024.01.206

Jin, H., Li, Z., Zhang, W., Liu, J., Xie, R., Tang, L., Zhu, J., 2022a. Iodide and chloride ions diffusivity, pore characterization and microstructures of concrete incorporating ground granulated blast furnace slag. J. Mater. Res. Technol. 16, 302–321. https://doi.org/https://doi.org/10.1016/j.jmrt.2021.11.155

Kessler, S., Thiel, C., Grosse, C.U., Gehlen, C., 2017. Effect of freeze–thaw damage on chloride ingress into concrete. Mater. And Struc. 50. https://doi.org/10.1617/s11527-016-0984-4

Kim, R., Min, J., Ahn, E., Choi, H., 2022. Assessment of degradation index in freeze-thaw damaged concrete using multi-channel contactless ultrasound. Constr. Build. Mater. 349. https://doi.org/10.1016/j.conbuildmat.2022.128815

Kessler, S., Thiel, C., Grosse, C.U., Gehlen, C., 2017. Effect of freeze–thaw damage on chloride ingress into concrete. Mater. And Struc. 50.https://doi.org/10.1617/s11527-016-0984-4

Ley, M.T., Parestegari, N., Behravan, A., Cook, D. and Hu, Q., 2023. Measuring concrete permeability with CHIP. Final report for NCHRP IDEA Project 232. Oklahoma State University, National Cooperative Highway Research Program (NCHRP), Innovations Deserving Exploratory

Analysis (IDEA) Programs, Transportation Research Board, National Academies of Sciences, Engineering, and Medicine.

Li, X., Sun, G., 2024. Optimal freeze-thaw resistance air-entrained concrete with designed nanoparticle 90 ortland 90 d bubble system. Constr. Build. Mater. 435, 136769. https://doi.org/https://doi.org/10.1016/j.conbuildmat.2024.136769

Lin, H., Han, Y., Liang, S., Gong, F., Han, S., Shi, C., Feng, P., 2022a. Effects of low temperatures and cryogenic freeze-thaw cycles on concrete mechanical properties: A literature review. Constr. Build. Mater. 345. https://doi.org/10.1016/j.conbuildmat.2022.128287

Lindvall, A., 2007. Chloride ingress data from field and laboratory exposure – Influence of salinity and temperature. Cem. Concr. Compos. 29, 88–93. https://doi.org/10.1016/j.cemconcomp.2006.08.004

Liu, K., Yan, J., Hu, Q., Sun, Y., Zou, C., 2016. Effects of parent concrete and mixing method on the resistance to freezing and thawing of air-entrained recycled aggregate concrete. Constr. Build. Mater. 106, 264–273. https://doi.org/10.1016/j.conbuildmat.2015.12.074

Liu, J., Liao, C., Jin, H., Jiang, Z., Xie, R., Tang, L., 2022. Electrically driven ionic transport in the RCM and RIM: Investigations based on experiments and numerical simulations. Constr. Build. Mater. 331, 127331. https://doi.org/10.1016/j.conbuildmat.2022.127331

Liu, L., Shen, D., Chen, H., Sun, W., Qian, Z., Zhao, H., Jiang, J., 2014. Analysis of damage development in cement paste due to ice nucleation at different temperatures. Cem. Concr. Compos. 53, 1–9. https://doi.org/https://doi.org/10.1016/j.cemconcomp.2014.06.007

Liu, L., Ye, G., Schlangen, E., Chen, H., Qian, Z., Sun, W., van Breugel, K., 2011. Modeling of the internal damage of saturated cement paste due to ice crystallization pressure during freezing. Cem. Concr. Compos. 33, 562–571. https://doi.org/https://doi.org/10.1016/j.cemconcomp.2011.03.001

Lu, Z., Feng, Z. gang, Yao, D., Li, X., Ji, H., 2021. Freeze-thaw resistance of ultra-high performance concrete: Dependence on concrete composition. Constr. Build. Mater. 293. https://doi.org/10.1016/j.conbuildmat.2021.123523

Luo, S., Bai, T., Guo, M., Wei, Y., Ma, W., 2022. Impact of freeze–thaw cycles on the long-term performance of concrete pavement and related improvement measures: A review. Mater. https://doi.org/10.3390/ma15134568

Ma, D., Zhang, M., Cui, J., 2023. A review on the deterioration of mechanical and durability performance of marine-concrete under the scouring action. J. Build. Eng. 66, 105924. https://doi.org/https://doi.org/10.1016/j.jobe.2023.105924

Moradllo, M.K. and Ley, M.T., 2017a. Quantitative measurement of the influence of degree of saturation on ion penetration in cement paste by using X-ray imaging. Constr. Build. Mater., 141, pp.113-129. https://doi.org/10.1016/j.conbuildmat.2017.03.007

Moradllo, M.K. and Ley, M.T., 2017b. Comparing ion diffusion in alternative cementitious materials in real time by using non-destructive X-ray imaging. Cem. Concr. Compos., 82, pp.67-79. https://doi.org/10.1016/j.cemconcomp.2017.05.014

Moradllo, M.K., Hu, Q. and Ley, M.T., 2017. Using X-ray imaging to investigate in-situ ion diffusion in cementitious materials. Constr. Build. Mater., 136, pp.88-98. https://doi.org/10.1016/j.conbuildmat.2017.01.038

Moradi-Marani, F., Shekarchi, M., Dousti, A. and Mobasher, B., 2010. Investigation of corrosion damage and repair system in a concrete jetty structure. J. Perform. Construct. Facil. 24(4), pp.294-301. https://doi.org/10.1061/(ASCE)CF.1943-5509.0000112

Mu, R., Miao, C., Luo, X., Sun, W., 2002. Interaction between loading, freeze–thaw cycles, and chloride salt attack of concrete with and without steel fiber reinforcement. Cem. Concr. Res. 32, 1061–1066. https://doi.org/https://doi.org/10.1016/S0008-8846(02)00746-9

Nili, M., Zaheri, M., 2011. Deicer salt-scaling resistance of non-air-entrained roller-compacted concrete pavements. Constr. Build. Mater. 25, 1671–1676. https://doi.org/https://doi.org/10.1016/j.conbuildmat.2010.10.004

Noushini, A., Samali, B., Vessalas, K., 2013a. Effect of polyvinyl alcohol (PVA) fibre on dynamic and material properties of fibre reinforced concrete. Constr. Build. Mater. 49, 374–383. https://doi.org/10.1016/j.conbuildmat.2013.08.035

Noushini, A., Vessalas, K., Ghosni, N., Samali, B., 2013b. Effect of polyvinyl alcohol fibre and fly ash on flexural tensile properties of concrete, in: From Materials to Structures: Advancement Through Innovation – Proceedings of the 22nd Australasian Conference on the Mechanics of Structures and Materials, ACMSM 2012. Pp. 1165–1170. https://doi.org/10.1201/b15320-207

Pruckner, F., Gjørv, O.E., 2004. Effect of CaCl2 and NaCl additions on concrete corrosivity. Cem. Concr. Res. 34, 1209–1217. https://doi.org/10.1016/j.cemconres.2003.12.015

Peng, R. xin, Qiu, W. liang, Teng, F., 2022. Investigation on seawater freeze-thaw damage deterioration of marine concrete structures in cold regions from multi-scale. Ocean. Eng. 248. https://doi.org/10.1016/j.oceaneng.2022.110867

Qaidi, S.M.A., Dinkha, Y.Z., Haido, J.H., Ali, M.H., Tayeh, B.A., 2021. Engineering properties of sustainable green concrete incorporating eco-friendly aggregate of crumb rubber: A review. J. Clean. Prod. 324, 129251. https://doi.org/https://doi.org/10.1016/j.jclepro.2021.129251

Qin, L., Zhai, C., Xu, J., Liu, S., Zhong, C., Yu, G., 2019. Evolution of the pore structure in coal subjected to freeze−thaw using liquid nitrogen to enhance coalbed methane extraction. J Pet Sci Eng 175, 129–139. https://doi.org/10.1016/j.petrol.2018.12.037

Rahat, M.H.H., Annand, D.M., Atwood, P., Behravan, A., Brand, A.S., 2024. Effect of Freeze/Thaw and Substrate Moisture Condition on the Concrete Repair-Substrate Interface, in:

Barman, M., Brink, A.-C. (Eds.), 13th International Conference on Concrete Pavements. Minneapolis, pp. 412–427.

Rahat, M.H.H., Tran, T.Q., Banik, D., Brand, A.S., 2025. Effects of polyvinyl alcohol fibers and curing duration on chloride ingress in concrete during freeze-thaw cycles. J. Build. Eng. (Under Review)

Rabi, M., Shamass, R., Cashell, K.A., 2022. Structural performance of stainless steel reinforced concrete members: A review. Constr. Build. Mater. https://doi.org/10.1016/j.conbuildmat.2022.126673

Reiterman, P., Keppert, M., 2020. Effect of various de-icers containing chloride ions on scaling resistance and chloride penetration depth of highway concrete. Roads and Bridges-Drogi I Mosty 19, 51–64. https://doi.org/10.7409/rabdim.020.003

Şahin, H.G., Mardani, A., Özen, S., Emin, A., 2023. Utilization of high-range water reducing admixture having air-entraining agents in cementitious systems. J. Build. Eng. https://doi.org/10.1016/j.jobe.2022.105565

Şahin, Y., Akkaya, Y., Taşdemir, M.A., 2021. Effects of freezing conditions on the frost resistance and microstructure of concrete. Constr. Build. Mater. 270. https://doi.org/10.1016/j.conbuildmat.2020.121458

Sang, Y., Pan, Y., Ying, W., Yang, Y., 2022. Assessment of mechanical performance and ice content of concrete at low temperature using impact-echo method. Constr. Build. Mater. 346. https://doi.org/10.1016/j.conbuildmat.2022.128286

Sarsembayeva, A., Zhussupbekov, A., 2021. Experimental study of deicing chemical redistribution and moisture mass transfer in highway subsoils during the unidirectional freezing. Transp. Geotec. 26. https://doi.org/10.1016/j.trgeo.2020.100426

Shah, H.A., Yuan, Q., Zuo, S., 2021. Air entrainment in fresh concrete and its effects on hardened concrete-a review. Constr. Build. Mater.. https://doi.org/10.1016/j.conbuildmat.2020.121835

Shang, H.S., Song, Y.P., 2006. Experimental study of strength and deformation of plain concrete under biaxial compression after freezing and thawing cycles. Cem. Concr. Res. 36, 1857–1864. https://doi.org/10.1016/j.cemconres.2006.05.018

Siegert, M., Alley, R.B., Rignot, E., Englander, J., Corell, R., 2020. Twenty-first century sea-level rise could exceed IPCC projections for strong-warming futures. One Ear. https://doi.org/10.1016/j.oneear.2020.11.002

Skripkiunas, G., Nagrockiene, D., Girskas, G., Vaičiene, M., Baranauskaite, E., 2013. The cement type effect on freeze – Thaw and deicing salt resistance of concrete, in: Procedia Eng. Elsevier Ltd, pp. 1045–1051. https://doi.org/10.1016/j.proeng.2013.04.132

Sun, L.F., Jiang, K., Zhu, X., Xu, L., 2020. An alternating experimental study on the combined effect of freeze-thaw and chloride penetration in concrete. Constr. Build. Mater. 252. https://doi.org/10.1016/j.conbuildmat.2020.119025

Sun, M., Xin, D., Zou, C., 2019. Damage evolution and plasticity development of concrete materials subjected to freeze-thaw during the load process. Mech. Of Mater. 139, 103192. https://doi.org/https://doi.org/10.1016/j.mechmat.2019.103192

Scherer, G.W., 1993. Freezing gels. J. Non. Cryst. Solids 155, 1–25. https://doi.org/10.1016/0022-3093(93)90467-C

Sun, M., Xin, D., Zou, C., 2019. Damage evolution and plasticity development of concrete materials subjected to freeze-thaw during the load process. Mech. Mater. 139, 103192. https://doi.org/https://doi.org/10.1016/j.mechmat.2019.103192

Tennakoon, C., Shayan, A., Sanjayan, J.G., Xu, A., 2017. Chloride ingress and steel corrosion in geopolymer concrete based on long term tests. Mater. Des. 116, 287–299. https://doi.org/10.1016/j.matdes.2016.12.030

Thong, C.C., Teo, D.C.L., Ng, C.K., 2016. Application of polyvinyl alcohol (PVA) in cement-based composite materials: A review of its engineering properties and microstructure behavior. Constr. Build. Mater.. https://doi.org/10.1016/j.conbuildmat.2015.12.188

Tian, Y., Zhang, G., Ye, H., Zeng, Q., Zhang, Z., Tian, Z., Jin, X., Jin, N., Chen, Z., Wang, J., 2023. Corrosion of steel rebar in concrete induced by chloride ions under natural environments. Constr. Build. Mater.. https://doi.org/10.1016/j.conbuildmat.2023.130504

Tikalsky, P.J., Pospisil, J., MacDonald, W., 2004. A method for assessment of the freeze-thaw resistance of preformed foam cellular concrete. Cem. Concr. Res. 34, 889–893. https://doi.org/10.1016/j.cemconres.2003.11.005

Ting, M.Z.Y., Wong, K.S., Rahman, M.E., Meheron, S.J., 2021. Deterioration of marine concrete exposed to wetting-drying action. J. Clean. Prod. https://doi.org/10.1016/j.jclepro.2020.123383

Valenza, J.J., Scherer, G.W., 2007. A review of salt scaling: I. Phenomenology. Cem. Concr. Res. 37, 1007–1021. https://doi.org/https://doi.org/10.1016/j.cemconres.2007.03.005

Wang, R., Hu, Z., Li, Y., Wang, K., Zhang, H., 2022. Review on the deterioration and approaches to enhance the durability of concrete in the freeze–thaw environment. Constr. Build. Mater. https://doi.org/10.1016/j.conbuildmat.2022.126371

Wang, Y., Cao, Y., Zhang, P., Ma, Y., Zhao, T., Wang, H., Zhang, Z., 2019. Water absorption and chloride diffusivity of concrete under the coupling effect of uniaxial compressive load and freeze–thaw cycles. Constr. Build. Mater. 209, 566–576. https://doi.org/10.1016/j.conbuildmat.2019.03.091

Xiao, J., Lu, D., Ying, J., 2013. Durability of recycled aggregate concrete: An overview. J. Adv. Concr. Technol.. https://doi.org/10.3151/jact.11.347

Xu, J., Jiang, L., Wang, W., Jiang, Y., 2011. Influence of CaCl2 and NaCl from different sources on chloride threshold value for the corrosion of steel reinforcement in concrete. Constr. Build. Mater. 25, 663–669. https://doi.org/10.1016/j.conbuildmat.2010.07.023

Yan, L., Jenkins, C.H. and Pendleton, R.L., 2000. Polyolefin fiber-reinforced concrete composites: Part I. Damping and frequency characteristics. Cem. Concr. Res., 30(3), pp.391-401. .https://doi.org/10.1016/S0008-8846(99)00267-7

Yew, M.K., Bin Mahmud, H., Ang, B.C., Yew, M.C., 2015. Effects of low volume fraction of polyvinyl alcohol fibers on the mechanical properties of oil palm shell lightweight concrete. Adv. Mater. Sci. Eng 2015. https://doi.org/10.1155/2015/425236

Yi, Y., Zhu, D., Guo, S., Zhang, Z., Shi, C., 2020. A review on the deterioration and approaches to enhance the durability of concrete in the marine environment. Cem. Concr. Compos. 113. https://doi.org/10.1016/j.cemconcomp.2020.103695

Zhang, G., Yu, H., Li, H., Yang, Y., 2019. Experimental study of deformation of early age concrete suffering from frost damage. Constr. Build. Mater. 215, 410–421. https://doi.org/10.1016/j.conbuildmat.2019.04.187

Zhang, P., Cong, Y., Vogel, M., Liu, Z., Müller, H.S., Zhu, Y., Zhao, T., 2017a. Steel reinforcement corrosion in concrete under combined actions: The role of freeze-thaw cycles, chloride ingress, and surface impregnation. Constr. Build. Mater. 148, 113–121. https://doi.org/10.1016/j.conbuildmat.2017.05.078

Zhang, P., Wittmann, F.H., Lura, P., Müller, H.S., Han, S., Zhao, T., 2018. Application of neutron imaging to investigate fundamental aspects of durability of cement-based materials: A review. Cem. Concr. Res. https://doi.org/10.1016/j.cemconres.2018.03.003

Zhang, P., Wittmann, F.H., Vogel, M., Müller, H.S., Zhao, T., 2017b. Influence of freeze-thaw cycles on capillary absorption and chloride penetration into concrete. Cem. Concr. Res. 100, 60–67. https://doi.org/10.1016/j.cemconres.2017.05.018

Chapter 4. Effects of cellulose nanofiber gels on the chloride ingress and freeze/thaw properties of cement paste[3]

The contributions of the authors to this manuscript are described as follows:

Md Hasibul Hasan Rahat: Conceptualization, Methodology, Formal analysis, Investigation, Writing–original draft; Writing–review and editing.

Kaushanie Gunarathne: Methodology, Formal analysis, Investigation, Writing–review and editing;

Thomas S. Carnes: Writing–review and editing, Methodology, Investigation, Formal analysis;

Benjamin S. Hsiao: Resources, Writing–review and editing, Supervision, Project administration, Funding acquisition;

Alexander S. Brand: Conceptualization, Writing–review and editing, Writing–original draft, Supervision, Project administration, Methodology, Funding acquisition.

[3] **Rahat, M.H.H.,** Gunarathne, K., Carnes, T.S., Hsiao, B.S., & Brand, A.S. (2025). Effect of Cellulose Nanofiber Gels on the Chloride Ingress and Freeze/Thaw Properties of Cementitious Paste. *Construction and Building Materials*. 472, 2025, 140997. https://doi.org/10.1016/j.conbuildmat.2025.140997

Effects of cellulose nanofiber gels on the chloride ingress and freeze/thaw properties of cement paste

Md. Hasibul Hasan Rahat,[1*] Kaushanie Gunarathne,[2] Thomas S. Carnes,[1]

Benjamin S. Hsiao,[2] and Alexander S. Brand[1,3,4*]

[1] The Charles E. Via, Jr. Department of Civil and Environmental Engineering, Virginia Polytechnic Institute and State University, Blacksburg, Virginia 24061, USA

[2]Department of Chemistry, Stony Brook University, Stony Brook, New York 11794, USA

[3] Department of Materials Science and Engineering, Virginia Polytechnic Institute and State University, Blacksburg, Virginia 24061, USA

[4] Myers-Lawson School of Construction, Virginia Polytechnic Institute and State University, Blacksburg, Virginia 24061, USA

* Corresponding authors: rahatm21@vt.edu (MHH. Rahat) and asbrand@vt.edu (AS. Brand)

4.1 Abstract

The issues of freeze/thaw and chloride ingress pose key durability concerns for concrete materials. This study investigated the effects of cellulose nanofiber (CNF) gels on cement paste's freeze/thaw durability and chloride ingress. Paste specimens were created by replacing water in the mixture with nitro-oxidized CNF suspensions, which form hydrogels in the presence of metal ions (*e.g.*, Na^+, Ca^{2+}) in the pore solution. Three different CNF sources at concentrations of 1% or 2% by mass of water were studied. It was found that specimens containing CNF suspensions exhibited improved freeze/thaw resistance characteristics when compared to specimens without CNF suspensions. In addition, transmission X-ray microscopy was used to determine diffusion coefficients, and it was found that specimens containing CNF suspensions had lower or comparable diffusion coefficients compared to those without CNF suspensions. For instance, after 14 days of ponding, the CP specimen exhibited a diffusion coefficient of 0.39×10^{-12} m^2 s^{-1}, while specimens with CNF-1 and CNF-3 had values of 0.16×10^{-12} m^2 s^{-1} and 0.33×10^{-12} m^2 s^{-1}, respectively, corresponding to approximately 59% and 15% lower than the value of CP. However, CNF suspensions prepared from different feedstocks did not yield similar results, so further study is required to establish what CNF characteristics are necessary to yield maximum benefit.

Keywords: Freeze/thaw resistance, Transmission X-ray microscopy, Cellulose nanofiber gels, Calorimetry, Diffusion coefficients

4.2 Introduction

In regions subject to temperatures below freezing, freeze/thaw cycling poses a durability issue for concrete materials [1–3]. Damage can accumulate with each cycle of freezing and thawing, and, over time, degradation of the concrete often occurs [1,4]. To mitigate the amount of damage or to

reduce the rate of damage accumulation, different methods are typically employed. Air entrainment and the incorporation of supplementary cementitious materials are two predominant approaches to improving the microstructural integrity of concrete to address the problem [1].

In addition to freeze/thaw, chloride ingress can also cause degradation in concrete structures as it contributes to the acceleration of steel reinforcement corrosion [5–7]. Specifically, chloride ingress is a major concern when concretes are exposed to saltwater conditions, such as near the ocean, or when subjected to deicing salts [1,8]. In order to reduce the risk of reinforcement corrosion, traditional preventative measures, such as partial replacement of 97 ortland cement with supplementary cementitious materials and reducing the water to cementitious material ratio, are often undertaken to reduce the chloride ion diffusion rate [8].

The combined degradation of freeze/thaw and chloride-induced corrosion in concrete materials is typically encountered in northern coastal regions, where deicing chemicals are used and the environment can be dense with saltwater exposure [9,10]. As a result, infrastructure containing reinforced concrete can become highly vulnerable to freeze/thaw cycles, and the embedded steel can be exposed and subjected to corrosion [11]. Chloride ion ingress, from sources such as deicing salts, further accelerates corrosion and jeopardizes structural integrity [12,13].

The diffusion coefficient (Dc) is crucial in quantifying ion mobility within materials [13]. In the context of concrete mixtures, the ion transport rate is typically evaluated using methods such as ASTM C1202, ASTM C1556, and AASHTO T358, with ASTM C1556 being one of the few standards that provides a quantitative measure of Dc. However, the destructive nature and prolonged duration of ASTM C1556 testing have urged a rapid, more economical, and non-destructive alternative. Transmission X-ray microscopy (TXM) has recently emerged as an innovative imaging technique for cementitious materials, effectively overcoming the limitations of traditional destructive or correlational methods [14–16]. By analyzing variations in gray value of X-ray radiographs, TXM offers direct, practical, and realistic insights into ion transport behavior, enabling the efficient and time-dependent determination of the Dc in cement-based materials [17,18].

In addition to more traditional measures to reduce damage in concrete materials caused by freeze/thaw action and chloride ingress, other methods have also been suggested. One approach is the use of nanocellulose products, including cellulose nanofibers (CNF) [19], cellulose nanocrystals (CNC) and nanofibrils [20,21], and cellulose/polyvinyl alcohol hydrogel [22], as nanoscale additives that can simultaneously enhance the mechanical properties and reduce the volume change due to ice crystallization. For example, several recent studies have investigated the inclusion of CNF into the concrete matrix [23–27], and the results indicated that the inclusion of CNF in concretes led to improved freeze/thaw performance, such as decreased mass loss, when compared to specimens that did not contain CNF [24,25]. In addition to the freeze/thaw resistance, it has also been reported that mortar incorporating CNF was less susceptible to chloride penetration when compared to mortar without CNF [28]. Furthermore, several studies have examined the strength of cementitious materials containing CNF and reported the increase in mechanical

strengths compared to those without CNF [20,23,24,29]. Some studies also reported that the setting time of concrete containing nanocellulose could increase compared to those without CNF [23,29]. Additionally, the inclusion of cellulose nanocrystals has been observed to reduce porosity and permeability [30], although other studies did not find this to be the case [20,31]. However, none of these studies considered that nitro-oxidized CNF suspensions, which are negatively charged, can produce hydrogel in the presence of metal ions, and are promising as anti-freezing agents [32–34].

Conventional CNFs, typically used in a dry or dispersed state, are relatively longer and more flexible, yet they may not form a continuous network independently, while CNCs, on the other hand, are much shorter and rigid, which limits their ability to create the interconnected structure needed to modify the microstructure effectively [35]. In contrast, a CNF gel is produced when a nitro-oxidized negatively charged CNF suspension undergoes gelation through metal ion-triggered cross-linking, resulting in a continuous three-dimensional network [33,34,36]. Although previous studies have incorporated small amounts (0.1 to 5 weight percent of cement) of CNFs or CNCs to enhance freeze/thaw resistance and reduce chloride ingress [20,21,23–27], they do not separate the specific impact of nanocellulose on durability. This study completely replaces the mixing water from the mix design with a nitro-oxidized CNF suspension that forms a robust gel network within the cement paste matrix by cross-linking in the presence of metal ions (*e.g.*, Na^+, Ca^{2+}) that exist in the cement paste pore solution. This gel network in the cement matrix can lower the freezing point of the pore solution, which can better resist freeze/thaw cycles, and improve the microstructure, which can reduce chloride ingress rate in the matrix.

4.2.1 Significance of the study

The significance of the study lies in its novel approach of completely replacing water in a cementitious paste with a negatively charged nitro-oxidized CNF suspension to investigate their effects on the freeze/thaw durability, an aspect not explored in the literature. By utilizing metal ion-triggered crosslinking, the CNF suspension rapidly forms a hydrogel within the cement matrix, which can enhance freeze/thaw durability and reduce chloride ingress, addressing key challenges in cold region infrastructures. Moreover, TXM for non-destructive quantification of chloride ingress provides unique insights into ion transport within these innovative composites. Overall, this work deepens the understanding of cementitious material behavior and paves the way for developing more sustainable and resilient concrete solutions.

4.3 Experimental design

4.3.1 Preparation and characterization of CNF

4.3.1.1 Preparation of CNF

Carboxylated CNF were prepared from three different raw lignocellulose biomass feedstocks using a zero-waste nitro-oxidation process (NOP) according to earlier studies [36,37]. The three feedstocks were a sugarcane bagasse obtained from a farm in Brazil, cabbage obtained from a local grocery store in Long Island, New York, USA, and jute obtained from Toptrans Bangladesh Ltd,

Bangladesh. Briefly, 1 g of the ground feedstock sample was soaked in 14 mL of 65 % HNO_3, followed by addition of 1 g of NaNO2. Upon addition of NaNO2, the round bottom reactor was immediately sealed to prevent the loss of Nox fumes created by the reaction. The reactor was held at 50 ℃ for 9 h, then quenched with 250 mL of deionized water. The supernatant was decanted 2 to 3 times before being washed by centrifugation at 5000 relative centrifugal force for 10 min to a pH level equal to or greater than 2.5. The treated fibers were dialyzed using deionized water until there was no further change in conductivity within 24 h. To yield carboxylate functional groups, fiber slurries were treated with NaHCO3 until the pH value of the suspension reached 7.5. The treated carboxylated cellulose microfibers were subsequently dialyzed using deionized water until there was no longer a change in conductivity within 24 h. The slurry was passed through a homogenizer at 250 bar for 1 pass to defibrillate the electro-swollen microfibers into nanofibers.

4.3.1.2 Potentiometric titration measurements of CNFs

The carboxylate content (COO- groups) and degree of oxidation (DO) in CNF was determined using the potentiometric titration method. In this method, ~0.5 g of freeze-dried CNF sample was dispersed in 70 mL of distilled water. Subsequently, 5 mL of 0.01 M NaCl and 5 mL of 0.05 M HNO_3 were added to the suspension and stirred overnight. A blank sample was also prepared at the same composition but without nanofibers. Both solutions were titrated with 0.05 M NaOH at a rate of 2 mL min^{-1}. The carboxylate content of CNF was calculated using the following equation:

$$DO\ (mmol\ g^{-1}) = \frac{\Delta V_{NaOH}\ *\ C_{NaOH}}{m_{sample}} * 1000 \qquad (1)$$

where ΔV_{NaOH} is the volumetric consumption of NaOH to neutralize oxidized cellulose (L), C_{NaOH} is concentration of NaOH (mol L^{-1}), and m_{sample} is the mass of freeze-dried sample (g). *Figure 4-1* shows the potentiometric titration curves of the blank and CNFs extracted from sugarcane bagasse, cabbage, and jute. The DO values of CNFs from sugarcane bagasse, cabbage, and jute biomasses were 1.39 mmol g^{-1}, 1.35 mmol g^{-1}, and 1.51 mmol g^{-1}, respectively.

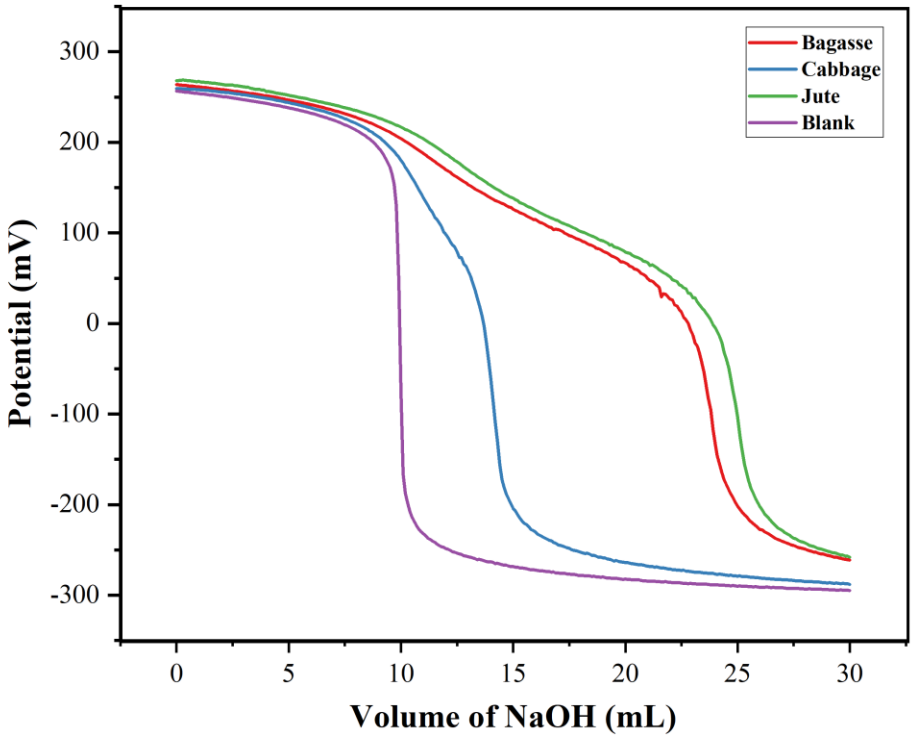

Figure 4- 1 Potentiometric titration curves of blank, CNF extracted from sugarcane bagasse, cabbage, and jute.

4.3.1.3 Fourier transformation infrared spectroscopy (FTIR)

The FTIR curves were recorded using a Thermo Fisher Scientific instrument covering the range from 600 cm^{-1} to 3500 cm^{-1}. For the analysis, freeze-dried solid samples were used in attenuated total reflectance (ATR) mode. *Figure 4- 2* illustrates the FTIR spectra for extracted CNFs. The spectrum analysis displayed a significant peak around 1725 cm^{-1}, which indicates the presence of carbonyl stretching (–C=O) typically found in oxidized cellulose.

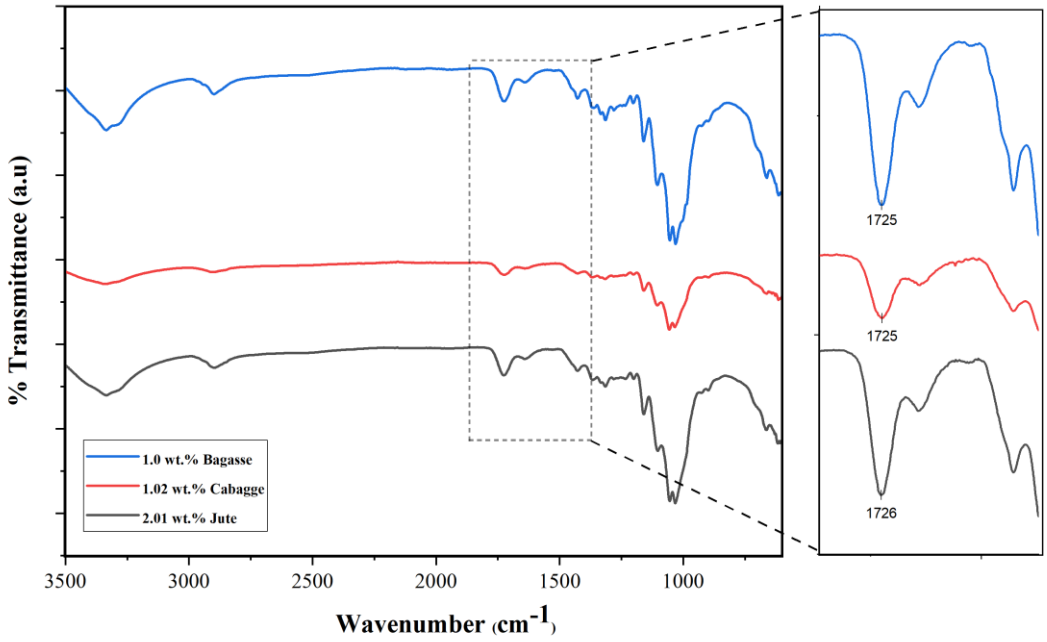

Figure 4- 2 FTIR spectra of extracted carboxycellulose nanofibers.

4.3.1.4 Transmission electron microscopy (TEM)

TEM measurements of CNFs were carried out using a JEOL JEM-1400 LaB_6 120 kV TEM at the Center for Functional Nanomaterials at Brookhaven National Laboratory. The TEM was operated at an accelerating voltage of 120 kV. For sample preparation, a 0.22 µL aliquot of a 0.1 wt.% homogenized CNF sample was deposited on freshly glow-discharged carbon-coated grids (200 mesh), followed by a 0.5 wt.% aqueous uranyl acetate solution to stain the sample. *Figure 4- 3* shows TEM images of CNFs derived from different feedstocks. The average fiber widths of CNFs from sugarcane bagasse, cabbage and jute were 4.44 nm ± 0.57 nm, 3.37 nm ± 0.23 nm, and 4.60 nm ± 0.80 nm, respectively, based on measurements of 20 nanofibers.

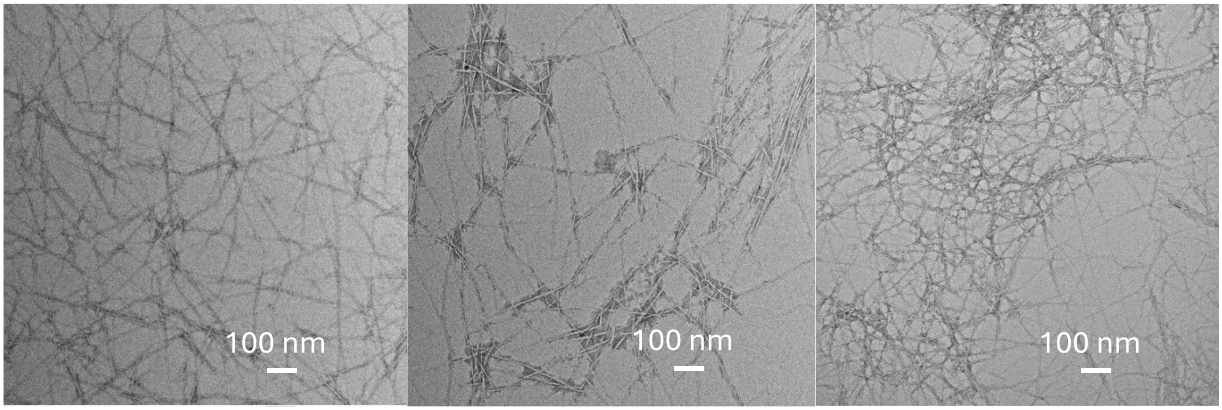

Figure 4- 3 TEM image of CNFs extracted from bagasse (left), cabbage (middle), and jute (right).

4.3.2 Cement specimen preparation and material properties

In this study, a cement paste using Type I/II ordinary 102ortland cement with a 0.5 water-to-cement ratio was employed for all specimens. Table 4- 1 shows the chemical compositions of the cement used. Four different mixtures were created: water as control and three different carboxylated CNF suspensions. To investigate the workability of the mixtures, a flow table test was conducted according to ASTM C1437 [38].

It is important to note that the CNF is initially prepared as a suspension with abundant carboxylate groups (as discussed in Section 2.1). However, when this nitro-oxidized CNF suspension is introduced into the cement mixture, the metal ions (*e.g.*, Na^+, Ca^{2+}) released from cement mineral dissolution interact with the negatively charged carboxylate groups on the CNF suspension. This ionic interaction induces rapid crosslinking [33,36], causing the CNF suspension to polymerize into a gel state and form CNF gels. This transformation is central to our approach, as the resulting gel structure is expected to enhance freeze/thaw resistance in the cement paste. Table 4- 2 displays the type of CNF suspensions used for each specimen group. From each mixture, three 50 mm diameter by 100 mm height cylinders and one 19 mm diameter by 25 mm height cylinder were cast. After casting, each specimen was moist cured for 14 days in a fog room.

Table 4- 1 Chemical compositions of cement.

Component	CaO	SiO_2	Al_2O_3	Fe_2O_3	SO_3	MgO	Na_2O
Content (%)	62.7661	20.8024	4.7341	3.565	4.0796	1.868	0.5194

Table 4- 2 Mixture compositions with different CNF suspensions

Mixture label	CNF type
CP	Control cement with water only
CNF-1	Mixture with 1.0 wt.% CNF extracted from sugarcane
CNF-2	Mixture with1.02 wt.% CNF extracted from cabbage
CNF-3	Mixture of 2.01 wt.% CNF extracted from jute

4.3.2.1 Isothermal calorimetry

The hydration process of paste specimens with varying CNFs, including total heat and thermal power of each mixture variation were quantified by isothermal calorimetry. Samples, weighing between 5.5 g and 6.5 g, were manually prepared with a w/c ratio of 0.5 in 15 mL in plastic containers and placed in a Calmetrix I-Cal Flex Calorimeter (Calmetrix Inc., Arlington, Massachusetts, USA) for 120 hours at an isothermal temperature of 23 °C.

4.3.2.2 Low temperature differential scanning calorimetry (LT-DSC)

A TA DSC Q2500 (TA Instruments, New Castle, Delaware, USA) was used to investigate the effects of the CNF addition on the freezing point, melting heat (MH), and amount of frozen water (FW) of pastes. All paste samples were subjected to 6 hours of sealed curing in aluminum crucibles. Approximately 40 mg to 50 mg of the paste samples were poured into aluminum crucibles and subjected to rapid cooling and heating conditions. Crucibles with paste samples were placed in DSC. The chosen heating rate was 5 °C min^{-1} [39–41]. Phase changes in the hydration products of cementitious materials did not occur within the temperature range of −30 °C to 25 °C, rather the only phase change observed was associated with the pore solution[42].

Homogenized CNF suspension samples were prepared as mentioned in Section 2.1. Each sample, weighing approximately 5 mg to 8 mg, was individually sealed in T-zero pans to prevent any water loss during DSC scanning. The pans were then cooled at a rate of 5 °C min^{-1} from 25 °C to −30 °C, then left for an isothermal period of 5 min to 10 min at −30 °C, and finally heated back to room temperature at the same rate. The melting of the FW produced an endothermic peak. The melting point of FW was defined as the temperature at which the tangent line intersects the baseline of the initial melting curve, as shown in *Figure 4- 4***.** The baseline was drawn by extending the flat, pre-melting segment of the curve before the onset of the thermal event. The endothermic peak temperature is commonly referred to as the freezing point [41,42].

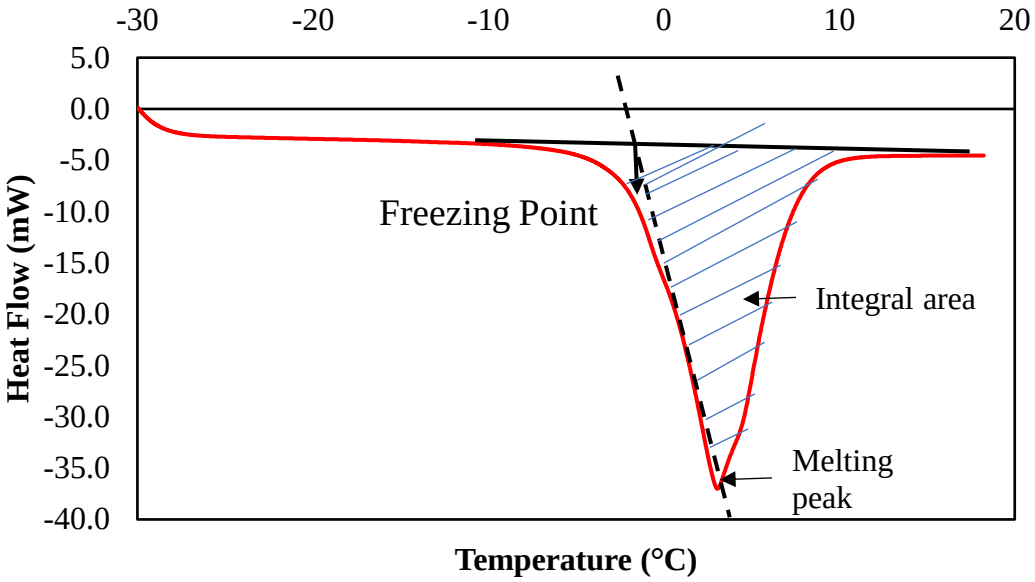

Figure 4- 4 LT-DSC heat flow curve of determination of freezing point; and MH (i.e., the amount of FW).

The integral area under the melting curve can be regarded as the quantity of FW in the frozen paste samples [43]. Subsequently, Equation 2 was used to determine the percentage of FW by employing the integral area of the melting peak [43,44], where Q is the enthalpy (J), H_f is the heat of fusion of water (333.5 + 2.26T J g^{-1}), T is the freezing point (°C), and m is the mass of the sample (g).

$$FW(\%) = \frac{Q}{H_f m} * 100 \quad (2)$$

4.3.2.3 Thermogravimetric analysis (TGA)

TGA was performed both on paste specimens and different CNFs. The specimens were initially finely ground using a mortar and pestle to perform TGA. Grinding was performed in a ventilated fume hood to minimize carbonation during sample preparation and reduce exposure to atmospheric CO_2. Additionally, the samples were immediately stored in a vacuum oven after grinding to limit carbonation further. Subsequently, a sample weighing approximately 10 mg to 20 mg was deposited onto the platinum pan of a discovery TGA 5500 (TA Instruments, New Castle, DE). The samples were heated in a nitrogen environment to 1000 °C at a rate of 20 °C min^{-1}. The CNF samples were heated in a nitrogen environment to 600 °C at a rate of 20 °C min^{-1}. The degree of hydration (DOH) of the paste samples was determined by TGA after 3 days and 14 days of hydration based on the quantification of chemically bound water (CBW) [45], as shown in Equation 3, where $\alpha(t)$ is the DOH of the sample at time t; $Wn(t)$ is the amount of bound water for

a sample at time *t* (in grams of water per 100 g of anhydrous cement); and *Wn(∞)* is the amount of bound water for a completely hydrated sample (in grams of water per 100 g of anhydrous cement).

$$\alpha(t) = \frac{W_n(t)}{W_n(\infty)} * 100 \quad (3)$$

The experimental determination of the $W_n(t)$ value can be achieved by employing Equation 4, provided that there is no carbonation present in the cement paste and that the anhydrous cement experiences minimal weight loss prior to reaching 1000 °C.

$$W_n(t) = \frac{\Delta \text{m } sample\ (105°\text{C} - 1000°\text{C})}{m\ sample\ (1000°\text{C})(\text{t})} * 100 \quad (4)$$

To determine the $W_n(\infty)$ value, the National Institute of Standards and Technology provided an approximate theoretical estimation of the amount of bound water produced after the completion of hydration of cement [46,47]. This study adopted the methodology proposed by Kolour *et al*. [27] to simplify the experimental protocol. As the mass loss above 600 °C was primarily due to the decomposition of calcite in various forms as a result of CO_2 loss, it was excluded from consideration as CBW. Therefore, in this study, Equation 4 was adapted up to 600 °C, deviating from the original extension to 1000 °C, to determine the DOH of the paste samples.

4.3.2.4 X-ray diffraction (XRD)

XRD was used to characterize the hydration products of the paste samples after 14 days of curing. The hydration of the samples was stopped after 14 days using ethanol and then samples were pulverized using a mortar and pestle and a micronizer. The XRD experiments were conducted using a Bruker D8 Advance XRD (Bruker, Billerica, Massachusetts, USA) with Cu Kα radiation (40 kV, 40 mA). The scanning range for the samples was 5° to 60° of 2θ with a step size of 0.02 per second.

4.3.2.5 Freeze/Thaw testing

After curing for 14 days, freeze/thaw testing was performed following ASTM C666 Procedure A [48] except that the specimen dimensions were changed to 50 mm diameter by 100 mm height cylinders due to limited CNF quantities. Specimens were subjected to freeze/thaw cycles until they failed. After every 28 cycles to 36 cycles, testing was performed to determine the transverse and longitudinal resonant frequency of each specimen per ASTM C215 [49]. In addition, ultrasonic pulse velocity (UPV) testing was conducted on these specimens per ASTM C597 [50]. From this testing, dynamic moduli, UPV, length change (ASTM C666), and mass loss (ASTM C666) can be compared between the specimens over the various freeze/thaw cycles.

4.3.2.5 Compression strength testing

Before and after performing freeze/thaw testing was completed on the 50 mm by 100 mm cylinders, the sample ends were sawcut, where compression strength testing was subsequently performed according to ASTM C39 using capping according to ASTM C1231 [51,52].

4.3.2.6 Transmission X-ray microscopy (TXM)

A TXM system was used to evaluate the apparent D_c of the paste samples. The TXM setup [53] (*Figure 4- 5*) was designed and constructed based on the methodology proposed by previous studies [14–18,54]. Table 4- 3 shows the X-ray source details for this setup. This experimental system was capable of acquiring a single X-ray radiograph in 10 s. To initiate the experiment, 19 mm diameter cement paste cylinders were prepared for each type of cementitious paste. The cylinders were then coated with hydrophobic wax on their sides and bottoms, leaving the top surface exposed for solution ponding to facilitate one-dimensional diffusion. *Figure 4- 6***(a)** shows the specimens after being coated with hydrophobic wax and *Figure 4- 6* **(b)** shows the specimens while immersed in the ponding solution.

Table 4- 3 X-ray source details for TXM experiments.

Parameter	TXM
Sensor Resolution (line pair per mm)	33.78
Pixel Size (μm)	19
Voltage (keV)	65
Current (μA)	7000
Exposure Time (s)	0.25

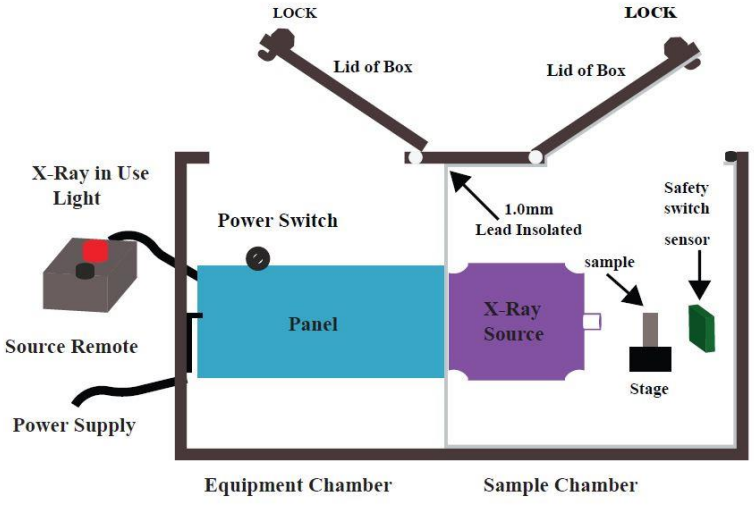

Figure 4- 5 Schematic diagram of the TXM system.

Figure 4- 6 Photographs of specimens coated in hydrophobic wax (a) and specimens immersed in the ponding solution (b).

In this study, a potassium iodide (KI) ponding solution with a concentration of 0.6 M was utilized. This concentration was selected to ensure the optimal visibility of the tracer within the cement paste samples. By employing X-ray imaging, the penetration of iodide into cement paste was quantified. As iodide and chloride ions are of similar size, TXM methods use iodide ingress as a representative indicator of chloride ingress [15]. However, it should be noted that iodide has a D_c that is 24 % higher than that of chloride, as reported by Moradllo *et al*. [14]. Therefore, the iodide D_c measured in this study represents a more conservative estimate than that observed for chloride diffusion.

All samples underwent an initial scanning process before they were immersed in 0.6 M KI solution. The initial scanned image for each group of samples is termed as the reference image. Subsequently, the samples were immersed in KI solution and rescanned after 3 days, 7 days, and 14 days, respectively. Changes in gray values were assessed by subtracting the reference image using a sequential approach and comparing the subsequent radiographs with the reference image. The red box in the subtracted image shown in *Figure 4- 7* represents the penetrated depth of iodide in the sample after 7 days of ponding in the KI solution. Radiographic analysis was conducted using a MATLAB code to align the images obtained at 3 days, 7 days, and 14 days intervals with their corresponding reference images for the samples. The alignment of the subsequent radiographs with the reference radiograph involved local displacements, including shifts and rotations. To minimize cupping artifacts [54–57], a region approximately 7.37 mm wide, equivalent to approximately 280 pixels in TXM radiographs, was defined, as depicted in *Figure 4- 7* Each line in the image corresponds to a specific depth and represents a grayscale value, which was computed by averaging the values from the 280 individual lines to obtain the final gray-value profile. Concrete is a heterogeneous composite material, meaning that its composition varies across different directions within the concrete matrix. To account for this variability, radiographs were obtained from multiple angles (0°, 60°, 120°, and 180°) for all samples to determine the apparent D_c.

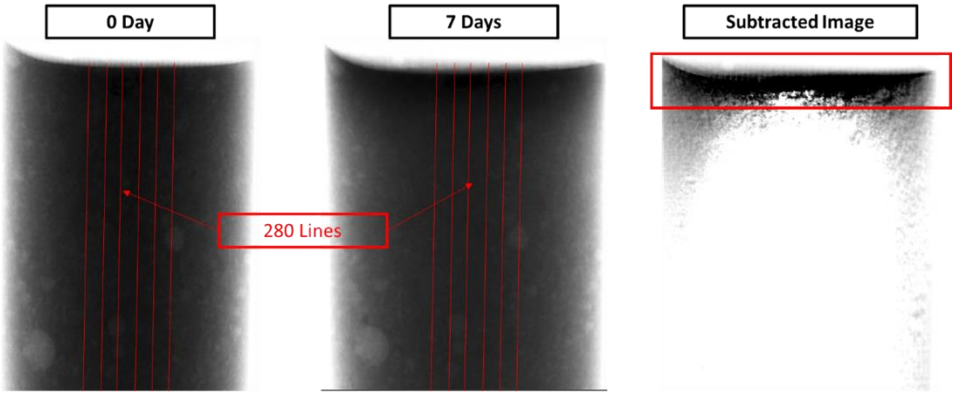

Figure 4- 7 Radiographic subtraction in a designated area of interest.

Finally, with the regression approach, the apparent D_c and surface concentration (C_s) was determined based on Fick's second law of diffusion, as demonstrated in ASTM C1556 [58]. The D_c value in this study combines the impact of fluid transport mechanisms such as diffusion, absorption, convection, and chemical binding into one term. The D_c value in this study combines the impact of fluid transport mechanisms such as diffusion, absorption, convection, and chemical binding into one term. Equation 5 illustrates the expression to determine the iodide concentration $C_{(x,t)}$ at depth of x from the surface after time t:

$$C_{(x,t)} = C_s\left(1 - erf\left(\frac{x}{2\sqrt{D_c t}}\right)\right) \quad (5)$$

where x is the distance from the sample surface, C_s is the surface iodide concentration, and erf is the Gaussian error function.

4.4 Results and discussion

4.4.1 Visual observations

During mixing, the consistency of the specimens varied depending on the type of CNF suspensions used or if water was used. It was observed from the flow table test that the mixture with only water was considerably more flowable than the CNF mixes, exhibiting a flowability of 140 %, in contrast to those incorporating CNF suspensions. During mixing, CNF suspensions rapidly polymerize into hydrogels by ionic crosslinking with metal ions (*e.g.*, Na^+, Ca^{2+}) in solution from cement mineral dissolution. Figure 4- 8 shows the dispersed CNF suspensions from before mixing and paste samples from different groups after the flow table test. The consistency of the mixtures varied with different CNF suspensions: CNF-3 showed the lowest workability, with a flowability of 105 %, CNF-2 had the highest workability, with a flowability of 120 %, and CNF-1 demonstrated a flowability of 109 %.

During the demolding of the cylindrical specimens, a significant disparity was observed in the mechanical properties. The specimens containing CNF suspensions demonstrated a noticeably softer and more malleable surface during handling when compared to the control group. This observation indicates that the presence of organic materials (e.g., lignin) in the CNF may have affected the hydration process, potentially leading to a retardation effect and resulting in a less rigid surface texture at the initial stages. This indicates that the CNF specimens had not gained as much strength as the CP specimens at the time of demolding, which is supported by the isothermal calorimetry data presented in Section 4.4.2. However, this difference diminished over time, and after a curing period of 14 days, all specimens exhibited comparable mechanical characteristics.

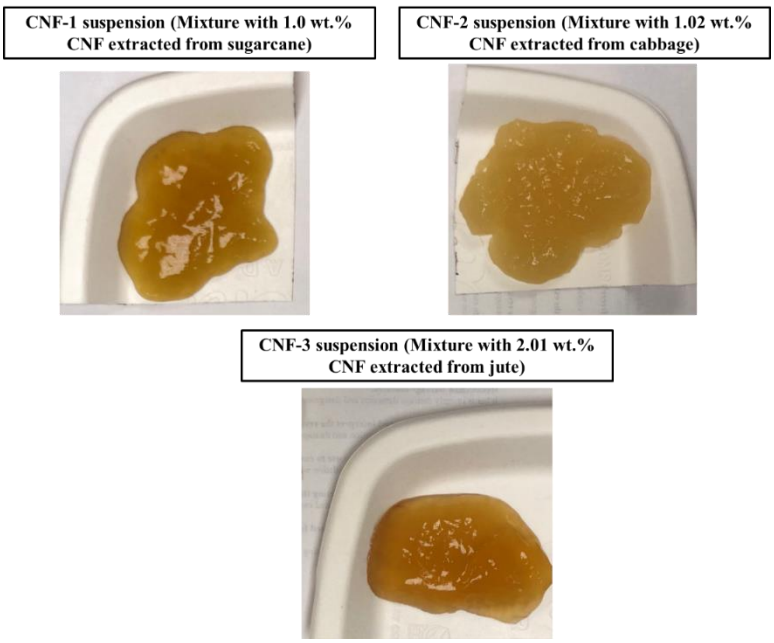

(a)

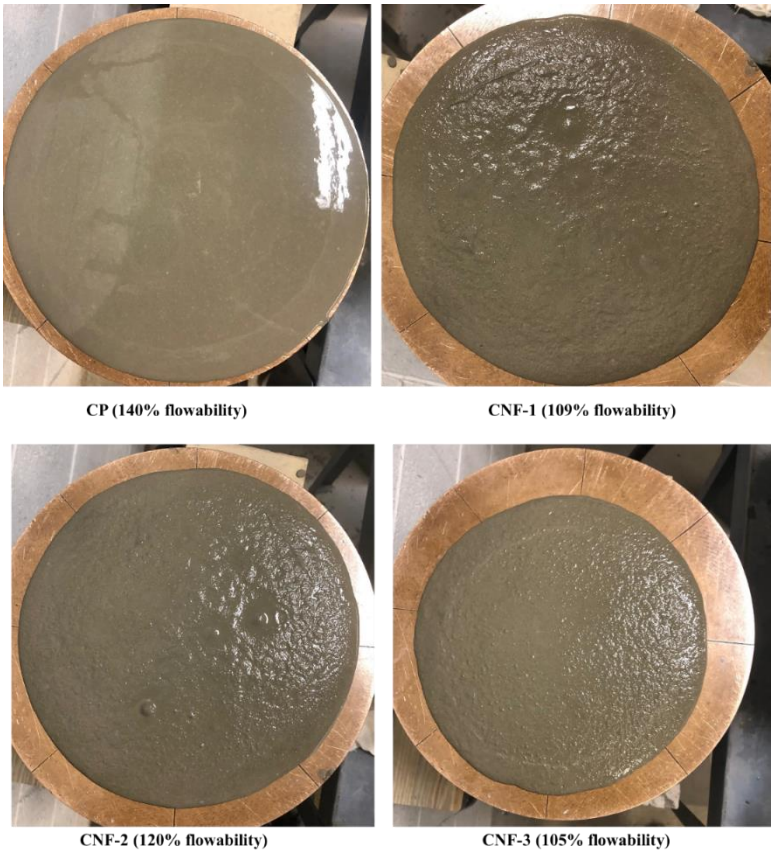

(b)

Figure 4- 8(a) Dispersed CNF suspensions from before mixing, and (b) paste samples from different groups after the flow table test.

4.4.2 Isothermal calorimetry

Figure 4- 9 shows the results from the isothermal calorimetry. The CNF specimens had reduced and delayed thermal power peaks when compared to the CP specimen. In addition, the total heat at each time was lower for the CNF samples as compared to the CP specimen. Zhang et al. [24] observed similar results, finding that peaks in the heat flow rate curves were delayed with the addition of CNF in the mixture [15].

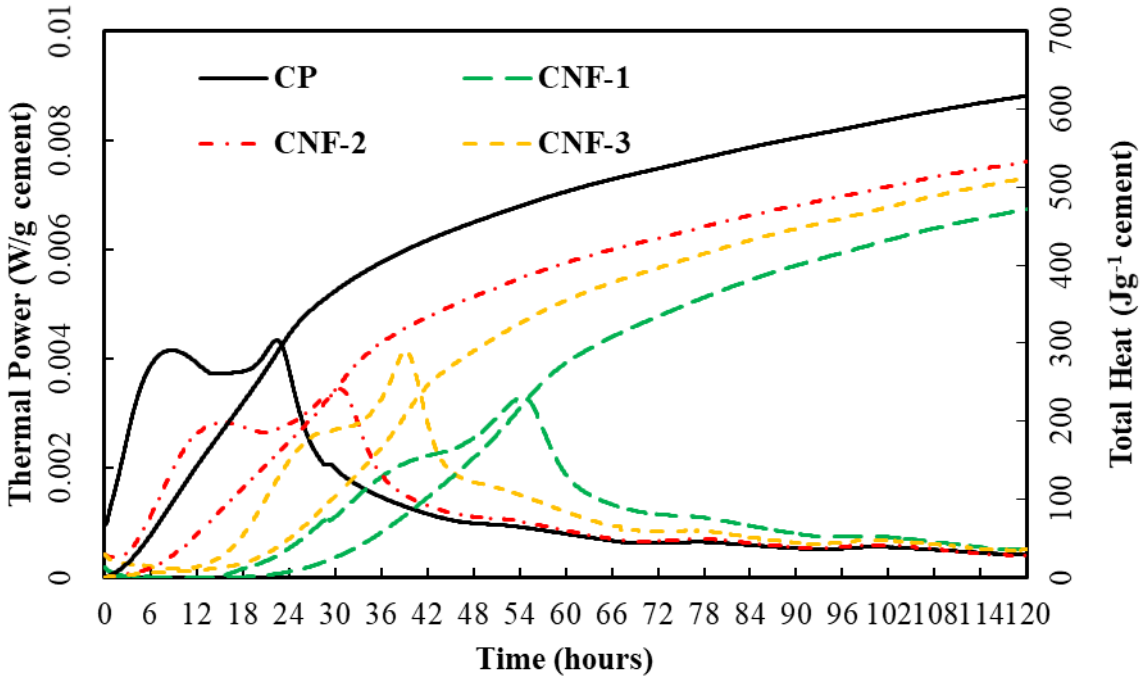

Figure 4- 9 Isothermal calorimetry results - thermal power and total heat versus time.

Table 4- 4 shows the total heat values for the samples at various time intervals and the comparison between the total heat value for each CNF mixture to that of CP. It is seen that for the CNF mixtures, the percentage of total heat as compared to that of CP value generally increased with time as expected, but the percentage was always less than 100 %. CNF-2 exhibited values closest to CP, reaching 86 % of the CP's total heat after 120 h. In contrast, CNF-1 and CNF-3 showed much lower percentages during the first 24 h to 48 h, but then steadily increased to approximately 76 % for CNF-1 and 83 % for CNF-3 of the CP's total heat after 120 h.

Table 4- 4 Total heat at various time intervals for all mixtures compared to that of the CP sample.

Mixture	Total Heat (W/g) / % Total Heat at that time of CP					
	12 h	24 h	48 h	72 h	96 h	120 h
CP	99.2	266	444	517	569	612
CNF-1	0.118 / 0.12%	2.93 / 1.1%	127 / 29%	322 / 62%	408 / 72%	466 / 76%
CNF-2	29.7 / 30%	144 / 54%	347 / 78%	427 / 83%	482 / 85%	528 / 86%
CNF-3	7.6 / 7.7%	30.3 / 11%	270 / 61%	387 / 75%	453 / 80%	506 / 83%

Table 4- 5 displays the time peaks in thermal power observed for each mixture and the amount of thermal power corresponding to each peak. As expected, based on the total heat results in Table 4-4, CP peaked at a much earlier time than the other samples. This explains why the percentage of total heat for the CNF samples as compared to CP increased dramatically as the time increased. Additionally, CNF-1 and CNF-3 mixtures did not exhibit peaks at the location where the first peak is normally expected, but rather exhibited a slowdown in the increase in thermal power before ramping into their peak values (labeled as the second peak in Table 4- 5).

Table 4- 5 Time and value of thermal power peaks.

Mixture	First peak time (h)	First peak thermal power (mJ g^{-1})	Second peak time (h)	Second peak thermal power (mJ g^{-1})
CP	8.5	4.16	22.5	4.33
CNF-1	Peak Unclear	N/A	54.5	3.31
CNF-2	16	2.83	31	3.43
CNF-3	Peak Unclear	N/A	39.5	4.12

Overall, CNF-2 had the least delay time for thermal power peaks and highest total heat after 120 h compared to CNF-1 and CNF-3. These results indicate that the hydration process in cement pastes containing CNF suspensions is delayed and progresses more slowly, potentially due to organic materials (e.g., lignin) in the CNF suspension. Lignin can retard hydration by interacting with calcium ions and slowing the formation of hydration products, which may explain the differences in physical properties observed between the specimens discussed in Section 4.3.1.

4.4.3 LT-DSC

The LT-DSC experiments provided the freezing points and MH values for the CNF suspensions derived from various sources. The CNF-1 suspension derived from bagasse exhibited a freezing point of –2.0 °C and a MH of 338.2 J g^{-1}. The CNF-2 suspension obtained from cabbage showed

a freezing point of –1.4 °C and a MH of 335.8 J g^{-1}. Lastly, the CNF-3 suspension derived from jute had a freezing point of –1.5 °C and a MH of 322.3 J g^{-1}.

Figure 4- 10 shows the freezing points of various paste samples for different curing periods. As depicted in *Figure 4- 10*, the incorporation of CNF suspensions has a favorable influence on reducing the freezing point of the pore solution in cement pastes. According to the LT-DSC results, CNF-2 exhibited the lowest freezing point, followed by CNF-3, CNF-1, and CP in descending order. During the 6-hour hydration period, the CNF-2 sample exhibited the lowest freezing point at –2.2 °C, whereas CP had the highest at –1.9 °C. Despite this, CNF-2 showed limited progress in hydration, as indicated by isothermal calorimetry, XRD, and TGA. With the increasing period of hydration, for instance, after 28 days of curing, CNF-2 maintained the lowest freezing point at –6.5 °C, surpassing CP, which registered –5.2 °C. This suggests that CNF-2's hydration improved significantly over time, enhancing its ability to lower the freezing point, unlike CNF-1 and CNF-3. However, after 28 days of curing, CNF-1 and CNF-3 also showed improved freezing points of –4.4 °C and –4.9 °C.

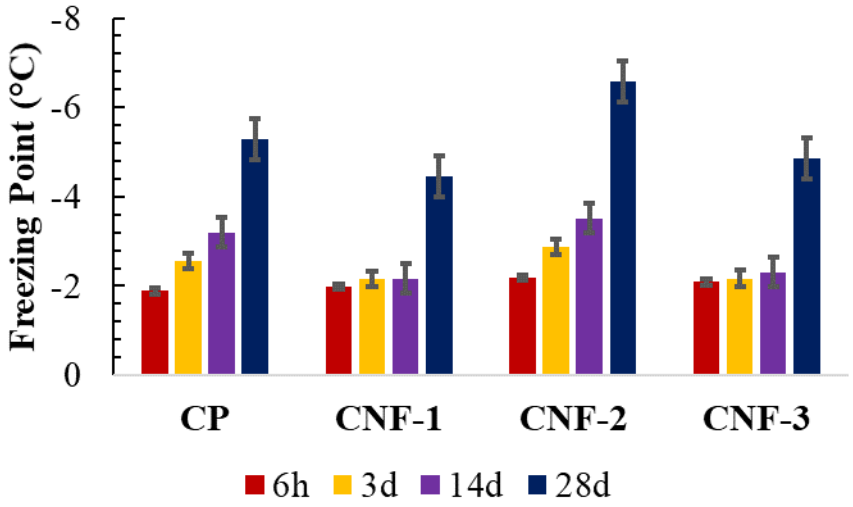

Figure 4- 10 Freezing points of different cement paste samples for different curing periods.

Figure 4- 11(a) and *Figure 4- 11*(b) show the MH and %FW content of different cement paste samples at various curing periods. It was found that the inclusion of CNF suspensions could increase the MH, indicating a lower consumption rate of free water due to limited hydration progress with 6 h of curing. For 6 h of curing, CP exhibited the lowest MH (–118.7 J g^{-1}) and FW (3.0%) among all samples. Among the CNF samples, CNF-2 had the lowest MH (–163.2 J g^{-1}) and FW (4.1 %), while CNF-3 had the highest MH (–169.8 J g^{-1}) and FW (4.2 %), followed by CNF-1 with a MH of –168.4 J g^{-1} and FW of 4.2 %. The integral area of the endothermic curves depicts the amount of FW in each sample, where a lower value signifies a higher heat of hydration in the samples [39–41]. Initially, the CP samples showed the lowest MH and FW values, consistent

with the isothermal calorimetry experiments. However, CNF-2 exhibited high values in both metrics after 6 hours but improved substantially with the increasing period of hydration. For instance, after 28 days, CNF-2 exhibited a MH of –74.9 J g^{-1} and FW of 1.9 %, closely aligning with CP (MH: –71.2 J g^{-1} and FW: 1.8 %). In contrast, CNF-1 and CNF-3 showed poorer performances until 14 d of curing. After 28 days, CNF-1 and CNF-3 showed improved results, with CNF-1 having a MH of –80.1 J g^{-1} and FW of 2.0 %, and CNF-3 having a MH of –75.5 J g^{-1} and FW of 1.9 %, demonstrating progress in hydration.

Overall, these LT-DSC results reveal that while CNF suspensions incorporation can initially retard hydration, the formation of a CNF gel ultimately enhances freeze/thaw resistance. The gel structure modifies the pore solution by reducing free water content and lowering the freezing point, thereby improving the durability of the cement paste.

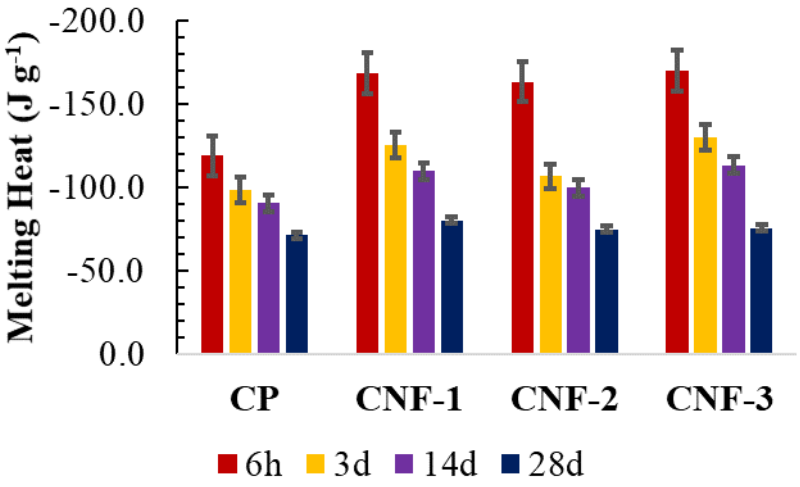

(a)

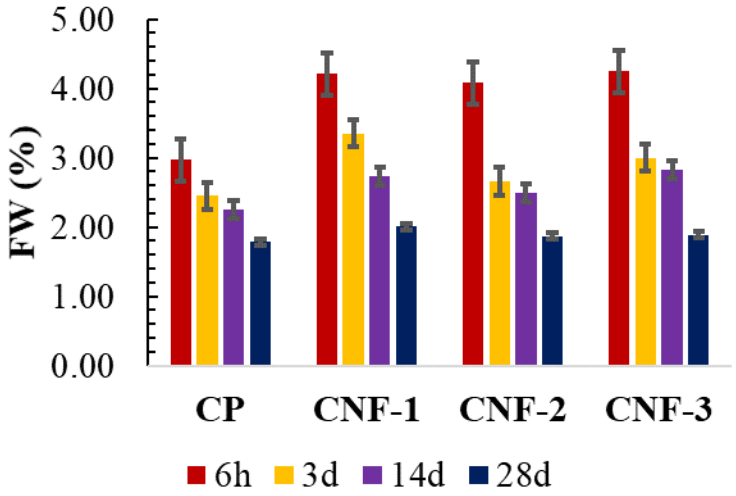

(b)

Figure 4- 11 (a) MH (J g^{-1}) and (b) FW (%) of cement paste samples for different curing periods.

4.4.4 XRD

Figure 4- 12 shows the results from XRD analysis. It was seen that the incorporation of CNF suspensions influenced the common phases such as portlandite and ettringite within the cement composites, but it did not result in the formation of any new phases. Interestingly, both CP and CNF-2 samples showed comparable intensities for all conventional phases, although CNF-2 exhibited slightly lower-intensity peaks than CP. In contrast, CNF-1 and CNF-2 displayed significantly lower intensity peaks than CP, with no distinguishable peaks for ettringite. The XRD results are consistent with the results of isothermal calorimetry. Taken together, these findings indicate a delayed hydration process for cement pastes containing CNF suspensions.

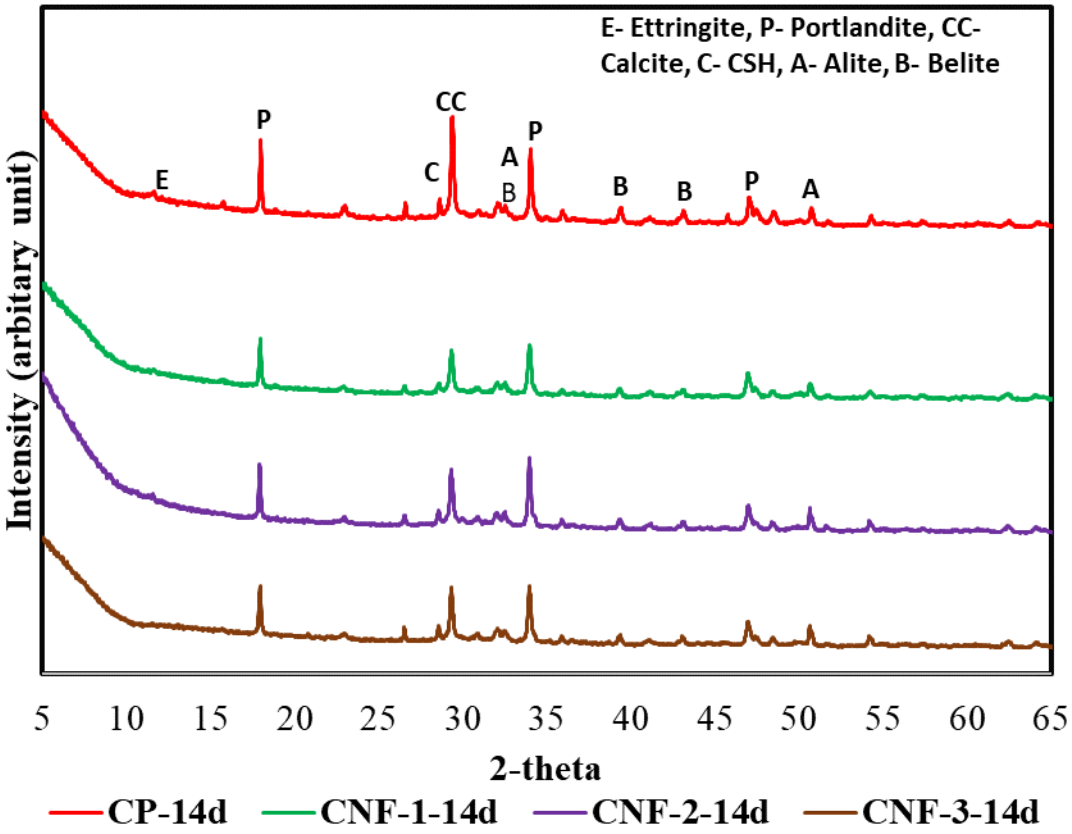

Figure 4- 12 XRD pattern of different cement paste samples for 14 d.

4.4.5 TGA

In TGA study of varying cement paste samples, the temperature range of 30 °C to 105 °C usually signifies the loss of free water, the decomposition of gypsum and ettringite (AFt), where the initiation of bound water loss from C-S-H gel can be observed within the range of 110 °C to 170 °C [56]. Additionally, the monosulfoaluminate (AFm) phase decomposition can be observed within the range of 150 °C to 170 °C, the portlandite decomposition can manifest between 400 °C and 550 °C, and calcium carbonate decomposition can occur between 600 °C and 850 °C [59]. For CNFs, the thermal degradation temperatures of CNF and their components vary based on the structure and composition. Cellulose degrades around 250 °C to 400 °C, hemicellulose around 200 °C to 300 °C, and lignin around 500 °C [33,60].

Figure 4- 13 shows the TGA profiles of the three CNF suspensions. The results revealed that 98 % to 99 % of the mass decomposed around 105 °C to 160 °C, primarily attributed to the loss of water. CNF-1, CNF-2, and CNF-3 suspensions showed their water loss peaks at 105 °C, 140 °C, and 150 °C, respectively, indicating varying water-CNF bonding strengths. The CNF decomposition occurred in the range of 200 °C to 600 °C, with distinct stages influenced by the

CNF type, implying the impact of the water interaction with the CNF scaffold at elevated temperatures. These results are consistent with the findings of previous studies [61,62].

Figure 4- 14 and *Figure 4- 15* show the TGA profiles of varying cement paste samples after 3 d and 14 d curing, respectively. The results in these figures indicate higher portlandite levels in the control samples compared to the CNF containing samples for both 3 d and 14 d curing. However, the weight loss peak at approximately 150 °C, associated with C–S–H and AFt decomposition, remained relatively consistent for all the samples after 3 d curing. In contrast, for 14 d curing, the control CP sample exhibited greater decomposition than the CNF containing samples. This reduced peak at 14 d could be attributed to reduced ettringite formation in the CNF containing samples. As explained in a prior study [26], the addition of CNF can mitigate ettringite formation in cement paste without sulfate exposure, owing to its capacity to bind with calcium ions.

The DOH values for the 3 d cured samples of CP, CNF-1, CNF-2, and CNF-3 were 38 %, 35 %, 38 %, and 35 %, respectively. This aligns with the isothermal calorimetry results, indicating a similar DOH for CP and CNF-2, whereas CNF-1 and CNF-3 exhibit a slower DOH. Conversely, for the 14 d samples, the DOH values of CP, CNF-1, CNF-2, and CNF-3 were 55 %, 53 %, 53 %, and 53 %, respectively. This result was attributed to CNF-1 and CNF-3 catching up with the hydration rate, in contrast to CNF-2, during the extended curing period.

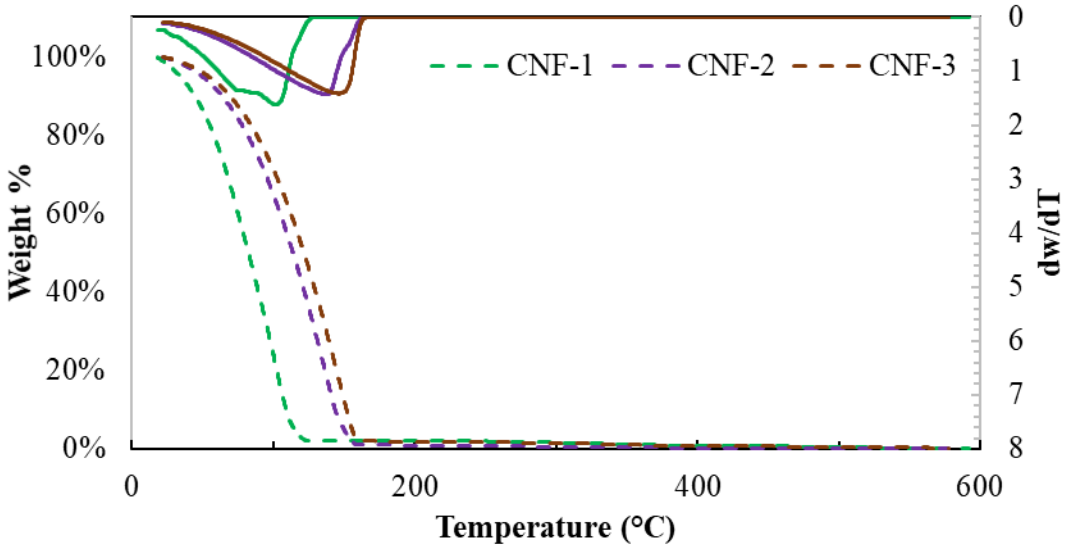

Figure 4- 13 TGA results of CNF suspensions (dashed lines represent the % weight loss profiles, and solid lines represent the DTA curves).

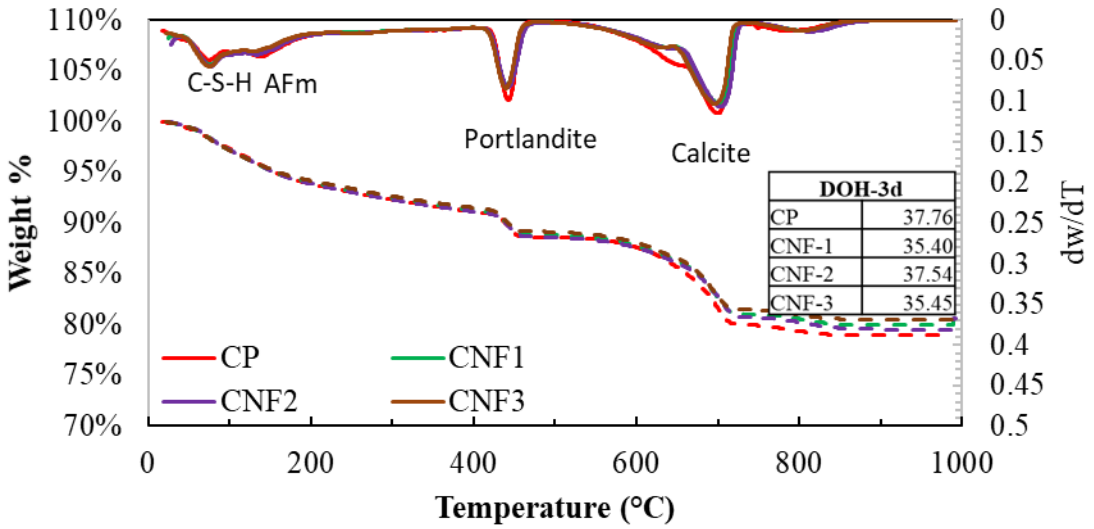

Figure 4- 14 TGA results and DOH values of varying paste samples cured for 3 days (dashed lines represent the % weight loss profiles, and solid lines represent the DTA curves).

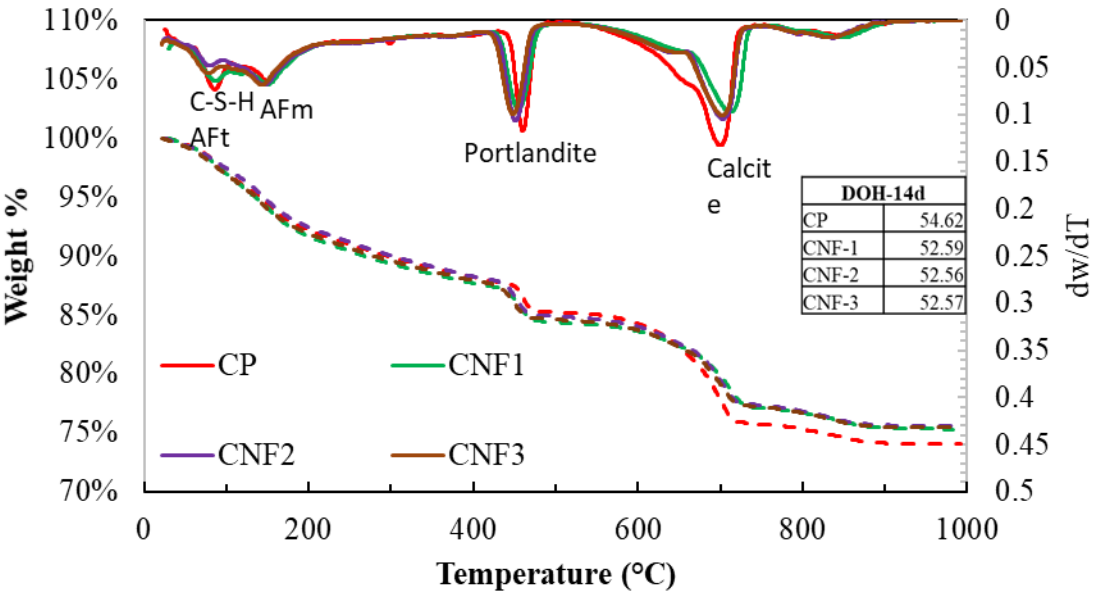

Figure 4- 15 TGA results and DOH values of varying paste samples cured for 14 days (dashed lines represent the % weight loss profiles, and solid lines represent the DTA curves).

4.4.6 Freeze/thaw test results

Figure 4- 16 shows the dynamic modulus of elasticity results at each freeze/thaw cycle interval. In addition, the percent change in dynamic modulus of elasticity with number of cycles can be found in *Figure 4- 17*. As observed in *Figure 4- 17*, CNF-2 had the smallest percent change in

dynamic modulus of elasticity, while the control sample had the largest percent change. This suggests that the relative freeze/thaw resistance was: CNF-2 > CNF-1 > CNF-3 > CP. However, when comparing the CP samples to each type of CNF sample at 130 cycles of freeze/thaw testing, there is not sufficient evidence to conclude the difference in percent change in dynamic modulus of elasticity is statistically significant (at a 0.05 significance level).

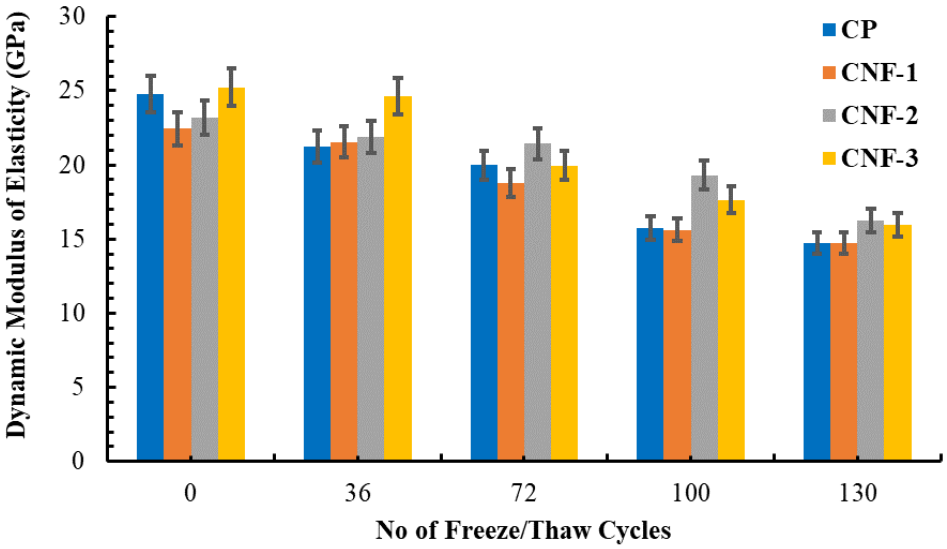

Figure 4- 16 Dynamic modulus of elasticity versus number of freeze/thaw cycles.

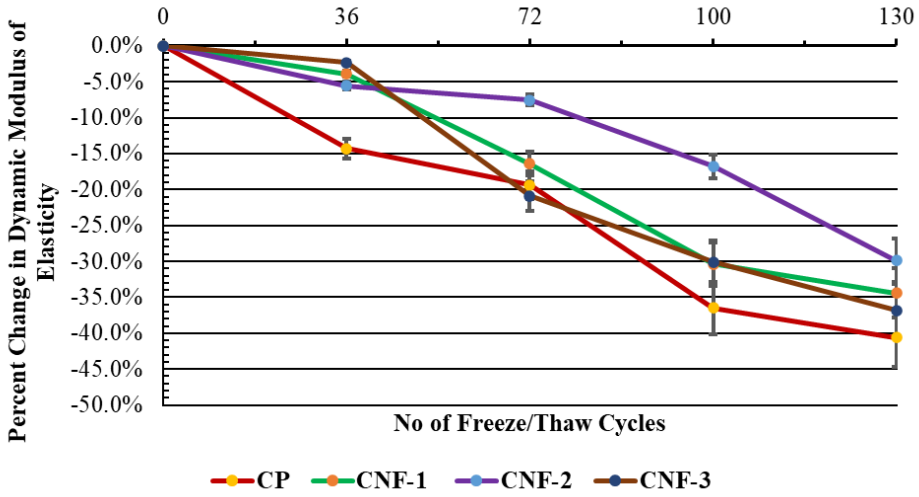

Figure 4- 17 Percent change in the dynamic modulus of elasticity versus the number of freeze/thaw cycles.

Figure 4- 18 illustrates the average ultrasonic pulse velocity of each specimen type at the various freeze/thaw cycles. Additionally, *Figure 4- 19* shows the average percent decrease in ultrasonic

pulse velocity with the number of cycles. In *Figure 4- 19*, it is observed that CNF-2 exhibited the least percent change in ultrasonic pulse velocity after 130 cycles, followed by CNF-3, CP, and CNF-1. Although CNF-2 exhibits the smallest percent change in UPV (*Figure 4- 19*), it only indicates that its UPV is less sensitive to freeze/thaw cycling effects. The actual freeze/thaw resistance should be assessed based on the average UPV values, as higher UPV values generally correlate with better structural integrity and lower internal damage. In our study, the average UPV values (*Figure 4- 18*) do not show a statistically significant difference among the specimens at 130 cycles (at a 0.05 significance level), suggesting that the overall freeze/thaw resistance of CNF-2 is comparable to that of CP samples.

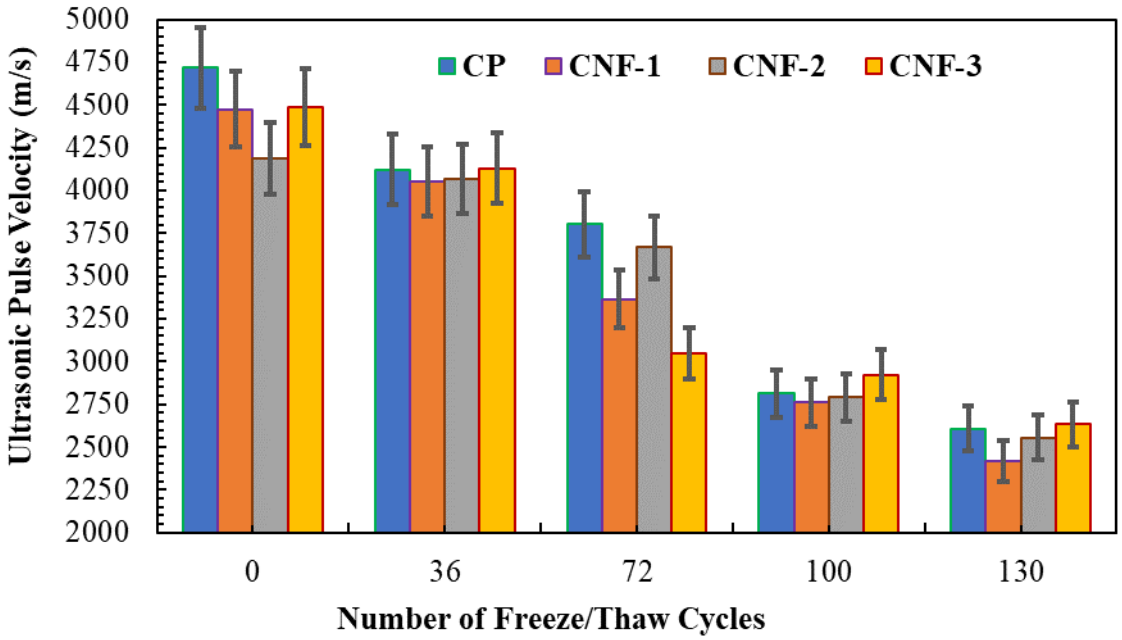

Figure 4- 18 Ultrasonic pulse velocity (UPV) results versus number of freeze/thaw cycles.

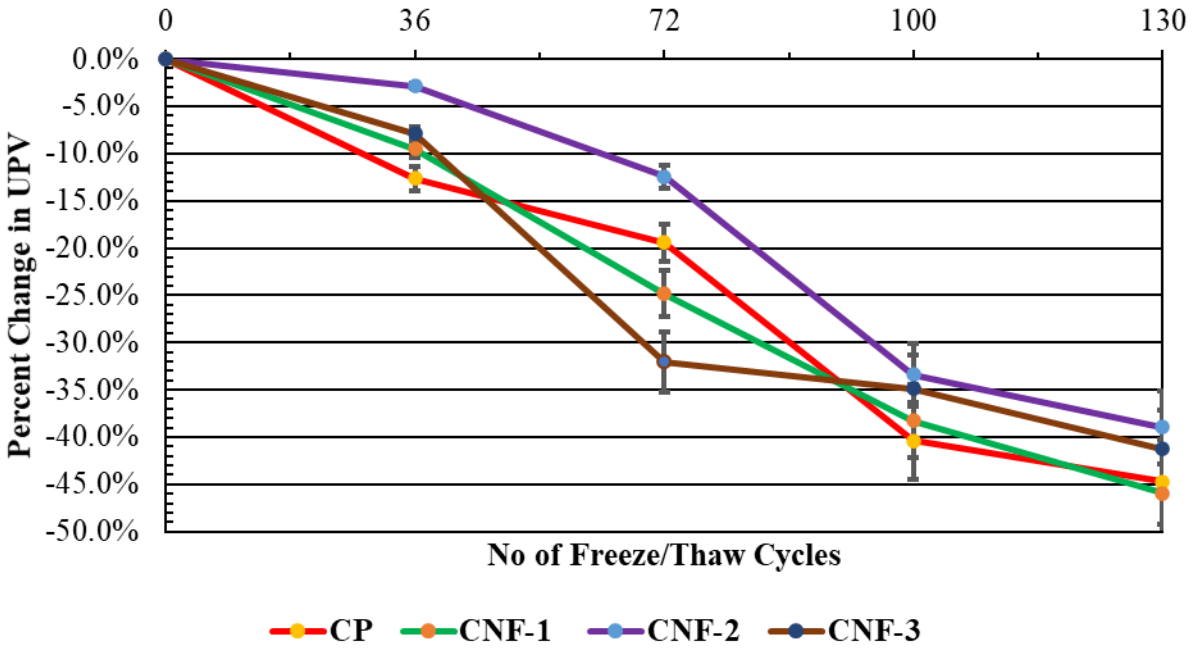

Figure 4- 19 Percent change in UPV versus number of freeze/thaw cycles.

Mass loss and reduction in length of each specimen was also recorded after each freeze/thaw interval. *Figure 4- 20* and *Figure 4- 21* report the percent mass loss versus the number of freeze/thaw cycles and percent length reduction versus the number of freeze/thaw cycles, respectively. As observed in these figures, CNF-2 exhibited the least percent mass loss, followed by CNF-3, CP, and CNF-1. Additionally, CNF-3 exhibited the least percent length reduction, followed by CNF-2, CNF-1, and CP. These results indicate that both CNF-2 and CNF-3 exhibited good freeze/thaw resistance when compared CNF-1 and CP. However, when comparing CP to different CNF samples at 130 cycles of freeze/thaw testing, the differences in percent mass loss and percent length change were also not statistically significant (at a 0.05 significance level).

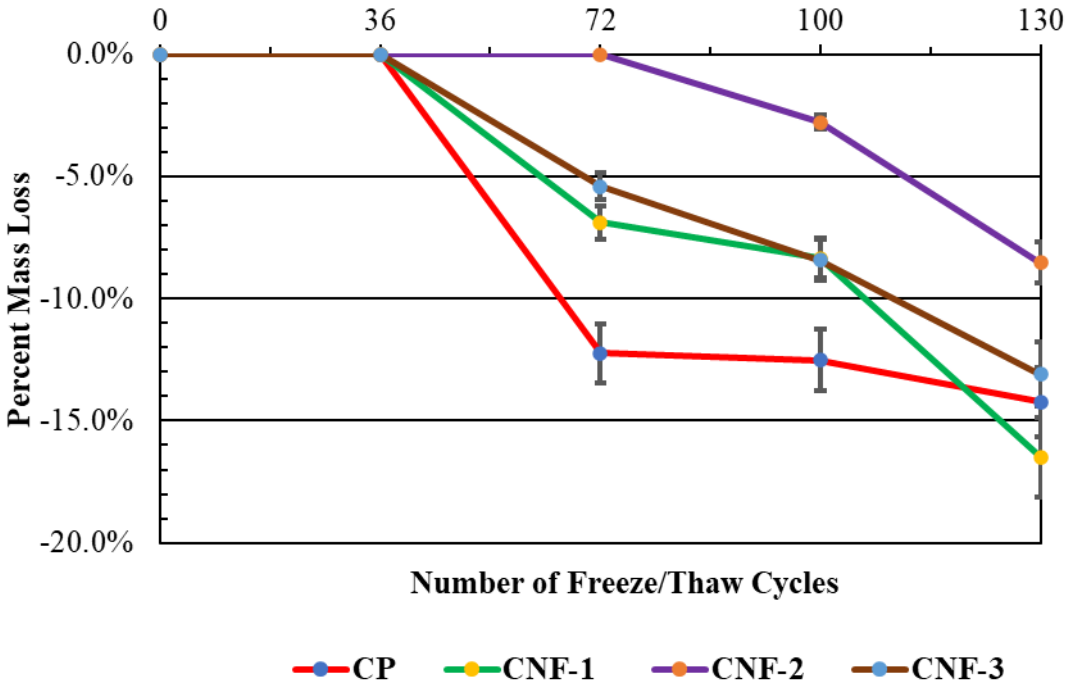

Figure 4- 20 Percent mass loss versus number of freeze/thaw cycles.

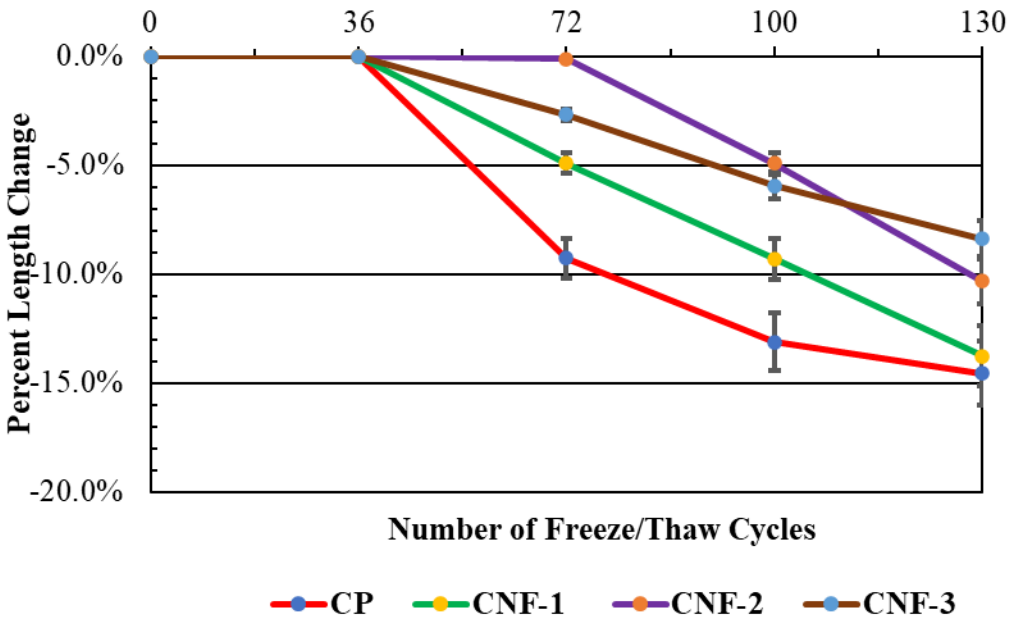

Figure 4- 21 Percent length decrease versus number of freeze/thaw cycles.

4.4.7 Compressive strength testing results

The compressive strength results for the varying samples before (3 d, 7 d, and 14 d) and after 130 freeze/thaw (F-T) cycles are presented in *Figure 4- 22*. Examining the 3 d curing period, the compressive strength values for CP, CNF-1, CNF-2, and CNF-3 were 17.7 MPa, 10.0 MPa, 10.2 MPa, and 10.8 MPa, respectively. All CNF samples displayed notably lower compressive strength than CP , which was attributed to the lower heat of hydration associated with the presence of CNF. Although CNF-3 possessed a lower DOH, it exhibited a higher compressive strength than CNF-2, possibly because of the higher CNF percentage in CNF-3 (2.0 wt%) compared to CNF-2 (1.0 wt%) and the influence of different CNF types.

Unpaired, two-tailed t-tests for the 3 d results indicated a statistically significant difference between the compressive strength of CP and those of CNF samples at a significance level of 0.05. However, there was insufficient evidence to conclude a statistically significant difference between the strength results of the paste samples prepared with CNF suspensions at 3 d, given that the p-value exceeded the significance level.

After 7 d and 14 d, the compressive strength increased for all samples. Similar to the 3-day results, the CNF samples exhibited lower compressive strength compared to CP, which could be attributed to the lower heat of hydration. The CNF-3 sample, despite having a lower DOH, displayed a higher compressive strength than CNF-2, likely due to its higher CNF percentage (2.0 wt% vs. 1.0 wt%) and different CNF types.

Unpaired, two-tailed t-tests for the 7 d results showed a statistically significant difference between the CP and CNF strengths, with sufficient evidence at the 0.05 significance level. Additionally, there was significant evidence to conclude a statistically significant difference between CNF suspensions at 7 d. For the 14 d results, there was a statistical difference between the CP and the CNF strengths. Additionally, CNF-3 displayed a significant difference from both CNF-1 and CNF-2. However, there is insufficient evidence to conclude a statistically significant difference between CNF-1 and CNF-2 after 14 d.

After 130 F-T cycles, CP, CNF-1, and CNF-2 exhibited similar average compressive strengths, whereas CNF-3 had the highest average compressive strength. CNF-2 and CNF-3 demonstrated the smallest percentage change in compressive strength (46 %), followed by CNF-1 (47 %), while CP displayed the largest percentage change (71 %). This indicates that CNF-2 and CNF-3 had the highest freeze/thaw resistance, whereas CP had the lowest. Comparing CP to each CNF sample, there wasn't sufficient evidence to conclude a statistically significant difference in the percent change in dynamic modulus of elasticity at 130 cycles of freeze/thaw testing (at a 0.05 significance level).

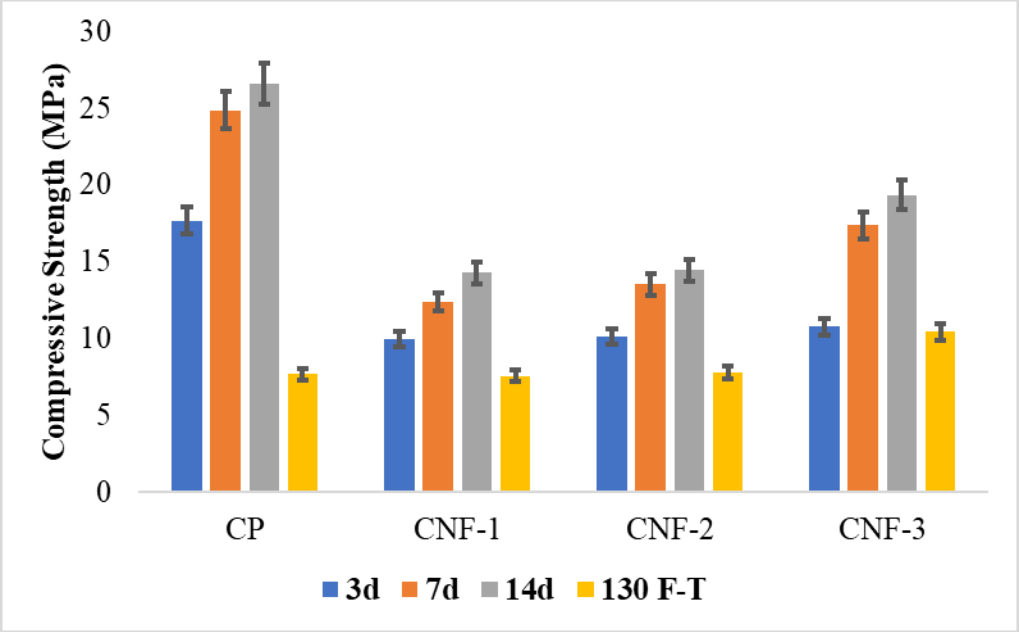

Figure 4- 22 Compressive strength of paste samples before and after exposing to 130 F-T cycles.

4.4.8 Time dependent diffusion coefficient and concentration profile

Figure 4- 23 depicts the average concentration profiles and D_c values for CP, CNF-1, CNF-2, and CNF-3 after 3 d, 7 d, and 14 d, respectively. In these figures, it is seen that all sample groups exhibit notably low D_c value. Analysis of the D_c for CP over ponding durations of 3 d, 7 d, and 14 d reported values of 5.71 x 10^{-12} m^2 s^{-1}, 1.27 x 10^{-12} m^2 s^{-1}, and 0.39 x 10^{-12} m^2 s^{-1}, respectively. Similarly, CNF-1 showed D_c values of 0.50 x 10^{-12} m^2 s^{-1} after 3 days, 0.44 x 10^{-12} m^2 s^{-1} after 7 days, and 0.16 x 10^{-12} m^2 s^{-1} after 14 days. For CNF-2, the corresponding D_c values were 2.69 x 10^{-12} m^2 s^{-1} after 3 days, 1.96 x 10^{-12} m^2 s^{-1} after 7 days, and 1.60 x 10^{-12} m^2 s^{-1} after 14 days. Finally, CNF-3 exhibited D_c values of 0.94 x 10^{-12} m^2 s^{-1}, 0.65 x 10^{-12} m^2 s^{-1}, and 0.33 x 10^{-12} m^2 s^{-1} after 3 days, 7 days, and 14 days of ponding, respectively. Additionally, during the ponding period, the iodide concentration reached a maximum value (C_{max}) of 9.8 % for CP, 10.0 % for CNF-1, 12.5 % for CNF-2, and 11.5 % for CNF-3 after 14 days within the first layer below the surface (Δx), followed by a gradual decrease in the iodide concentration at lower depths. This observed increase is likely due to the combination of capillary absorption and diffusion during the initial penetration of the solution [54,56,57].

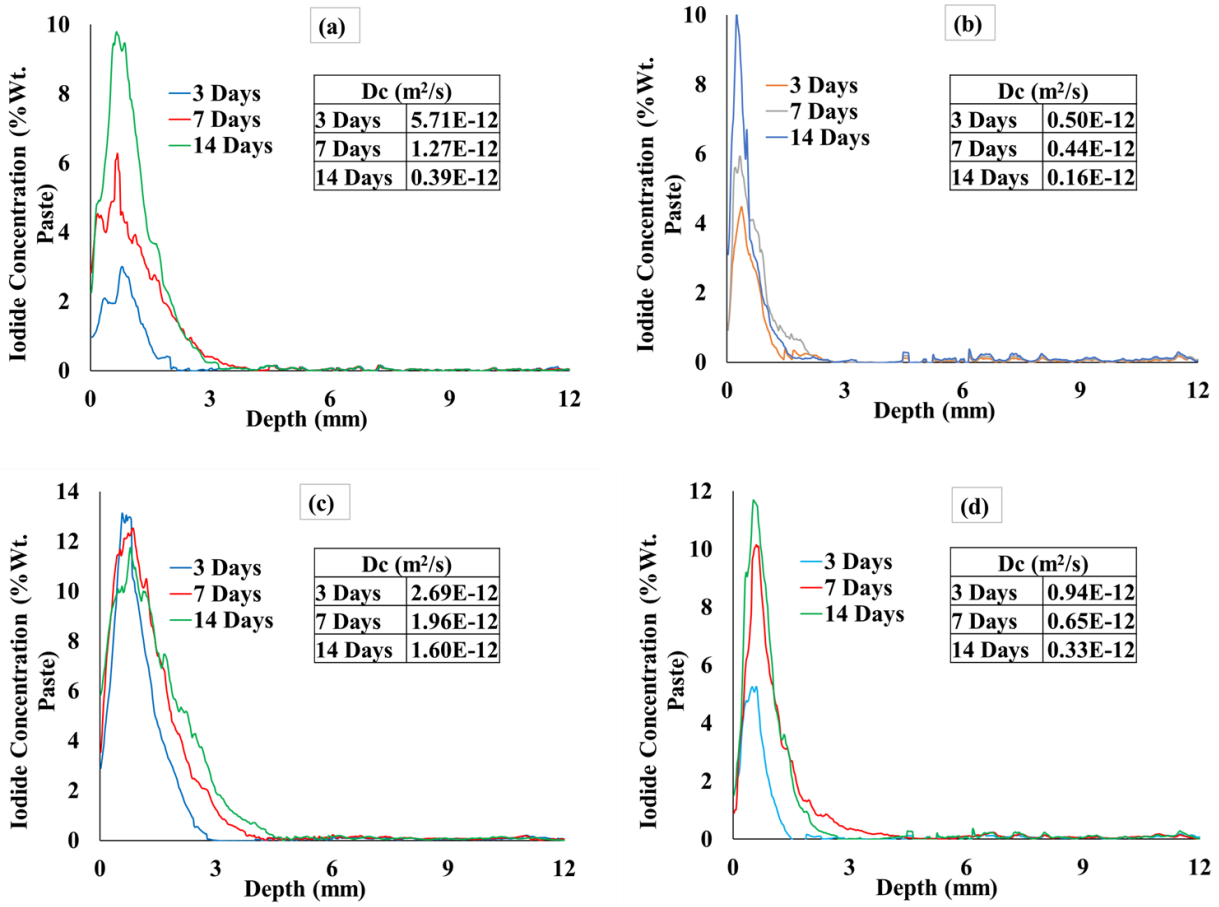

Figure 4- 23 Concentration profiles for (a) CP, (b) CNF-1, (c) CNF-2, and (d) CNF-3.

Upon analyzing the apparent D_c values presented in *Figure 4- 23*, a pattern becomes evident in all samples with lower D_c values than that of CP. Remarkably, CNF-1 and CNF-3 exhibited the highest resistance to diffusion, displaying the lowest D_c values, followed by the CP and CNF-2 samples. Interestingly, the previously observed ability of CNF-2 to mitigate freeze/thaw damage seems to conflict with its performance against diffusion, which suggest that the matrix of CNF-2 may be more porous than those of the other groups. Moreover, a noticeable improvement in the cement paste matrix performance against chloride ingress and diffusion mechanisms was evident when CNFs were incorporated.

A summary of the D_c values for all mixture types is presented in Table 6 (*Figure 4- 23* shows the average values obtained from this table). The variations in the apparent D_c values for different angles in Table 6 reflects the variations in the paste matrix in the tested samples at different angles. Unpaired two-tailed t-tests indicated a statistically significant difference between the D_c values for CNF-1 and CNF-2 at 3 d, 7 d, and 14 d; CNF-2 and CNF-3 at 3 d, 7 d, and 14 d; and CP and CNF-2 at 14 d at a significance level of 0.05. Additionally, at a 5 % significance level there was not enough evidence to conclude that there is a difference between the D_c values of the 3 d, 7 d, and 14 d samples of the same mixture compositions using unpaired two-tailed t-tests.

Table 4- 6 D_c (10^{-12} m^2 s^{-1}) values of different paste samples.

CP			
	3 Days	7 Days	14 Days
Angle	D_c	D_c	D_c
0	6.01	0.19	0.10
60	7.25	0.13	0.19
120	9.05	2.50	0.49
180	0.54	2.25	0.78
CNF-1			
	3 Days	7 Days	14 Days
Angle	D_c	D_c	D_c
0	0.11	0.71	0.07
60	0.95	0.79	0.10
120	0.81	0.13	0.32
180	0.12	0.12	0.15
CNF-2			
	3 Days	7 Days	14 Days
Angle	D_c	D_c	D_c
0	3.09	2.64	0.59
60	3.46	2.05	2.07
120	2.99	2.14	1.94
180	1.21	0.99	1.81
CNF-3			
	3 Days	7 Days	14 Days
Angle	D_c	D_c	D_c
0	0.71	0.44	0.31
60	1.48	1.01	0.38
120	0.49	0.64	0.37
180	1.06	0.52	0.23

4.5 Conclusions

In this study, the effects of three different nitro-oxidized CNF suspensions were examined on cement paste specimens. Based on visual observations, the inclusion of CNF suspensions appeared to thicken the paste mixtures and increase the time required for the paste to harden. Furthermore, it was observed that the inclusion of CNF suspensions delayed the hydration process, which may be attributed to the presence of organic materials in the CNF, such as lignin. This was evidenced by the results obtained from isothermal calorimetry, LT-DSC, XRD, and TGA. Notably, CNF-2 (derived from cabbage) demonstrated a faster hydration rate compared to CNF-1 (derived from bagasse) and CNF-3 (derived from jute). Furthermore, LT-DSC results showed inclusion of CNF suspensions lowered the freezing point of pore solution, with CNF-2 showing the lowest freezing point, followed by CNF-3, CNF-1, and CP. In compression testing of varying samples after being subjected to freezing and thawing, CP, CNF-1, and CNF-2 performed similarly, while CNF-3 exhibited the highest strength. However, CNF-2 and CNF-3 demonstrated the smallest percentage change in compressive strength (46 %), followed by CNF-1 (47 %), whereas CP displayed the largest percentage change (71 %). This indicated that CNF-2 and CNF-3 had the highest

freeze/thaw resistance, although the differences between the compression testing values were not significantly different. In freeze/thaw testing, CNF-2 performed best regarding the percent decrease in dynamic modulus, percent decrease in ultrasonic pulse velocity, and percent decrease in mass loss. These results indicate that the inclusion of CNF suspensions can improve the freeze/thaw characteristics of cementitious materials; however, the difference when comparing CNF samples to CP was not statistically significant for these parameters. TXM successfully determined the Dc values for all samples, in spite that they were all very small. CNF-1 and CNF-3 exhibited the highest resistance to diffusion, followed by CP and CNF-2. This underscores the potential of CNF suspensions to reduce diffusion rates and enhance the overall performance of cementitious matrices against chloride ingress or diffusion mechanisms.

Based on the above results, it is recommended that additional microstructural analysis be conducted on samples containing CNF suspensions to achieve a comprehensive understanding of microstructure of the samples. In addition, the impact of freeze/thaw cycles on chloride ingress should be investigated by the TXM method. Further investigation is also required to examine the cumulative impact of seawater exposure and freeze/thaw cycles on paste samples incorporated with CNF suspensions. While these results are promising, more work is needed to ensure that similar results can carry over to mortar and concrete mixtures.

Acknowledgement

This material is based upon work supported by the Broad Agency Announcement Program and the Cold Regions Research and Engineering Laboratory (ERDC-CRREL) under Contract No. W913E522C0001. The authors would like to express their gratitude for the support and resources provided by the facilities at the Materials Characterization Laboratory and Holden Hall at Virginia Tech, which were essential to the success of this study. Special thanks go to Dr. Thomas Staley for his invaluable guidance in conducting LT-DSC experiments and Dr. Rasel Das for assisting in the preparation of CNF using the NOP approach. The authors also acknowledge the use of transmission electron microscopy at the Center for Functional Nanomaterials (CFN), a U.S. DOE Office of Science User Facility, at Brookhaven National Laboratory (DE-SC0012704). The authors also thank Prof. Miriam Rafailovich from the Materials Science and Chemical Engineering department at Stony Brook University, for granting access to the DSC facility.

Disclaimer

Any opinions, findings and conclusions or recommendations expressed in this material are those of the author(s) and do not necessarily reflect the views of the Broad Agency Announcement Program and ERDC-CRREL.

References

[1] M. Dabas, B. Martín-Pérez, H. Almansour, Combined Effects of Freeze-Thaw and Corrosion on Performance of RC Structures: State-of-the-Art Review, Journal of Performance of Constructed Facilities 35 (2021). https://doi.org/10.1061/(asce)cf.1943-5509.0001637.

[2] H.S. Shang, T.H. Yi, Freeze-thaw durability of air-entrained concrete, The Scientific World Journal 2013 (2013). https://doi.org/10.1155/2013/650791.

[3] P. Reiterman, O. Holčapek, O. Zobal, M. Keppert, Freeze-Thaw Resistance of Cement Screed with Various Supplementary Cementitious Materials, Reviews on Advanced Materials Science 58 (2019) 66–74. https://doi.org/10.1515/rams-2019-0006.

[4] Y. Şahin, Y. Akkaya, M.A. Taşdemir, Effects of freezing conditions on the frost resistance and microstructure of concrete, Construction Building Materials 270 (2021). https://doi.org/10.1016/j.conbuildmat.2020.121458.

[5] J. Bai, S. Wild, B.B. Sabir, Chloride ingress and strength loss in concrete with different PC-PFA-MK binder compositions exposed to synthetic seawater, Cement and Concrete Research 33 (2003) 353–362. https://doi.org/10.1016/S0008-8846(02)00961-4.

[6] S. Kessler, C. Thiel, C.U. Grosse, C. Gehlen, Effect of freeze–thaw damage on chloride ingress into concrete, Materials and Structures 50 (2017). https://doi.org/10.1617/s11527-016-0984-4.

[7] X.J. Gao, X.Y. Wang, Impacts of globalwarming and sea level rise on service life of chloride-exposed concrete structures, Sustainability (Switzerland) 9 (2017). https://doi.org/10.3390/su9030460.

[8] Y. Yi, D. Zhu, S. Guo, Z. Zhang, C. Shi, A review on the deterioration and approaches to enhance the durability of concrete in the marine environment, Cement and Concrete Composite 113 (2020). https://doi.org/10.1016/j.cemconcomp.2020.103695.

[9] F. Cui, L. Song, X. Wang, M. Li, P. Hu, S. Deng, X. Zhang, H. Li, Seismic Fragility Analysis of the Aging RC Columns under the Combined Action of Freeze–Thaw Cycles and Chloride-Induced Corrosion, Buildings 12 (2022). https://doi.org/10.3390/buildings12122223.

[10] M. Zhang, J. Cui, K. Liu, S. Sun, Study on the durability deterioration law of marine concrete with nano-particles under the coupled effects of freeze-thaw cycles, flexural fatigue load and Cl− erosion, Journal of Building Engineering 87 (2024) 109039. https://doi.org/https://doi.org/10.1016/j.jobe.2024.109039.

[11] B. Diao, Y. Sun, Y. Ye, S. Cheng, Impact of seawater corrosion and freeze-thaw cycles on the behavior of eccentrically loaded reinforced concrete columns, Ocean Systems Engineering 2 (2012) 159–171.

[12] P. Zhang, F.H. Wittmann, M. Vogel, H.S. Müller, T. Zhao, Influence of freeze-thaw cycles on capillary absorption and chloride penetration into concrete, Cement and Concrete Research 100 (2017) 60–67. https://doi.org/10.1016/j.cemconres.2017.05.018.

[13] A. Pilvar, A.A. Ramezanianpour, H. Rajaie, New method development for evaluation concrete chloride ion permeability, Construction and Building Materials 93 (2015) 790–797. https://doi.org/10.1016/j.conbuildmat.2015.05.092.

[14] M.K. Moradllo, M.T. Ley, Comparing ion diffusion in alternative cementitious materials in real time by using non-destructive X-ray imaging, Cem Concr Compos 82 (2017) 67–79. https://doi.org/10.1016/j.cemconcomp.2017.05.014.

[15] M.K. Moradllo, M.T. Ley, Quantitative measurement of the influence of degree of saturation on ion penetration in cement paste by using X-ray imaging, Construction and Building Materials 141 (2017) 113–129. https://doi.org/10.1016/j.conbuildmat.2017.03.007.

[16] M.K. Moradllo, Q. Hu, M.T. Ley, Using X-ray imaging to investigate in-situ ion diffusion in cementitious materials, Construction and Building Materials 136 (2017) 88–98. https://doi.org/10.1016/j.conbuildmat.2017.01.038.

[17] Ley, M.T., Parestegari, N., Behravan, A., Cook, D. and Hu, Q.,. *Measuring concrete permeability with CHIP*. Final report for NCHRP IDEA Project 232. Oklahoma State University, National Cooperative Highway Research Program (NCHRP), Innovations Deserving Exploratory Analysis (IDEA) Programs, Transportation Research Board, National Academies of Sciences, Engineering, and Medicine(2023).

[18] A. Behravan, M.T. Ley, A. Rywelski, N. Berke, Changes in the rate of ion penetration of alternative cementitious materials with time, Mater Des 197 (2021). https://doi.org/10.1016/j.matdes.2020.109236.

[19] J. Goncalves, Y. Boluk, V. Bindiganavile, Cellulose nanofibres mitigate chloride ion ingress in cement-based systems, Cement and Concrete Composite 114 (2020) 103780. https://doi.org/https://doi.org/10.1016/j.cemconcomp.2020.103780.

[20] D. Barnat-Hunek, M. Grzegorczyk-Frańczak, M. Szymańska-Chargot, G. Łagód, Effect of Eco-Friendly Cellulose Nanocrystals on Physical Properties of Cement Mortars, Polymers (Basel) 11 (2019). https://doi.org/10.3390/polym11122088.

[21] D. Barnat-Hunek, M. Szymańska-Chargot, M. Jarosz-Hadam, G. Łagód, Effect of cellulose nanofibrils and nanocrystals on physical properties of concrete, Construction and Building Materials 223 (2019) 1–11. https://doi.org/https://doi.org/10.1016/j.conbuildmat.2019.06.145.

[22] K. Wu, H. Han, L. Xu, Y. Gao, Z. Yang, Z. Jiang, G. De Schutter, The improvement of freezing–thawing resistance of concrete by cellulose/polyvinyl alcohol hydrogel, Construction and Building Materials 291 (2021). https://doi.org/10.1016/j.conbuildmat.2021.123274.

[23] L. Jiao, M. Su, L. Chen, Y. Wang, H. Zhu, H. Dai, Natural cellulose nanofibers as sustainable enhancers in construction cement, PLoS One 11 (2016). https://doi.org/10.1371/journal.pone.0168422.

[24] X. Zhang, C. Lei, Z. Li, A. Zhang, W. Zhao, W. Zhang, J. Xu, P. Guo, Effect of Cellulose Nanofibrils on the Physical Properties and Frost Resistance of Pervious Concrete, Materials 15 (2022). https://doi.org/10.3390/ma15227906.

[25] K. Wu, H. Han, L. Xu, Y. Gao, Z. Yang, Z. Jiang, G. De Schutter, The improvement of freezing–thawing resistance of concrete by cellulose/polyvinyl alcohol hydrogel, Construction and Building Materials 291 (2021). https://doi.org/10.1016/j.conbuildmat.2021.123274.

[26] K.S. Kamasamudram, W. Ashraf, E.N. Landis, R.I. Khan, Effects of ligno– and delignified–cellulose nanofibrils on the performance of cement-based materials, Journal of Materials Research and Technology 13 (2021) 321–335. https://doi.org/10.1016/j.jmrt.2021.04.090.

[27] H.H. Kolour, W. Ashraf, E.N. Landis, Hydration and early age properties of cement pastes modified with cellulose nanofibrils, in: Transportation Research Records, SAGE Publications Ltd, 2021: pp. 38–46. https://doi.org/10.1177/0361198120945993.

[28] J. Goncalves, Y. Boluk, V. Bindiganavile, Cellulose nanofibres mitigate chloride ion ingress in cement-based systems, Cement and Concrete Composite 114 (2020). https://doi.org/10.1016/j.cemconcomp.2020.103780.

[29] S. Nassiri, Z. Chen, G. Jian, T. Zhong, M.M. Haider, H. Li, C. Fernandez, M. Sinclair, T. Varga, L.S. Fifield, M. Wolcott, Comparison of unique effects of two contrasting types of cellulose nanomaterials on setting time, rheology, and compressive strength of cement paste, Cement and Concrete Composite 123 (2021). https://doi.org/10.1016/j.cemconcomp.2021.104201.

[30] A. Elmgerbi, I.A. Askar, A. Fine, G. Thonhauser, R. Ashena, Cellulose nanocrystals (CNCs) as a potential additive for improving API class G cement performance: An experimental study, Natural Gas Industry B 10 (2023) 233–244. https://doi.org/https://doi.org/10.1016/j.ngib.2023.05.001.

[31] T. Shi, Z. Li, J. Guo, H. Gong, C. Gu, Research progress on CNTs/CNFs-modified cement-based composites – A review, Construction and Building Materials 202 (2019) 290–307. https://doi.org/10.1016/j.conbuildmat.2019.01.024.
[32] X. Gao, J. Wu, Y. Wang, Y. Wang, Y. Zhang, T.T. Nguyen, M. Guo, Anti-freezing hydrogel regulated by ice-structuring proteins/cellulose nanofibers system as flexible sensor for winter sports, Int J Biol Macromol 265 (2024) 131118. https://doi.org/https://doi.org/10.1016/j.ijbiomac.2024.131118.
[33] P.R. Sharma, B. Zheng, S.K. Sharma, C. Zhan, R. Wang, S.R. Bhatia, B.S. Hsiao, High Aspect Ratio Carboxycellulose Nanofibers Prepared by Nitro-Oxidation Method and Their Nanopaper Properties, ACS Applied Nano Materials 1 (2018) 3969–3980. https://doi.org/10.1021/acsanm.8b00744.
[34] S.K. Sharma, P.R. Sharma, K.I. Johnson, Y. Madan, S. Li, G. Cai, I. Brahmbhatt, W. Borges, B.S. Hsiao, Chapter 6 - Plant-derived carboxycellulose: Highly efficient bionanomaterials for removal of toxic lead from contaminated water, in: S. Ahuja (Ed.), Sep Sci Technol, Academic Press, 2022: pp. 87–95. https://doi.org/https://doi.org/10.1016/B978-0-323-90763-7.00004-4.
[35] J. Han, Preparation and characterization of cellulose nanoparticles and their application in biopolymeric nanocomposites, Louisiana State University and Agricultural & Mechanical College, 2013.
[36] P.R. Sharma, R. Joshi, S.K. Sharma, B.S. Hsiao, A Simple Approach to Prepare Carboxycellulose Nanofibers from Untreated Biomass, Biomacromolecules 18 (2017) 2333–2342. https://doi.org/10.1021/acs.biomac.7b00544.
[37] R. Wang, H. He, P.R. Sharma, J. Tian, L.D. Söderberg, T. Rosén, B.S. Hsiao, Unexpected Gelation Behavior of Cellulose Nanofibers Dispersed in Glycols, Macromolecules 55 (2022) 9527–9536. https://doi.org/10.1021/acs.macromol.2c01035.
[38] ASTM C1437-20, Standard Test Method for Flow of Hydraulic Cement Mortar, ASTM International (2020). https://doi.org/10.1520/C1437.
[39] A. Alzaza, K. Ohenoja, I. Langås, B. Arntsen, M. Poikelispää, M. Illikainen, Low-temperature (−10 °C) curing of Portland cement paste – Synergetic effects of chloride-free antifreeze admixture, C–S–H seeds, and room-temperature pre-curing, Cement and Concrete Composite 125 (2022). https://doi.org/10.1016/j.cemconcomp.2021.104319.
[40] A. Alzaza, K. Ohenoja, V. Isteri, T. Hanein, D. Geddes, M. Poikelispää, M. Illikainen, Blending eco-efficient calcium sulfoaluminate belite ferrite cement to enhance the physico–mechanical properties of Portland cement paste cured in refrigerated and natural winter conditions, Cement and Concrete Composite 129 (2022). https://doi.org/10.1016/j.cemconcomp.2022.104469.
[41] G. Zhang, Y. Yang, H. Yang, H. Li, Calcium sulphoaluminate cement used as mineral accelerator to improve the property of Portland cement at sub-zero temperature, Cement and Concrete Composite 106 (2020). https://doi.org/10.1016/j.cemconcomp.2019.103452.

[42] S. Zhang, Y. Zhao, H. Ding, J. Qiu, C. Hou, Effect of sodium chloride concentration and pre-curing time on the properties of cemented paste backfill in a sub-zero environment, Journal of Cleaner Production 283 (2021). https://doi.org/10.1016/j.jclepro.2020.125310.
[43] A. Damasceni, L. Dei, E. Fratini, F. Ridi, S.H. Chen, P. Baglioni, A novel approach based on differential scanning calorimetry applied to the study of tricalcium silicate hydration kinetics, Journal of Physical Chemistry B 106 (2002) 11572–11578. https://doi.org/10.1021/jp020211l.
[44] E. Xanthakis, A. Le-Bail, H. Ramaswamy, Development of an innovative microwave assisted food freezing process, Innovative Food Science and Emerging Technologies 26 (2014) 176–181. https://doi.org/10.1016/j.ifset.2014.04.003.
[45] X. Feng, E.J. Garboczi, D.P. Bentz, P.E. Stutzman, T.O. Mason, X. Fenga, E.J. Garboczia, D.P. Bentza, P.E. Stutzmana, T.O. Masonb, Estimation of the degree of hydration of blended cement pastes by a scanning electron microscopy point-counting procedure, Cement and Concrete Research, *34*(10), pp.1787-1793. https://doi.org/10.1016/j.cemconres.2004.01.014
[46] D.C. Chu, J. Kleib, M. Amar, M. Benzerzour, N.E. Abriak, Determination of the degree of hydration of Portland cement using three different approaches: Scanning electron microscopy (SEM-BSE) and Thermogravimetric analysis (TGA), Case Studies in Construction Materials 15 (2021). https://doi.org/10.1016/j.cscm.2021.e00754.
[47] J.W. Bullard, D.L. Evans, P.J. Bond, The Virtual Cement and Concrete Testing Laboratory Consortium The Virtual Cement and Concrete Testing Laboratory Consortium Annual Report 2003, 2003.
[48] ASTM Standard C666/C666M-15, Standard Test Method for Resistance of Concrete to Rapid Freezing and Thawing, ASTM International (2015). https://doi.org/10.1520/C0666_C0666M-15.
[49] ASTM Standard C215-19, Standard Test Method for Fundamental Transverse, Longitudinal, and Torsional Resonant Frequencies of Concrete Specimens, ASTM International (2019). https://doi.org/10.1520/C0215-19.
[50] ASTM Standard C597-22, Standard Test Method for Ultrasonic Pulse Velocity Through Concrete, ASTM International (2022). https://doi.org/10.1520/C0597-22.
[51] ASTM Standard C39/C39M-21, Standard Test Method for Compressive Strength of Cylindrical Concrete Specimens, ASTM International (2021). https://doi.org/10.1520/C0039_C0039M-21.
[52] ASTM Standard C1231/C1231M/23, Standard Practice for Use of Unbonded Caps in Determination of Compressive Strength of Hardened Cylindrical Concrete Specimens, ASTM International (2023). https://doi.org/10.1520/C1231_C1231M-23.
[53] Md.H.H. Rahat, T.Q. Tran, B.D.J.E. Love, A. Behravan, A.S. Brand, Investigating the Impact of Freeze–Thaw Damage on Chloride Ingress in Concrete, in: Cold Regions Engineering 2024, n.d.: pp. 575–585. https://doi.org/10.1061/9780784485460.053.

[54] A. Behravan, M.T. Ley, D. Cook, Q. Hu, A. Rywelski, R. Brorsen, Measuring the Diffusion Coefficient of Paste and Concrete by Using Dental X-ray Equipment, CivilEng 4 (2023) 224–247. https://doi.org/10.3390/civileng4010014.

[55] A. Behravan, M.T. Ley, A. Rywelski, N. Berke, Changes in the rate of ion penetration of alternative cementitious materials with time, Mater Des 197 (2021). https://doi.org/10.1016/j.matdes.2020.109236.

[56] M. Khanzadeh Moradllo, M.T. Ley, Quantitative measurement of the influence of degree of saturation on ion penetration in cement paste by using X-ray imaging, Construction and Building Materials 141 (2017) 113–129. https://doi.org/10.1016/j.conbuildmat.2017.03.007.

[57] M. Khanzadeh Moradllo, M.T. Ley, Comparing ion diffusion in alternative cementitious materials in real time by using non-destructive X-ray imaging, Cement and Concrete Composite 82 (2017) 67–79. https://doi.org/10.1016/j.cemconcomp.2017.05.014.

[58] ASTM C1556-22, Standard Test Method for Determining the Apparent Chloride Diffusion Coefficient of Cementitious Mixtures by Bulk Diffusion 1, ASTM International (2022). https://doi.org/10.1520/C1556-22.

[59] N. Nair, M.I. Haque, S. Siddique, R.I. Khan, W. Ashraf, K. Gourlay, S. Shah, Role of delignified and lignin-containing cellulose nanofibers in enhancing durability performances of portland cement composites, Cement and Concrete Composite 145 (2024). https://doi.org/10.1016/j.cemconcomp.2023.105316.

[60] H.J. Kim, S. Roy, J.W. Rhim, Effects of various types of cellulose nanofibers on the physical properties of the CNF-based films, Journal of Environmental Chemical Engineering 9 (2021). https://doi.org/10.1016/j.jece.2021.106043.

[61] Z. Xu, H. Zhou, S. Tan, X. Jiang, W. Wu, J. Shi, P. Chen, Ultralight super-hydrophobic carbon aerogels based on cellulose nanofibers/poly(vinyl alcohol)/graphene oxide (CNFs/PVA/GO) for highly effective oil-water separation, Beilstein Journal of Nanotechnology 9 (2018) 508–519. https://doi.org/10.3762/bjnano.9.49.

[62] W. Zhu, Y. Zhang, X. Wang, Y. Wu, M. Han, J. You, C. Jia, J. Kim, Aerogel nanoarchitectonics based on cellulose nanocrystals and nanofibers from eucalyptus pulp: preparation and comparative study, Cellulose 29 (2022) 817–833. https://doi.org/10.1007/s10570-021-04370-z.

Chapter 5. Effect of Freeze/Thaw and Substrate Moisture Condition on the Concrete Repair-Substrate Interface[4]

The contributions of the authors to this manuscript are described as follows:

Md Hasibul Hasan Rahat: Conceptualization, Methodology, Formal analysis, Investigation, Writing–original draft; Writing–review and editing.

Douglas Annand: Methodology, Formal analysis, Investigation, Writing–review and editing;

Paul Atwood: Methodology, Investigation;

Amir Behravan: Methodology, Formal analysis;

Alexander S. Brand: Conceptualization, Writing–review and editing, Writing–original draft, Supervision, Project administration, Methodology.

[4] **Rahat, M. H. H.**, Annand, D., Atwood, P., Behravan, A., & Brand, A. S. (2024). Effect of Freeze/Thaw and Substrate Moisture Condition on the Concrete Repair-Substrate Interface. In *13th International Conference on Concrete Pavements | Minneapolis, Minnesota, USA*. https://doi.org/10.33593/vabb8064.

Effect of Freeze/Thaw and Substrate Moisture Condition on the Concrete Repair-Substrate Interface

Rahat, M.H.H.[1], Annand, D.M.[2], Atwood, P.J.[3], Behravan, A.[4] and Brand, A.S.[5]

[1]Md Hasibul Hasan Rahat; MSc; MBA; Graduate Research Assistant in the Via Department of Civil and Environmental Engineering; Virginia Tech, USA; rahatm21@vt.edu

[2] Douglas M. Annand; MSc; EIT; Structural Engineer at Whitman, Requardt, and Associates; USA; dannand@vt.edu

3 Paul Atwood; MSc; Via Department of Civil and Environmental Engineering; Virginia Tech, USA; pjatwood@vt.edu

[4] Amir Behravan; PhD; PE; Research Scientist at Virginia Transportation Research Council; VDOT, USA; Amir.Behravan@vdot.virginia.gov

[5] Alexander S. Brand; PhD; PE; Assistant Professor in the Via Department of Civil and Environmental Engineering; Virginia Tech; USA; asbrand@vt.edu

*Corresponding Author: rahatm21@vt.edu, asbrand@vt.edu

5.1 Abstract

The impact of moisture conditions on the overlay transition zone (OTZ) in cement-based concrete pavement repairs was investigated in this study. The OTZ plays a crucial role in bond formation between the repair material and substrate, similar to the interfacial transition zone in concrete. The mechanical properties, fracture properties, and chloride diffusion characteristics of the OTZ were examined and also the effect of freeze/thaw (F-T) cycling were explored, which is a common environmental condition experienced by concrete pavements. A novel technique, transmission X-ray microscopy (TXM), was used to quantify the time-dependent chloride diffusion coefficient within the OTZ before and after F-T cycles. The findings reveal that, while moisture levels do not appear to directly impact F-T damage resistance in mechanical tests, the moisture conditions significantly influence fracture properties. For instance, the average peak load reductions were 65% and 81% for repair specimens prepared against substrates at saturated surface dry (SSD) and oven dry conditions, respectively. Additionally, the TXM results show that the OTZ interface has a higher diffusion coefficient – upwards of nine orders of magnitude higher – than the concrete substrate. Between the substrate moisture conditions, the SSD specimens showed better performance against diffusion than the Sub-SSD. In conclusion, this study provides valuable insights into the complex relationship between moisture conditions, F-T cycling, and fracture properties of OTZ in concrete pavement repairs. These findings contribute to a more informed approach to pavement repair practices with potential implications for enhancing the longevity and performance of repaired concrete pavements.

Keywords: Freeze/Thaw cycle, Repair, Overlay Transition Zone, Diffusion, Fracture

5.2 Introduction

In repairs of concrete pavements with a cement-based repair material, an overlay transition zone (OTZ) is known to form (Beushausen et al., 2017; Li et al., 2001.; Zhou et al., 2016), which is analogous to the interfacial transition zone (ITZ) that is known to form between cement paste and aggregates (Scrivener et al., 2004). While a number of factors will affect the mechanical bond between the repair and the substrate, such as surface roughness, repair material design, use of bonding agents, *etc*. (Fathy et al., 2022), the importance of surface moisture condition of the substrate has received little attention relative to these other factors. While relatively few studies (*e.g.*, Beushausen et al., 2017; Courard et al., 2011; Júlio et al., 2004; Lukovic and Ye, 2016) have considered the effect of substrate moisture condition on the bond performance, no studies have considered how the substrate moisture condition impacts the fracture properties and durability of the bond. Previous research by the authors has established that the ITZ with recycled concrete aggregates is drastically affected by the aggregate moisture condition (Brand and Roesler, 2018), so this study hypothesized that the OTZ would be affected similarly. Specifically, this study focused on how the substrate moisture condition influences the bond formation and the OTZ by extension. Mechanical and fracture properties and the chloride diffusion along the OTZ were all explored in this study, including how freeze/thaw (F-T) affects this bond.

5.2.1 Significance of the Study

The performance of bonded concrete overlays and concrete-concrete pavement repairs (*e.g.*, partial and full depth repairs, patching) can be significantly diminished by F-T cycling and chloride ingress (Freeseman et al., 2022; Guo et al., 2018; Li et al., 2021; Ram et al., 2016). Previous data in the literature have not sufficiently established the impact of substrate moisture condition at the time of repair casting on the fracture and F-T durability properties and on the chloride ingress along the OTZ. This study is also the first to utilize a novel non-destructive technique, transmission X-ray microscopy (TXM), to quantify the time-dependent diffusion coefficient along the OTZ.

5.3 Experimental Design

5.3.1 Materials and Mix Design

The water-to-cement material (w/c) ratio employed in this study was determined to be 0.45, based on the ACI 211-1 design procedure (Dixon et al., 1991). This ratio was used to mix both the substrate and the repair portion of the concrete. The concrete mix design used in this study is presented in Table 1. The concrete was not air-entrained.

Table 5- 1 Concrete mix design

Component	**Design (lb/yd^3)**	**Design (kg/m^3)**
Cement	744.4	441.6
Water	335.0	198.7
Fine Aggregate (FA)	1561.0	926.1
Coarse Aggregate (CA)	1305.1	774.3

The concrete mix design used Type I/II portland cement and a polycarboxylate superplasticizer dosed at 97.59 ml per 100 kg of cement. The specific gravity values for cement, fine aggregate (FA), and coarse aggregate (CA) were 3.15, 2.57, and 2.77, respectively. Additionally, the absorption capacity of FA and CA was 3.6% and 1.4%, respectively. The aggregates were oven dried and cooled prior to mixing, and the mixing water was adjusted accordingly to account for aggregate absorption.

5.3.2 Sample Preparation

The substrate material used in this study was prepared according to ASTM C192. Specifically, the specimens were batched in prism molds measuring 75 mm by 75 mm by 305 mm for flexural strength testing and 80 mm by 150 mm by 700 mm for fracture testing and cylinder molds measuring 100 mm diameter and 200 mm height. After a moist curing period of 35 days, both the beam and cylinder specimens underwent saw-cutting at the midspan. Following the cutting process, the substrate halves underwent a thorough cleaning and scrubbing procedure in water to eliminate residual debris. Subsequently, the cleaned substrate halves were transferred to an environmental chamber where they were exposed to a predetermined relative humidity level for 18 ± 2 h. The moisture conditions assessed in this study included three distinct states: saturated surface dry (SSD), sub-saturated surface dry (Sub-SSD), and oven dry (OD). An environmental chamber was used to ensure consistent substrate moisture conditions during all testing procedures. The use of an environmental chamber facilitated conditioning of the specimens within a controlled environment, wherein the temperature and humidity were regulated to ensure the highest precision across a wide range of desired moisture conditions. The environmental chamber maintained a constant 23^{o}C temperature and relative humidity levels of 98%, 80%, and 10% to achieve the SSD, Sub-SSD, and OD conditions, respectively.

Following the completion of the substrate conditioning, the substrate halves were removed from the chamber and subsequently repositioned within the molds. The repair concrete was cast alongside the substrate halves within the molds. The repair concrete used the same mix design as the substrate concrete. The experimental procedure was carried out for every specified moisture condition. Subsequently, the specimens designated for substrate repair underwent a moist curing process spanning an additional 35 days in preparation for the subsequent experimental testing phase.

5.3.3 Experimental Procedure

Strength testing was performed before and after F-T cycling. Fracture testing was conducted to investigate the impact of moisture content on the OTZ before but not after F-T cycling. Compressive and flexural strength tests followed ASTM C39 and ASTM C293, respectively. Fracture testing followed the RILEM draft standards (RILEM TC 89-FMT, 1990a, 1990b). After completing the sample preparation, compressive and flexural testing specimens underwent 20 F-T cycles in accordance with the guidelines outlined in ASTM C666.

5.3.3 Transmission X-ray Microscope (TXM)

A custom-built TXM system was utilized to quantify the apparent diffusion coefficient (Dc) in the OTZ of the substrate-repair concrete. To investigate the Dc of the OTZ of the repair substrate-repair concrete in terms of F-T cycles, 125 F-T cycles were conducted, and two different moisture conditions were considered: SSD and Sub-SSD. This system was constructed following the design by Behravan et al. (2023). *Figure 5- 1* shows the schematic of the system. To track the gray value changes over time, images were taken in a consistent orientation. *Figure 5- 2*(c) shows the sample test setup used with TXM to ensure consistent orientations for each image. It should be noted that the TXM system is very fast to complete the measurement: the exposure time is 0.25 s and it takes only 5 seconds to complete the X-ray imaging.

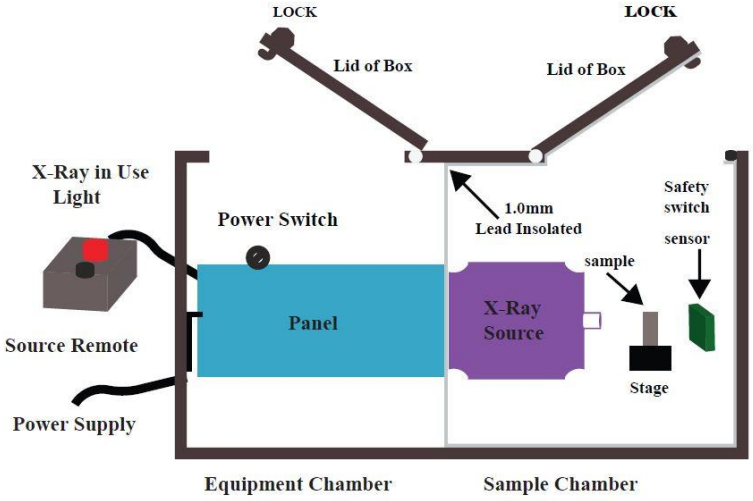

Figure 5- 1 Schematic view of TXM system.

5.3.3.1 Sample Preparation for Diffusion Test in TXM

To measure the chloride ion diffusion rate of the OTZ, 19 mm diameter cores were cut from the OTZ of the substrate-repair concrete prior F-T testing. Except for the top surface, the sides of the specimens were sealed with a hydrophobic wax. This allowed one-dimensional diffusion from the top surface of the specimen, following ASTM C1556. A hexagonal nut was glued to the bottom of each specimen to fit the X-ray stage, which ensured that the same orientation was scanned for each measurement, as shown in *Figure 5- 2*(a).

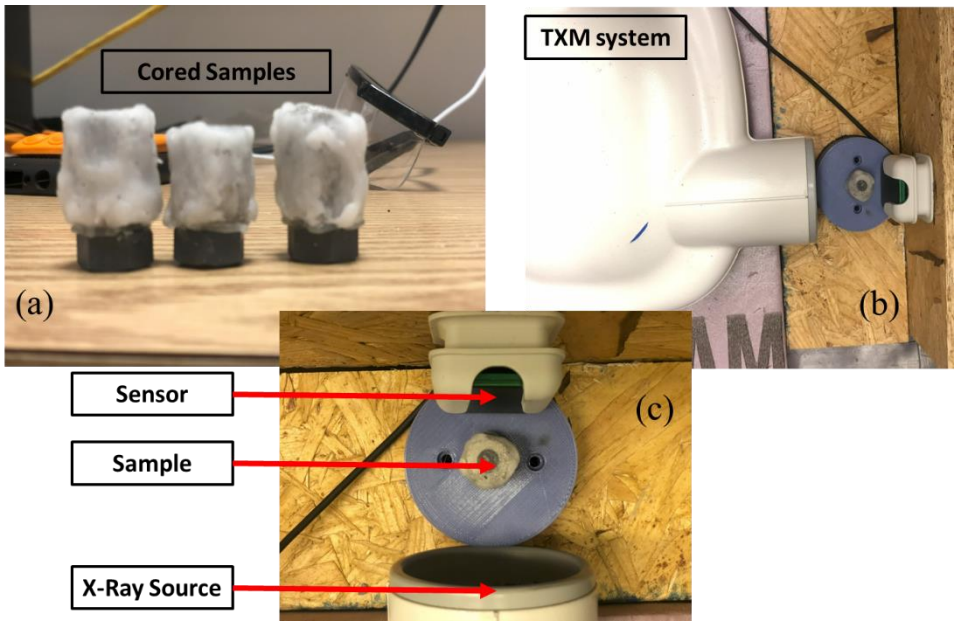

Figure 5- 2 (a) Cored prepared specimens for the TXM system; (b) TXM system; and (c) specimen on the stage ready for X-ray imaging.

A 0.6 M potassium iodide (KI) solution was used to pond the cored specimens. This concentration was chosen to ensure satisfactory contrast between the tracer and specimens. X-ray imaging can be used to detect iodide diffusing through concrete. Iodide and chloride ions are similar in size, and iodide has 24% higher diffusion coefficient than chloride; thus, iodide diffusion serves as a more conservative measurement of chloride diffusion (Behravan et al., 2023; Khanzadeh Moradllo et al., 2017).

5.3.3.2 Data Collection and Analysis Method

In this study, all core specimens were scanned to capture the initial images of the original specimens and the initial gray values were determined, which are referred to as the reference image. After that, the core specimens were ponded in 0.6 M KI solution, and the specimens were again scanned to capture images of the specimens after 3 days and 7 days so that the images could be easily compared with the reference image to evaluate the changes in gray values. For the specimens that underwent F-T cycles, a reference image was taken after 125 F-T cycles, and the specimens were then placed in 0.6 M KI solution and subjected to the same procedures to capture X-ray images.

To conduct the radiographic analysis, a software code was employed (Behravan et al., 2023) to align the radiographic images captured at 3-day and 7-day intervals following the ponding process with the corresponding reference image for each individual specimen. The alignment procedure involves the application of local displacements, specifically shifts and rotations, to the subsequent radiograph of a given specimen. This was performed to project the radiograph onto the reference

radiograph. *Figure 5- 3* shows the subtracted image of 3 days ponded specimen from the reference image under different moisture conditions, where the iodide concentration at the OTZ interface is visible in the subtracted image. The iodide concentration along the OTZ interface exhibits a "V" shape, which supports the findings of Li et al., (2023). To determine the mean gray values at various depths for each specimen, a region with a width of approximately 3.93 mm (equivalent to approximately 120 pixels in TXM radiographs) was employed, as shown in *Figure 5- 3*. This action was undertaken to mitigate the occurrence of cupping artifacts (Behravan et al., 2023). Every line exhibited a grayscale value corresponding to a distinct depth. The final profile of the gray values was determined by calculating the average of 120 individual lines. According to Beharavan et al. (2023), diverse angle radiographs are recommended for calculating the apparent diffusion coefficient (Dc) for concrete specimens, and the results should be reported as the average Dc. Because concrete is composite in nature, focusing only on the central strip of radiographs for analysis can be compromised by aggregate inconsistencies. In this study, radiographs were taken at angle of 0^{o} and 180^{o} for all specimens to calculate the apparent Dc.

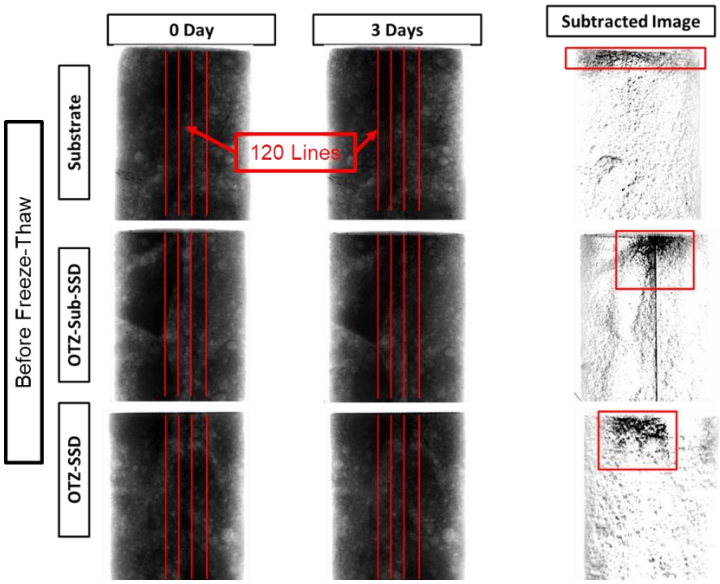

Figure 5- 3 Subtracted Radiograph for different moisture conditions in a specific region of interest.

Finally, the concentration profiles were analyzed using fitting procedures following Fick's second law of diffusion, as described in Equation (1), following ASTM C1556. By applying curve-fitting techniques to individual concentration profiles, it was possible to determine the values of the apparent diffusion coefficient (Dc) and surface concentration (Cs) for each specimen. The obtained Dc includes various liquid-transport mechanisms (*i.e.*, diffusion),

$$C_{(x,t)} = C_s\left(1 - \text{erf}\left(\frac{x}{2\sqrt{D_c t}}\right)\right) \qquad (1)$$

where, x = distance from the specimen surface, Dc = apparent diffusion coefficient, Cs = surface iodide concentration, and $C_{(x,t)}$ = iodide concentration at depth of x from the surface after time t.

5.4 Results and Discussions

5.4.1 Compressive and Flexural Strength

To investigate the internal microstructure damage after 20 freeze-thaw (F-T) cycles, compressive and flexural strength tests were conducted. The compressive strength and flexural strength results before and after F-T are depicted in Figure 5- 4.

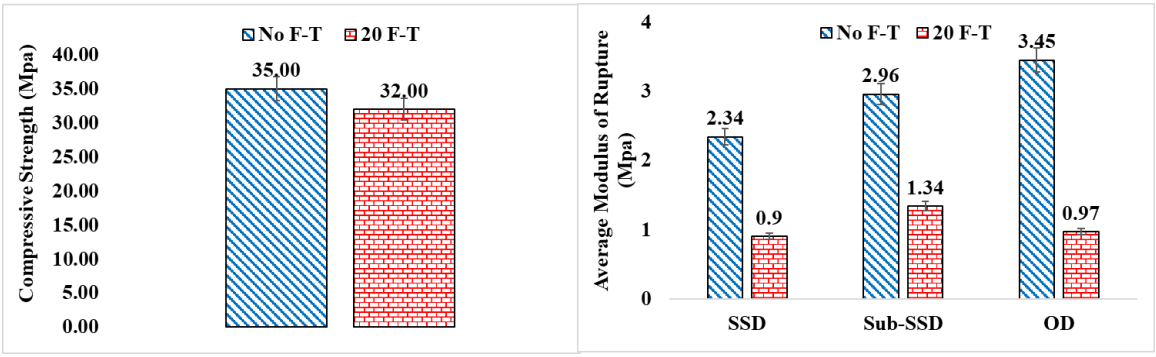

Figure 5- 4 Compressive strength of the concrete mix before and after F-T, and (b) flexural strength before and after F-T.

Figure 5- 4 reveals a 10% decline in compressive strength after 20 F-T cycles for the substrate concrete specimens, which is consistent with prior research (Komar and Boyd, 2017), since the concrete was not air entrained. Examining the data in Figure 4(b) shows no clear connection between moisture and F-T damage resistance. The Sub-SSD specimens had the highest flexural strength after the F-T cycles, while the SSD specimens had the lowest. All the specimens experienced a major decrease in flexural strength after 20 F-T cycles, with a reduction of over 50%. This is consistent with Sun et al. (1999), who found decreases of 33% and 25% for w/c ratios of 0.45 and 0.32 after 20 F-T cycles. The reductions observed in this study were more severe than those reported in other studies. This was likely due to the OTZ between the substrate-repair material and its inability to resist F-T damage, because higher porosity increases OTZ saturation (Beushausen et al., 2017), leading to greater F-T damage. The literature suggests that initial cracks along the ITZ propagate during F-T cycling, leading to increased degradation in this region (Yang et al., 2018).

5.4.2 Fracture Properties

The results of peak load (P_{max}), modulus of elasticity (E), critical stress intensity factor (K_{IC}), critical crack tip opening displacement ($CTOD_c$), initial fracture energy (G_{IC}), and total fracture energy (G_F) from fracture testing for different moisture conditions are displayed in Table 2. A few instances of premature failure were observed during testing. These failures have been thoroughly reported and are clearly distinguishable from the rest of the data in the presentation.

A comprehensive analysis of the fracture test results presented in Table 5- 2 provides several crucial insights. The specimens cast at Sub-SSD substrate moisture conditions and those subjected to OD conditions displayed unloading failures, indicating potential deficiencies in the bonding strength between the substrate and repair materials, which likely contributed to the lack of adhesion observed during both loading and unloading phases. The fracture parameters, including the peak load, critical stress intensity factor, and both the initial and total fracture energies, demonstrated a noticeable decline, highlighting compromised structural integrity when bonding issues were present. For the SSD and OD specimens the average peak load reductions were 65% and 81%, respectively, which is consistent with previous studies on OTZ weakness between the substrate and repair concrete (Li et al., 2023). The coefficient of variation (COV) for the substrate-repaired specimens was notably high, indicating a substantial variation in the measured data, emphasizing the inherent unpredictability of the fracture response. The increase in the coefficient of variation (COV) from SSD to OD indicates that unpredictability is exacerbated at lower moisture levels. Increased unpredictability may lead to reluctance to use the OD condition for field repairs, as the outcomes could vary considerably. Furthermore, Sub-SSD specimens exhibited relative weak bond strengths, with three instances of failure occurring before the material could respond to any unloading response. All specimens exhibited failure directly through the OTZ, indicating insufficient adhesion between the interfaces. Finally, these findings highlight the complex challenges involved in achieving robust adhesion and predictable fracture behavior within bonded overlays, particularly when faced with varying moisture conditions and interface gradation issues.

Table 5- 2 Fracture properties of different moisture conditions specimens

Substrate Condition	No.	P_{max} (kN)	E (GPa)	K_{IC} (MPa-$m^{1/2}$)	$CTOD_c$ (mm)	G_{IC} (N/m)	G_F (N/m)
Substrate	1	4.76	27.7	2.117	0.0680	161.7	244.1
	2	3.46	28.3	1.249	0.0235	55.1	138.9
	3	3.58	23.6	1.034	0.0247	45.2	161.3
	4	4.45	33.7	1.879	0.0465	104.8	242.0
	Avg.	4.06	28.3	1.570	0.0407	91.7	196.6
	COV	15.7%	14.6	32.6%	51.8%	58.3%	27.7%
SSD	1	1.37	25.9	0.355	.0049	4.9	14.1
	2	0.64	19.0	0.168	0.0023	1.5	13.8
	3	1.22	24.9	0.315	.0049	4.0	10.2
	4	0.93	17.9	0.271	.0060	4.1	11.1
	Avg.	1.04	21.9	0.277	.0045	3.6	12.3
	COV	31.1%	4.1%	29.05	34.7%	40.6%	15.8%
Sub-SSD	1	0.89	15.9	-	-	-	1.26
	2	1.66	28.3	-	-	-	1.33
	3	1.58	23.1	0.311	.0040	4.7	4.7
	4	1.58	26.1	-	-	-	24.3
	Avg.	1.43	23.4	-	-	-	-
	COV	21.8%	20.1%	-	-	-	7.9
OD	1	0.79	21.5	0.234	0.0048	2.6	8.1
	2	1.14	29.8	0.420	0.0087	5.9	14.3
	3	0.27	8.0	0.088	0.0029	1.0	4.1
	4	0.95	18.0	-	-	-	1.2
	Avg.	0.79	19.3	0.247	0.0055	3.2	6.9
	COV	47.6%	46.7%	67.3%	54.1%	78.9%	81.9%

5.4.3 Concentration Profile and Time-Dependent Diffusion Coefficient of OTZ

For the TXM study, only SSD and Sub-SSD conditions were considered due to the higher coefficient of variation (COV) observed in the fracture testing results for the OD condition. The Dc within the OTZ of substrate-repaired concrete was quantified before and after subjecting the specimens to 125 F-T cycles using TXM. It should be noted that the concentration profile and Dc represent the averages from radiographs scanned at 0° and 180° of the specimens. The changes in the concentration profiles for specimens subjected to 3- and 7-day ponding periods before the freeze-thaw cycles are illustrated in Figure 5- 5.

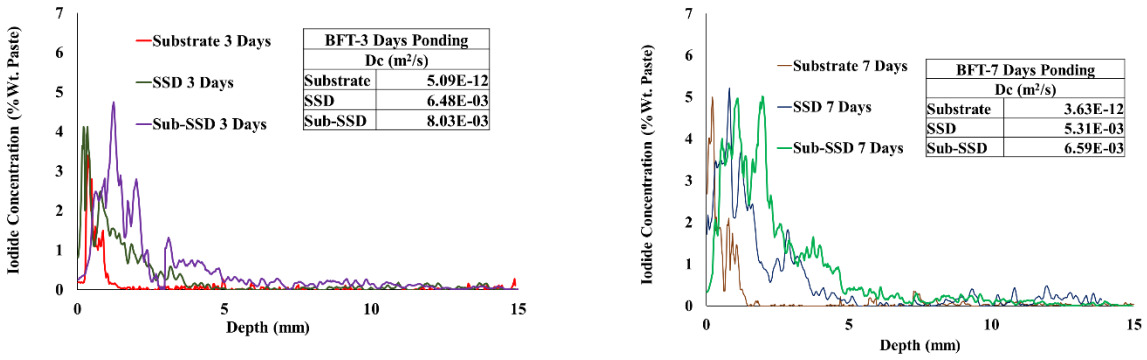

(a) (b)

Figure 5- 5 (a) 3-day concentration profile before F-T cycle, and (b) 7-day concentration profile before F-T cycle.

Figure 5- 5(a) reveals the data of 3-day ponding period before subjecting F-T cycles. When examining the Dc of the OTZ of the Sub-SSD specimens, these specimens exhibited the highest iodide concentration, measuring at 4.75%, along with a Dc of 8.03×10^{-3} m^2/s. In contrast, the OTZ of the SSD specimens showed a slightly lower maximum iodide concentration of 4.1% and a Dc of 6.48×10^{-3} m^2/s. Meanwhile, the substrate specimens displayed iodide concentration of 4.5% and a Dc of 5.09×10^{-12} m^2/s, which is a value consistent with the literature. Conventional Dc values for concrete is in the range of 5.0×10^{-11} to 5×10^{-13} m^2/s (Alexander et al., 2017). Therefore, these data suggest that the Dc of the OTZ is nine orders of magnitude higher than the bulk concrete; this is the first study to quantify Dc of the OTZ, so there are no existent data to corroborate this dramatic difference.

Figure 5- 5(b) shows the data after ponding for 7 days, it was observed that the OTZ of the Sub-SSD specimens exhibited a maximum iodide concentration of 5.0%, with a Dc of 6.59×10^{-3} m^2/s. The OTZ of the SSD specimens displayed a maximum concentration of 5.1% and a Dc of 5.31×10^{-3} m^2/s. Meanwhile, the substrate specimens maintained a concentration of 5.0% but had a considerably lower Dc of 3.63×10^{-12} m^2/s, this Dc value for the concrete substrate specimens align with the findings of Behravan et al., (2023). Additionally, it is worth noting that SSD specimens exhibited a lower diffusion coefficient at OTZ interface than the Sub-SSD specimens, which could be attributed to the higher moisture content, which allows for better hydration at the repair-substrate interface, resulting in increased C-S-H contents.

Figure 5- 6 depicts the average the concentration profiles and Dc values for specimens subjected to 3-day and 7-day ponding following 125 F-T cycles. Notably, detectable concentration peaks were evident at greater depths within specimens across all tests. The Dc values for substrate specimens after 3 and 7 days were 4.41×10^{-5} m^2/s, and 3.57×10^{-5} m^2/s respectively. This substantial increase in the Dc values can be attributed to the damage caused to the microstructure of the concrete owing to repeated F-T cycles. Notably, the concrete specimens used in this study were not air-entrained, making it more susceptible to the adverse effects of F-T cycles.

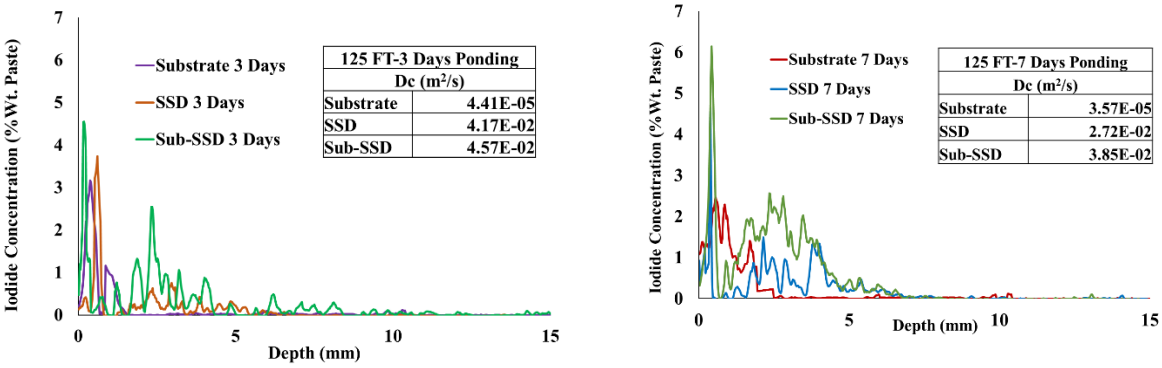

(a) (b)

Figure 5- 6 (a) 3-day concentration profile after 125 F-T cycle, and (b) 7day concentration profile after 125 F-T cycle.

Table 5- 3 Dc (m^2s^{-1}) values for the OTZ and substrate specimens

Specimen Name	Ponding Time (Day)	No. of F-T	Angle (Degree)	D_c	Average
Substrate	3	0	0	3.07E-12	5.09E-12
	3	0	180	7.10E-12	
	7	0	0	6.22E-12	3.63E-12
	7	0	180	1.03E-12	
	3	125	0	1.07E-05	4.41E-05
	3	125	180	7.74E-05	
	7	125	0	1.35E-05	3.57E-05
	7	125	180	5.78E-05	
SSD	3	0	0	4.75E-03	6.48E-03
	3	0	180	8.20E-03	
	7	0	0	6.75E-03	5.31E-03
	7	0	180	3.87E-03	
	3	125	0	5.23E-02	4.17E-02
	3	125	180	3.11E-02	
	7	125	0	3.65E-02	2.72E-02
	7	125	180	1.78E-02	
Sub-SSD	3	0	0	9.13E-03	8.03E-03
	3	0	180	6.94E-03	
	7	0	0	9.65E-03	6.59E-03
	7	0	180	6.75E-03	
	3	125	0	2.71E-02	4.57E-02
	3	125	180	6.43E-02	
	7	125	0	2.10E-02	3.85E-02
	7	125	180	5.60E-02	

On the other hand, OTZ of the Sub-SSD specimens consistently displayed a higher iodide concentration at greater depths compared to the SSD specimens and the concrete substrate. When examining the Dc values for Sub-SSD and SSD specimens after 3 and 7 days of ponding, a clear trend emerged. The OTZ of the Sub-SSD specimens exhibited Dc values of $4.57x10^{-2}$ m^2/s and $3.85x10^{-2}$ m^2/s, after 3 and 7 days respectively. Meanwhile, the OTZ of the SSD specimens exhibited Dc values of $4.17x10^{-2}$ m^2/s and $2.72x10^{-2}$ m^2/s, after 3 and 7 days respectively. The differing response is a result of the porosity of the OTZ interfaces with varying moisture conditions. During the F-T cycles, these OTZ interfaces provide accommodation for water volume expansion during freezing, preventing a drastic increase in the diffusion coefficient, as observed in the concrete substrate specimens.

Finally, the results suggest that Sub-SSD exhibited lower resistance to diffusion than the SSD specimens, both before and after exposure to 125 F-T cycles. Since the presented concentration profiles and Dc values represent the average of the measurements of radiographs taken at angles of 0° and 180°, to obtain a thorough understanding of the Dc values before and after 125 F-T cycles under various conditions, Table 3 shows that the apparent Dc values vary for the two different angles and this inconsistency can be attributed to differences in the paste aggregate matrix at different angles within the concrete specimens.

5.5 Conclusions and Recommendations

5.5.1 Conclusions

The study examined the impact of freeze-thaw (F-T) cycles and moisture conditions on the durability and performance of a substrate-repaired concrete's overlay transition zone (OTZ). Three surface moisture conditions, saturated surface drying (SSD), subsaturated surface drying (Sub-SSD), and oven dry (OD) were employed. TXM was used to investigate the effect of F-T cycles and moisture conditions on the diffusion coefficient within the OTZ of the substrate-repaired concrete. Time-dependent concentration profiles were developed, and time-dependent apparent diffusion coefficients (Dc) were calculated for the substrate-repaired concrete interface under various moisture conditions before and after exposure to the F-T cycles. A comprehensive analysis was conducted to assess the overall impact of F-T cycles and moisture conditions on substrate-repair concrete, including the evaluation of fracture properties, compressive and flexural strengths. The findings of this study suggest the following conclusions:

- Moisture levels did not show a clear correlation with F-T damage resistance from the mechanical experiments results.
- Compressive strength decreased by 10% after 20 F-T cycles, indicating mechanical property degradation.
- Although Sub-SSD specimens exhibited the highest flexural strength after 20 F-T cycles, all specimens experienced over a 50% reduction, highlighting OTZ vulnerability.
- The Decline in fracture parameters underlines compromised structural integrity in the presence of bonding issues.
- Two of the three moisture conditions experienced premature failure, resulting in a substantial reduction in the fracture properties between the substrate and repair specimens. For the SSD and

OD specimens the average peak load reductions were 65% and 81%, respectively, which is consistent with previous studies on OTZ weakness between the substrate and repair concrete.

- Results indicate the diffusion coefficient of the OTZ is up to nine orders of magnitude greater than the concrete substrate.
- Before F-T cycles the Sub-SSD specimens had the highest concentration and diffusion coefficient than the other specimens.

After 125 F-T cycles, concentration peaks at greater depths were observed in all categories. Sub-SSD specimens showed higher iodide concentration at greater depths compared to SSD specimens and the concrete substrate. Additionally, the diffusion coefficient for concrete substrate specimens significantly increased at both 3- and 7-days intervals due to microstructural damage from repeated F-T cycles without air entrainment.

5.5.2 Recommendations

In future investigations into the transport properties of the OTZ, it is advisable to explore various factors that can affect its behavior, such as different water-to-cement ratios and curing periods, the use of fiber-reinforced concrete, the use of air entrainment, and the effects of an increased number of freeze-thaw cycles. To gain a more comprehensive understanding of the OTZ interface, it is also recommended to incorporate non-destructive testing methods, including ultrasonic pulse velocity, surface resistivity, and resonant frequency analysis. This broader approach will enable a thorough evaluation of the relationship between substrate moisture repair-substrate concrete.

Acknowledgement

This material is based upon work supported in part by the Broad Agency Announcement Program and the Cold Regions Research and Engineering Laboratory (ERDC-CRREL) under Contract No. W913E522C0001.

Disclaimer

Any opinions, findings and conclusions or recommendations expressed in this material are those of the author(s) and do not necessarily reflect the views of the Broad Agency Announcement Program and ERDC-CRREL.

References

ASTM C192, 2019. Standard practice for making and curing concrete test specimens in the laboratory, ASTM International, West Conshohocken, PA.

ASTM C39, 2021. Standard test method for compressive strength of cylindrical concrete specimens, ASTM International, West Conshohocken, PA.

ASTM C1556, 2016. Standard test method for determining the apparent chloride diffusion coefficient of cementitious mixtures by bulk diffusion, ASTM International, West Conshohocken, PA.

ASTM C293, 2016. Standard test method for flexural strength of concrete (using simple beam with center-point loading), ASTM International, West Conshohocken, PA.

ASTM C1202, 2022. Standard test method for electrical indication of concrete's ability to resist chloride ion penetration, ASTM International, West Conshohocken, PA.

Alexander, M., Bentur, A., & Mindess, S. (2017). *Durability of concrete: Design and construction*. CRC Press/Taylor & Francis Group.

Baloch, W. L., Siad, H., Lachemi, M., & Sahmaran, M. (2021). A review on the durability of concrete-to-concrete bond in recent rehabilitated structures. *Journal of Building Engineering*, *44*, 103315. https://doi.org/10.1016/j.jobe.2021.103315

Bao, J., Wei, J., Zhang, P., Zhuang, Z., & Zhao, T. (2022). Experimental and theoretical investigation of chloride ingress into concrete exposed to real marine environment. *Cement and Concrete Composites*, *130*, 104511. https://doi.org/10.1016/j.cemconcomp.2022.104511

Behravan, A., Ley, M.T., Cook, D., Hu, Q., Rywelski, A., Brorsen, R., 2023. Measuring the diffusion coefficient of paste and concrete by using dental x-ray equipment. *CivilEng* 4, 224–247. https://doi.org/10.3390/civileng4010014

Behravan, A., Ley, M. T., Rywelski, A., & Berke, N. (2021). Changes in the rate of ion penetration of alternative cementitious materials with Time. *Materials &Design*, *197*, 109236. https://doi.org/10.1016/j.matdes.2020.109236

Beushausen, H., Höhlig, B., & Talotti, M. (2017). The influence of substrate moisture preparation on bond strength of concrete overlays and the microstructure of the OTZ. *Cement and Concrete Research*, *92*, 84–91. https://doi.org/10.1016/j.cemconres.2016.11.017

Brand, A. S., & Roesler, J. (2018). Interfacial transition zone of cement composites with recycled concrete aggregate of different moisture states. *Advances in Civil Engineering Materials*, *7*(1), 20170090. https://doi.org/10.1520/acem20170090

Chu, Y., Zhang, D., Liu, H., Wu, X., Zhai, P., Sheng, T., 2022. Experimental study on mechanical properties, acoustic emission characteristics and energy evolution of coal samples after freezing with liquid nitrogen. *Fuel* 321,123955. https://doi.org/10.1016/j.fuel.2022.123955

Courard, L., Lenaers, J.-F., Michel, F., & Garbacz, A. (2011). Saturation level of the superficial zone of concrete and adhesion of Repair Systems. *Construction and Building Materials*, *25*(5), 2488–2494. https://doi.org/10.1016/j.conbuildmat.2010.11.076

Darma, I.S., Sugiyama, T., Promentilla, M.A.B., 2013. Application of X-ray CT to study diffusivity in cracked concrete through the observation of tracer transport. *Journal of Advanced Concrete Technology* 11, 266–281. https://doi.org/10.3151/jact.11.266

Dixon, D. E., Prestrera, J. R., Burg, G. R., Chairman, S. A., Abdun-Nur, E. A., Barton, S. G., ... & Lee, S. H. (1991). Standard practice for selecting proportions for normal, heavyweight, and mass concrete (ACI 211.1-91). *Farmington Hills: ACI*.

Fathy, A., Zhu, H., & Kohail, M. (2022). Factors affecting the fresh-to-hardened concrete repair system. *Construction and Building Materials*, *320*, 126279. https://doi.org/10.1016/j.conbuildmat.2021.126279

Freeseman, K., Wang, K., Tan, Y., 2022. Bond strength and chloride resistance of epoxy and concrete overlays on bridge decks. *International Journal of Pavement Engineering* 23, 916–921. https://doi.org/10.1080/10298436.2020.1778693

Guo, T., Xie, Y., & Weng, X. (2018). Evaluation of the bond strength of a novel concrete for rapid patch repair of pavements. *Construction and Building Materials*, *186*, 790–800. https://doi.org/10.1016/j.conbuildmat.2018.08.007

Júlio, E. N. B. S., Branco, F. A. B., & Silva, V. D. (2004). Concrete-to-concrete bond strength. influence of the roughness of the substrate surface. *Construction and Building Materials*, *18*(9), 675–681. https://doi.org/10.1016/j.conbuildmat.2004.04.023

Khanzadeh Moradllo, M., Hu, Q., Ley, M.T., (2017). Using X-ray imaging to investigate in-situ ion diffusion in cementitious materials. *Construction and Building Materials* 136, 88–98. https://doi.org/10.1016/j.conbuildmat.2017.01.038

Komar, A. J., & Boyd, A. J. (2017). Evaluating freeze-thaw deterioration with tensile strength. *IOP Conference Series: Materials Science and Engineering*, *216*, 012024. https://doi.org/10.1088/1757-899x/216/1/012024

Li, G., Xie, H., & Xiong, G. (2001). Transition zone studies of new-to-old concrete with different binders. *Cement and Concrete Composites*, *23*(4–5), 381–387. https://doi.org/10.1016/s0958-9465(01)00002-6

Li, G., Zhou, Q., Wang, W., Lu, Chunhao, Chen, C., Guo, Z., Lu, Caifeng, 2023. Chloride diffusion along the interface between concrete matrix and repair materials under flexural loading. *Construction and Building Materials* 372, 130829. https://doi.org/10.1016/j.conbuildmat.2023.130829

Li, Z., Dang, Y., Tang, Z., Xie, N., Lu, S., Shi, X., 2021. Optimal overlays for preservation of concrete in cold climate: decision-making by the method of fuzzy comprehensive evaluation combined with AHP. *Journal of Infrastructure Preservation and Resilience 2, 31*. https://doi.org/10.1186/s43065-021-00046-x

Lin, H., Han, Y., Liang, S., Gong, F., Han, S., Shi, C., Feng, P., 2022. Effects of low temperatures and cryogenic freeze-thaw cycles on concrete mechanical properties: A literature review. *Construction and Building Materials* 345, 128287. https://doi.org/10.1016/j.conbuildmat.2022.128287

Liu, K., Yan, J., Hu, Q., Sun, Y., Zou, C., 2016. Effects of parent concrete and mixing method on the resistance to freezing and thawing of air-entrained recycled aggregate concrete. *Construction and Building Materials* 106, 264–273. https://doi.org/10.1016/j.conbuildmat.2015.12.074

Lukovic, M., Ye, G., 2016. Effect of moisture exchange on interface formation in the repair system studied by X-ray absorption. *Materials 9(1), 2.* https://doi.org/10.3390/ma9010002

Qin, L., Zhai, C., Xu, J., Liu, S., Zhong, C., & Yu, G. (2019). Evolution of the pore structure in coal subjected to freeze−thaw using liquid nitrogen to enhance coalbed methane extraction. *Journal of Petroleum Science and Engineering*, *175*, 129–139. https://doi.org/10.1016/j.petrol.2018.12.037

Ram, P., Olek, J., Jain, J., 2016. Field trials of rapid-setting repair materials. West Lafayette, IN. https://doi.org/10.5703/1288284315185

RILEM TC 89-FMT, Determination of fracture parameters (KI_C and $CTOD_C$) of plain concrete using three-point bend tests, *Materials and Structures*. 23 (1990) 457–460. doi:10.1007/BF02472029.

RILEM TC 89-FMT, Size-effect method for determining fracture energy and process zone size of concrete, *Materials and Structures*. 23 (1990) 461–465. doi:10.1007/BF02472030.

Şahin, Y., Akkaya, Y., & Taşdemir, M. A. (2021). Effects of freezing conditions on the frost resistance and microstructure of concrete. *Construction and Building Materials*, *270*, 121458. https://doi.org/10.1016/j.conbuildmat.2020.121458

Sang, Y., Pan, Y., Ying, W., & Yang, Y. (2022). Assessment of mechanical performance and ice content of concrete at low temperature using impact-echo method. *Construction and Building Materials*, *346*, 128286. https://doi.org/10.1016/j.conbuildmat.2022.128286

Sant, G., & Weiss, J. (2009). Using X-ray absorption to assess moisture movement in cement-based materials. *Journal of ASTM International*, *6*(9), JAI102234. https://doi.org/10.1520/jai102234

Scrivener, K. L., Crumbie, A. K., & Laugesen, P. (2004). The interfacial transition zone (Itz) between cement paste and aggregate in concrete. *Interface Science*, *12*(4), 411–421. https://doi.org/10.1023/b:ints.0000042339.92990.4c

Shi, X., Xie, N., Fortune, K., & Gong, J. (2012). Durability of steel reinforced concrete in Chloride Environments: An overview. *Construction and Building Materials*, *30*, 125–138. https://doi.org/10.1016/j.conbuildmat.2011.12.038

Skripkiūnas, G., Nagrockienė, D., Girskas, G., Vaičienė, M., & Baranauskaitė, E. (2013). The cement type effect on freeze – thaw and deicing salt resistance of concrete. *Procedia Engineering*, *57*, 1045–1051. https://doi.org/10.1016/j.proeng.2013.04.132

Wang, R., Hu, Z., Li, Y., Wang, K., & Zhang, H. (2022). Review on the deterioration and approaches to enhance the durability of concrete in the freeze–thaw environment. *Construction and Building Materials*, *321*, 126371. https://doi.org/10.1016/j.conbuildmat.2022.126371

Zhang, G., Yu, H., Li, H., Yang, Y., 2019. Experimental study of deformation of early age concrete suffering from frost damage. *Construction and Building Materials* 215, 410–421. https://doi.org/10.1016/j.conbuildmat.2019.04.187

Zhang, P., Cong, Y., Vogel, M., Liu, Z., Müller, H.S., Zhu, Y., Zhao, T., 2017. Steel reinforcement corrosion in concrete under combined actions: The role of freeze-thaw cycles, chloride ingress, and surface impregnation. *Construction and Building Materials* 148, 113–121. https://doi.org/10.1016/j.conbuildmat.2017.05.078

Zhou, J., Ye, G., van Breugel, K., 2016. Cement hydration and microstructure in concrete repairs with cementitious repair materials. *Construction and Building Materials* 112, 765–772. https://doi.org/10.1016/j.conbuildmat.2016.02.203

Chapter 6. Impact of water-to-cement ratios of repair mixes on the durability of concrete repair-substrate interfaces during freeze-thaw cycles[5]

The contributions of the authors to this manuscript are described as follows:

Md Hasibul Hasan Rahat: Conceptualization, Methodology, Formal analysis, Investigation, Writing–original draft; Writing–review and editing.

Janelle Y Davis: Methodology, Investigation;

Alexander S. Brand: Conceptualization, Writing–review and editing, Writing–original draft, Supervision, Project administration, Methodology.

[5] **Rahat, M.H.H.**, Davis, J., & Brand, A.S. (2025). The Impact of Water-to-Cement Ratios on the Durability and Performance of Concrete Repair-Substrate Interfaces. *Journal of Building Engineering* (under review)

Impact of water-to-cement ratios of repair mixes on the durability of concrete repair-substrate interfaces during freeze-thaw cycles

Md Hasibul Hasan Rahat[1*], Janelle Y. Davis[2] and Alexander S. Brand[3*]

[1] Graduate Research Assistant, The Charles E. Via, Jr. Department of Civil and Environmental Engineering, Virginia Polytechnic Institute and State University, Blacksburg, Virginia

[2] Undergraduate Student, Kevin T. Crofton Department of Aerospace and Ocean Engineering, Virginia Polytechnic Institute and State University, Blacksburg, Virginia

[3] Assistant Professor, The Charles E. Via, Jr. Department of Civil and Environmental Engineering, Department of Materials Science and Engineering, Myers-Lawson School of Construction, Virginia Polytechnic Institute and State University, Blacksburg, Virginia

* Corresponding authors: rahatm21@vt.edu (Md Hasibul Hasan Rahat) and asbrand@vt.edu (Alexander S. Brand)

6.1 Abstract

This study investigates the impact of varying water-to-cement (w/c) ratios in repair mixtures on the durability of concrete repair-substrate interfaces subjected to freeze-thaw (F-T) cycles. Repair mixtures with w/c ratios of 0.38, 0.40, and 0.45 were applied to a substrate (w/c = 0.45) under saturated surface-dry (SSD) conditions to assess their influence on the overlay transition zone (OTZ), the weakest region of repair-substrate concrete analogous to the interfacial transition zone between aggregates and paste in concrete. Mechanical properties, water absorption, rapid chloride penetrability, ultrasonic pulse velocity, F-T resistance, and diffusion coefficient were evaluated at the repair-substrate interfaces. Results showed that the lowest w/c ratio (0.38) in Repair-1 significantly improved durability, yielding a 22% reduction in chloride penetration and a 45% lower initial sorptivity compared to the highest w/c ratio in Repair-3. After 240 freeze-thaw cycles, Repair-1 exhibited a 405% increase in the apparent diffusion coefficient (D_c), compared to 221% for the substrate, underscoring persistent porosity challenges in the OTZ. These findings suggest that while reducing the w/c ratio in repair mixes enhances interface durability, the OTZ remains a critical point of vulnerability under freeze-thaw exposure. In the absence of surface preparation, employing a lower w/c ratio is recommended to mitigate OTZ deficiencies and improve the long-term performance of concrete repairs in cold environments.

Keywords: freeze-thaw resistance, transmission X-ray microscopy, concrete repair, overlay transition zone, chloride ingress, diffusion coefficients

6.2 Introduction

Concrete is one of the most widely used construction materials in modern society, valued for its availability and cost-effectiveness (Imbabi et al. 2012; Rabi et al. 2022). However, its performance can be undermined by a variety of deterioration mechanisms, including alkali-silica reaction, chloride attack, corrosion, freeze-thaw (F-T) damage, environmental impacts, *etc.* (Baloch et al. 2021; Brandt 2008; Shi et al. 2012; Wang et al. 2022). This deterioration often manifests as delamination, cracking, and spalling, with structures in cold regions being particularly vulnerable to damage from repeated F-T cycles (Lin et al. 2022). Such degradation reduces the service life of concrete structures and necessitates timely repair or rehabilitation, which typically involves removing the damaged sections and applying cement-based overlays to mitigate further damage (Skripkiunas et al. 2013).

However, selecting an appropriate repair material and ensuring strong interfacial bonding at the interface is critical to achieving a durable and practical repair. A critical aspect of concrete repairs is the formation of an overlay transition zone (OTZ), which functions similarly to the interfacial transition zone (ITZ) between cement paste and aggregates in concrete (Beushausen et al. 2017; Li et al. 2001; Zhou et al. 2016). The mechanical bond strength between the repair overlay and substrate is influenced by multiple factors, including surface roughness, substrate moisture conditions, repair mix composition, and the use of bonding agents (Beushausen et al. 2017; Courard et al. 2011; Fathy et al. 2022; Júlio et al. 2004; Lukovic and Ye 2016; Rahat et al. 2024a). Despite advances in understanding these factors, the impact of the water-to-cement (w/c) ratio of repair mixes on the durability of the repair-substrate interface during F-T cycles has not been thoroughly explored.

Research has shown that aggregate moisture conditions play a significant role in ITZ development when using recycled concrete aggregates (Brand and Roesler 2018; Le et al. 2017). Extending this understanding, (Rahat et al. 2024a) hypothesized that the OTZ might exhibit similar behavior and conducted studies assessing the impact of substrate moisture conditions on bond formation. This study included analyses of mechanical and fracture properties, the apparent diffusion coefficient along the OTZ, and the effects of F-T cycles on bond performance. Although no definitive correlation between substrate moisture levels and F-T damage resistance was observed, results indicated that repairs performed on substrates with saturated surface-dry (SSD) conditions showed enhanced performance, pointing to the need for further exploration of other influencing factors.

Based on these findings, the present study investigates how varying w/c ratios in repair mixes affect bond formation and OTZ durability under repeated F-T cycles. This research also evaluates mechanical properties, rapid chloride penetrability, water absorption, ultrasonic pulse velocity (UPV), the apparent diffusion coefficient in the OTZ, and bond performance after F-T exposure. The outcomes of this study aim to provide deeper insights into the design of more resilient concrete repair systems for cold environments.

6.2.1 Significance of the Study

The performance of bonded concrete overlays and concrete pavement repairs (*e.g.*, partial and full-depth repairs) can be significantly diminished by F-T cycling and chloride ingress (Freeseman et al. 2022; Guo et al. 2018; Li et al. 2021; Ram et al. 2016). However, the impact of the w/c ratio in repair mixes during casting on F-T durability, water absorption, and chloride ingress along the OTZ has not been well-established in the literature. This study addresses this gap by investigating the influence of different w/c ratios in repair mixes on bond formation and OTZ durability under repeated F-T cycles. This study also utilizes a novel non-destructive technique, transmission X-ray microscopy (TXM), to quantify the time-dependent apparent diffusion coefficient (D_c) along the OTZ before and after F-T cycles.

6.3 Experimental Design

6.3.1 Materials and Mix Design

In this study, a w/c ratio of 0.45 was used for the concrete substrate (Substrate), following the ACI 211-1 design procedure (Dixon et al. 1991). Three different water-to-cement (w/c) ratios were used for the repair sections: 0.38 for Repair-Substrate 1 (Repair-1), 0.40 for Repair-Substrate 2 (Repair-2), and 0.45 for Repair-Substrate 3 (Repair-3). The concrete was not air-entrained to assess F-T effects on non-air-entrained concrete and examine how substrate moisture conditions influence durability and interface performance. The mix design incorporated Type I/II portland cement and a polycarboxylate superplasticizer dosed at 98 ml per 100 kg of cement. Table 6- 1 and

Table 6- 2 provide details on the chemical composition of the cement and the concrete mix designs used in this research. The specific gravity values for the cement, fine aggregate (FA), and coarse aggregate (CA) were 3.15, 2.57, and 2.77, respectively. The absorption capacity of FA and CA was 3.6% and 1.4%, respectively. The maximum aggregate size of CA used in this study was 19 mm. Before mixing, the aggregates were oven-dried and cooled, and the mixing water was adjusted to achieve an SSD condition to compensate for the aggregate absorption. The FA used in this study was natural river sand composed predominantly of siliceous minerals. In contrast, the CA was crushed limestone, a carbonate-rich material widely used in concrete applications. Although detailed chemical and mineralogical characterization was not performed, both aggregates complied with ASTM C33 requirements.

While the cement contents used in this study (as shown in

Table 6- 2) were higher than typical field values, they were deliberately chosen to maintain constant water content across all repair mixes and systematically isolate the effect of the w/c ratio on durability. This experimental design ensures that observed performance differences are attributable solely to changes in the w/c ratio, minimizing confounding effects from other parameters. These laboratory-controlled conditions support mechanistic understanding and will inform future optimization for practical applications.

Table 6- 1 Chemical composition of cement

Component	CaO	SiO_2	Al_2O_3	Fe_2O_3	SO_3	MgO	Na_2O
Content (%)	62.9	20.8	4.6	3.6	4.1	1.9	0.5

Table 6- 2 Mix design of concrete

Groups	Cement (kg/m^3)	FA (kg/m^3)	CA (kg/m^3)	Water (kg/m^3)	Substrate w/c	Repair w/c
Substrate	481.1	698.7	913.1	216.5	0.45	-
Repair-Substrate 1	569.8	626.4	923.4	216.5	-	0.38
Repair-Substrate 2	541.4	649.7	923.4	216.5	-	0.40
Repair-Substrate 3	481.1	698.7	913.1	216.5	-	0.45

6.3.2 Replicate Preparation Procedure

The substrate material for this study was prepared following ASTM C192 guidelines. A total of 24 beam prisms (75 mm by 75 mm by 300 mm) and 24 cylinders (100 mm diameter by 200 mm height) were cast. After a 28-day moist curing period, the beam specimens were saw-cut at their midspan, and cylinder specimens were saw-cut along the axis. The substrate halves were cleaned and scrubbed in water following the cutting process to remove residual debris. The cleaned substrate halves were then transferred to an environmental chamber, where they were conditioned at 98 % relative humidity and 23 ^{o}C for 18 h ± 2 h. This conditioning was selected based on the findings of (Rahat et al. 2024a), which indicated that this moisture condition enhances the bond strength at the repair-substrate interface.

Following the completion of the substrate conditioning, the substrate halves were removed from the chamber and subsequently repositioned within the molds. The repair concrete mixes were cast alongside the substrate halves within the molds. The molds were cleaned and lightly oiled before use. Freshly mixed repair concrete was poured in two layers, each compacted manually using a standard tamping rod to minimize entrapped air and ensure good contact with the pre-conditioned substrate surface. After casting, the specimens were covered with plastic sheeting for 24 hours before commencing moist curing. The specimens designated for repair-substrate underwent a moist curing process for an additional 28 days in preparation for the subsequent experimental testing phase. Before casting the repair materials, no mechanical surface roughening or bonding agent was applied to the substrate. This decision was made to (1) preserve the integrity of the OTZ for diffusion coefficient analysis and (2) avoid variability from inconsistent surface preparation across specimens. The experimental procedure was conducted on the repair-substrate concrete specimens, which were divided into three groups and termed Repair-1 (w/c of 0.38), Repair-2 (w/c

of 0.40), and Repair-3 (w/c of 0.45). Figure 6- 1 depicts a process of repair-substrate specimen preparation.

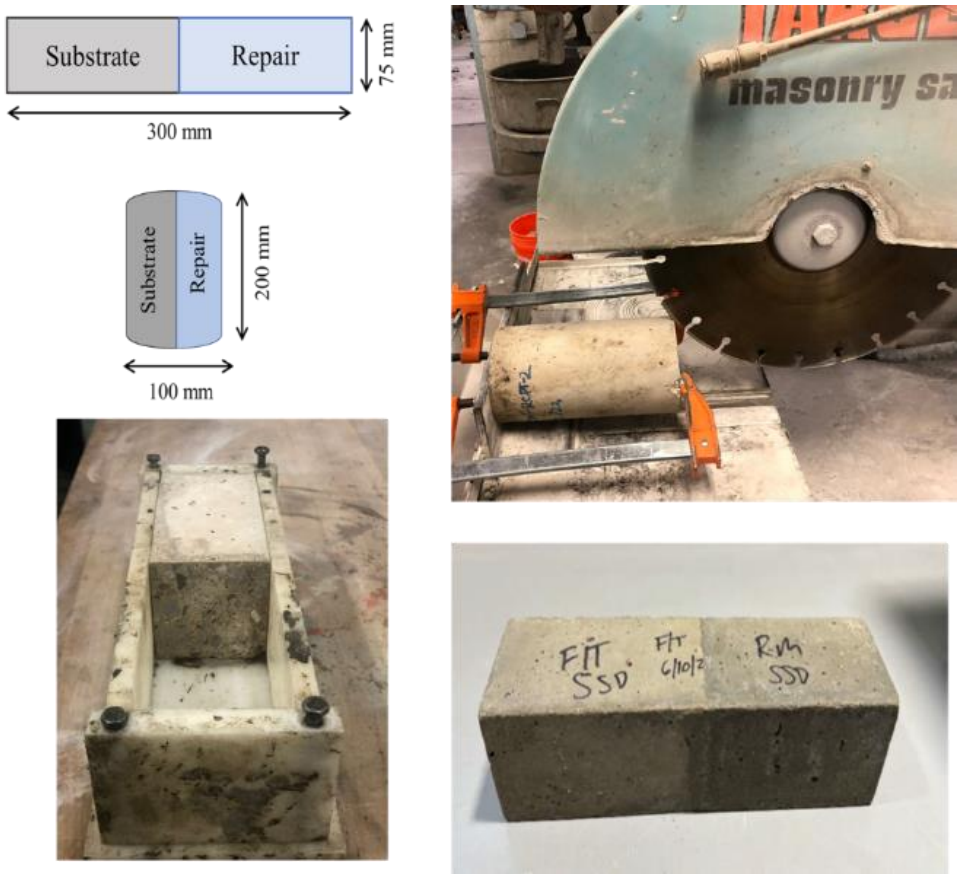

Figure 6- 1 Process of preparing repair-substrate specimen.

6.3.2 Replicate Testing Procedure

6.3.2.1 Water Absorption Test

In this study, ASTM C1585 was employed to evaluate the water absorption rate along the interface of the repair-substrate concrete specimen to explicitly see how much more water is absorbed due to the interface. Three cylindrical specimens from each group, as shown in Figure 6- 2, with dimensions of 50 mm in thickness and 100 mm in diameter, were prepared and conditioned to a specific moisture content before having their bottom surfaces exposed to water. The specimens were conditioned for 18 days, starting with 3 days in an environment maintained at 50 °C and 80 % relative humidity. Subsequently, the specimens were stored in air containers at 23 °C for 15 days to allow moisture redistribution before testing. The specimens were then sealed with hydrophobic wax on all sides, exposing only the top surface to initiate sorptivity from one direction. During testing, mass changes were recorded frequently over the first 6 hours of water

contact (initial sorptivity), with daily measurements taken over the next 8 days (secondary sorptivity). The absorbed water was then determined by the cross-sectional area of the exposed specimen using Equation 1, I is the water absorption, m_t represents the change in specimen mass in grams, at the time t, a is the exposed area of the specimen, in mm^2, and d represents the density of water in g mm^{-3} and a value of 0.001 g mm^{-3} is used.

$$I = \frac{m_t}{a \times d} \tag{1}$$

The absorbed water volumes were plotted as a function of the square root of time. The initial sorptivity was calculated as the slope of the curve during the first 6 h, while the secondary sorptivity was determined from the slope of the measurements taken between 1 day and 8 days, following the guidelines provided in ASTM C1585. The water absorption test, though applied across the specimen cross-section, was designed to emphasize moisture uptake along the OTZ by slicing across the bonded interface. Specimens were sealed laterally and base-side to enforce one-dimensional flow across the interface. While complete separation of interface-only absorption is not feasible using ASTM C1585, the testing configuration emphasizes interface effects and is consistent with reported methods.

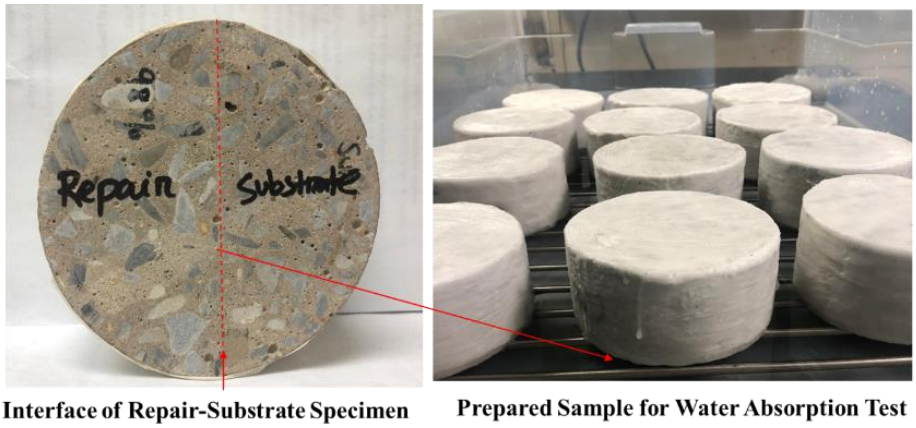

Figure 6- 2 Specimens prepared for evaluating water absorption along the interface of repair-substrate concrete.

6.3.2.2 Rapid Chloride Penetrability Test (RCPT)

The RCPT test was conducted following ASTM C1202 to explicitly assess the impact of the repair-substrate interface on chloride penetrability. Cylindrical specimens (100 mm diameter, 200 mm height) were moist-cured for 28 days, after which three 50 mm thick slices were extracted from each cylinder. The slices were sealed with epoxy on the circumference, exposing only the top and bottom surfaces, ensuring chloride penetration along the interface. The specimens were then vacuum-saturated for 24 hours to reach SSD conditions. The test was performed by applying 60 V

across the specimen for 6 hours, with one side exposed to 3% NaCl solution and the other to 0.3 N NaOH solution. The total charge passed (in coulombs) was recorded, indicating the chloride ion penetrability at the interface.

6.3.2.3 Freeze/Thaw Testing

A total of 12 concrete specimens (75 mm by 75 mm by 300 mm) from all groups underwent a 28-day moist curing period in a fog room. Subsequently, the specimens were exposed to F-T cycles following ASTM C666 Procedure A. The primary deviation from the ASTM C666 standard was the curing duration, which was extended from 14 days to 28 days in this study to evaluate the impact of prolonged curing on F-T resistance. Each F-T cycle lasted 4.5 h. During the freezing phase, the temperature was rapidly reduced from 4.4 °C to –18 °C within 1 h, maintaining the –18 °C for 2 h. In the subsequent thawing phase, the temperature increased from –18 °C to 4.4 °C in 0.5 h and remained steady at 4.4°C for an additional hour. Mass loss (ML) and relative dynamic modulus of elasticity (RDME) measurements were taken after every 28 to 36 F-T cycles, utilizing Equations 2 and 3. In these equations, m_o is the mass of the specimen at 0 F-T cycles, m_n represents the mass of the specimens after n F-T cycles, Δm is the percentage (%) of the ML of the concrete specimens after n F-T cycles, n_o is the fundamental transverse frequency of the specimens at 0 F-T cycles, n_n represents the fundamental transverse frequency of the specimens after n F-T cycles, and P_n is the RDME of the concrete specimens after n F-T cycles.

$$\Delta m = \frac{m_o - m_n}{m_o} \times 100 \tag{2}$$

$$RDME, P_n = \frac{n_n^2}{n_0^2} \tag{3}$$

Additionally, UPV (ASTM C597) was measured along the interface of the repair-substrate concrete specimens, and the fundamental transverse frequency (ASTM C215) was recorded before the start of F-T cycles and at intervals of approximately every 28 to 36 F-T cycles. Furthermore, both the compressive strength (ASTM C39) and flexural strength (ASTM C293) were assessed before the initiation of F-T cycles and after the specimens failed due to exposure to F-T cycles for all concrete samples.

6.3.2.4 TXM Testing Procedure

A custom built TXM was used to assess the apparent D_c along the OTZ of the repair-substrate concrete specimens before and after 300 F-T cycles. The schematic of the TXM setup is shown in Figure 6- 3**(a)** (Rahat et al. 2024a; b) and was developed following previous studies (Behravan et al. 2021, 2023; Ley 2023; Moradllo et al. 2017; Moradllo and Ley 2017a; b). The TXM system enables quick, non-destructive testing, capturing an X-ray radiograph in about 10 s. **Table 3** provides the specifications of the X-ray source. As shown in Figure 6- 3**(b)**, the figure illustrates core cutting and sample preparation for TXM testing, including extraction along the OTZ and

sealing for diffusion analysis. Two concrete cores measuring 19 mm in diameter and 25 mm in height were extracted from the specimens. Two replicate cores were extracted per group for each test condition. Specifically, one core was taken from the top and one from the bottom region of a single repair-substrate prism, totaling two cores per specimen. This allowed for vertical profile averaging and minimized local variability before and after exposure to 300 F-T cycles. These cores were sealed by applying a hydrophobic wax layer to the sides and bottom, while the top surface remained uncoated to allow for solution ponding and facilitate 1D diffusion.

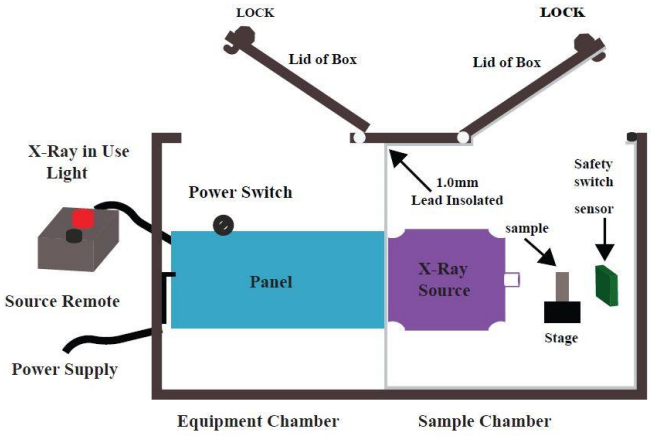

(a)

(b)

Figure 6- 3 (a) Schematic illustration of the TXM system, (b) procedure of core cutting and sample preparation for TXM experiment

Table 6- 3 X-ray source details

Sensor Resolution (line pairs per millimeter)	33.78
Pixel Size (μm)	19
Voltage (keV)	65
Current (μA)	7000
Exposure Time (s)	0.25

A potassium iodide (KI) solution with a concentration of 0.6 M was utilized to pond the cored specimens. This specific concentration was selected to ensure optimal contrast between the tracer and the specimens. X-ray imaging can be employed to observe the diffusion of iodide through the concrete. Since iodide and chloride ions are similar in size, and iodide has a D_c 24 % higher than that of chloride, the diffusion of iodide can be considered a more conservative measure of chloride diffusion (Behravan et al. 2023; Moradllo and Ley 2017a).

In this study, two replicate cores from each group were tested. All core specimens were initially scanned to capture their original images, and the initial gray values were determined, serving as the reference image. Subsequently, the core specimens were immersed in a 0.6 M KI solution and then rescanned after 3 days, 14 days and 28 days to obtain images for comparison with the reference image, enabling the evaluation of changes in gray values. For the specimens subjected to F-T cycles, a reference image was captured after 300 F-T cycles, followed by immersion in the 0.6 M KI solution and the same scanning procedures to capture X-ray images. While numerous studies have investigated chloride diffusion in concrete (Florea and Brouwers 2012; Jasielec et al. 2020), research on iodide diffusion is still relatively scarce. This study utilized KI as a tracer for NaCl, taking advantage of its chemical stability and diffusion characteristics that closely resemble those of chloride ions (Moradllo and Ley 2017a; b). Both iodide (I^-) and chloride (Cl^-) are monovalent anions with similar properties, making iodide a suitable substitute for chloride in diffusion studies (Jin et al. 2024). In contrast to chloride, iodide exhibits minimal reactivity in the alkaline environment of concrete, resulting in only minor reaction products, such as $3CaO{\cdot}Al_2O_3{\cdot}CaI_2{\cdot}8H_2O$, with unhydrated cement phases like C_3A (Jin et al. 2024). This reduced reactivity ensures that the cement matrix remains largely unaffected during testing. Previous research corroborates iodide's effectiveness for quantifying diffusion kinetics in concrete (Jin et al. 2022, 2024; Liu et al. 2022).

To conduct the radiographic analysis, a software code was utilized to align the radiographic images captured at intervals of 3 days, 14 days, and 28 days following the ponding process with the corresponding reference image for each individual specimen. The alignment process involved applying local displacements, such as shifts and rotations, to the subsequent radiograph of a given specimen in order to superimpose it onto the reference radiograph. Figure 6- 4 presents the subtracted image of the 3-day ponded specimen compared to the reference image, revealing the iodide concentration at the OTZ interface. The iodide concentration along the OTZ interface

exhibited a "V" shape, confirming the findings of a previous study (Li et al. 2023a). To determine the mean gray values at various depths for each specimen, a region approximately 7.9 mm wide (equivalent to approximately 300 pixels in TXM radiographs) was used, as shown in Fig. 3, to minimize the occurrence of cupping artifacts (Behravan et al. 2023). Each line represented a grayscale value corresponding to a distinct depth. The final profile of the gray values was obtained by averaging 300 individual lines. According to Beharavan et al., (Behravan et al. 2023), it is recommended to use various angle radiographs to calculate the apparent D_c for concrete specimens and to report the results as an average D_c. Given that concrete is a heterogeneous composite material, analyzing only the central strip of the radiographs may be influenced by inconsistencies in the aggregates. In this study, radiographs were taken at 0° and 180° angles for all specimens to accurately calculate the average D_c.

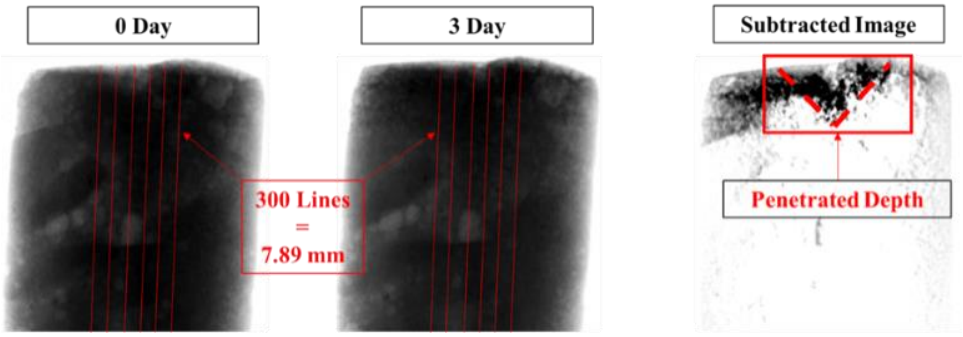

Figure 6- 4 Subtraction of radiographs within a specified area of interest at an interface of repair-substrate concrete core.

Finally, by using nonlinear regression, the apparent D_c is calculated using a solution derived from Fick's second law of diffusion, as applied in Equation 3 according to ASTM C1556, which defines the solution for the 1D diffusion condition. In this equation, x represents the distance from the sample surface, C_s is the surface iodide concentration, $C_{(x,t)}$ denotes the iodide concentration at a depth of x from the surface after time t, and *erf* stands for the Gaussian error function. The D_c value in this study combines the impact of fluid transport mechanisms such as diffusion, absorption, convection, and chemical binding into one term.

$$C_{(x,t)} = C_s\left(1 - erf\left(\frac{x}{2\sqrt{D_c t}}\right)\right) \quad (3)$$

6.4 Results and Disscussions

6.4.1 Water Absorption Results

Figure 6- 5 shows the water absorption results of different repair-substrate concrete specimens. In Figure 6- 5, it is evident that Repair-3 specimens exhibited the highest water absorption after 8 days of testing, followed by Repair-2 and Repair-1 specimens. The substrate specimens showed the lowest water absorption compared to all other specimens.

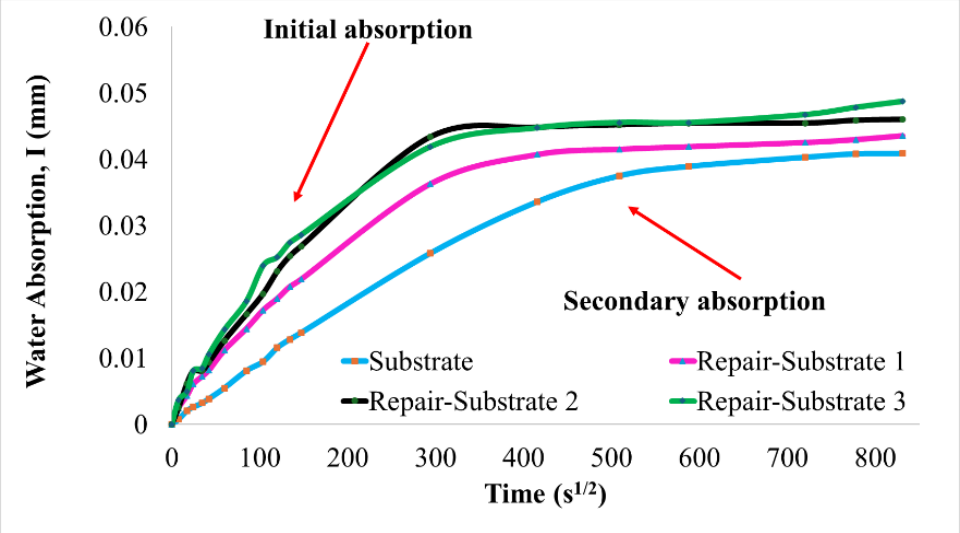

Figure 6- 5 Water absorption results of different repair-substrate concrete specimens.

The initial sorptivity (occurring in the first 6 h) and secondary sorptivity (occurring from 6 h to 8 days) values for all specimen groups were calculated from Figure 6- 5, following ASTM C1585. The results show that the Repair-2 and Repair-3 specimens exhibited the highest initial sorptivity at 1.7 x 10^{-4} mm $s^{-1/2}$, followed by Repair-1 at 1.6 x 10^{-4} mm $s^{-1/2}$, and the Substrate specimens with the lowest value of 0.9 x 10^{-4} mm $s^{-1/2}$ after 6 h of water absorption. The initial sorptivity of substrate specimens aligns with a previous study by (Castro et al. 2011). Compared to the substrate, Repair-2 and Repair-3's initial sorptivity was 89 % higher, whereas Repair-1 showed increases of 78 %.

This increased initial sorptivity in the repair-substrate specimens is likely due to the elevated porosity in the OTZ of repair-substrate specimens. The OTZ often exhibits higher porosity (Luković et al. 2014), which can facilitate water penetration due to weaker bonding, microcracking, or insufficient compaction during the repair process

Regarding secondary sorptivity, the substrate specimens exhibited the highest value at 0.3 x 10^{-4} mm $s^{-1/2}$, while all repair groups (Repair-1, Repair-2, and Repair-3) showed much lower values at 0.1 x 10^{-4} mm $s^{-1/2}$. This suggests that although the initial sorptivity was higher in the repair specimens due to OTZ porosity, the overall matrix of the repair mixes was less permeable during the long-term absorption phase, as reflected by the lower secondary sorptivity values. Table 6- 4

presents the summary of initial and secondary sorptivity data of all the replicates used in this experiment.

Table 6- 4 Summary of initial and secondary sorptivity data (x 10^{-4} mm $s^{-1/2}$)

Initial sorptivity				
	Substrate	Repair-Substrate 1	Repair-Substrate 2	Repair-Substrate 3
Replicate 1	0.5	1.7	1.2	1.5
Replicate 2	1.1	1.3	1.4	1.6
Replicate 3	1.0	1.9	2.5	2.0
Average	0.9	1.6	1.7	1.7
Standard deviation	0.3	0.3	0.5	0.2
Secondary sorptivity				
	Substrate	Repair-Substrate 1	Repair-Substrate 2	Repair-Substrate 3
Replicate 1	4.3	0.1	0.1	0.1
Replicate 2	2.5	0.1	0.1	0.1
Replicate 3	2.0	0.1	0.1	0.1
Average	3.0	0.1	0.1	0.1
Standard deviation	1.0	0.01	0.02	0.01

For both initial and secondary sorptivity results, a statistically significant difference was observed at a significance level of 0.05 when comparing the substrate specimens with Repair-1, Repair-2, and Repair-3. However, there is insufficient evidence to conclude a statistically significant difference among the specimens within the Repair groups for initial sorptivity. Moreover, the secondary sorptivity results indicated a strong correlation among the Repair groups, with P-values of 1.0000 suggesting a consistent performance across these groups.

6.4.2 RCPT Results

Figure 6- 6 shows the RCPT results for the repair-substrate specimens. The Substrate had a total passed charge of 3050 C, indicating moderate chloride penetrability as per ASTM C1202. The RCPT value of substrate specimens aligns with findings in the literature for concrete with a w/c ratio of 0.45 (Bassuoni et al. 2006). In comparison, the Repair-1, Repair-2, and Repair-3 specimens exhibited total passed charges of 6510 C, 7040 C, and 7050 C, respectively, classifying them as having a high rate of chloride ion penetrability.

The repair groups showed significant increases in chloride penetrability compared to the substrate: 113 % (Repair-1), 131 % (Repair-2), and 131 % (Repair-3). This suggests that the OTZ is more porous, allowing greater chloride penetration and making them prone to faster degradation in environments exposed to chloride ions, such as marine structures or deicing salts. Among the repair-substrate systems, Repair-1 (w/c 0.38) exhibited the best performance in terms of chloride ion penetrability, followed by Repair-2 (w/c 0.42) and Repair-3 (w/c 0.45). These findings are

similar to the initial sorptivity results, where Repair-1 performed better, followed by Repair-2 and Repair-3.

Finally, a statistically significant difference was observed at a significance level of 0.05 when comparing RCPT results of the Substrate specimens with Repair-1, Repair-2, and Repair-3. However, insufficient evidence exists to conclude a statistically significant difference among the specimens within the Repair groups for RCPT results.

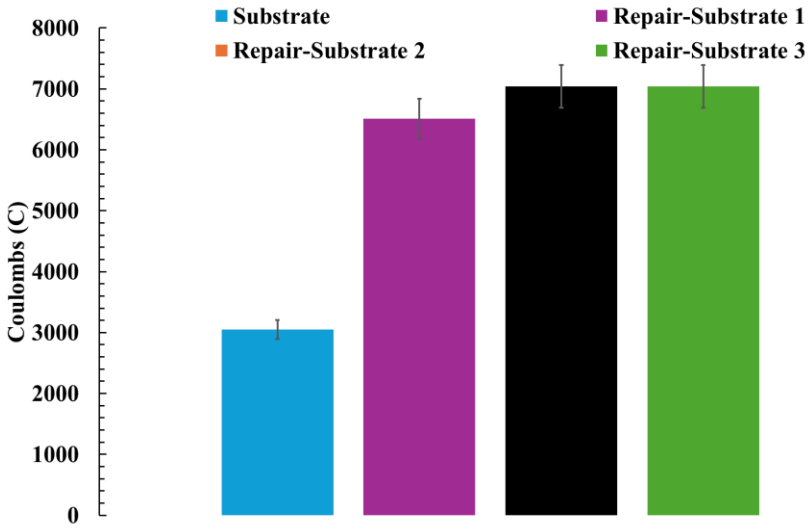

Figure 6- 6 RCPT results of different repair-substrate concrete specimens; error bars represent one standard deviation.

6.4.3 Freeze/Thaw Test Results

Figure 6- 7**(a), (b), and (c)** depict the changes in ML and RDME, as well as the dynamic modulus of elasticity (DME) values for concrete samples from all the concrete specimen groups. The degree of deterioration of concrete specimens during F-T cycles is directly related to their RDME changes. According to ASTM C666 procedure A, testing should be conducted on each specimen until it has undergone 300 cycles or until its relative dynamic modulus of elasticity decreases to 60 % of the initial modulus. The results in Figure 6- 7 **(a) and (b)** indicate that the Substrate specimens successfully withstood 300 F-T cycles. In contrast, the Repair-1 and Repair-2 specimens failed after 240 F-T cycles, while the Repair-3 specimens exhibited failure after 180 F-T cycles. This data highlights the differing resilience of the repair methods in comparison to the original substrate.

ML in this study is a combination of surface scaling and liquid uptake, reflecting the mass of debris scaled from the surface due to F-T damage and the increased mass of the remaining concrete caused by water absorption into internal cracks and pores during the F-T cycles. As illustrated in Figure 6- 7**(a)**, the Substrate specimens underwent ML of 0.1 % after 300 F-T cycles, which aligns with findings in the literature for concrete with a w/c ratio of 0.45 (Jiang et al. 2015). In contrast,

Repair-1 and Repair-2 exhibited mass losses of 0.2 % and 0.3 %, respectively, after 240 F-T cycles. Repair-3 specimens showed a mass loss of 0.2 % following 180 cycles.

As shown in Figure 6- 7 **(b)**, the Substrate specimens underwent RDME of 56 % after 300 F-T cycles, which aligns with findings in the literature for concrete with a w/c ratio of 0.45 (Meng et al. 2020). Repair-1 and Repair-2 exhibited RDME of 54 % and 52 %, respectively, after 240 F-T cycles, whereas Substrate specimens showed an RDME of 68 %. Repair-3 specimens exhibited an RDME of 53 % after 180 F-T cycles, compared to Substrate specimens, which showed an RDME of 77 %. In contrast, after 180 F-T cycles, Repair-1 demonstrated an RDME of 71 %, while Repair-2 had an RDME of 65 %.

Repair-1 exhibited the best overall performance among all Repair groups, followed by Repair-2 and then Repair-3, as indicated by both the ML and RDME results. This suggests that the performance of the repair-substrate composite system improves with a lower w/c ratio in the repair materials. With a w/c ratio of 0.38, Repair-1 outperformed the others due to its denser microstructure, which leads to reduced porosity and improved durability. This enhanced matrix structure effectively minimizes moisture ingress and the resulting F-T damage by limiting the formation and expansion of ice within the pore spaces.

After 240 F-T cycles, no statistically significant differences in both ML and RDME were found at a significance level of 0.05 when comparing the Substrate specimens to Repair-1 and Repair-2. Similarly, after 180 F-T cycles, no significant differences in ML and RDME were observed at the same significance level when comparing the Substrate specimens to Repair-3. Additionally, there was insufficient evidence to indicate a statistically significant difference between Repair-1 and Repair-2 after 240 F-T cycles. Likewise, after 180 F-T cycles, no statistically significant differences in ML and RDME were observed at the 0.05 significance level when comparing Repair-3 with Repair-1 and Repair-2.

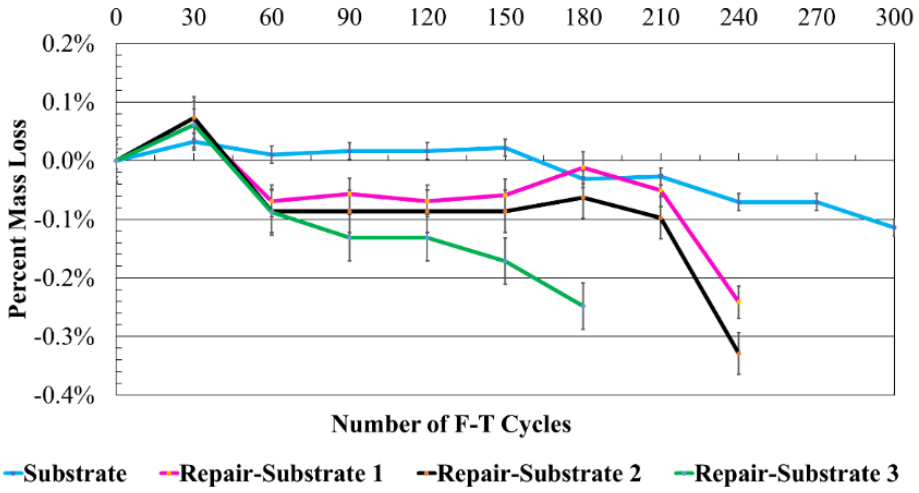
0
30
60
90
120
150
180
210
240
270
300
0.2%
0.1%
0.0%
-0.1%
-0.2%
-0.3%
-0.4%
Percent Mass Loss
Number of F-T Cycles
Substrate
Repair-Substrate 1
Repair-Substrate 2
Repair-Substrate 3

(a)

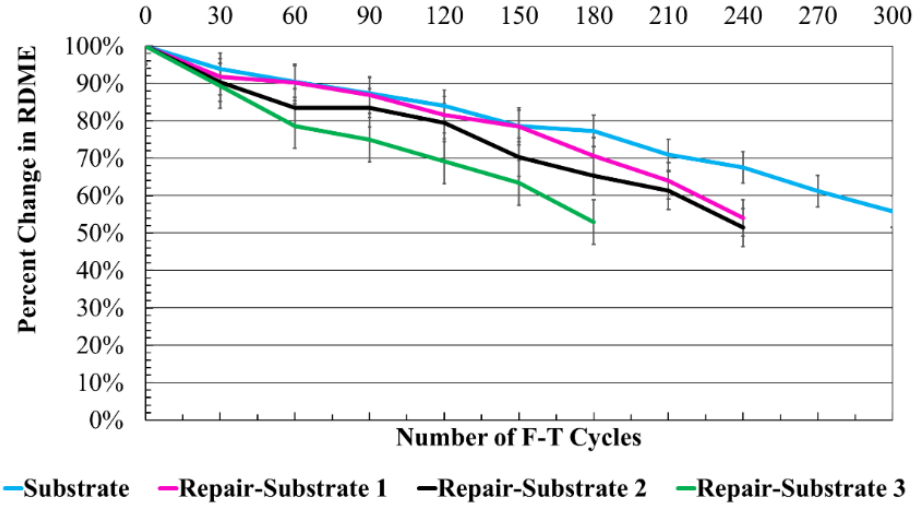
0
30
60
90
120
150
180
210
240
270
300
100%
90%
80%
70%
60%
50%
40%
30%
20%
10%
0%
Percent Change in RDME
Number of F-T Cycles
Substrate
Repair-Substrate 1
Repair-Substrate 2
Repair-Substrate 3

(b)

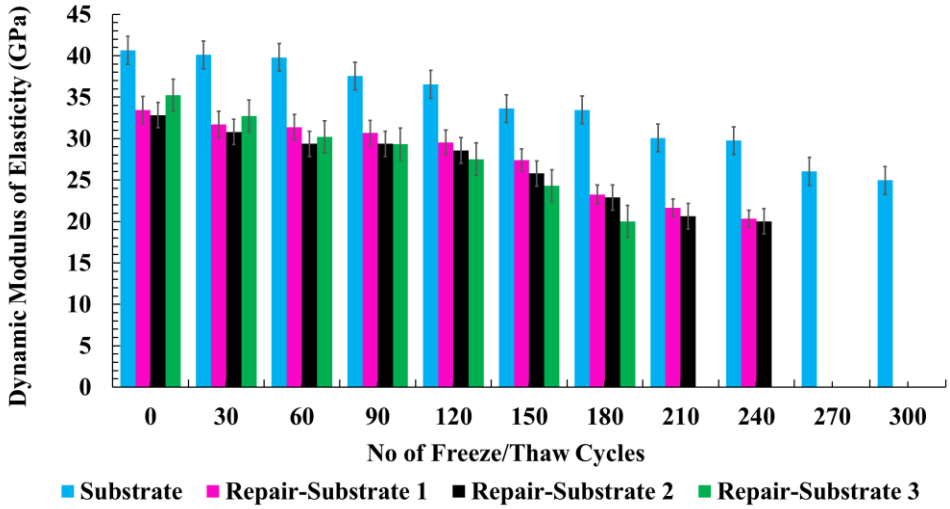

(c)

Figure 6- 7 Change of (a) mass and (b) RDME, and (c) DME value over F-T cycles for different concrete groups. The error bars represent one standard deviation.

6.4.4 UPV Results

The percent change in UPV and UPV values during F-T cycles for all groups of specimens are depicted in Figure 6- 8 **(a) and (b)**. It is apparent that Substrate specimens consistently maintained higher UPV values compared to Repair specimens. The initial UPV values for Substrate, Repair-1, Repair-2, and Repair-3 are 4250 m s^{-1}, 3860 m s^{-1}, 3820 m s^{-1}, and 3750 m s^{-1} respectively. It is evident that Substrate specimens have the highest initial UPV value, followed by Repair-1, Repair-2, and Repair-3.

As shown in Figure 6- 8 **(a)**, the Substrate specimens experienced a 30.0% decrease in UPV value after undergoing 300 F-T cycles. This finding aligns with previous literature regarding concrete with a w/c ratio of 0.45 (El-Mir and El-Zahab 2022). Repair-1 and Repair-2 exhibited UPV value changes of 42 % and 47 %, respectively, following 240 F-T cycles, while the Substrate specimens recorded a change of 23 %. Additionally, Repair-3 specimens demonstrated a 45 % change in UPV value after 180 cycles, in contrast to the Substrate specimens, which showed a 20 % change. Notably, after 180 F-T cycles, Repair-1 exhibited a change in UPV of 31 %, whereas Repair-2 recorded a change of 33 %.

Repair-1 demonstrated the best overall performance among all the Repair groups, followed by Repair-2 and then Repair-3, as evidenced by the UPV results, which align with the findings reported in *Section 3.3* for ML and RDME. This indicates that the effectiveness of the repair-substrate composite system improves as the w/c ratio in the repair materials decreases. With a w/c ratio of 0.38, Repair-1 surpassed the others due to its denser microstructure, which contributes to

reduced porosity and enhanced durability. This improved matrix structure effectively minimizes moisture ingress and the associated F-T damage by restricting the formation and expansion of ice within the pore spaces.

After 240 F-T cycles, statistically significant differences in UPV values were observed at the 0.05 significance level when comparing the Substrate specimens with Repair-1 and Repair-2. Similarly, after 180 F-T cycles, significant differences in UPV values were noted at the same significance level when comparing the Substrate specimens to Repair-3. Furthermore, there was insufficient evidence to demonstrate a statistically significant difference between Repair-1 and Repair-2 following 240 F-T cycles. Likewise, after 180 cycles, no statistically significant differences in UPV values were found at the 0.05 significance level when comparing Repair-3 with both Repair-1 and Repair-2.

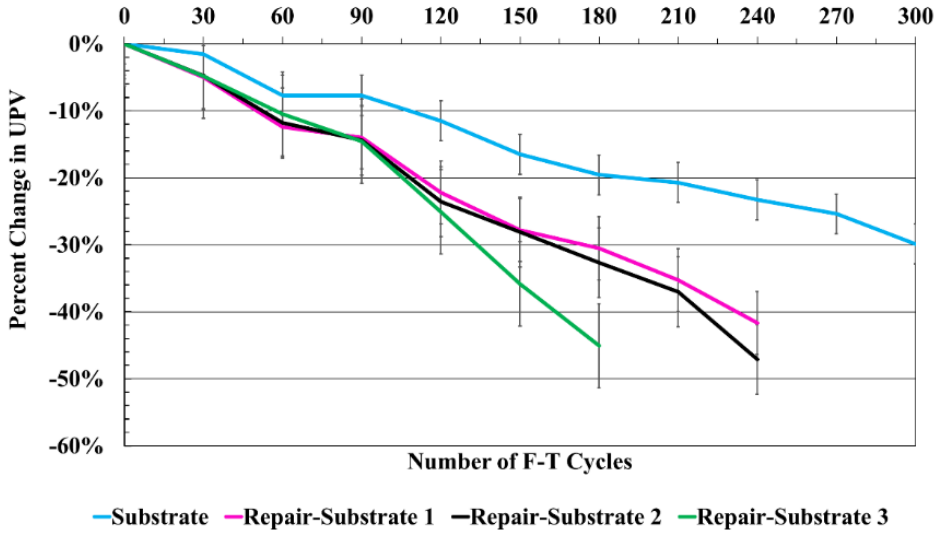

(a)

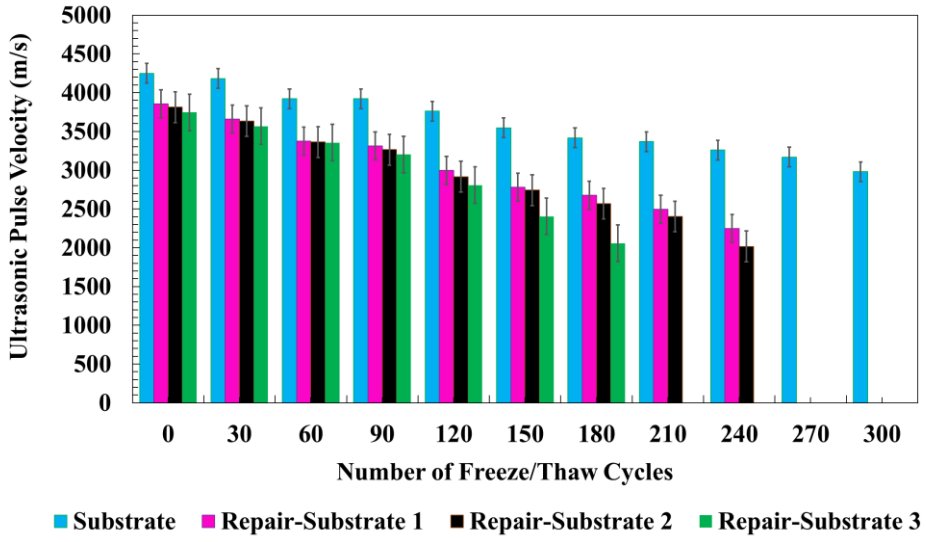

(b)

Figure 6- 8 (a) Percent change in UPV and (b) UPV value over F-T cycles for different concrete groups. The error bars represent one standard deviation.

6.4.5 Strength Testing Results

Compressive strength was performed using 100 mm (diameter) by 200 mm (height) cylinders per ASTM C39, while flexural strength (modulus of rupture) was measured using 75 mm by 75 mm

by 300 mm prisms per ASTM C293. The specimens were taken from identical batches to those subjected to F-T cycles. Figure 6- 9 presents the compressive and flexural strength results for the different concrete groups before and after F-T cycles. Before being subjected to F-T cycles, the compressive strength of the Substrate, Repair-1, Repair-2, and Repair-3 specimens was measured at 39.0 MPa, 35.2 MPa, 34.4 MPa, and 33.0 MPa, respectively. Similarly, the modulus of rupture for these groups was recorded as 6.80 MPa, 2.05 MPa, 1.95 MPa, and 1.95 MPa, respectively. The Substrate group exhibited the highest compressive and modulus of rupture, indicating superior structural integrity compared to the repair materials. It is noteworthy that although the compressive strength of the repair groups was comparable to that of the substrate, the modulus of rupture values revealed a significant disparity. The repair materials exhibited roughly one-fourth of the flexural strength of the substrate, highlighting potential weaknesses when subjected to bending or tensile loads. This discrepancy suggests that while compressive loads may not drastically compromise the integrity of repair materials, their flexural response might be a significant limitation in applications where tensile stress is a concern.

Among the repair groups, Repair-1 demonstrated superior performance in both compressive and flexural strength compared to Repair-2 and Repair-3. This can be attributed to the repair material's lower w/c ratio in the Repair-1 mix, which likely contributed to denser microstructures and enhanced mechanical properties. The reduced w/c ratio typically results in improved bond strength and lower porosity, which may explain Repair-1's comparative advantage in resisting both compressive and flexural stress.

Unpaired, two-tailed t-tests conducted on the before F-T cycle results revealed statistically significant differences in compressive and flexural strength values among Substrate, Repair-1, Repair-2, and Repair-3 at the 0.05 significance level.

After 300 F-T cycles, Substrate specimens showed a decrease in compressive strength and flexural strength of 39 % and 41 %, respectively. In comparison, after 240 F-T cycles, Repair-1 and Repair-2 specimens experienced compressive strength reductions of 63 % and 68 %, and flexural strength reductions of 35 % and 37 %, respectively. Additionally, Repair-3 specimens demonstrated decreases in compressive strength and flexural strength of 68 % and 42 % after 180 F-T cycles. The results underscore that while Repair groups showed greater compressive strength reductions under F-T cycles than the Substrate group, their flexural performance had similar percentage reductions. Although Repair-1 and Repair-2 showed improved flexural durability compared to Repair-3, they remained significantly lower than the Substrate, suggesting that optimized mix design alone may not fully close the gap in flexural performance under F-T exposure.

Unpaired, two-tailed t-tests conducted on the after F-T cycles results indicated a statistically significant difference in compressive and flexural strength values between the Substrate and Repair-1 (after 240 F-T cycles), Repair-2 (also after 240 F-T cycles), and Repair-3 (after 180 F-T cycles) at a significance level of 0.05. However, there is insufficient evidence to establish statistically significant differences in compressive and flexural strength values among Repair-1, Repair-2, and Repair-3.

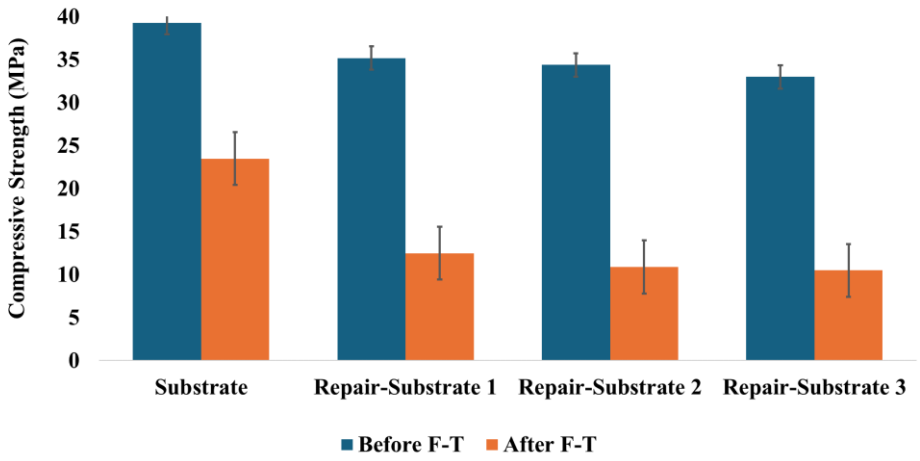

(a)

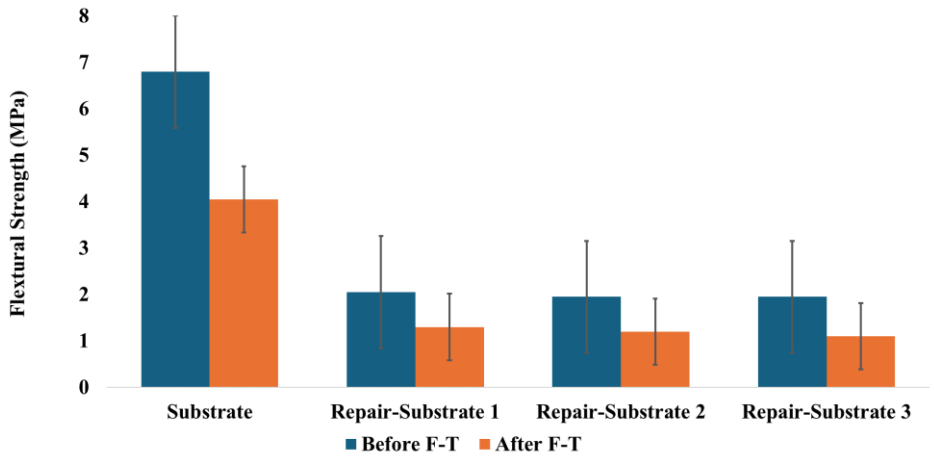

(b)

Figure 6- 9 (a) Compressive strength, and (b) modulus of rupture of different concrete groups for before and after F-T cycles, error bars represent one standard deviation.

6.4.6 Time-Dependent D_c and Concentration Profile

Figure 6- 10 depicts the average concentration profiles and apparent D_c values for all groups of concrete specimens after 3, 14, and 28 days of ponding before the F-T cycles. Based on the data from Figure 6- 10**,** substrate concrete specimens exhibited the lowest apparent D_c value before undergoing F-T cycles, similar to the concrete specimens with a 0.45 w/c ratio. For the repair-substrate specimens, it is evident that all the groups Repair-1, Repair-2, and Repair-3 exhibited higher apparent D_c values than substrate specimens. These findings are consistent with the results of the RCPT test. Table 6- 5 shows the average D_c values for Substrate, Repair-1, Repair-2, and Repair-3 specimens after 3 days, 14 days, and 28 days of ponding before F-T cycles.

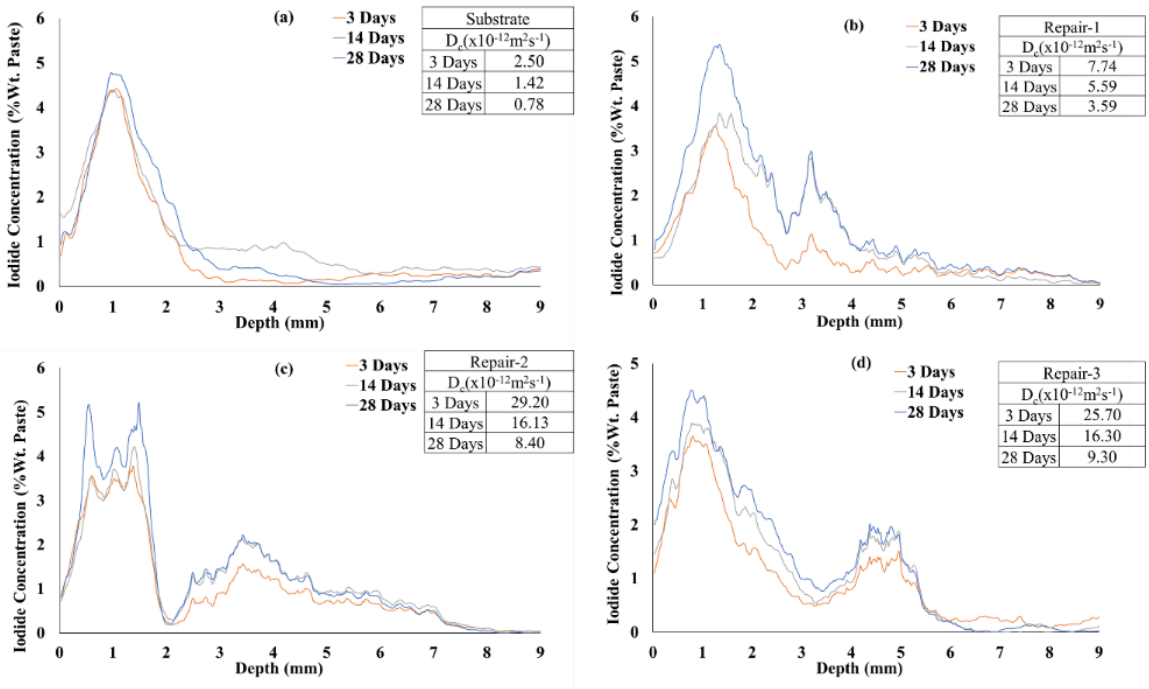

Figure 6- 10 Concentration profiles for the following concrete samples before undergoing F-T cycles: (a) Substrate, (b) Repair-1, (c) Repair-2, and (d) Repair-3.

Table 6- 5 Average D_c (x 10^{-12} m^2 s^{-1}) values for concrete samples before F-T cycles

	Substrate		Repair-1		Repair-2		Repair-3	
Ponding Duration	Average	Standard Deviation	Average	Standard Deviation	Average	Standard Deviation	Average	Standard Deviation
3 Days	2.50	0.45	7.74	2.12	29.2	2.68	25.7	2.59
14 Days	1.42	0.81	5.59	3.06	16.1	3.36	16.30	1.10
28 Days	0.78	0.32	3.59	0.58	8.40	1.39	9.30	2.64

These D_c values confirm that the Repair-1 specimens exhibit lower apparent D_c than other repair groups. The lower w/c in Repair-1 leads to reduced D_c values, indicating enhanced resistance to ion ingress at the OTZ of the repair-substrate specimens. This improvement can be attributed to the lower w/c in Repair-1, which likely resulted in a denser matrix with fewer interconnected capillary pores, reducing the overall penetrability to chloride ions.

However, the Repair-2 and Repair-3 specimens demonstrated higher apparent D_c values than Repair-1, suggesting that the higher w/c ratios in these repair materials were less effective in

improving resistance to ion ingress at the OTZ of the repair-substrate concrete specimens. Despite better performance among the repair groups, Repair-1 still exhibited higher apparent D_c values than the substrate specimens. After 28 days of immersion in a 0.6 M KI solution, the D_c values of Repair-1, Repair-2, and Repair-3 were 460 %, 1080 %, and 1190 % higher, respectively, compared to the substrate D_c. This indicates that the OTZ in the repair-substrate interface remains more porous than the substrate alone, allowing rapid ion penetration. As a result, the repair-substrate systems may be more vulnerable to accelerated degradation in environments exposed to chloride ions, such as marine structures or those subjected to deicing salts.

It can be seen from the above figures over the 28-day ponding period, the iodide concentration reached its peak (C_{max}) of 4.7 % in Substrate within the surface layers just below the surface (Δx), followed by a gradual decrease at greater depths. In contrast, the iodide concentration peaked at 5.2 % in Repair-1, 5.2 % in Repair-2, and 4.7 % in Repair-3 within Δx. This rise is likely attributed to capillary absorption, convection, and diffusion during the initial solution penetration, which is termed as maximum phenomenon in the literature (Behravan et al. 2023; Moradllo and Ley 2017a; Zacchei and Bastidas-Arteaga 2022). For the Repair groups, the concentration profiles showed that after reaching C_{max}, the iodide concentration approached zero and then exhibited minor secondary peaks before gradually declining at greater depths. This behavior suggests the presence of physical impediments, such as coarse aggregates (Jiang et al. 2020; Ju et al. 2022; Li et al. 2023b), which may disrupt ion ingress and lead to localized reductions in concentration. These barriers cause ions to penetrate in a staggered pattern, resulting in an intermediate peak before further diffusion occurs.

Several minor peaks in the repair groups at greater depths imply higher diffusion rates compared to the substrate group. This increased diffusion is likely due to greater porosity at the OTZ between the repair and substrate materials. The OTZ can form preferential pathways or micro-channels that facilitate deeper ion penetration. The repair group's higher porosity contrasts with the substrate's more compact matrix, which acts as an effective barrier to deeper ion transport and explains the absence of secondary peaks in its concentration profile. These observations indicate that the microstructural characteristics of the OTZ play a crucial role in ion transport. The higher porosity and presence of microchannels in the OTZ contribute to increased ion diffusion, making it a critical zone for ingress.

Figure 6- 11 depicts the average concentration profiles and apparent D_c values for Substrate and Repair-1 concrete specimens after 3, 14, and 28 days of ponding after F-T cycles. It is important to note that all specimens from the Repair-2 and Repair-3 groups failed during the coring process required for TXM analysis after the F-T cycles. Consequently, the authors were only able to collect cores from the Substrate and Repair-1 specimens for this analysis. Table 6- 6 shows the average D_c values for Substrate, and Repair-1 specimens after 3, 14, and 28 days of ponding after F-T cycles.

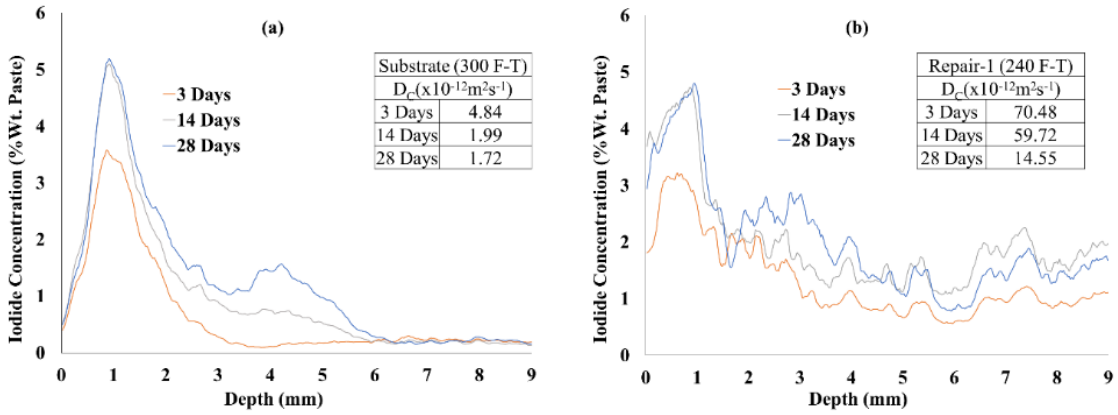

Figure 6- 11 Concentration profiles for the following concrete samples after undergoing F-T cycles: (a) Substrate (300 F-T cycles), (b) Repair-1 (240 F-T cycles).

Table 6- 6 Average D_c (x 10^{-12} m^2 s^{-1}) values for concrete samples after F-T cycles

	Substrate (300 F-T cycles)		Repair-1 (240 F-T cycles)	
Ponding Duration	Average	Standard Deviation	Average	Standard Deviation
3 Days	4.84	1.33	70.5	2.36
14 Days	1.99	0.32	59.7	4.24
28 Days	1.72	0.24	14.6	2.79

Based on the analysis of Figure 6- 11 and Table 6- 6, both Substrate and Repair-1 specimens exhibited significant increases in apparent D_c values following F-T cycles. Repair-1 specimens failed after 240 F-T cycles, while Substrate specimens endured up to 300 F-T cycles before failure. After 28 days of ponding in a 0.6M KI solution, Repair-1 specimens demonstrated a remarkable 405 % increase in D_c values after 240 F-T cycles compared to their initial values prior to F-T cycles. In contrast, Substrate specimens exhibited a 221 % increase in D_c values after 300 F-T cycles.

When comparing D_c values at their respective points of failure during F-T cycles, Repair-1 specimens exhibited an 846 % higher D_c compared to Substrate specimens at the point of their failure. This contrasts with pre-F-T cycle measurements, where Repair-1 specimens already exhibited a 460 % higher D_c than Substrate specimens. This substantial increase indicates that Repair-1 specimens experienced severe internal damage during F-T cycles, likely due to the propagation of microcracks. These microcracks could have formed interconnected microchannels, significantly enhancing diffusion rates within the OTZ of Repair-1 specimens. Moreover, Repair-1's OTZ, being inherently weaker than that of the Substrate specimens, further exacerbated this

damage mechanism. The enhanced diffusion within Repair-1's OTZ highlights the role of microstructural deficiencies in accelerating damage progression under repeated F-T cycling.

Table 6- 7 and Table 6- 8 summarize the D_c values before and after F-T cycles for all groups of concrete specimens. The variations in the apparent D_c values for different angles in the table result from variations in the paste-aggregate matrix within the concrete samples at various angles.

The unpaired, two-tailed t-tests indicate statistically significant differences in the D_c values between Substrate and Repair-1, Repair-2, and Repair-3 specimens at 3, 14, and 28 days of ponding before F-T cycles. After F-T cycles, statistically significant differences were observed only between Substrate and Repair-1 specimens at the 5 % significance level.

Table 6- 7 D_c (x 10^{-12} m^2 s^{-1}) values before F-T cycles

Substrate						
	3 Days		14 Days		28 Days	
Angle	S1	S2	S1	S2	S1	S2
0	2.09	3.15	0.88	1.16	1.08	0.75
180	2.40	2.37	2.62	1.02	0.35	0.94
Average	2.50 ± 0.44		1.42 ± 0.79		0.78 ± 0.31	
Standard Deviation	0.45		0.81		0.32	
Repair-1						
	3 Days		14 Days		28 Days	
Angle	S1	S2	S1	S2	S1	S2
0	4.82	9.84	5.77	7.23	3.75	2.89
180	8.44	7.84	1.23	8.12	3.45	4.28
Average	7.74 ± 2.07		5.59 ± 3.00		3.59 ± 0.57	
Standard Deviation	2.12		3.06		0.58	
Repair-2						
	3 Days		14 Days		28 Days	
Angle	S1	S2	S1	S2	S1	S2
0	29.5	30.8	11.2	16.9	9.95	8.58
180	31.1	25.3	18.6	17.8	8.39	6.57
Average	29.2 ± 2.62		16.1 ± 3.29		8.37 ± 1.36	
Standard Deviation	2.68		3.36		1.39	
Repair-3						
	3 Days		14 Days		28 Days	
Angle	S1	S2	S1	S2	S1	S2
0	29.5	25.0	15.8	17.5	8.54	6.71
180	24.2	24.0	15.0	16.8	13.0	8.90
Average	25.7 ± 2.54		16.3 ± 1.07		9.28 ± 2.59	
Standard Deviation	2.59		1.10		2.64	

Note: the value after the ± symbol represents a 95 % confidence interval. S1 and S2 refer to Sample 1 and Sample 2, respectively.

Table 6- 8 D_c (x 10^{-12} m^2 s^{-1}) values after F-T cycles

Substrate						
	3 Days		14 Days		28 Days	
Angle	S1	S2	S1	S2	S1	S2
0	4.54	5.97	1.56	1.98	2.05	1.63
180	5.76	3.08	2.09	2.32	1.47	1.71
Average	4.84 ± 1.30		1.99 ± 0.31		1.72 ± 0.24	
Standard Deviation	1.33		0.32		0.24	
Repair-1						
	3 Days		14 Days		28 Days	
Angle	S1	S2	S1	S2	S1	S2
0	72.8	71.2	59.9	53.9	12.8	11.8
180	70.7	67.2	61.2	63.9	15.6	18.0
Average	70.5 ± 2.31		59.7 ± 4.15		14.6 ± 2.74	
Standard Deviation	2.36		4.24		2.79	

Note: the value after the ± symbol represents a 95 % confidence interval.
S1 and S2 refer to Sample 1 and Sample 2, respectively.

6.5 Conclusions and Recommendations

This study evaluated the impact of varying w/c ratios in repair mixes on the durability of concrete repair-substrate interfaces subjected to F-T cycles. The findings provide key insights into the performance of repair-substrate systems, particularly emphasizing the OTZ as a critical factor in durability under harsh environmental conditions.

- ✓ Repair-1 (w/c = 0.38) consistently outperformed Repair-2 (w/c = 0.40) and Repair-3 (w/c = 0.45) in terms of lower water absorption, reduced chloride ion penetrability, and higher resistance to F-T damage. This improved performance is likely due to a denser microstructure, which could result from the lower w/c ratio.
- ✓ Substrate specimens exhibited superior resilience, enduring 300 F-T cycles with minimal ML and RDME reduction. Repair-1 demonstrated the highest durability among repair mixes, failing after 240 F-T cycles, compared to 180 cycles for Repair-3. However, the OTZ continued to serve as a pathway for increased diffusion, especially after F-T cycling.
- ✓ The D_c value in the OTZ from TXM analysis showed a notable increase after F-T cycles. Repair specimens, especially Repair-1, demonstrated better resistance to diffusion than other repair groups but were still more vulnerable than the Substrate specimen. OTZ porosity remained a challenge, with Repair-1 showing a 405 % increase in D_c post-F-T cycles, compared to 221 % for the Substrate. These results highlight the critical role of repair material mix design in mitigating OTZ deficiencies and suggest strategies to improve concrete repair resilience in cold environments.

Future research should focus on incorporating supplementary cementitious materials, fibers, or nanomaterials into repair mixes to address OTZ vulnerabilities and enhance resistance to chloride ingress and F-T damage. Expanding TXM and similar non-destructive testing techniques can provide valuable insights into ion transport mechanisms and microstructural evolution under environmental stressors. Additionally, validating these findings under real-world environmental conditions is essential to optimize repair mix designs for diverse applications and ensure long-term durability. These strategies collectively aim to improve the resilience of concrete repairs in cold environments.

Acknowledgement

This material is based upon work supported by the Broad Agency Announcement Program and the Cold Regions Research and Engineering Laboratory (ERDC-CRREL) under Contract No. W913E522C0001.

Disclaimer

Any opinions, findings and conclusions or recommendations expressed in this material are those of the author(s) and do not necessarily reflect the views of the Broad Agency Announcement Program and ERDC-CRREL.

References

ASTM C33/C33M-24a, Specification for Concrete Aggregates, (2024). https://doi.org/10.1520/C0033_C0033M-24A.

ASTM C192M-15, Standard Practice for Making and Curing Concrete Test Specimens in the Laboratory 1, (2019). https://doi.org/10.1520/C0192_C0192M-19.

ASTM C1585M-20, Standard Test Method for Measurement of Rate of Absorption of Water by Hydraulic-Cement Concretes, (2020). https://doi.org/10.1520/C1585-20.

ASTM C1202M-22, Standard Test Method for Electrical Indication of Concretes Ability to Resist Chloride Ion Penetration, (2022). https://doi.org/10.1520/C1202-22E01.

ASTM C666/C666M-15, Standard Test Method for Resistance of Concrete to Rapid Freezing and Thawing, ASTM International (2015). https://doi.org/10.1520/C0666_C0666M-15.

ASTM C597-22, Standard Test Method for Ultrasonic Pulse Velocity Through Concrete, ASTM International (2022). https://doi.org/10.1520/C0597-22.

ASTM C215-19, Standard Test Method for Fundamental Transverse, Longitudinal, and Torsional Resonant Frequencies of Concrete Specimens, ASTM International (2019). https://doi.org/10.1520/C0215-19.

ASTM C39/C39M-21, Standard Test Method for Compressive Strength of Cylindrical Concrete Specimens, ASTM International (2021). https://doi.org/10.1520/C0039_C0039M-21.

ASTM C293M-16, Standard Test Method for Flexural Strength of Concrete (Using Simple Beam With Center-Point Loading) 1, (2016). https://doi.org/10.1520/C0293_C0293M-16.

ASTM C1556-22, Standard Test Method for Determining the Apparent Chloride Diffusion Coefficient of Cementitious Mixtures by Bulk Diffusion 1, ASTM International (2022). https://doi.org/10.1520/C1556-22.

Baloch, W. L., H. Siad, M. Lachemi, and M. Sahmaran. 2021. “A review on the durability of concrete-to-concrete bond in recent rehabilitated structures.” *Journal of Building Engineering*, 44: 103315. https://doi.org/https://doi.org/10.1016/j.jobe.2021.103315.

Bassuoni, M. T., M. L. Nehdi, and T. R. Greenough. 2006. *Enhancing the reliability of evaluating chloride ingress in concrete using the ASTM C 1202 rapid chloride penetrability test*. ASTM International West Conshohocken, PA, USA. https://doi.org/10.1520/JAI13403

Behravan, A., M. T. Ley, D. Cook, Q. Hu, A. Rywelski, and R. Brorsen. 2023. “Measuring the Diffusion Coefficient of Paste and Concrete by Using Dental X-ray Equipment.” *CivilEng*, 4 (1): 224–247. MDPI. https://doi.org/10.3390/civileng4010014.

Behravan, A., M. T. Ley, A. Rywelski, and N. Berke. 2021. “Changes in the rate of ion penetration of alternative cementitious materials with time.” *Mater Des*, 197. Elsevier Ltd. https://doi.org/10.1016/j.matdes.2020.109236.

Beushausen, H., B. Höhlig, and M. Talotti. 2017. “The influence of substrate moisture preparation on bond strength of concrete overlays and the microstructure of the OTZ.” *Cem Concr Res*, 92: 84–91. Elsevier Ltd. https://doi.org/10.1016/j.cemconres.2016.11.017.

Brand, A. S., and J. Roesler. 2018. “Interfacial transition zone of cement composites with recycled concrete aggregate of different moisture states.” *Adv Civ Eng Mater*, 7 (1): 87–102. ASTM International. https://doi.org/10.1520/ACEM20170090.

Brandt, A. M. 2008. “Fibre reinforced cement-based (FRC) composites after over 40 years of development in building and civil engineering.” *Compos Struct*, 86 (1–3): 3–9. https://doi.org/10.1016/j.compstruct.2008.03.006.

Castro, J., D. Bentz, and J. Weiss. 2011. “Effect of sample conditioning on the water absorption of concrete.” *Cem Concr Compos*, 33 (8): 805–813. https://doi.org/https://doi.org/10.1016/j.cemconcomp.2011.05.007.

Courard, L., J. F. Lenaers, F. Michel, and A. Garbacz. 2011. “Saturation level of the superficial zone of concrete and adhesion of repair systems.” *Constr Build Mater*, 25 (5): 2488–2494. https://doi.org/10.1016/j.conbuildmat.2010.11.076.

Dixon, et al., 1991. “Standard Practice for Selecting Proportions for Normal, Heavyweight, and Mass Concrete (ACI 211.1-91) Chairman, Subcommittee A.”

El-Mir, A., and S. El-Zahab. 2022. “Assessment of the compressive strength of self-consolidating concrete subjected to freeze-thaw cycles using ultrasonic pulse velocity method.” *Russian Journal of Nondestructive Testing*, 58 (2): 108–117. Springer. https://doi.org/10.1134/S1061830922020024

Fathy, A., H. Zhu, and M. Kohail. 2022. “Factors affecting the fresh-to-hardened concrete repair system.” *Constr Build Mater* 320. https://doi.org/10.1016/j.conbuildmat.2021.126279.

Florea, M. V. A., and H. J. H. Brouwers. 2012. “Chloride binding related to hydration products: Part I: Ordinary Portland Cement.” *Cem Concr Res*, 42 (2): 282–290. https://doi.org/10.1016/j.cemconres.2011.09.016

Freeseman, K., K. Wang, and Y. Tan. 2022. “Bond strength and chloride resistance of epoxy and concrete overlays on bridge decks.” *International Journal of Pavement Engineering*, 23 (3): 916–921. Taylor and Francis Ltd. https://doi.org/10.1080/10298436.2020.1778693.

Guo, T., Y. Xie, and X. Weng. 2018. “Evaluation of the bond strength of a novel concrete for rapid patch repair of pavements.” *Constr Build Mater*, 186: 790–800. Elsevier Ltd. https://doi.org/10.1016/j.conbuildmat.2018.08.007.

Imbabi, M. S., C. Carrigan, and S. McKenna. 2012. “Trends and developments in green cement and concrete technology.” *International Journal of Sustainable Built Environment*. 1 (2012) 194–216. https://doi.org/10.1016/j.ijsbe.2013.05.001.

Jasielec, J. J., J. Stec, K. Szyszkiewicz-Warzecha, A. Łagosz, J. Deja, A. Lewenstam, and R. Filipek. 2020. “Effective and Apparent Diffusion Coefficients of Chloride Ions and

Chloride Binding Kinetics Parameters in Mortars: Non-Stationary Diffusion–Reaction Model and the Inverse Problem." *Materials*, 13 (23). https://doi.org/10.3390/ma13235522.

Jiang, H., Y. Tian, N. Jin, X. Jin, Z. Tian, D. Yan, and H. Ye. 2020. "Effect of aggregates spatial distribution on three-dimensional transport of chloride ions in reinforced concrete." *Constr Build Mater*, 259: 119694. https://doi.org/https://doi.org/10.1016/j.conbuildmat.2020.119694.

Jiang, L., D. Niu, L. Yuan, and Q. Fei. 2015. "Durability of concrete under sulfate attack exposed to freeze–thaw cycles." *Cold Reg Sci Technol*, 112: 112–117. https://doi.org/https://doi.org/10.1016/j.coldregions.2014.12.006.

Jin, H., L. Cheng, J. Liu, and S. Zhong. 2024. "Investigation of natural diffusion behavior in concrete using iodide replacing chloride ions: The impact of mineral admixtures types and dosages." *Journal of Materials Research and Technology*, 29: 1834–1861. https://doi.org/10.1016/j.jmrt.2024.01.206

Jin, H., Z. Li, W. Zhang, J. Liu, R. Xie, L. Tang, and J. Zhu. 2022. "Iodide and chloride ions diffusivity, pore characterization and microstructures of concrete incorporating ground granulated blast furnace slag." *Journal of Materials Research and Technology*, 16: 302–321. https://doi.org/https://doi.org/10.1016/j.jmrt.2021.11.155.

Ju, X., L. Wu, M. Liu, H. Jiang, and W. Zhang. 2022. "Modelling of chloride concentration profiles in concrete by the consideration of concrete material factors under marine tidal environment." *J Mar Sci Eng*, 10 (7): 917. https://doi.org/10.3390/jmse10070917

Júlio, E. N. B. S., F. A. B. Branco, and V. D. Silva. 2004. "Concrete-to-concrete bond strength. Influence of the roughness of the substrate surface." *Constr Build Mater*, 18 (9): 675–681. https://doi.org/10.1016/j.conbuildmat.2004.04.023.

Le, T., G. Le Saout, E. Garcia-Diaz, D. Betrancourt, and S. Rémond. 2017. "Hardened behavior of mortar based on recycled aggregate: Influence of saturation state at macro- and microscopic scales." *Constr Build Mater*, 141: 479–490. https://doi.org/https://doi.org/10.1016/j.conbuildmat.2017.02.035.

Ley, M. T. , P. N. , B. A. , C. D. and H. Q. 2023. *Measuring concrete permeability with CHIP.Final report for NCHRP IDEA Project 232*.

Li, G., H. Xie, and G. Xiong. 2001. "Transition zone studies of new-to-old concrete with different binders." *Cem Concr Compos*, 23 (4–5): 381–387. https://doi.org/10.1016/S0958-9465(01)00002-6

Li, G., Q. Zhou, W. Wang, C. Lu, C. Chen, Z. Guo, and C. Lu. 2023a. "Chloride diffusion along the interface between concrete matrix and repair materials under flexural loading." *Constr Build Mater*, 372. Elsevier Ltd. https://doi.org/10.1016/j.conbuildmat.2023.130829.

Li, Q., Y. Liu, Y. Tian, G. Zhang, H. Feng, N. Jin, X. Jin, H. Wu, Y. Shao, and D. Yan. 2023b. "Statistic investigation on chloride ions distribution based on numerical reconstruction of in situ meso-structure of concrete." *Constr Build Mater*, 409: 133931. https://doi.org/10.1016/j.conbuildmat.2023.133931

Li, Z., Y. Dang, Z. Tang, N. Xie, S. Lu, and X. Shi. 2021. "Optimal overlays for preservation of

concrete in cold climate: decision-making by the method of fuzzy comprehensive evaluation combined with AHP." *Journal of Infrastructure Preservation and Resilience*, 2 (1). Springer Science and Business Media LLC. https://doi.org/10.1186/s43065-021-00046-x.

Lin, H., Y. Han, S. Liang, F. Gong, S. Han, C. Shi, and P. Feng. 2022. "Effects of low temperatures and cryogenic freeze-thaw cycles on concrete mechanical properties: A literature review." *Constr Build Mater*, 345. Elsevier Ltd. https://doi.org/10.1016/j.conbuildmat.2022.128287.

Liu, J., C. Liao, H. Jin, Z. Jiang, R. Xie, and L. Tang. 2022. "Electrically driven ionic transport in the RCM and RIM: Investigations based on experiments and numerical simulations." *Constr Build Mater*, 331: 127331. https://doi.org/10.1016/j.conbuildmat.2022.127331

Luković, M., B. Šavija, H. Dong, E. Schlangen, and G. Ye. 2014. "Micromechanical Study of the Interface Properties in Concrete Repair Systems." *Journal of Advanced Concrete Technology*, 12 (9): 320–339. https://doi.org/10.3151/jact.12.320.

Lukovic, M., and G. Ye. 2016. "Effect of moisture exchange on interface formation in the repair system studied by X-ray absorption." *Materials*, 9 (1). MDPI AG. https://doi.org/10.3390/ma9010002.

Meng, C., W. Li, L. Cai, X. Shi, and C. Jiang. 2020. "Experimental research on durability of high-performance synthetic fibers reinforced concrete: Resistance to sulfate attack and freezing-thawing." *Constr Build Mater*, 262: 120055. https://doi.org/https://doi.org/10.1016/j.conbuildmat.2020.120055.

Moradllo, M. K., Q. Hu, and M. T. Ley. 2017. "Using X-ray imaging to investigate in-situ ion diffusion in cementitious materials." *Constr Build Mater*, 136: 88–98. Elsevier Ltd. https://doi.org/10.1016/j.conbuildmat.2017.01.038.

Moradllo, M. K., and M. T. Ley. 2017a. "Comparing ion diffusion in alternative cementitious materials in real time by using non-destructive X-ray imaging." *Cem Concr Compos*, 82: 67–79. Elsevier Ltd. https://doi.org/10.1016/j.cemconcomp.2017.05.014.

Moradllo, M. K., and M. T. Ley. 2017b. "Quantitative measurement of the influence of degree of saturation on ion penetration in cement paste by using X-ray imaging." *Constr Build Mater*, 141: 113–129. Elsevier Ltd. https://doi.org/10.1016/j.conbuildmat.2017.03.007.

Rabi, M., R. Shamass, and K. A. Cashell. 2022. "Structural performance of stainless steel reinforced concrete members: A review." *Constr Build Mater*.https://doi.org/10.1016/j.conbuildmat.2022.126673.

Rahat, M. H. H., D. M. Annand, P. Atwood, A. Behravan, and A. S. Brand. 2024a. "Effect of Freeze/Thaw and Substrate Moisture Condition on the Concrete Repair-Substrate Interface." *13th International Conference on Concrete Pavements*, M. Barman and A.-C. Brink, eds., 412–427. Minneapolis.

Rahat, Md. H. H., T. Q. Tran, B. D. J. E. Love, A. Behravan, and A. S. Brand. 2024b. "Investigating the Impact of Freeze–Thaw Damage on Chloride Ingress in Concrete." *Cold Regions Engineering 2024*, 575–585. https://doi.org/10.1061/9780784485460.053

Ram, P., J. Olek, and J. Jain. 2016. "Field Trials of Rapid-Setting Repair Materials."Joint Transportation Research Program, Indiana Department of Transportation and Purdue

University, West Lafayette, Indiana, (2013). https://doi.org/10.5703/1288284315185

Shi, X., N. Xie, K. Fortune, and J. Gong. 2012. "Durability of steel reinforced concrete in chloride environments: An overview." *Constr Build Mater*. https://doi.org/10.1016/j.conbuildmat.2011.12.038.

Skripkiunas, G., D. Nagrockiene, G. Girskas, M. Vaičiene, and E. Baranauskaite. 2013. "The cement type effect on freeze - Thaw and deicing salt resistance of concrete." *Procedia Eng*, 1045–1051. https://doi.org/10.1016/j.proeng.2013.04.132.

Wang, R., Z. Hu, Y. Li, K. Wang, and H. Zhang. 2022. "Review on the deterioration and approaches to enhance the durability of concrete in the freeze–thaw environment." *Constr Build Mater*.https://doi.org/10.1016/j.conbuildmat.2022.126371.

Zacchei, E., and E. Bastidas-Arteaga. 2022. "Multifactorial chloride ingress model for reinforced concrete structures subjected to unsaturated conditions." *Buildings*, 12 (2): 107. MDPI. https://doi.org/10.3390/buildings12020107

Zhou, J., G. Ye, and K. van Breugel. 2016. "Cement hydration and microstructure in concrete repairs with cementitious repair materials." *Constr Build Mater*, 112: 765–772. Elsevier Ltd. https://doi.org/10.1016/j.conbuildmat.2016.02.203.

Chapter 7. In-situ neutron radiography for real-time monitoring of pore-water movement in portland cement mortar exposed to sub-zero temperature[6]

The contributions of the authors to this manuscript are described as follows:

Md Hasibul Hasan Rahat: Conceptualization, Methodology, Formal analysis, Investigation, Writing–original draft, Writing–review and editing.

James R. Torres: Methodology, Formal analysis, Investigation, Writing–review and editing.

Yuxuan Zhang: Methodology, Formal analysis, Investigation.

Sepehr Akhtarshenas: Methodology, Formal analysis, Investigation.

Dip Banik: Methodology, Investigation.

Stefan Jacobsen: Methodology, Supervision, Writing–review and editing.

Sherif L. Abdelaziz: Supervision, Funding acquisition, Writing–review and editing.

Alexander S. Brand: Conceptualization, Methodology, Investigation, Supervision, Writing–original draft, Writing–review and editing.

[6] **Rahat, M.H.H.**, Torres, J.R., Zhang, Y., Sepehr, A., Banik, D., Jacobsen, S., Abdelaziz, S.L., & Brand, A.S. (2025). In-situ neutron radiography for real-time monitoring of pore-water movement in portland cement mortar exposed to sub-zero temperature. (under review by CRREL)

In-situ neutron radiography for real-time monitoring of pore-water movement in portland cement mortar exposed to sub-zero temperature

Md. Hasibul Hasan Rahat,[1*] James R. Torres,[2] Yuxuan Zhang,[2] Sepehr Akhtarshenas,[1] Dip Banik,[1] Stefan Jacobsen,[3] Sherif L. Abdelaziz,[1] and Alexander S. Brand[1,4,5*]

[1] The Charles E. Via, Jr. Department of Civil and Environmental Engineering, Virginia Polytechnic Institute and State University, Blacksburg, Virginia 24061, USA
[2] Neutron Scattering Division, Oak Ridge National Laboratory, One Bethel Valley Road, Oak Ridge, TN 37830, USA
[3]Department of Structural Engineering, Norwegian University of Science and Technology, 7491 Trondheim, Norway
[4] Department of Materials Science and Engineering, Virginia Polytechnic Institute and State University, Blacksburg, Virginia 24061, USA
[5] Myers-Lawson School of Construction, Virginia Polytechnic Institute and State University, Blacksburg, Virginia 24061, USA
* Corresponding authors: rahatm21@vt.edu (MHH. Rahat) and asbrand@vt.edu (AS. Brand)

7.1 Abstract

Neutron radiography was employed in this study to monitor real-time pore water movement in portland cement mortar exposed to subzero temperatures, providing novel insights into freeze-thaw (F-T) damage mechanisms. Deuterated water (D_2O) was used to hydrate the cement in the mortar specimens, and the pore structure was saturated with water (H_2O), allowing for a contrast that enabled detailed tracking of water movement. The mortar sample was placed on a chiller plate set to subzero temperatures, thereby providing a one-dimensional temperature gradient vertically in the sample. Neutron radiography revealed that unfrozen water migrated upward as the freezing front advanced, and this mechanism can create hydraulic pressure within the mortar microstructure, which may contribute to the initiation and propagation of microcracks during F-T cycles. Additional characterization of the concrete made with D_2O showed a marked contrast to the samples made with H_2O, including delayed hydration, diminished compressive strength, and greater porosity. Therefore, while mortar made with D_2O allowed for greater neutron contrast to the pores filled with H_2O, further study is required to produce mortars with similar properties to those made with H_2O. In addition, further refinement is needed to the radiography experiment to allow for greater control of temperatures and potential quantification of the water concentration.
Keywords: Freeze-thaw resistance, Neutron radiography, Macropores, air-void system, hydration kinetics

7.2 Introduction

The main goal of this study is to expand the understanding of damage accumulation in portland cement concrete resulting from freeze-thaw (F-T) cycles in cold climates. Concrete is the most widely used construction material globally [1,2], including in colder regions, where F-T damage is acknowledged as the leading cause of diminished durability in concrete structures [3–10]. While

engineers have created empirical approaches to lessen the impact of F-T damage, mechanistic solutions remain elusive due to the complex and not fully understood mechanisms of damage accumulation. It is well known that the expansion of water by 9 % upon freezing contributes to damage; however, this is not the sole reason for the damage, as damage still occurs in partially saturated concrete [11]. In fact, additional mechanisms have been proposed [12,13], and the existing data show conflicting views on how these proposed mechanisms relate to each other and whether all, some, or none of them are the true causes of damage accumulation. In the process of F-T cycling, concrete damage occurs due to various mechanisms, such as the volume expansion of water when it freezes, the hydraulic and osmotic pressures exerted by pore water, the stresses arising from cryosuction and ice crystallization, and the formation of micro-ice lenses [12,14–16]. All these factors contribute to internal stresses that can result in cracking and deterioration. To fully comprehend the intricate processes leading to F-T damage in concrete, monitoring the movement of pore water and potentially ice crystallization within the concrete macropores during exposure to subzero temperatures, in real-time, in both quantitative and non-destructive manners is crucial to understanding these mechanisms. This study aims to observe the movement of pore water within the concrete macropores in real-time while exposed to subzero temperatures, with the expected outcome being new insights to design more resilient concrete infrastructure in cold and Arctic regions.

Choosing an appropriate technique for imaging the internal structure of composite materials like concrete is determined by the specific characteristics of the studied material. Neutron radiography and synchrotron X-ray tomography are viable methods for this investigation [17,18]. Although synchrotron X-ray tomography provides detailed structural characterization, neutron radiography is particularly effective for examining water movement within concrete due to its high sensitivity to hydrogen, superior contrast in complex and dense materials [19,20], and capability to provide detailed insights into moisture dynamics [21–26].

Previous studies utilizing neutron radiography have successfully quantified water absorption processes, the degree of pore saturation, and the spatial distribution of water within concrete and mortar, demonstrating its capability to analyze moisture ingress and redistribution under various environmental conditions [25–27]. Lucero *et al.*, [25] investigated the absorption of salt solutions into the mortar using neutron imaging, revealing changes in transport properties due to pore blocking by reaction products such as Friedel's salt and calcium oxychloride. Kichanov *et al.*, [28] conducted neutron tomography to evaluate the 3D distribution of pores and cracks in cement-based materials for radioactive waste conditioning, supporting matrix optimization for long-term durability. Additionally, neutron imaging has been utilized to examine concrete under high temperatures, helping researchers understand moisture migration under thermal gradients [20,29]. Recent methodological advancements further enhance the applicability of neutron radiography for evaluating concrete durability and service life prediction by developing methodologies to quantify settlement and water content distribution in fresh concrete using neutron imaging, overcoming traditional limitations in laboratory measurements [30,31]. Neutron imaging has also been employed to monitor internal curing, carbonation processes, and internal structural features within

concrete, significantly expanding the range of possible investigations [32–35]. Considering these capabilities and demonstrated outcomes, neutron radiography is chosen as the primary imaging method for this study.

7.2.1 Significance of the study

The significance of this study is that it will monitor the pore water movement in the mortar macropores in real time during freezing for the first-time using neutron radiography. While similar experiments to track water movement have been conducted while heating concrete [20,29], and one workshop presentation has reported preliminary neutron imaging under F-T conditions[36], no study in the literature has presented a neutron imaging study of water movement during freezing of concrete. This study will provide fundamental *in-situ* insights into the timing and movement of water within mortar macropores under F-T cycles, aiding future research and the design of more resilient concrete structures. This work will also help guide other researchers who are interested in using neutron imaging to study moisture movement in cement-based materials during freeze-thaw conditions.

7.3 Experimental methodology

7.3.1 Materials and mix design

This study prepared mortar specimens using deuterated water (D_2O). To compare hydration kinetics, pore structure, freezing points of pores, air-void system, and mechanical properties of the D_2O mortar group, an additional set of specimens was prepared using water (H_2O). Mortar mixtures were proportioned according to the volumetric method outlined in ACI 211.1 [37]. Type I/II portland cement was used and had a specific gravity of 3.15. The fine aggregate (FA) was a natural quartz sand with a fineness modulus of 2.6, while the coarse aggregate (CA) was a crushed limestone with a maximum particle size of 5 mm. The FA and CA had absorption capacities of 1.3% and 1.1% by mass, respectively. Before mixing, the aggregates were oven-dried and cooled to room temperature. The mixing water was adjusted to account for their absorption capacity, ensuring a saturated surface dry condition. Since D_2O is denser than H_2O, equal volumetric water contents yielded different water-to-cement ratios (w/c): 0.54 for the H_2O mortar mix and 0.60 for the D_2O mortar mix. No admixtures (*e.g.*, AEA, water reducers, and superplasticizers) were added, so pore-water movement was governed solely by the cement–aggregate matrix, unmodified by chemical admixtures. The chemical composition of the cement, and the mass (kg/m^3) and volume-based mix designs are given in Table 7- 1 and Table 7- 2.

Table 7- 1 Chemical composition of cement

Component	CaO	SiO_2	Al_2O_3	Fe_2O_3	SO_3	MgO	Na_2O
Content (%)	62.77	20.80	4.73	3.57	4.08	1.87	0.52

Table 7- 2 Mix design of mortar

Mortar Component	D_2O Mortar		H_2O Mortar	
	Quantity (kg/m^3)	Volume (m^3)	Quantity (kg/m^3)	Volume (m^3)
Cement	433.1	0.138	433.1	0.138
FA	712.6	0.269	712.6	0.269
CA	913.1	0.338	913.1	0.338
Water	278.3	0.251	252.3	0.252

7.3.2 Isothermal calorimetry

The hydration kinetics of paste samples prepared with D_2O and H_2O, maintaining the same w/c as the mortar mix design mentioned in section 2.1, were evaluated using isothermal calorimetry to assess total heat and thermal power. Paste specimens weighing between 7.5 g and 8.5 g were manually mixed in 15 mL plastic containers. These samples were then placed in a Calmetrix I-Cal Flex Calorimeter (Calmetrix Inc., Arlington, MA, USA) and monitored for 72 hours under a stable temperature of 23 °C.

7.3.3 Low temperature differential scanning calorimetry (LT-DSC)

A TA DSC Q2500 (TA Instruments, New Castle, Delaware, USA) was utilized to examine the impact of D_2O incorporation on the freezing point, melting heat (MH), and frozen water (FW) content in cement pastes. Paste samples cured for 3 days, 14 days, and 28 days, weighing approximately 30 mg to 40 mg, were placed in aluminum crucibles and subjected to rapid cooling and heating cycles. The crucibles containing the samples were positioned in the DSC, and a 5 °C min^{-1} heating rate was applied [38–40]. Within the temperature range of −30 °C to 25 °C, no phase transitions were observed in the hydration products of cementitious materials; instead, the only detected phase change was associated with the pore water [41].

The melting of FW resulted in an endothermic peak, with the freezing point of pore water defined in a simplified way as the temperature at which the tangent line intersects the baseline of the lowest part of the melting curve, as illustrated in Figure 7- 1**.** In reality there is a gradual freezing of pore water as temperature is lowered in saturated hardened cement paste. The smaller the pore size of a pore, the lower is the freezing point of the water in the pore. This endothermic peak temperature is commonly referred to as the freezing point [38,41].

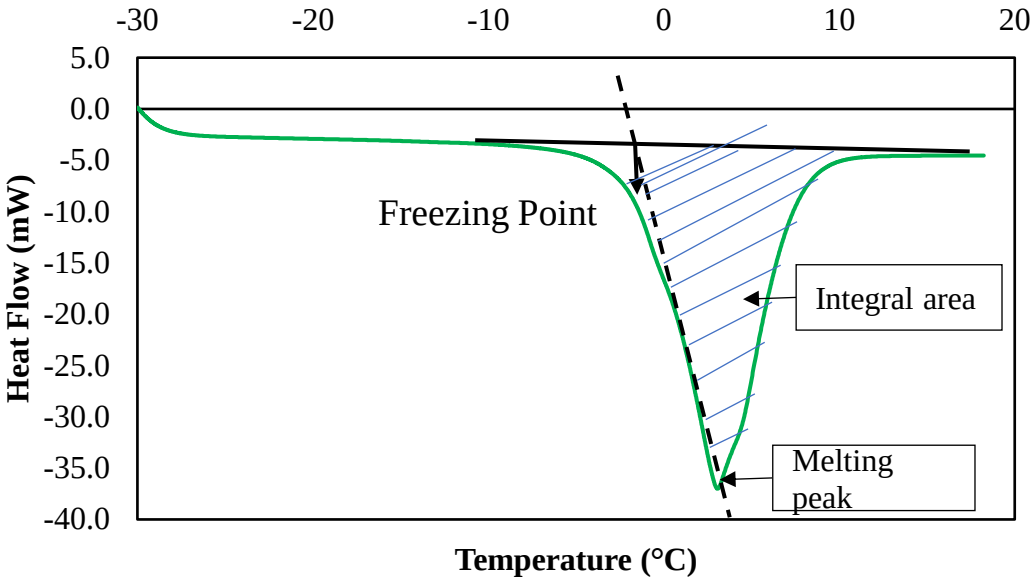

Figure 7- 1 LT-DSC heat flow curve of determination of freezing point; and MH (i.e., the amount of FW).

The total area under the melting curve represents the amount of FW present in the paste samples [42]. The percentage of FW was then calculated using Equation 1, which incorporates the integral area of the melting peak [42,43].

$$FW(\%) = \frac{Q}{H_f \times m} * 100 \quad (1)$$

where, Q is the enthalpy (J), m is the mass of the sample (g), H_f is the temperature-dependent heat of fusion of water (J g^{-1}) calculated using the same linear relationship used by Jacobsen *et al.* [44], as shown in Equation 2, and X is the freezing point of water in the concrete pore (°C).

$$H_f = 333.6 + 2.2\,X \quad (2)$$

7.3.4 Thermogravimetric analysis (TGA)

TGA was conducted on paste specimens prepared with D_2O and H_2O. Before analysis, the specimens were finely pulverized using a mortar and pestle in a ventilated fume hood. Each sample weighing approximately 15 mg to 25 mg was then placed onto the platinum pan of a Discovery TGA 5500 (TA Instruments, New Castle, DE, USA). The samples were heated in a nitrogen atmosphere up to 1000 °C at a controlled rate of 20 °C min^{-1}. The degree of hydration (DOH) of the paste samples was assessed after 3 days and 14 days of hydration by quantifying the chemically

bound water (CBW) [45]. This was determined using Equation 3, where *α(t)* represents the DOH at a given time *t*, W_n *(t)* is the chemically bound water content at time *t* (expressed in grams of water per 100 g of anhydrous cement), and W_n *(∞)* denotes the chemically bound water content for a fully hydrated sample (in grams of water per 100 g of anhydrous cement).

$$\alpha(t) = \frac{W_n(t)}{W_n(\infty)} * 100 \tag{3}$$

Equation 4 can be employed to experimentally determine the W_n *(t)* value, provided that no carbonation is present in the cement paste and that the anhydrous cement experiences minimal weight loss prior to reaching 1000 °C.

$$W_n(t) = \frac{\Delta \text{m } sample\ (105°\text{C} - 1000°\text{C})}{m\ sample\ (1000°\text{C})(\text{t})} * 100 \tag{4}$$

To estimate the value of W_n (∞), the National Institute of Standards and Technology provided a theoretical approximation of the bound water[46,47]. Although originally developed for H_2O-based matrix, this approximation can also be applied to D_2O-based matrix. This study utilized the approach outlined by Kolour *et al.* [48] to simplify the experimental procedure. Since the mass loss above 600 °C primarily resulted from the decomposition of various calcite forms due to CO_2 release since carbonation was not completely prevented, it was not considered part of the CBW. Consequently, in this study, Equation 3 was modified to account for mass loss only up to 600 °C, diverging from its original application extending to 1000 °C to determine the paste sample DOH.

7.3.5 X-ray diffraction (XRD)

XRD was employed to analyze the hydration products of the paste samples after 3 days and 14 days of curing. The hydration of the samples was stopped using ethanol, and then the samples were pulverized using a mortar and pestle and micronized. XRD analysis was performed using a Bruker D8 Advance diffractometer (Bruker, Billerica, MA, USA) equipped with Cu Kα radiation (40 kV, 40 mA). Data were collected over a scanning range of 5° to 55° (2θ) with a step size of 0.02° per second.

7.3.6 Hardened air-void content

In this study, the air-void system in hardened mortar was analyzed using the point count method in accordance with ASTM C457 Procedure B [49]. The specimens were polished and scanned with a digital scanner. To enhance contrast, the surface was stained with a black permanent marker to darken the cement paste. Air voids were filled with fine Aluminum Oxide (Al_2O_3) powder with a particle size range of 1 µm, following the procedure described by ASTM C457. The scanned images were then processed using ImageJ for quantitative analysis of the air-void system. A grid was overlaid for manual assessment, with a pixel size of 10.6 µm and a total scanned area of 5.0 cm by 5.0 cm. This analysis enabled the determination of key air-void parameters, including the

air content (A), paste-air ratio (p/A), average chord length ($\bar{l}$), void frequency (n), specific surface (α), and spacing factor ($\bar{L}$) for hardened D_2O and H_2O mortar specimens.

7.3.7 N_2 gas adsorption

Nitrogen adsorption measurements were performed using a Quantachrome NOVA 2200 (Quantachrome Instruments, Boynton Beach, FL, USA) gas sorption analyzer to characterize the pore structure of the paste samples. Before analysis, the samples underwent an outgassing process under vacuum at 3.5×10^{-5} torr and 100 °C for approximately 24 hours to remove any physically adsorbed moisture or contaminants. After degassing, the adsorption cells were transferred into the analysis chamber, and nitrogen adsorption-desorption measurements were conducted at –196 °C, with the cells placed in liquid nitrogen. During the analysis, adsorption and desorption isotherms were recorded across a relative pressure (P/P_0) range of 0.002 to 0.9. The Multi-point Brunauer-Emmett-Teller (BET) method was applied to determine the specific surface area (SSA), using the data within a P/P_0 range of 0.07 to 0.3. For pore volume analysis, the Barrett-Joyner-Halenda (BJH) method was employed over the full relative pressure range; however, calculations were based on the adsorption branch of the isotherm. The adsorption isotherm was selected because it provides more reliable data for relatively smaller pores, as they fill progressively with increasing pressure, avoiding hysteresis effects that can complicate desorption-based analysis. This approach ensures a more accurate assessment of the fine pore structure and pore size distribution while ignoring alterations (coarsening) of the pore structure due to drying in the outgassing process before N_2-BET analysis. The total accessible pore volume for nitrogen, corresponding to pore sizes in the 0.4 nm to 8.5 nm range, was quantified using this method.

7.3.8 Compressive strength

For each sample group, nine 50 mm by 50 mm by 50 mm mortar cube specimens were prepared and cured in lime-saturated plain water, and compression strength testing was performed on specimens cured for 3 days, 14 days, and 28 days according to ASTM C109 [50]. Three replicates were tested at each age.

7.3.9 Preparation for neutron radiography experiment

The neutron radiography experiment for this study was conducted at the Multimodal Advanced Radiography Station (MARS) on the CG-1D beamline of the High Flux Isotope Reactor (HFIR) at Oak Ridge National Laboratory (ORNL). Preparing for the MARS HFIR beamline CG-1D investigation required a crucial step in calculating the optimal mortar sample thickness. This thickness calculation was followed by systematically applying various characterization techniques to assess the constituent materials intended to prepare mortar samples, explicitly focusing on achieving the necessary chemical compositions. The ORNL Neutron Imaging Toolbox (NEUIT) web application [51] was utilized to develop an effective chemical formula that incorporated the determined chemical compositions. The aim was to establish a predictive formula determining the minimum sample thickness required for neutron signal transmission exceeding 20%. A w/c of 0.54 was selected for the mortar mix design; for this mix design, it was found that a 15 mm thick mortar sample had a transmission rate of 25.035% and an attenuation rate of 74.965%, which satisfied the

required threshold of >20% transmission rate. For the web-based calculation and actual sample preparation, D_2O was used instead of H_2O due to its lower neutron attenuation, which enhances transmission and allows the use of thicker samples while maintaining imaging quality [26].

In this study, neutron radiography was employed to investigate pore water movement within a mortar sample subjected to one-dimensional cooling, with the aim of reducing the interior temperature toward −12.5 °C. Figure 7- 2 **(a)** shows the schematic of the experimental setup and Figure 7- 2 **(b)** shows the experimental setup at the MARS beamline. The mortar sample (15 × 150 × 150 mm^3) was created using D_2O and cured in a fog room for 14 days. Following curing, it was kept in an environmental chamber at 50% relative humidity (RH) and 23 ℃ for 8 days to facilitate drying. The dried sample was then vacuum-saturated with H_2O for 5 hours to ensure complete filling of the pores. Since H_2O and D_2O exhibit different contrasts in neutron imaging, this procedure enabled the distinct tracking of H_2O movement within the D_2O prepared mortar pore system [26].

Subsequently, the sample was positioned on a cooling stage controlled by an external chiller, with its 150 × 150 mm^2 face exposed to the neutron beam. To prevent moisture ingress or loss during imaging, all sample sides except the bottom were sealed with black glass foam, which was then placed on the cooling stage. The black glass foam was chosen based on a previous study[20], demonstrating its effectiveness as a thermal insulator and a vapor barrier during neutron radiography. Two thermocouples, labeled Thermocouple 1 and Thermocouple 2, were embedded at discrete locations within the mortar, as shown in Figure 7- 3, to correlate radiographic data with temperature measurements, and this setup allowed the identification of the onset of pore water freezing as indicated by a temperature drop. RH sensors were also embedded in positions adjacent to the thermocouples to monitor internal moisture conditions; however, the RH sensors failed to provide any usable data during the experiment.

A similar experimental setup was reported by Toropovs *et al*. [20] for studying moisture distribution in concrete subjected to high temperatures. In the present study, a single mortar sample was imaged, with each radiograph captured over a 90-second exposure. 2D radiographic images were acquired at 90-second intervals during the cooling process, facilitating real-time monitoring of water movement.

An external water bath chiller, operating within a temperature range of −20 °C to 20 °C, regulated the cooling stage. A glycol water mixture was used to avoid freezing and enabling the chiller to maintain a setpoint of –12.5 ℃, with imaging initiated once the sample's bottom reached this temperature. Thermal insulation on the cooling stage minimized temperature losses, while a copper plate ensured efficient heat transfer to the sample. Before initiating the F-T cycles, the sample was preconditioned in a refrigerator at 4.4 ℃ for 2 hours to stabilize its surface temperature and mitigate ambient temperature influence hindering the freezing cycle. Each experimental cycle comprised a 10-hour freezing period at −12.5 °C followed by a 1-hour thawing period until the sample temperature reached 15 °C.

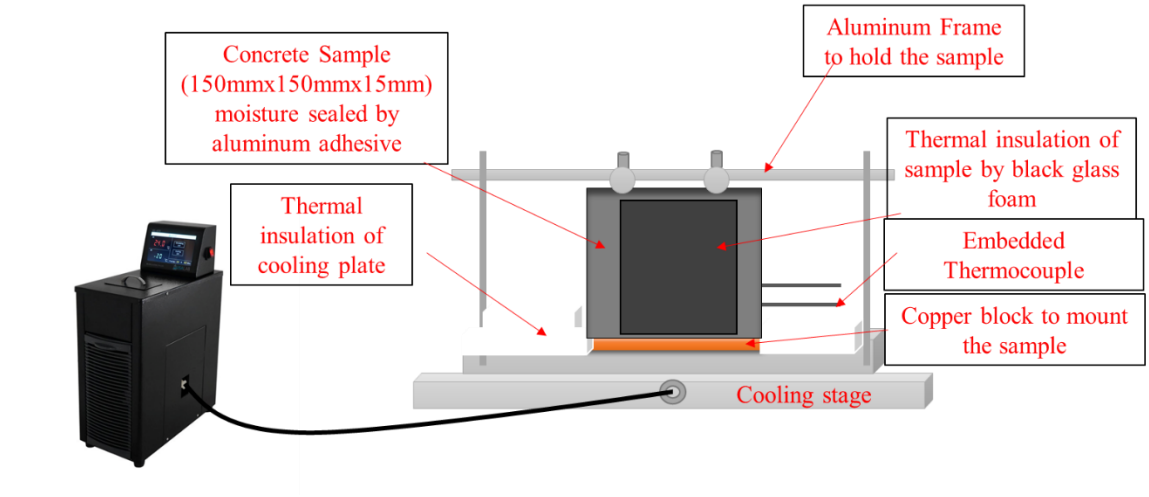

(a)

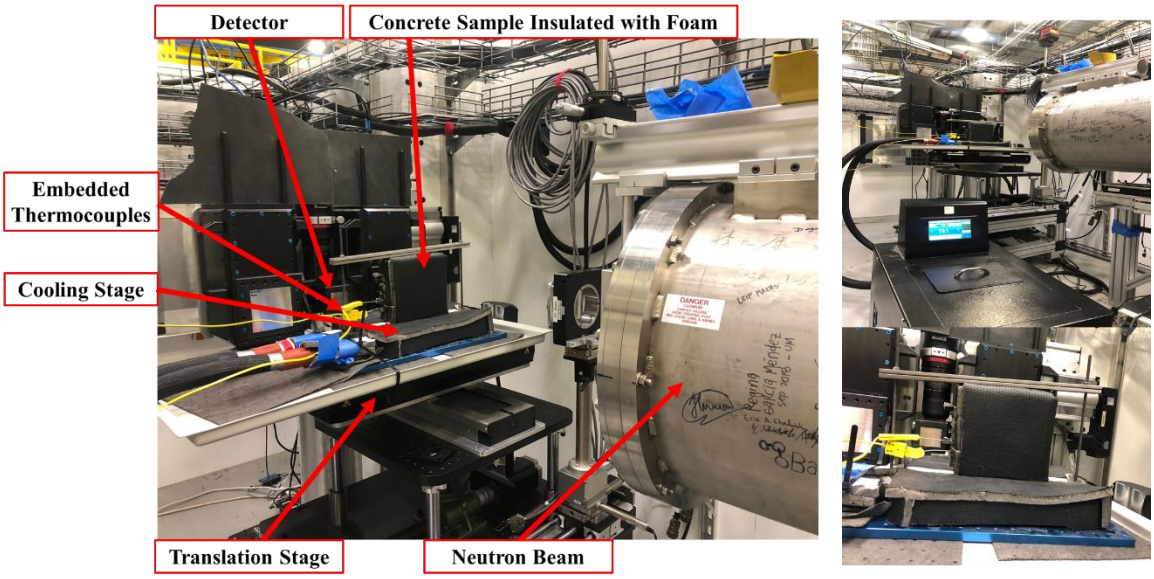

(b)

Figure 7- 2 (a) Schematic of experimental setup, and (b) experimental setup for neutron radiography at MARS beamline.

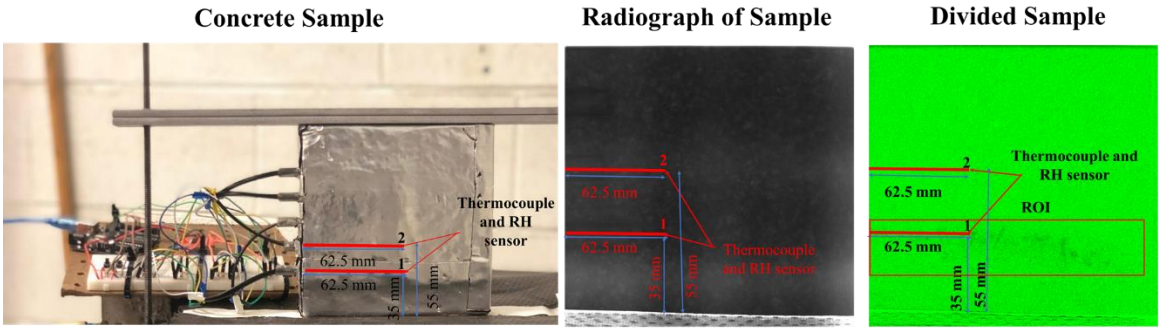

Figure 7- 3 Location of embedded thermocouple and RH sensor.

7.3.10 Neutron radiography and image processing and analysis

Radiographs were collected using a QHY600M sCMOS camera (QHYCCD, Suzhou, China) optically coupled to a 40-micron-thick, gadolinium-oxide-based scintillator. The relatively high thickness of the sample, including hydration water and foam insulation, led to low transmission (~15% to 20%) and thus exhibited beam hardening effects. To compensate, the exposure time per radiograph was set to 90 seconds with field of view of ~10 × 10 cm^2. Radiographs with a pixel size of 15.6 µm were acquired continuously as the temperature varied. The raw 16-bit images were normalized to open beam images (without a sample) as in Equation 5 and registered *via* rigid body translations to account for sample drift. The final step consisted of dividing the image stack by a sample image above the freezing point, as shown in Figure 7- 4. In this way, the relative change in pixel intensity reveals the freezing dynamics of water. Neutron transmission follows the Beer-Lambert Law, as shown in Equation 5:

$$T(x,y) = \frac{I_S}{I_0} = \exp(-\Sigma d) \tag{5}$$

where I_S and I_0 are the image intensities per pixel (x, y) with and without a sample in the beam, respectively, d is the sample thickness, and Σ is the macroscopic neutron cross section. However, beam-hardening effects were evident in the radiographs. Figure 7- 4. shows a representative neutron radiograph where conventional image normalization corrections were attempted but failed, as evident by the bright spots/bands, which are leftover beam structures that would normally be corrected.

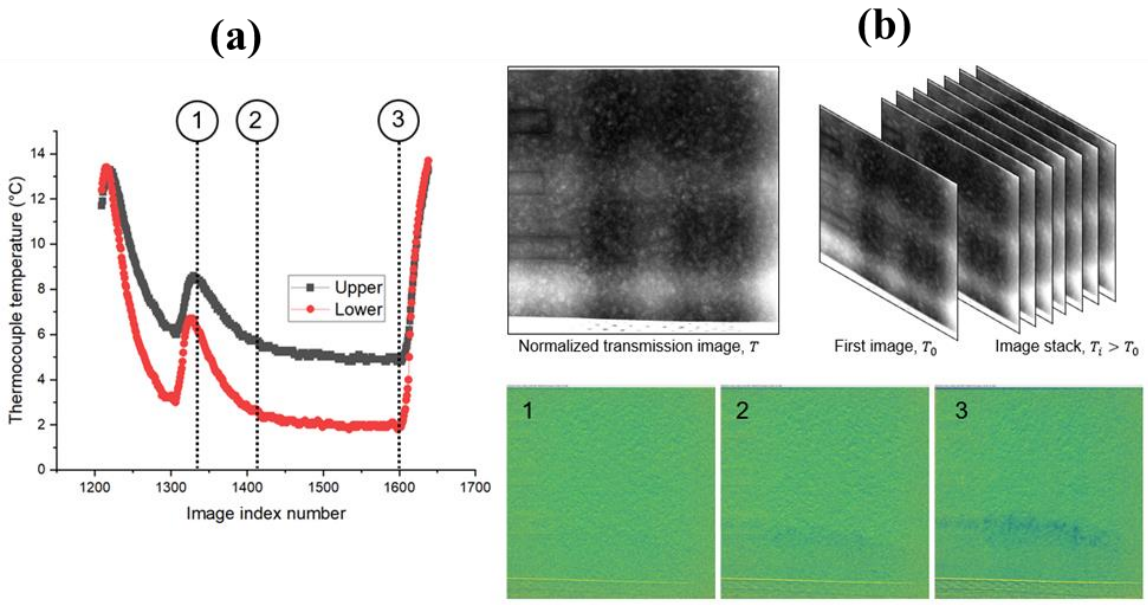

Figure 7- 4 Neutron imaging during freezing: (a) Temperature profiles from upper and lower thermocouples over time; (b) schematic of image processing normalization, registration, and division by a reference image above freezing processed radiographs at selected image index numbers (1–3) showing water redistribution during freezing.

7.4 Results and discussions

7.4.1 Isothermal calorimetry results

Figure 7- 5 presents the results obtained from the isothermal calorimetry. The D_2O sample displayed lower and delayed thermal power peaks compared to the H_2O sample. Additionally, the total heat measured at each time interval was less for the D_2O sample than for the H_2O Sample. Previous studies reported analogous findings, observing that the incorporation of D_2O in the mixture resulted in delayed hydration compared to the mixture created with H_2O [26]. This delayed hydration may be attributed to confined D_2O in cement paste exhibiting slower molecular dynamics than H_2O due to a stronger hydrogen-bond network that limits water mobility and delays hydration kinetics [52].

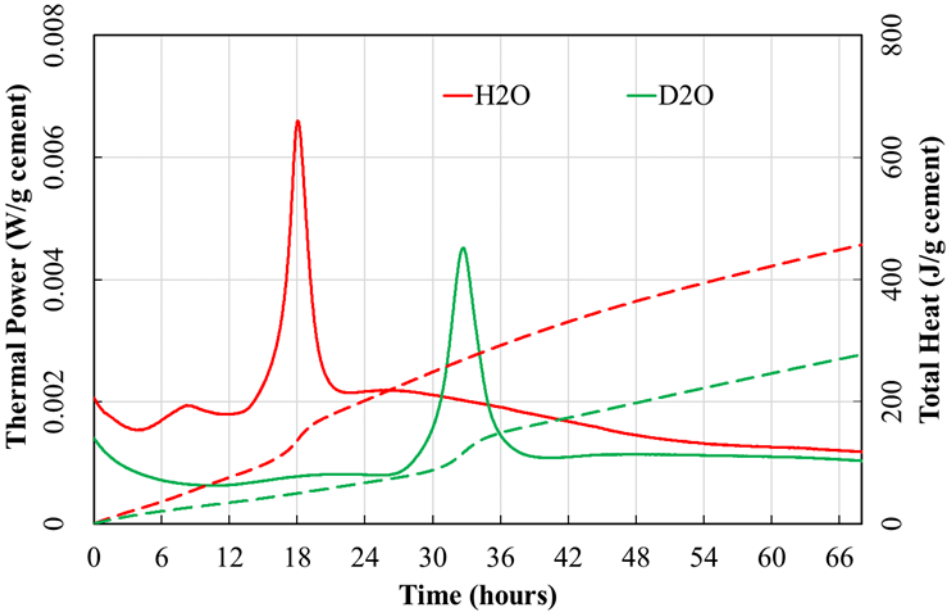

Figure 7- 5 Isothermal calorimetry results - thermal power and total heat versus time (solid lines represent the thermal power curves, and dashed lines represent the total heat curves).

Table 7- 3 presents the total heat values of the samples at various time intervals and compares the D_2O sample with the H_2O sample. As anticipated, the total heat percentage of the D_2O sample relative to the H_2O sample increased over time due to its delayed hydration, although it remained below 100 %. Notably, after 72 hours, the D_2O sample reached 77 % of the H_2O sample's total heat.

Table 7- 3 Total heat at various time intervals for all mixtures compared to the H_2O sample.

Mixture	Total Heat (W g^{-1}) / % Total Heat at that time of H_2O			
	12 h	24 h	48 h	72 h
H_2O	56.7	179	349	462
D_2O	18.6 / 33%	88.5 / 49%	186 / 53%	355 / 77%

Table 7- 4 summarizes the timing and magnitude of the thermal power peaks for each sample group. In agreement with the total heat data in Table 7- 3, the H_2O samples exhibit an early first peak at 8.2 hours (1.93×10^{-3} mJ g^{-1}) and a second peak at 18.2 hours (6.60×10^{-3} mJ g^{-1}). In contrast, the D_2O samples do not display a distinct first peak; instead, they show a reduction in the rate of thermal power increase before reaching a clearly defined second peak at 32.98 hours (4.52×10^{-3} mJ g^{-1}). This delayed peak in the D_2O samples contributes to the progressively higher

cumulative total heat observed over time in the H_2O samples compared to in D_2O, see Figure 7-5.

Table 7- 4 Time and value of thermal power peaks.

Mixture	First peak time (h)	First peak thermal power (mJ g^{-1})	Second peak time (h)	Second peak thermal power (mJ g^{-1})
H_2O	8.2	1.93	18.2	6.60
D_2O	Peak Unclear	N/A	32.98	4.52

7.4.2 LT-DSC results

Figure 7- 6 shows the freezing points of D_2O and H_2O incorporated paste samples for different curing periods. For H_2O samples, the freezing point decreases with curing time from −2.6 °C at 3 days to −3.2 °C at 14 days and further to −5.3 °C at 28 days, indicating continued hydration and pore refinement. D_2O samples exhibit consistently higher freezing points but follow a similar trend, decreasing from −0.5 °C at 3 days to −1.3 °C at 14 and −4.1 °C at 28 days.

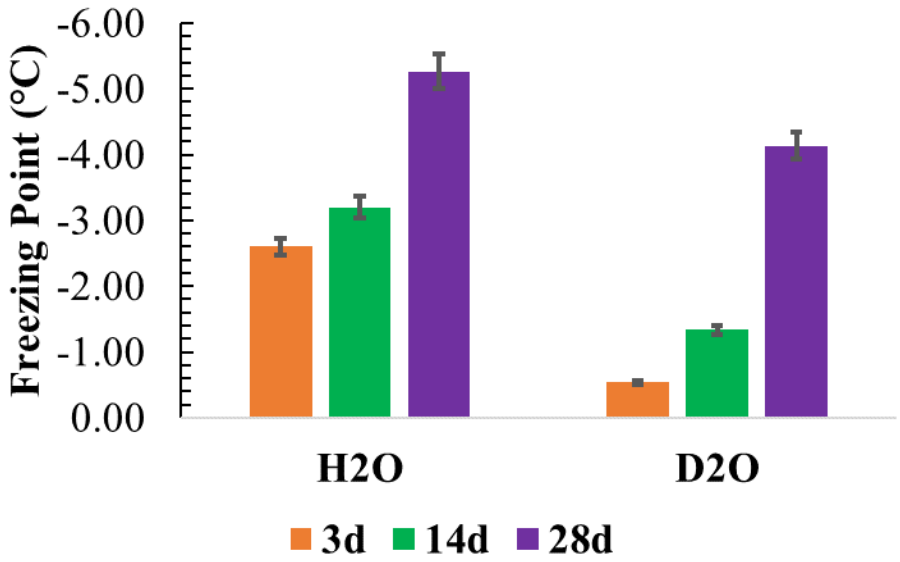

Figure 7- 6 Freezing points of different cement paste samples for different curing periods (error bars represent one standard deviation).

Figure 7- 7 **(a)** and **(b)** show the MH and %FW content of cement paste samples created with H_2O and D_2O at various curing periods. D_2O samples consistently exhibited higher MH and FW values than H_2O samples, indicating slower hydration, which aligns with the isothermal calorimetry

results. For three days of curing, H_2O samples exhibited lower MH (–98.3 J g^{-1}) and FW (2.5 %) than D_2O samples, which showed MH of −165.7 J g^{-1} and FW of 4.1 %.

The integral area of the endothermic curves represents the amount of FW in each sample, where a lower value corresponds to lower and refined pore volume where porewater freezes at lower temperature due to a higher degree of hydration [39,40,53]. Initially, H_2O samples showed low MH and FW values, consistent with the isothermal calorimetry findings. However, D_2O samples exhibited higher values in both metrics, MH and FW, after 3 days of curing but showed significant improvement with increasing hydration periods. For instance, after 28 days, D_2O samples exhibited an MH of –88.5 J g^{-1} and FW of 2.2 %, approaching the values observed for H_2O samples (MH: –71.2 J g^{-1} and FW: 1.8 %). This indicates that the hydration of D_2O samples gradually approaches that of H_2O samples over time, reflecting the continuous but slower hydration in D_2O samples.

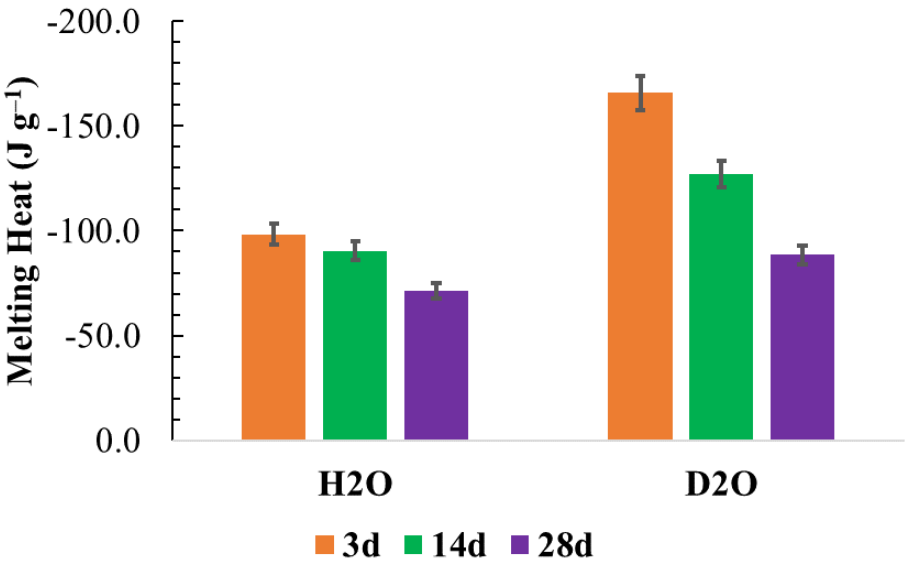

(a)

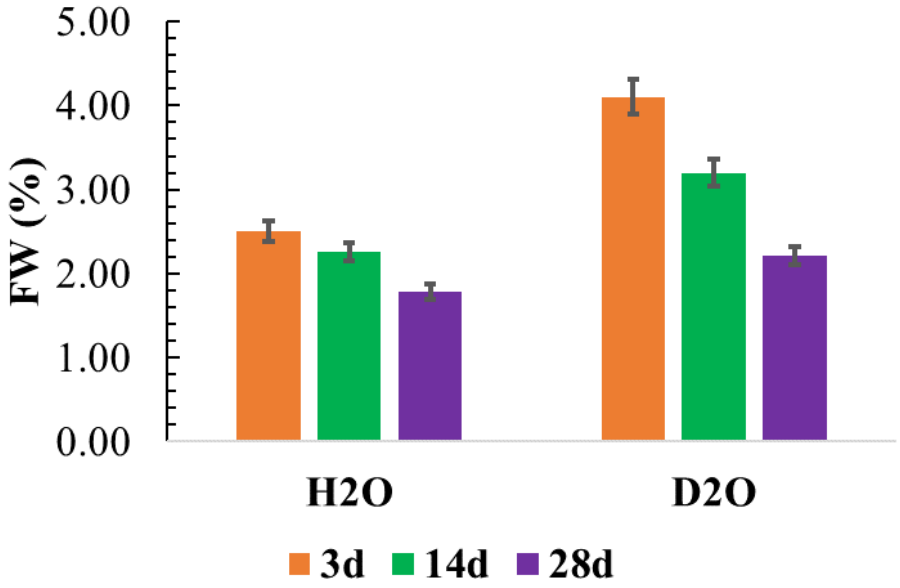

(b)

Figure 7- 7 (a) MH (J g^{-1}), and (b) FW (%) of cement paste samples for different curing periods (error bars represent one standard deviation).

7.4.3 TGA results

In TGA of cement paste samples, the temperature interval of 30 °C to 105 °C generally signifies the evaporation of free water and the decomposition of gypsum and ettringite (AFt) [54]. During

this stage, the initial loss of bound water from the C-S-H can also be observed between 110 °C and 170 °C [54]. Additionally, the breakdown of the monosulfoaluminate (AFm) phase occurs within the temperature range of 150 °C to 170 °C, and the decomposition of portlandite takes place between 400 °C and 550 °C. In comparison, calcium carbonate decomposes from 600 °C to 850 °C [54].

Figure 7- 8 shows the TGA profiles of cement paste samples prepared with H_2O and D_2O cured for 3 days and 14 days, respectively. The results indicate that the H_2O samples exhibit higher portlandite content than the D_2O samples for both curing durations, as evidenced by the more pronounced weight loss peaks between 400 °C and 550 °C corresponding to portlandite decomposition. Additionally, the mass loss peak around 154 °C, associated with the decomposition of C-S-H and AFm phases, follows a consistent trend with the portlandite peaks across all samples. Moreover, the 14-day cured samples generally show lower mass loss than the three-day cured samples, indicating more advanced hydration and a denser microstructure over time. Notably, the D_2O samples cured for three days maintain the highest weight percentage throughout the temperature range, suggesting slower hydration kinetics, likely due to the isotopic effect of deuterium.

The DOH value of the H_2O sample cured for 3 days achieved 37.7 %, while DOH of D_2O sample cured for 3 days reached only 12.0 %, indicating slower hydration kinetics in the D_2O sample than in the H_2O sample. However, after 14 days, the DOH for the D_2O sample increased significantly to 43.9 %, suggesting that despite hydration is slower in the D_2O early stage, it progresses steadily over time. The H_2O sample cured for 14 days attained a higher DOH of 49.6 %. These trends align with the isothermal calorimetry results, showing slower but continuous hydration in D_2O samples. This confirms that while D_2O reduces the initial hydration rate, the reaction continues over an extended curing period.

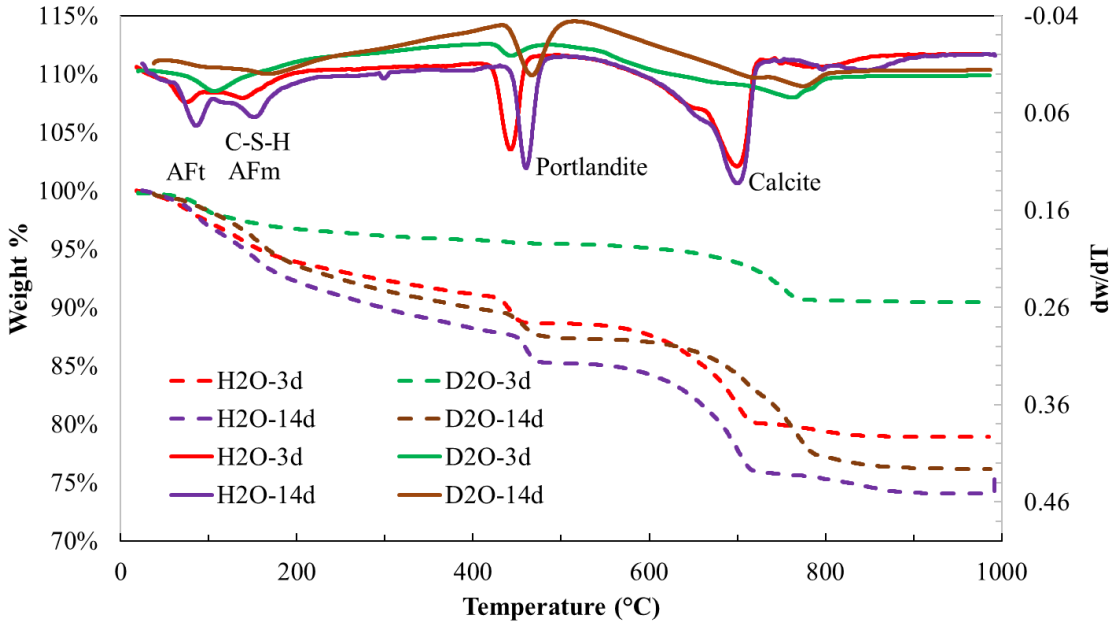

Figure 7- 8 TGA results of paste samples cured for 3 and 14 days (dashed lines represent the % weight loss profiles, and solid lines represent the DTA curves).

7.4.4 XRD results

Figure 7- 9 **(a) and (b)** show the XRD patterns of cement paste samples cured for 3 days and 14 days created with H_2O and D_2O, revealing that D_2O significantly influences the formation and intensity of key hydration phases, including portlandite and C-S-H. Specifically, the D_2O samples exhibit lower peak intensities for portlandite and C-S-H while retaining more pronounced peaks for clinker phases, particularly alite and belite, which suggests a slower hydration process due to isotopic effects that reduce water mobility and reactivity [52,55]. This slower phase transformation highlights the impact of D_2O on hydration dynamics and the reduced formation of conventional hydration products, aligning with isothermal calorimetry findings and underscoring the unique retardation effects of D_2O on cementitious matrix.

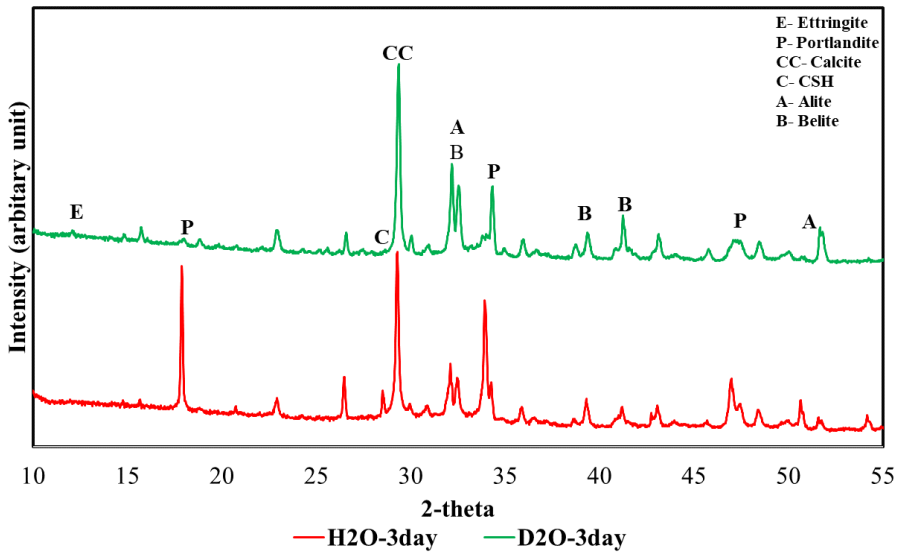

(a)

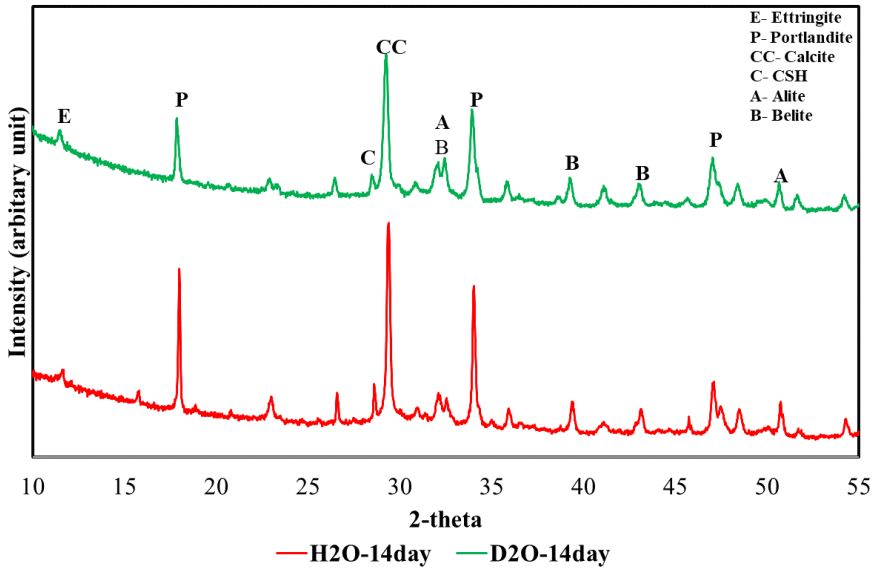

(b)

Figure 7- 9 XRD pattern of different cement paste samples cured for (a) 3 days, and (b) 14 days.

7.4.5 Hardened air-void content results

Table 7- 5 summarizes the hardened air-void characteristics of the mortar groups. The D_2O mortar specimen exhibits a slightly higher total air content (5.6%) than the H_2O mix (5.3%). In addition, the void frequency is higher in the D_2O specimen (0.172 mm^{-1} *vs.* 0.163 mm^{-1}), indicating a denser distribution of air voids. The average chord length is also slightly lower for the D_2O specimen (0.323 mm) than for the H_2O specimen (0.328 mm). Furthermore, the paste-air volume ratio value is lower for the D_2O specimen (5.158) than the H_2O specimen (5.451), which reflects the slightly higher air void content in D_2O. Both group's mortar specimens show an identical specific surface value of 12 mm^{-1} and a consistent spacing factor of 0.16 mm. Both groups meet the ASTM C457 requirement for moderate F-T exposure (spacing factor < 0.20 mm). It should be noted that no AEA admixtures were added to either of the mortar mixtures. These results imply that the D_2O-based mortar may offer a slightly more refined and evenly distributed air-void system than the H_2O-based mortar.

Table 7- 5 Hardened air-void system data for mortar specimens

	A (%)	n (mm^{-1})	p/A	$\bar{l}$ (mm)	α (mm^{-1})	$\bar{L}$ (mm)
D_2O	5.6	0.172	5.158	0.323	12	0.16
H_2O	5.3	0.163	5.451	0.328	12	0.16

7.4.6 N_2 gas adsorption results

Table 7- 6 shows the data obtained from the N_2 gas adsorption experiment for both D_2O- and H_2O-incorporated paste samples. The adsorption data illustrate distinct differences in the measured properties of the cement paste created with H_2O compared to D_2O, offering valuable insights into the pore structure and microstructural density. When utilizing H_2O, the average SSA is measured at 18.75 $m^2\ g^{-1}$, with a specific pore volume of 0.037 $cm^3\ g^{-1}$. In comparison, D_2O samples exhibit values nearly double those of the H_2O samples, presenting an average SSA of 40.60 $m^2\ g^{-1}$ and a specific pore volume of 0.077 $cm^3\ g^{-1}$. The elevated SSA and pore volume measured with D_2O indicates a more finely divided porous microstructure. Conversely, the lower values measured with H_2O imply a relatively denser microstructure characterized by fewer and/or less accessible pores. Although surface area and pore volume differ, the average pore radii are nearly identical (around 0.459 nm for H_2O and 0.453 nm for D_2O). This indicates that the intrinsic pore size distribution and the fundamental pore dimensions of the cement paste remain consistent. In addition to the accessibility issues it is noticeable that the BET specific surfaces are quite low compared to classic values for well hydrated portland cement measured and calculated with sorption and BET: in the order of 100-200 $m^2\ g^{-1}$. This indicates that the pre-drying with outgassing and 100 °C drying has caused some damage to the pore structure. In addition, the degree of hydration is low: < 0.5 according to the TGA results in *section 7.4.3*, which also contributes to low SSA.

In summary, the data indicate that the cement paste exhibits a more porous microstructure when utilizing D_2O instead of H_2O. At the same time, results obtained with H_2O reflect a relatively denser structure with reduced accessibility to the pore space.

Unpaired, two-tailed t-tests indicated a statistically significant difference between H_2O and D_2O samples in SSA and specific pore volume at the 0.05 significance level. However, there was insufficient evidence for the pore radius measurement to conclude a statistically significant difference between the two groups.

Table 7- 6 Specific surface area, specific pore volumes, and pore radius of paste samples

	H2O			D2O		
SN	SSA ($m^2\ g^{-1}$)	Specific Pore Volume ($cm^3\ g^{-1}$)	Pore Radius (nm)	SSA ($m^2\ g^{-1}$)	Specific Pore Volume ($cm^3\ g^{-1}$)	Pore Radius (nm)
1	17.96	0.035	0.45	39.83	0.076	0.45
2	19.01	0.037	0.46	38.66	0.074	0.46
3	19.00	0.038	0.47	42.23	0.080	0.45
4	19.02	0.038	0.46	41.71	0.079	0.45
Avg	18.75	0.037	0.46	40.60	0.077	0.45
STD	0.539	0.001	0.01	1.66	0.002	0.00

****Note: Avg stands for average; STD stands for standard deviation.*

7.4.7 Compressive strength testing results

Figure 7- 10 shows compressive strength for H_2O and D_2O specimens cured for 3 days, 14 days, and 28 days. For H_2O specimens, the compressive strength increases from 9.5 MPa at 3 days to 24.9 MPa at 14 days, a 162% increase. At 28 days, strength reaches 29.3 MPa, a 208% increase compared to 3 days. In contrast, D_2O specimens start at 2.9 MPa at 3 days, then increase by 676% to 22.5 MPa at 14 days and by 855% to 27.7 MPa at 28 days. These results indicate that although D_2O specimens show slower early hydration, they gain strength more rapidly with time.

Unpaired, two-tailed t-tests for the 3-day and 14-day results indicated a statistically significant difference in the compressive strength between H_2O and D_2O specimens at a significance level of 0.05. However, at 28 days, there was insufficient evidence to conclude a statistically significant difference in compressive strength between the mortar specimens prepared with D_2O and H_2O, as the p-value exceeded the significance level.

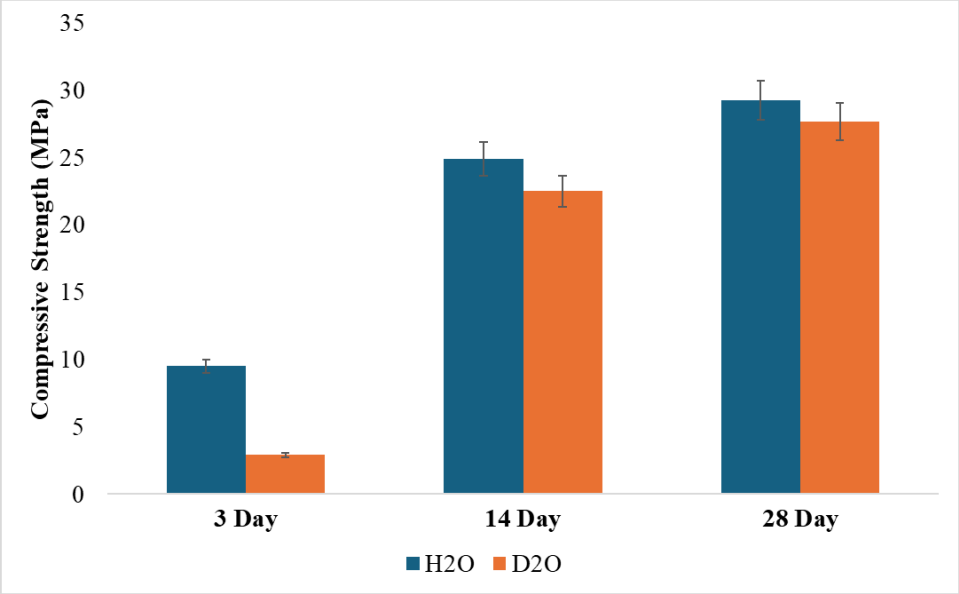

Figure 7- 10 Compressive strength of paste samples (error bars represent one standard deviation).

7.4.8 Neutron radiography results

Figure 7- 11 shows a series of neutron radiographs taken at different intervals, focusing on the region of interest (ROI) where Thermocouple 1 was embedded. At the initial stage (0 min), the temperature at the ROI was 12.4 °C, well above freezing, and the divided image revealed no change in pixel intensity. As freezing initiated at the bottom of the specimen at −12.5 °C, the temperature at the ROI gradually began to drop from 12.4 °C. After 51 minutes, the ROI temperature decreased to 7.6 °C. However, the divided image showed no noticeable contrast shift, suggesting that pore water within this region had not yet undergone any phase change or redistribution. By 300 minutes, however, the temperature reached 2.7 °C, and the corresponding divided image displayed a subtle contrast shift in the ROI, indicating that water was beginning to migrate in the ROI macropores from the bottom area of the ROI. At 500 minutes, the temperature at the ROI dropped further to 1.9 °C, and the divided image revealed an even more pronounced change in pixel intensity, suggesting a higher local moisture content in that area. Figure 7- 12 offers additional insight by illustrating the relative change in ROI intensity over time, with each data point color-coded to represent the corresponding temperature, thereby emphasizing the relationship between the cooling trajectory and the progressive increase in pixel intensity.

In this study, mortar samples were created using D_2O, dried, and then vacuum saturated with H_2O. According to LT DSC data, the pore water in the D_2O samples has a freezing point of −4.1 °C, slightly higher than in paste with H2O: around -5 C . The most reasonable explanation for the contrast shifts in the ROI is the upward movement of unfrozen water, driven by the freezing front

advancing from below. Apparently, ice forms in the mortar pores at the lower part of the sample, which was continuously maintained at −12.5 °C, and moves unfrozen pore water upwards into regions that remain above the freezing point. The thermocouple measurements confirm that the ROI remains near 1 °C to 2 °C when these contrast changes become most evident, implying that a liquid waterfront persists above the frozen zone. This liquid accumulation suggests that the pores were only partially saturated before freezing began. As ice forms at lower elevations, additional pore water is forced into the upper pores, increasing local saturation.

The radiographic evidence of incremental grayscale changes, coupled with temperature data, thus provides valuable insight into how pore water moves during freezing. It highlights that partial saturation and upward pore water movement are key factors in generating hydraulic pressure within the mortar microstructure. This mechanism can potentially initiate and propagate microcracks, leading to F-T deterioration of concrete materials.

However, several limitations restricted additional analysis beyond Figure 7- 12. Due to limited beamtime, only one non-air-entrained sample was imaged, preventing comparative studies. RH sensors embedded in the sample failed to provide usable data, and the external chiller was unable to sufficiently lower the temperature of the upper regions, likely due to the effects of ambient temperature and the sample's thermal mass. These factors and partial saturation of the pores limited observable water movement above the ROI.

Beam hardening artifacts caused by sample thickness also reduced image quality despite normalization efforts. Planned dry-state imaging before saturation was not feasible due to safety concerns over potential contamination during vacuum saturation. Additionally, pressure sensors could not be embedded due to constraints on sample thickness. Such sensors would have allowed direct measurement of pore pressure build-up during freezing, providing critical data to correlate water movement with internal stress development, one of the key mechanisms driving F-T damage and microcracking. While CT imaging could provide 3D insights, the required cylindrical geometry and slower acquisition times are not ideal for capturing dynamic water movement at high temporal resolution.

Future work should address these limitations by incorporating multiple sample types (*e.g.*, with AEA), improving cooling control and sensor reliability, enabling dry-state imaging under safe conditions, and exploring complementary 3D imaging techniques to understand F-T damage mechanisms in concrete better.

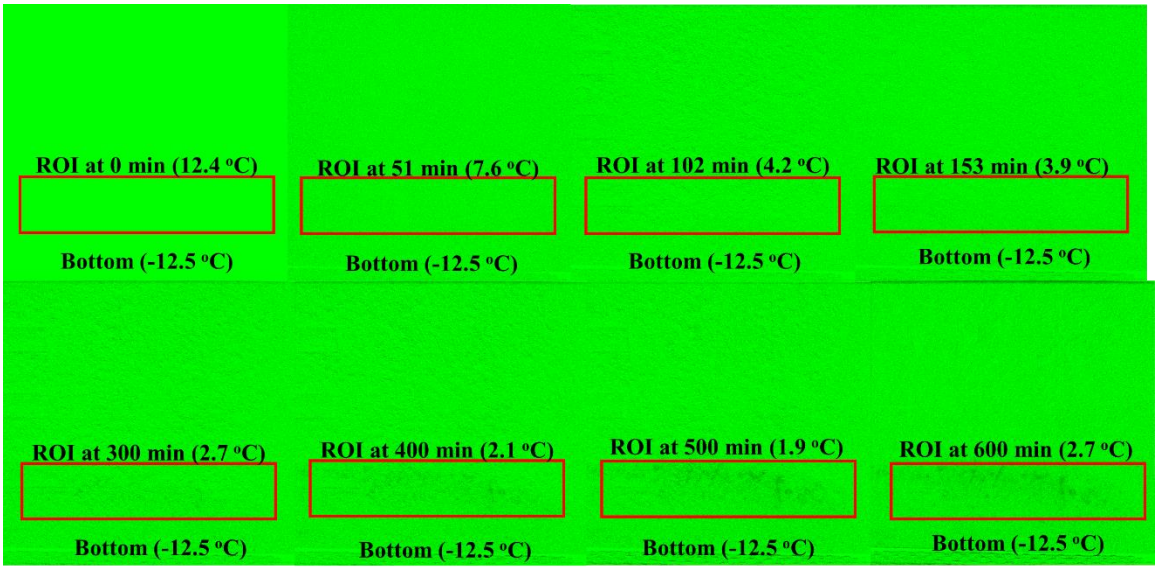

Figure 7- 11 Divided neutron radiographs above the freezing point as a function of time; the bottom refers to the chiller plate; the listed temperature for each ROI is from Thermocouple 1, located 62.5 mm from the left edge and 35 mm above the chiller plate, aligned with the ROI.

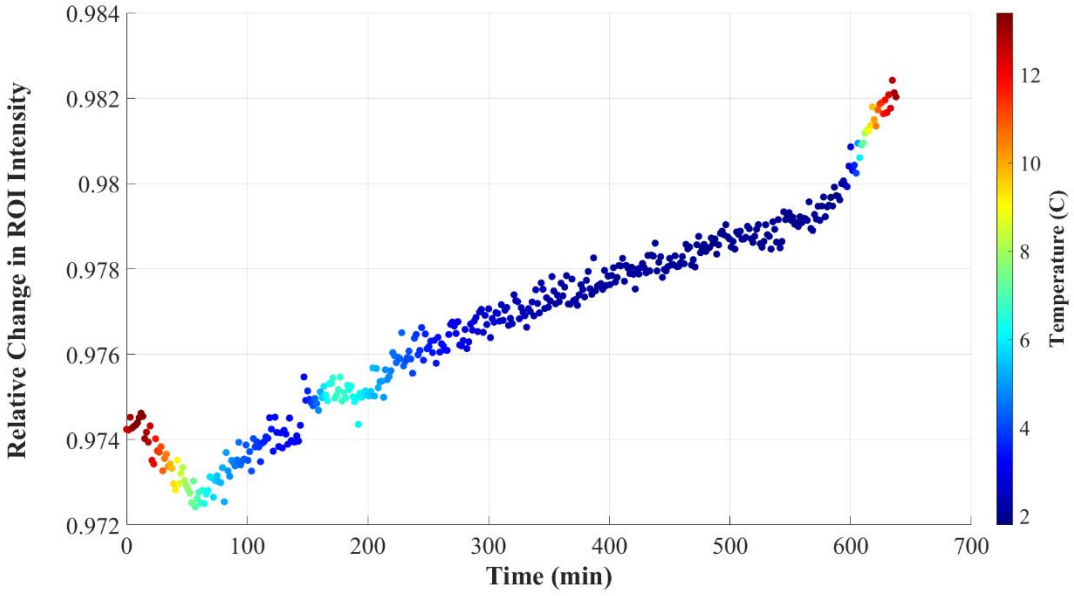

Figure 7- 12 Relative change in ROI intensity over time.

7.4 Conclusions

In this study, neutron radiography successfully monitored real-time pore water movement in mortar macropores during exposure at subzero temperature. In addition, this study examined the effects of D_2O on the hydration kinetics and pore structure.

The results of isothermal calorimetry, LT-DSC, XRD, and TGA collectively demonstrated that incorporating D_2O delayed the hydration kinetics compared to H_2O. This delay was attributed to the stronger hydrogen bonding in D_2O, which restricted molecular mobility and decelerated hydration reactions. Despite the initial delay, the compressive strength of D_2O specimens ultimately became comparable to H_2O specimens by 28 days, indicating that the hydration process continued steadily.

D_2O specimens exhibited a similar air-void system in hardened air-void analysis compared to H_2O specimens. N_2 gas adsorption analysis also indicated that D_2O samples had a more porous microstructure with higher specific surface area and pore volume than H_2O samples, reflecting a less dense microstructure.

In compression testing, D_2O and H_2O specimens showed no significant difference in strength at 28 days, confirming that while D_2O delays early hydration and results in lower early strength, it does not compromise the long-term strength of mortar.

Neutron radiography revealed that as the specimen was cooled at subzero temperature, the freezing front advanced from the bottom. As the freezing front advanced, the region of interest remained above the freezing point, causing unfrozen water to migrate upward in the pore system. This pore water movement was observed as incremental changes in image relative intensity and confirmed by thermocouple measurements showing temperatures near 1 °C to 2 °C in the ROI. These observations indicate that pore water movement from lower to upper regions can be critical in creating hydraulic pressure in the mortar microstructure, potentially initiating and propagating microcracks that lead to F-T deterioration.

Finally, partial saturation and pore water movement are key mechanisms behind F-T damage in concrete. This study provides novel insights into water dynamics within concrete microstructure under subzero conditions. It demonstrates the capability of neutron radiography as a powerful tool for real-time monitoring of pore water movement in mortar macropores.

7.5 Limitations and recommendations

This study was limited by beam hardening and the intrinsic beam structure effects on the MARS beamline, which compromised radiographic image quality. Additionally, the constraints on sample thickness restricted the integration of standard RH sensors, limiting the ability to monitor freezing dynamics fully. Also in this study, no admixtures (*e.g.,* AEA, water reducers, and superplasticizers) were added, so pore-water movement was governed solely by the cement–aggregate matrix, unmodified by chemical admixtures. To address these limitations, future studies should utilize the Versatile Neutron Imaging Instrument (VENUS) beamline for its imaging capacity, improved spatial resolution, and advanced imaging modes suitable for capturing fine

microstructural and moisture-related changes in concrete, allowing for enhanced image correction and integration of humidity sensors. Additionally, applying combined neutron and X-ray imaging systems, such as the Neutron and X-ray Tomography (NEXT) beamlines, could help differentiate between liquid water and ice due to their complementary contrast mechanisms. It is also recommended that neutron radiography be used to track the pore structure of concrete samples before, during, and after saturation (dry/wet) and before and after F-T cycles with different concrete mix designs, including air-entrained and non-air-entrained concrete samples. This approach would provide a more comprehensive understanding of moisture distribution, pore dynamics, and F-T damage mechanisms, enhancing the applicability of the findings to real-world conditions.

Acknowledgements

This material is based upon work supported by the Broad Agency Announcement Program and the Cold Regions Research and Engineering Laboratory (ERDC-CRREL) under Contract No. W913E522C0001.

A portion of this research used resources at the High Flux Isotope Reactor, a DOE Office of Science User Facility operated by the Oak Ridge National Laboratory. The beam time was allocated to MARS on proposal number IPTS-32819.1.

Special thanks go to Dr. Thomas Staley from the Department of Materials Science and Engineering at Virginia Tech for his invaluable guidance in conducting TGA and LT-DSC experiments. Also, thanks to Sung-Won Cho for assisting with the isothermal Calorimetry experiments.

Disclaimer

Any opinions, findings and conclusions or recommendations expressed in this material are those of the author(s) and do not necessarily reflect the views of the Broad Agency Announcement Program and ERDC-CRREL.

This manuscript has been authored in part by UT-Battelle, LLC, under contract DE-AC05-00OR22725 with the US Department of Energy (DOE). The publisher acknowledges the US government license to provide public access under the DOE Public Access Plan (https://energy.gov/doe-public-access-plan).

References

[1] W.L. Baloch, H. Siad, M. Lachemi, M. Sahmaran, A review on the durability of concrete-to-concrete bond in recent rehabilitated structures, Journal of Building Engineering 44 (2021) 103315. https://doi.org/https://doi.org/10.1016/j.jobe.2021.103315.

[2] H.A. Shah, Q. Yuan, S. Zuo, Air entrainment in fresh concrete and its effects on hardened concrete-a review, Constr Build Mater 274 (2021). https://doi.org/10.1016/j.conbuildmat.2020.121835.

[3] A.J.K. Komar, A.J. Boyd, Evaluating Freeze-Thaw Deterioration with Tensile Strength, in: IOP Conf Ser Mater Sci Eng, Institute of Physics Publishing, 2017. https://doi.org/10.1088/1757-899X/216/1/012024.
[4] H.S. Shang, T.H. Yi, Freeze-thaw durability of air-entrained concrete, The Scientific World Journal 2013 (2013). https://doi.org/10.1155/2013/650791.
[5] P. Reiterman, O. Holčapek, O. Zobal, M. Keppert, Freeze-Thaw Resistance of Cement Screed with Various Supplementary Cementitious Materials, Reviews on Advanced Materials Science 58 (2019) 66–74. https://doi.org/10.1515/rams-2019-0006.
[6] P. Zhang, F.H. Wittmann, M. Vogel, H.S. Müller, T. Zhao, Influence of freeze-thaw cycles on capillary absorption and chloride penetration into concrete, Cem Concr Res 100 (2017) 60–67. https://doi.org/10.1016/j.cemconres.2017.05.018.
[7] F. Gong, S. Jacobsen, Modeling of water transport in highly saturated concrete with wet surface during freeze/thaw, Cem Concr Res 115 (2019) 294–307. https://doi.org/https://doi.org/10.1016/j.cemconres.2018.08.013.
[8] L. Qin, C. Zhai, J. Xu, S. Liu, C. Zhong, G. Yu, Evolution of the pore structure in coal subjected to freeze−thaw using liquid nitrogen to enhance coalbed methane extraction, J Pet Sci Eng 175 (2019) 129–139. https://doi.org/10.1016/j.petrol.2018.12.037.
[9] A. Çavdar, Investigation of freeze-thaw effects on mechanical properties of fiber reinforced cement mortars, Compos B Eng 58 (2014) 463–472. https://doi.org/10.1016/j.compositesb.2013.11.013.
[10] Z. Lu, Z. gang Feng, D. Yao, X. Li, H. Ji, Freeze-thaw resistance of Ultra-High performance concrete: Dependence on concrete composition, Constr Build Mater 293 (2021). https://doi.org/10.1016/j.conbuildmat.2021.123523.
[11] Y. Xu, H. Ye, Q. Yuan, C. Shi, Y. Gao, Q. Fu, The durability of concrete subject to mechanical load coupled with freeze–thaw cycles: A review, Archives of Civil and Mechanical Engineering 22 (2022) 47.
[12] J. Guo, W. Sun, Y. Xu, W. Lin, W. Jing, Damage Mechanism and Modeling of Concrete in Freeze–Thaw Cycles: A Review, Buildings 12 (2022). https://doi.org/10.3390/buildings12091317.
[13] X. Su, Study on the Frost Mechanism of Concrete, in: 5th International Conference on Civil Engineering and Transportation, Atlantis Press, 2015: pp. 531–534.
[14] H. Lin, Y. Han, S. Liang, F. Gong, S. Han, C. Shi, P. Feng, Effects of low temperatures and cryogenic freeze-thaw cycles on concrete mechanical properties: A literature review, Constr Build Mater 345 (2022). https://doi.org/10.1016/j.conbuildmat.2022.128287.
[15] M. Sun, C. Zou, D. Xin, Pore structure evolution mechanism of cement mortar containing diatomite subjected to freeze-thaw cycles by multifractal analysis, Cem Concr Compos 114 (2020) 103731.
[16] Y. Şahin, Y. Akkaya, M.A. Taşdemir, Effects of freezing conditions on the frost resistance and microstructure of concrete, Constr Build Mater 270 (2021). https://doi.org/10.1016/j.conbuildmat.2020.121458.

[17] A. du Plessis, W.P. Boshoff, A review of X-ray computed tomography of concrete and asphalt construction materials, Constr Build Mater 199 (2019) 637–651. https://doi.org/https://doi.org/10.1016/j.conbuildmat.2018.12.049.

[18] P. Zhang, F.H. Wittmann, T. Zhao, E.H. Lehmann, P. Vontobel, Neutron radiography, a powerful method to determine time-dependent moisture distributions in concrete, Nuclear Engineering and Design 241 (2011) 4758–4766.

[19] P. Zhang, F.H. Wittmann, P. Lura, H.S. Müller, S. Han, T. Zhao, Application of neutron imaging to investigate fundamental aspects of durability of cement-based materials: A review, Cem Concr Res 108 (2018) 152–166. https://doi.org/10.1016/j.cemconres.2018.03.003.

[20] N. Toropovs, F. Lo Monte, M. Wyrzykowski, B. Weber, G. Sahmenko, P. Vontobel, R. Felicetti, P. Lura, Real-time measurements of temperature, pressure and moisture profiles in High-Performance Concrete exposed to high temperatures during neutron radiography imaging, Cem Concr Res 68 (2015) 166–173.

[21] E.H. Lehmann, P. Vontobel, L. Wiezel, Properties of the radiography facility NEUTRA at SINQ and its potential for use as European reference facility, Nondestructive Testing and Evaluation 16 (2001) 191–202.

[22] E.H. Lehmann, P. Vontobel, N. Kardjilov, Hydrogen distribution measurements by neutrons, Applied Radiation and Isotopes 61 (2004) 503–509. https://doi.org/https://doi.org/10.1016/j.apradiso.2004.03.075.

[23] D.S. Hussey, D. Spernjak, A.Z. Weber, R. Mukundan, J. Fairweather, E.L. Brosha, J. Davey, J.S. Spendelow, D.L. Jacobson, R.L. Borup, Accurate measurement of the through-plane water content of proton-exchange membranes using neutron radiography, J Appl Phys 112 (2012).

[24] V.F. Sears, Neutron scattering lengths and cross sections, Neutron News 3 (1992) 26–37.

[25] C. Lucero, R. Spragg, D. Bentz, D. Hussey, D. Jacobson, J. Weiss, Neutron Radiography Measurement of Salt Solution Absorption in Mortar, (2017). https://doi.org/https://doi.org/10.14359/51689488.

[26] M.N. Goodwin, R.M. Ghantous, W.J. Weiss, S.R. Reese, Neutron radiography of cement paste made with light and heavy water, J Radioanal Nucl Chem 331 (2022) 5113–5121. https://doi.org/10.1007/s10967-022-08493-w.

[27] W. Li, M. Pour-Ghaz, P. Trtik, M. Wyrzykowski, B. Münch, P. Lura, P. Vontobel, E. Lehmann, W.J. Weiss, Using neutron radiography to assess water absorption in air entrained mortar, Constr Build Mater 110 (2016) 98–105. https://doi.org/https://doi.org/10.1016/j.conbuildmat.2016.02.001.

[28] S.E. Kichanov, K.M. Nazarov, D.P. Kozlenko, M. Balasoiu, M. Nicu, L. Ionascu, A.C. Dragolici, F. Dragolici, B.N. Savenko, Neutron tomography studies of cement-based materials used for radioactive waste conditioning, Rom. J. Phys 64 (2019).

[29] D. Dauti, A. Tengattini, S. Dal Pont, N. Toropovs, M. Briffaut, B. Weber, Analysis of moisture migration in concrete at high temperature through in-situ neutron tomography,

Cem Concr Res 111 (2018) 41–55. https://doi.org/https://doi.org/10.1016/j.cemconres.2018.06.010.
[30] M.K. Moradllo, S.R. Reese, W.J. Weiss, Using Neutron Radiography to Quantify the Settlement of Fresh Concrete, Adv Civ Eng Mater 8 (2019) 71–87. https://doi.org/10.1520/ACEM20180086.
[31] L.A. de Siqueira Neto, O.B. Isgor, S.R. Reese, W.J. Weiss, Using Neutron Radiography to Quantify the Water Content of Axisymmetric Cylindrical Cement-Based Material Samples, Available at SSRN 4728861 (2016). https://doi.org/https://dx.doi.org/10.2139/ssrn.4728861.
[32] Y. Seki, A. Taketani, T. Hashiguchi, S. Wang, M. Mizuta, Y. Wakabayashi, Y. Otake, Y. Yamagata, H. Baba, K. Kino, K. Hirota, S. Tanaka, Fast neutron transmission imaging of the interior of large-scale concrete structures using a newly developed pixel-type detector, Nucl Instrum Methods Phys Res A 870 (2017) 148–155. https://doi.org/https://doi.org/10.1016/j.nima.2017.07.022.
[33] T.H. Vu, N. Gowripalan, P. De Silva, A. Paradowska, U. Garbe, P. Kidd, V. Sirivivatnanon, Assessing carbonation in one-part fly ash/slag geopolymer mortar: Change in pore characteristics using the state-of-the-art technique neutron tomography, Cem Concr Compos 114 (2020) 103759. https://doi.org/https://doi.org/10.1016/j.cemconcomp.2020.103759.
[34] P. Trtik, B. Münch, W.J. Weiss, A. Kaestner, I. Jerjen, L. Josic, E. Lehmann, P. Lura, Release of internal curing water from lightweight aggregates in cement paste investigated by neutron and X-ray tomography, Nucl Instrum Methods Phys Res A 651 (2011) 244–249. https://doi.org/https://doi.org/10.1016/j.nima.2011.02.012.
[35] D. Snoeck, W. Goethals, J. Hovind, P. Trtik, T. Van Mullem, P. Van den Heede, N. De Belie, Internal curing of cement pastes by means of superabsorbent polymers visualized by neutron tomography, Cem Concr Res 147 (2021) 106528. https://doi.org/https://doi.org/10.1016/j.cemconres.2021.106528.
[36] M. Tange Hasholt, K. Frid, F. Spörel, J. Lahdensivu, E. Helsing, M. Müller, A. Faheem, S. Al Haj Sleiman, S. Jacobsen, Nordic Concrete Research workshop:“Accelerated freeze-thaw testing of concrete”, Lyngby, 20th April 2022, (2022).
[37] D.E. Dixon, et. al, Standard Practice for Selecting Proportions for Normal, Heavyweight, and Mass Concrete (ACI 211.1-91) Chairman, Subcommittee A, (1991).
[38] G. Zhang, Y. Yang, H. Yang, H. Li, Calcium sulphoaluminate cement used as mineral accelerator to improve the property of Portland cement at sub-zero temperature, Cem Concr Compos 106 (2020). https://doi.org/10.1016/j.cemconcomp.2019.103452.
[39] A. Alzaza, K. Ohenoja, I. Langås, B. Arntsen, M. Poikelispää, M. Illikainen, Low-temperature (−10 °C) curing of Portland cement paste – Synergetic effects of chloride-free antifreeze admixture, C–S–H seeds, and room-temperature pre-curing, Cem Concr Compos 125 (2022) 104319. https://doi.org/https://doi.org/10.1016/j.cemconcomp.2021.104319.
[40] A. Alzaza, K. Ohenoja, V. Isteri, T. Hanein, D. Geddes, M. Poikelispää, M. Illikainen,

Blending eco-efficient calcium sulfoaluminate belite ferrite cement to enhance the physico–mechanical properties of Portland cement paste cured in refrigerated and natural winter conditions, Cem Concr Compos 129 (2022). https://doi.org/10.1016/j.cemconcomp.2022.104469.

[41] S. Zhang, Y. Zhao, H. Ding, J. Qiu, C. Hou, Effect of sodium chloride concentration and pre-curing time on the properties of cemented paste backfill in a sub-zero environment, J Clean Prod 283 (2021). https://doi.org/10.1016/j.jclepro.2020.125310.

[42] A. Damasceni, L. Dei, E. Fratini, F. Ridi, S.H. Chen, P. Baglioni, A novel approach based on differential scanning calorimetry applied to the study of tricalcium silicate hydration kinetics, Journal of Physical Chemistry B 106 (2002) 11572–11578. https://doi.org/10.1021/jp020211l.

[43] E. Xanthakis, A. Le-Bail, H. Ramaswamy, Development of an innovative microwave assisted food freezing process, Innovative Food Science and Emerging Technologies 26 (2014) 176–181. https://doi.org/10.1016/j.ifset.2014.04.003.

[44] S. Jacobsen, E.J. Sellevold, S. Matala, Frost durability of high strength concrete: Effect of internal cracking on ice formation, Cem Concr Res 26 (1996) 919–931. https://doi.org/https://doi.org/10.1016/0008-8846(96)00066-X.

[45] X. Feng, E.J. Garboczi, D.P. Bentz, P.E. Stutzman, T.O. Mason, X. Fenga, E.J. Garboczia, D.P. Bentza, P.E. Stutzmana, T.O. Masonb, Estimation of the degree of hydration of blended cement pastes by a scanning electron microscopy point-counting procedure, 2004. www.sciencedirect.com.

[46] D.C. Chu, J. Kleib, M. Amar, M. Benzerzour, N.E. Abriak, Determination of the degree of hydration of Portland cement using three different approaches: Scanning electron microscopy (SEM-BSE) and Thermogravimetric analysis (TGA), Case Studies in Construction Materials 15 (2021). https://doi.org/10.1016/j.cscm.2021.e00754.

[47] J.W. Bullard, D.L. Evans, P.J. Bond, The Virtual Cement and Concrete Testing Laboratory Consortium The Virtual Cement and Concrete Testing Laboratory Consortium Annual Report 2003, 2003.

[48] H.H. Kolour, W. Ashraf, E.N. Landis, Hydration and early age properties of cement pastes modified with cellulose nanofibrils, in: Transp Res Rec, SAGE Publications Ltd, 2021: pp. 38–46. https://doi.org/10.1177/0361198120945993.

[49] Standard Test Method for Microscopical Determination of Parameters of the Air-Void System in Hardened Concrete 1, (n.d.). https://doi.org/10.1520/C0457_C0457M-16.

[50] ASTM Standard C39/C39M-21, Standard Test Method for Compressive Strength of Cylindrical Concrete Specimens, ASTM International (2021). https://doi.org/10.1520/C0039_C0039M-21.

[51] Y. Zhang, J.-C. Bilheux, H.Z. Bilheux, J.Y.Y. Lin, An interactive web-based tool to guide the preparation of neutron imaging experiments at oak ridge national laboratory, J Phys Commun 3 (2019) 103003.

[52] I. Padureanu, D. Aranghel, G.H. Rotarescu, F. Dragolici, C. Turcanu, R. Brzozowski, M.

Stepinski, P.J. Szalanski, Z.A. Kozlov, V.A. Semenov, Structure and dynamics of confined H~ 2O and D~ 2O in cement paste matrix studied by quasielastic and inelastic neutron scattering, Romanian Journal of Physics 50 (2005) 551.

[53] G. Zhang, Y. Yang, H. Yang, H. Li, Calcium sulphoaluminate cement used as mineral accelerator to improve the property of Portland cement at sub-zero temperature, Cem Concr Compos 106 (2020) 103452. https://doi.org/https://doi.org/10.1016/j.cemconcomp.2019.103452.

[54] N. Nair, M.I. Haque, S. Siddique, R.I. Khan, W. Ashraf, K. Gourlay, S. Shah, Role of delignified and lignin-containing cellulose nanofibers in enhancing durability performances of portland cement composites, Cem Concr Compos 145 (2024). https://doi.org/10.1016/j.cemconcomp.2023.105316.

[55] G. Jakli, W.A. Van Hook, Isotope Effects in Aqueous Systems. Excess Thermodynamic Properties of 1,3-Dimethylurea Solutions in H2O and D2O, J Chem Eng Data 42 (1997) 1274–1279. https://doi.org/10.1021/je970163b.

Chapter 8. Conclusions and recommendations

8.1 Overview

This dissertation provides a comprehensive investigation into the durability performance of cementitious materials under Arctic environmental stressors, with a specific focus on the synergistic effects of freeze-thaw (F-T) cycles and chloride ingress. Given climate change's accelerating impacts, particularly in high-latitude regions such as Alaska, concrete structures are increasingly susceptible to degradation mechanisms that reduce service life and increase maintenance obligations. The research conducted in this dissertation was motivated by the need to enhance the long-term resilience of Arctic infrastructure.

The study was structured around three primary research aims: (1) understanding the mechanisms of F-T damage and chloride ingress in concrete, (2) improving cementitious material durability and repair strategies through novel additives and techniques, and (3) enabling real-time monitoring of pore water movement during F-T exposure. Six experimental studies were conducted and reported in Chapters 2, 3, 4, 5, 6, and 7 to achieve these goals, integrating advanced techniques such as Transmission X-ray Microscopy (TXM) and Neutron Radiography (NR) to reveal microstructural and time-dependent deterioration phenomena.

This dissertation has contributed to advancing the global understanding of how concrete infrastructure performs under extreme environmental stressors, such as freeze-thaw cycles and chloride exposure, which are increasingly established due to climate change. The integration of optimized curing practices, fiber reinforcement (PVA, CNF), and moisture-sensitive repair strategies has enhanced the durability and sustainability of cementitious systems across diverse climatic conditions. Moreover, the application of real-time neutron imaging to visualize pore water dynamics represents a methodological innovation that can be applied worldwide to better predict degradation and inform the design of resilient infrastructure. Together, these contributions support international efforts toward climate-adaptive, low-maintenance, and long-lasting concrete infrastructure.

8.2 Major findings

The major findings of this dissertation are as follows:

- ✓ **Impact of curing and fiber reinforcement:** Conventional air-entrained concrete outperformed PVA fiber-reinforced concrete in resisting F-T damage and chloride ingress due to a more robust air-void system. Longer curing durations significantly improved resistance across all metrics, underscoring the importance of adequate curing in cold-region applications.
- ✓ **Combined effects of seawater and F-T exposure:** Synergistic seawater exposure and F-T cycling significantly accelerated deterioration, increasing chloride ingress, mass loss, and decreasing RDME. F-T damage increased permeability, while chlorides weakened the microstructure, compounding overall degradation. These results underscore the need for protection strategies that resist chloride penetration and F-T

damage, such as optimized air-void systems and extended curing duration in the arctic coastal concrete structure.

- ✓ **Role of CNF gels:** CNF suspensions prepared *via* nitro-oxidation create hydrogel-like networks within the cement matrix, aided by ionic interactions with metal ions from the pore solution. These networks improved F-T resistance and reduced chloride diffusivity. TXM confirmed slower chloride diffusion and a denser microstructure in CNF-modified systems, indicating enhanced durability.
- ✓ **Durability of concrete repairs:** Repair overlays with lower water-to-cement (w/c) ratios applied to saturated surface-dry (SSD) substrates demonstrated superior mechanical performance and reduced chloride ingress. The overlay transition zone (OTZ), identified as the weakest region, benefited significantly from moisture optimization and mix design adjustments.
- ✓ **Neutron radiography for real-time pore water monitoring:** *In situ* neutron imaging successfully captured water movements in concrete pores during freezing. Water was observed to move upward ahead of the freezing front, which can generate hydraulic pressure and induce microcracking. This provides the first *in-situ* neutron imaging evidence of water dynamics as a function of freezing contributing to F-T damage.

8.3 Significance and study importance

This dissertation makes several significant contributions to the field of concrete durability and infrastructure resilience:

- ✓ The first application of TXM to chloride ingress in concrete exposed to F-T cycles, offering a non-destructive means to quantify ion diffusion under complex exposure conditions.
- ✓ Using *in situ* neutron radiography for the first time in the literature to monitor pore water movement during freezing in cementitious materials provides critical *in-situ* data on hydraulic pressure development and damage onset.
- ✓ Introduction of CNF-based cement paste systems, derived from bio waste, as a sustainable approach to improving F-T resistance and reducing ion diffusion.
- ✓ Mechanistic understanding of repair performance under F-T conditions, establishing repair practices for optimizing bond durability through moisture control and mix proportioning.
- ✓ Integration of performance metrics (*e.g.*, RDME, UPV, SR, D_c) with imaging, mechanical, and fracture analysis to comprehensively assess cementitious material response against F-T damage.

Together, these contributions support the development of advanced resilient concrete systems and maintenance practices tailored to the demands of Arctic and coastal environments.

8.4 Recommendation for future work

Based on this dissertation's findings, several opportunities exist to expand understanding and enhance the applicability of the proposed approaches. The following recommendations are

offered for future work to refine cementitious material performance in Arctic coastal regions and support practical implementation.

- ✓ Further research should focus on optimizing the dosage and dispersion of PVA fibers to preserve the integrity of the air void system in F-T environments. Controlled studies aligning air content between fiber and non-fiber mixes are needed to isolate fiber effects and clarify their role in F-T resistance and chloride ingress.
- ✓ A more detailed examination of the fiber-cement paste interface and air-void stability using SEM, nano-CT, or μXCT could reveal critical insights into microcrack development under cyclic freezing, especially in fiber-reinforced systems.
- ✓ Investigate the long-term behavior, chemical interaction, and pore structure of different CNF-based cementitious materials, particularly under repeated F-T and chloride exposure.
- ✓ Future studies should examine a broader range of moisture conditions, repair materials (including fibers and air entraining admixtures), and extended F-T cycles to assess the durability of the overlay transition zone (OTZ).
- ✓ The chloride diffusion coefficients obtained using TXM under F-T conditions could be integrated into predictive multi-physics models to simulate long-term deterioration scenarios in Arctic environments.
- ✓ Future work should cover high-capability neutron imaging with improved spatial resolution and neutron flux to enhance image quality and capture detailed microstructural and moisture changes. It should also include integrating humidity and pressure sensors, and examining various concrete mix designs, including air-entrained and non-air-entrained samples, to better understand moisture distribution, pore dynamics, and freeze-thaw damage mechanisms under realistic conditions.
- ✓ Finally, Pilot-scale or field implementation studies should be conducted in Arctic and sub-Arctic environments (*e.g.*, Alaska) to validate laboratory results under real service conditions, particularly in curing, exposure sequencing, and combined degradation mechanisms.

8.5 Limitations

This dissertation presents novel findings on the durability of cementitious materials under Arctic exposure conditions using advanced testing and imaging techniques. However, several limitations were identified across the experimental studies:

- ✓ The study focused on a fixed set of concrete mix designs. Supplementary cementitious materials-based concretes, alternative binder systems, and recycled aggregate concretes were not considered, limiting the applicability of the results to a broader range of material classes.

- ✓ PVA fiber dispersion, alignment, and interaction with air entrainment were not directly characterized. Reduced workability and possible fiber clustering may have interfered

with air bubble formation and stability. Air content was not equalized between fiber and non-fiber mixes, making it difficult to isolate the specific effects of fiber inclusion on freeze-thaw and chloride resistance. No SEM or XCT analysis was performed to examine the fiber–paste interface.

- ✓ CNF suspensions were evaluated only in cement paste systems. Their performance in mortar or concrete, including interactions with aggregates, workability effects, and scaling behavior, was not investigated. This limits the direct applicability of findings to structural-scale concrete.
- ✓ Repair-substrate interfaces were cast under well-controlled laboratory conditions without any surface preparation. This approach does not reflect field-relevant factors such as substrate roughness, ambient humidity, or temperature gradients, which could significantly influence the durability of the OTZ.
- ✓ While RDME, UPV, SR, and mechanical strength tests were used to assess F-T durability, no real-time techniques (*i.e.*, strain gauges) were employed to monitor damage initiation and progression during F-T cycling.
- ✓ In the neutron radiography experiments, beam hardening artifacts and limited neutron transmission affected image quality and reduced the quantitative resolution for tracking water movement. These limitations compromised the spatial accuracy of moisture redistribution measurements during freezing. Additionally, relative humidity (RH) sensors embedded in the specimens failed under subzero conditions, preventing *in-situ* monitoring of internal moisture profiles. Furthermore, elevated ambient temperature at the ORNL MARS beamline hindered the cooling stage from reaching the target subzero temperature before imaging, which delayed the initiation of pore water freezing and affected the initial conditions of the experiment.

8.6 Practical applications

The findings of this dissertation have direct implications for improving the resilience and service life of concrete infrastructure in Arctic and coastal environments:

- ✓ The demonstrated influence of extended curing and air void optimization supports the importance of tailored mix design and curing protocols in Arctic concretes. These findings support updates to the mix guidelines for the Alaska Department of Transportation (AKDOT), the United States Army Corps of Engineers (USACE), and municipalities in cold regions.
- ✓ The interference of PVA fibers with air entrainment highlights a key trade-off between improving mechanical strength and preserving F-T durability. These findings guide fiber selection and dosage for AEA-based concrete mix in Arctic regions.

- ✓ The successful use of bio-based CNF suspensions to improve F-T and chloride resistance suggests a promising, sustainable additive for cold-weather concrete. CNFs can be incorporated into concrete used for DOT pavement repairs, airfield slabs, and coastal structures to enhance F-T durability and reduce chloride penetration in harsh environments.
- ✓ Findings on the performance of OTZ under F-T exposure provide a framework for optimizing surface preparation, moisture conditioning, and w/c ratio selection during patch repair. This can inform Arctic concrete repair protocols for airfields, bridges, and ports.
- ✓ TXM can analyze concrete cores from pavements, airfields, or bridge decks to develop time-dependent ion ingress rates. This helps government agencies and engineers assess how well structures resist chloride ingress over time and supports decisions on maintenance, repair, or material upgrades in Arctic and coastal environments.
- ✓ Neutron imaging provides critical insights into the timing of pore water movement and temperature changes during freezing at specific locations within concrete. This information can help design teams better understand F-T dynamics, predict damage risk more accurately, and optimize mix design for Arctic-resilient concrete.

Together, these applications highlight the value of this research in guiding the design, repair, and assessment of durable concrete infrastructure for Arctic and coastal regions.